

1949

Integration of Remotely Sensed Data and Field Studies for Lithological and Structural Mapping of Orogenic Gold Occurrences in the Barramiya–Mueilha Sector, Central Eastern Desert, Egypt

Thesis for the Degree of Doctor of Philosophy (PhD)

by

Ali Shebl Ali Elshazly Rady

supervisor: Dr. Árpád Csámer

UNIVERSITY OF DEBRECEN
Doctoral Council of Natural Sciences and Information Technology
Doctoral School of Earth Sciences
Debrecen, 2024

Hereby I declare that I prepared this thesis within the Doctoral Council of Natural Sciences and Information Technology, Doctoral School of Earth Sciences, University of Debrecen in order to obtain a PhD Degree in Natural Sciences/Earth Science. The results published in the thesis are not reported in any other PhD theses.

Debrecen, 06 June 2024 …….

signature of the candidate

Hereby I confirm that Ali Shebl Ali Elshazly Rady candidate conducted his studies with my supervision within the Natural and anthropogenic processes of the lithosphere and hydrosphere Doctoral Program of the Doctoral School of Earth Sciences between 2020 and 2024. The independent studies and research work of the candidate significantly contributed to the results published in the thesis. I also declare that the results published in the thesis are not reported in any other theses. I support the acceptance of the thesis.

Debrecen, 06 June 2024 …….

signature of the supervisor

Integration of Remotely Sensed Data and Field Studies for Lithological and Structural Mapping of Orogenic Gold Occurrences in the Barramiya–Mueilha Sector, Central Eastern Desert, Egypt

Dissertation submitted in partial fulfillment of the requirements for the doctoral (PhD) degree in Earth Sciences

Written by **Ali Shebl Ali Elshazly Rady** certified by degree of Master of Geology

Prepared in the framework of the Doctoral School of Earth Sciences of the University of Debrecen, Natural and anthropogenic processes of the lithosphere and hydrosphere Doctoral Program

Dissertation advisor: Dr. Árpád Csámer

The official opponents of the dissertation:

Dr. …….. ……

Dr. …….. ……

The evaluation committee:

Chairperson:	Dr. ……..	……
members:	Dr. ……..	……
	Dr. ……..	……
	Dr. ……..	……
	Dr. ……..	……

The date of the dissertation defence:…….20….

DEDICATION

To the everlasting soul of my father, a great soul that never dies.

That man is a success –who has lived well, laughed often, and loved much.

Who has gained the respect of intelligent men and the love of children,

and accomplished his task.

Who leaves the world better than he found it,

who looked for the best in others and gave the best he had.

TABLE OF CONTENTS

CHAPTER 1: INTRODUCTION 9

1.1 THE STUDY AREA WITHIN REGIONAL GEOLOGICAL CONTEXT 10
1.2 RESEARCH NOVELTY AND SCOPE OF THE PRESENT STUDY 13

CHAPTER 2: MATERIALS AND METHODS 14

2.1 MATERIALS USED 14
2.2 METHODS 15
2.2.1 Image Processing Techniques 15
2.2.2 Machine Learning Algorithms (MLAs) 16
2.2.3 Structural Analysis 23
2.2.4 Airborne geophysical data processing methods 23
2.2.5 SEM-EDX 25
2.2.6 Whole-rock geochemistry 26

CHAPTER 3: GEOLOGICAL SETTING 27

3.1 OPHIOLITIC GROUP 27
3.1.1 Serpentinites and talc-carbonate rocks 28
3.1.2 Ophiolitic metagabbros 31
3.1.3 Ophiolitic mélange matrix 31
3.2 ISLAND ARC ASSEMBLAGE (METAVOLCANIC/VOLCANICLASTIC ROCKS) 33
3.3 METAGABBRO-DIORITE ROCKS 35
3.4 GRANITIC ROCKS 35
3.4.1 Syn-orogenic granitoids 36
3.4.2 Late-orogenic granites 36
3.5 DIKES 37
3.6 PHANEROZOIC SEDIMENTS 39

CHAPTER 4: RESULTS 40

4.1 LITHOLOGICAL MAPPING UTILIZING MULTISOURCE REMOTE SENSING DATA (MULTISPECTRAL) AND MACHINE LEARNING ALGORITHMS 40
4.1.1 Classification Results 40
4.2 LITHOLOGICAL MAPPING USING PRISMA HYPERSPECTRAL DATA AND ENSEMBLE MACHINE LEARNING (BAGGING AND BOOSTING) 43
4.2.1 Results 45
4.3 STRUCTURAL ANALYSIS 49
4.3.1 Results 49
4.3.2 Accuracy Assessment using Density and Validation Analysis 50
4.4 TEXTURAL ANALYSIS 54
4.4.1 Lithological mapping 54
4.4.2 Comprehensive structural analysis 55

4.5 Integrating Remote Sensing and Geophysics for Mineralized Zone Delineation 57
4.5.1 Relative Band Depths (RBDs) *57*
4.5.2 DPCA *59*
4.5.3 DPCA applied to Band Ratios *60*
4.5.4 Constrained Energy Minimization (CEM) *62*
4.5.5 Geophysical data findings *63*
4.5.6 Field verification and petrographic investigations *64*
4.6 Petrographic and geochemical characterization of the rock units 69
4.6.1 Petrographic investigations, XRD analysis, SEM-EDX, and Geochemical analysis *69*
4.6.2 Petrographic characteristics *69*
4.6.3 X-ray diffraction (XRD) investigations *78*
4.6.4 SEM-EDX *81*
4.6.5 Whole-rock geochemistry *86*

CHAPTER 5: DISCUSSION 101

5.1 Lithological mapping advancements 101
5.2 Structural analysis enhancements using lineament extraction. 102
5.3 Structural analysis enhancements using textural analysis. 103
5.4 Prospective mineralization identification 104
5.5 Mueilha's Rare-Metal bearing granite 107
5.6 Orogenic Gold Mineralization 109

CHAPTER 6: CONCLUSIONS 111

REFERENCES 113

ACKNOWLEDGEMENTS 127

APPENDICES 128

MOST IMPORTANT ACRONYM AND ABBREVIATIONS

ANS	Arabian Nubian Shield
CED	Central Eastern Desert
MLAs	Machine Learning Algorithms
FCC	False Color Composite
BR	Band Ratio
RBD	Relative Absorption Band Depth
DPCA	Directed Principal Component Analysis
CEM	Constrained Energy Minimization Method
MLC	Maximum Likelihood Classifier
ANN	Artificial Neural Networks
SVM	Support Vector Machine
RF	Random Forest
XGB	The extreme gradient boosting
RADI	filter radius
GTHR	edge gradient threshold
LTHR	curve length threshold
FTHR	line fitting threshold
ATHR	angular difference threshold
DTHR	linking distance threshold
RTP	reduction-to-pole
CET	Center for Exploration Targeting
OA	Overall Accuracy
VNIR	visible and near-infrared
SWIR	Short-Wave Infrared
CFT	Circular Feature Transform
ACT	Amplitude Contrast Transform

Chapter 1: INTRODUCTION

Throughout human life history, minerals in general and specifically gold have had a voluminous influence. For thousands of years, gold not only has been mined and used but also worshipped. For instance, one of the earliest known geological maps with gold mining insights dates back to the time of the Pharaohs, specifically from the 12th century BC. This map, known as the Turin Papyrus, depicts Egypt, the upper Nile, and the gold mines of Nubia. It illustrates the distribution of various rock units and provides information about quarrying and mining activities. The map was created for Ramesses IV's quarrying expedition to the Wadi Hammamat in the Eastern Desert, which is north of the study area and exposes the Precambrian rocks of the Arabian-Nubian Shield. The Wadi Hammamat rocks have documented these activities with hieroglyphic inscriptions since that time.

Currently, gold demand is as eager as ever. With the advent of new scientific technologies, tools, and datasets, exploration programs could make their best use in the investigation of different kinds of gold mineralizations and shed light on its associated co and by-products not only in greenfields but in brownfields as well. Therefore, the current study aims to integrate various remote sensing datasets, machine learning algorithms, geophysical measurements, fieldwork, petrographic investigations, and geochemical analysis in order to provide a dependable lithological and hydrothermal alteration mapping.

The process of selecting a suitable case study for the research venture was profoundly intriguing. Given our aspiration to introduce an innovative approach to lithological mapping, it was imperative that we chose an area of intricate terrain. This choice would enable us to rigorously test our findings within the context of complex landscapes, thereby substantiating the applicability of our outcomes in analogous terrains. Amidst the realm of possible options for case studies, one stood out with distinctive significance — the Arabian Nubian Shield (ANS). This geological treasure, renowned for its diverse mineral deposits encompassing gold, copper, rare earth elements, and more, had received significantly less attention than its mineral-rich counterparts in regions, such as Australia, Canada, the USA, and China. Consequently, a section of the Arabian Nubian Shield emerged as the prime candidate for my PhD research. This decision was predominantly influenced by the accessibility of the designated study area and the remarkable spectrum of lithological variations it offered. Situated in the southern expanse of the

Central Eastern Desert (CED), Egypt, this chosen study area is named the Barramiya–Mueilha sector.

The second major trigger for the current research is enhancing our national economy. Mining should be a key contributor to the Egyptian economy, providing a major boost to our financial sector as well as an engine for regional development and the creation of added value. Consequently, detecting and mapping new gold localities will enhance the economic resources of Egypt which are considered a foothold on the way toward the inclusive and Sustainable Development Strategy (SDS) of Egypt's Vision.

1.1 The study area within regional geological context

The current study area is situated in the Eastern Desert of Egypt (Figure 1-1). The latter (Eastern Desert) together with a considerable part of southern Sinai constitutes the main Egyptian Precambrian lithologies of the Nubian shield, which in turn is a part of ANS. Arabian Nubian Shield is considered one of the enormous Neoproterozoic juvenile crust exposures on our planet [1]. During the East-African orogeny, the ANS took shape through the amalgamation of island arcs resulting from the convergence of East and West Gondwana and the closure of the Mozambique Ocean. Subsequently, and due to a crustal extension, considerable granitoid magmas have been intruded and post-amalgamation depositional basins were generated [2]. To the west of the Red Sea, the ANS spans from Egypt to Ethiopia, passing through Sudan and Eritrea (Figure 1-2a). On the eastern side of the Red Sea, the ANS stretches from Palestine to Yemen, traversing Jordan and Saudi Arabia.

Generally, the Egyptian Precambrian basement rocks are a consequence of complicated magmatic, sedimentary, and metamorphic processes (Proterozoic orogenic evolution) following terrane collision and accretion onto a pre-Pan-African continent to the west of the Nile [3]. As a result of this collision, a regional metamorphic effect is proposed by Finger and Helmy [4] between 650 and 620 Ma. A bit closer to the study area, it stretches from latitude 24° 48" to 25° 19" N, and longitude 33° 48" to 34° 05" E (Figure 1-2b). The study area is located between the Nile and the Red Sea. It is situated about 95 km and 105 km from Idfu, and Marsa Alam cities, respectively. The Barramiya–Mueilha sector is fairly accessible. It can be reached through the Idfu–Marsa Alam asphaltic high road. Numerous well-developed wadis dissect the study area. The wadis are the essential entrances to the area and are named from north to south Wadi Miyah,

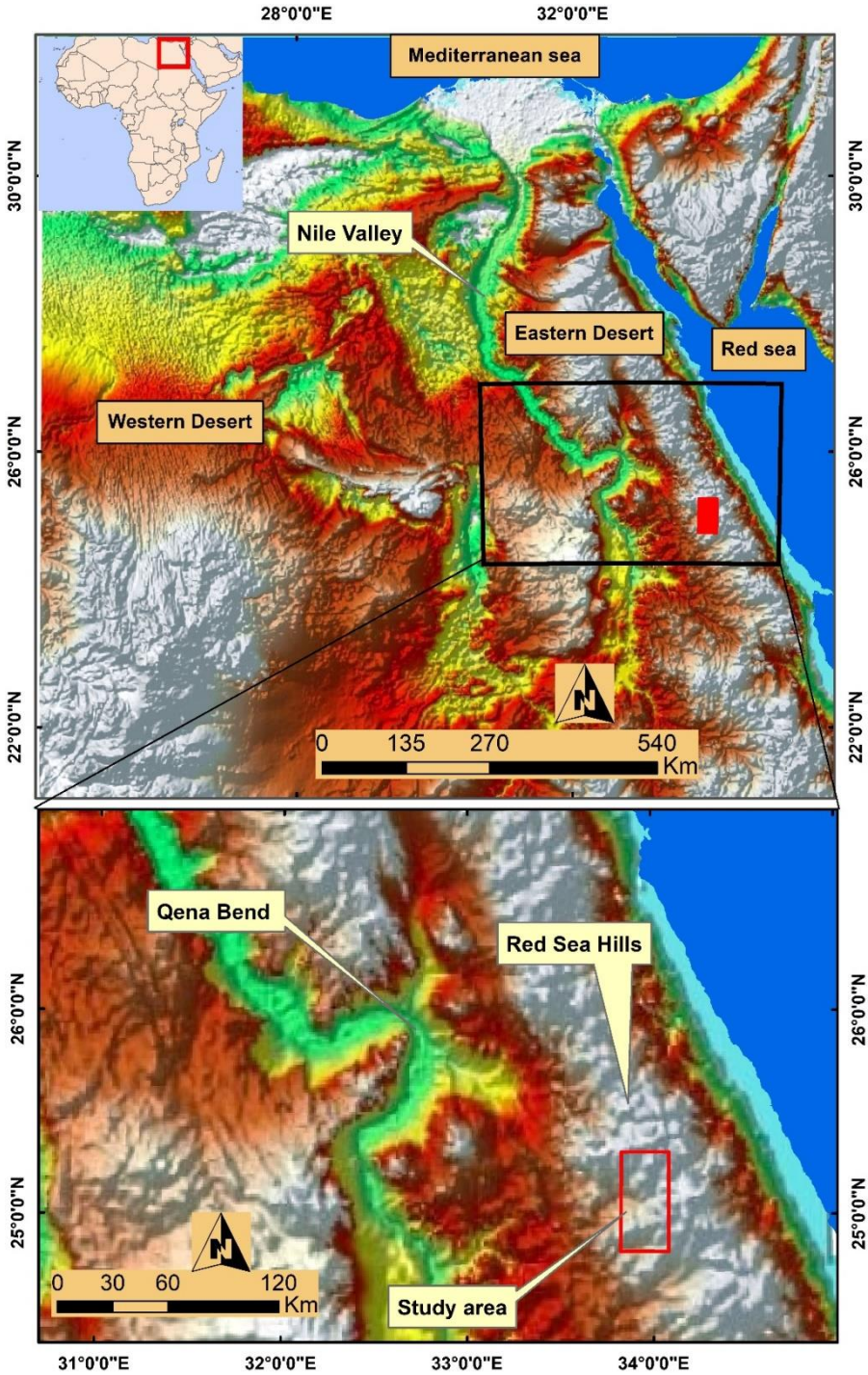


Fig. 1-1: Location of the study area (red rectangle over the Egyptian Eastern Desert).

Wadi Barramiya, Wadi Beizah, Wadi Dungash, Wadi Mueilha, and Wadi Rod El-Liqah (Appendix. 1-1).

From the Digital Elevation Model (DEM) and our field observations, the study area is mountainous (Appendix. 1-1). The most conspicuous peaks of the considered area are Gabal Barramiya (668 m), Gabal Um Salatit (659

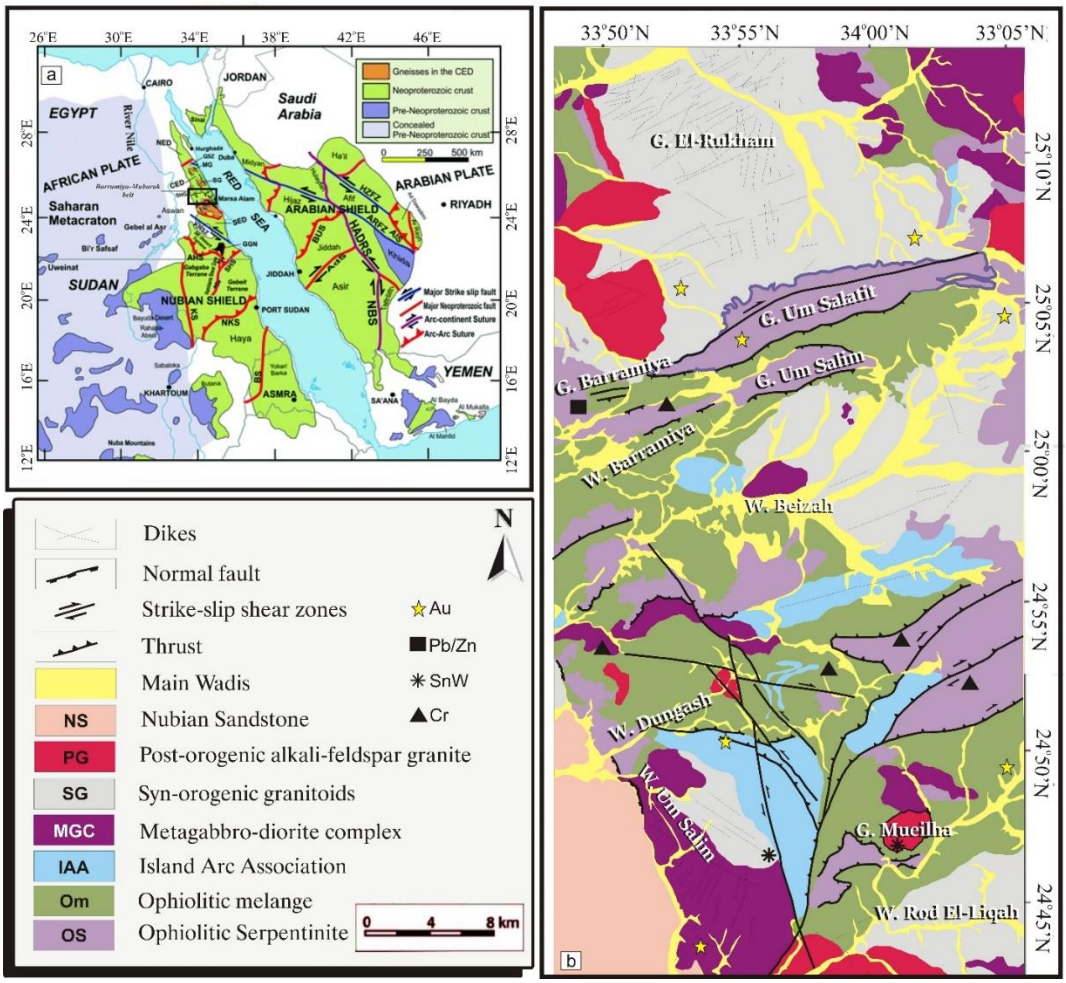


Fig. 1-2: (a) Simplified geological map of the Arabian Nubian Shield showing the location of the Barramiya-Mubarak belt (small black rectangle) where the study area is located, and (b) a geological map of the study area showing its lithological units.

m), and Gabal Um Salim (653 m), which are composed of serpentinite rocks mainly. Gabal El-Rukham (694 m) is represented by a locally sheared syn-orogenic granitoid, and Gabal Mueilha (450 m) primarily consists of post-orogenic alkali-feldspar granite.

1.2 Research novelty and Scope of the Present Study

To ensure a scientific novelty in the study area, findings of the most relevant previous works [5–12] have been carefully studied to formulate a strong scientific background for the study area from different aspects. Considering these previous studies, novel techniques are proposed in the current research that prove their applicable eligibility over and beyond the limits of the considered area. This study aimed to create detailed lithological maps, identify gold mineralization and hydrothermal alteration zones, and to assess of the influence of geological structures on mineralization were aimed. This approach combines remote sensing (optical, radar, DEMs), and geophysical data, GIS, fieldwork, petrographic analysis, mineralogical investigations, image processing, machine learning, and textural analysis. Towards our aim, several datasets and techniques are integrated to achieve the following aspects:

1. Detailed lithological mapping with the power of machine learning algorithms (MLAs) and remote sensing data. A novel approach was proposed by supplementing optical, radar, and DEMs to deliver reliable lithological mapping. Additionally, the effect of data dimensionality in delivering accurate results will be assessed.
2. Lithological mapping by using PRISMA hyperspectral data, and ensemble machine learning (Bagging and boosting).
3. Comprehensive lithological and structural analysis using textural parameters over Sentinel 2 and PRISM data. This analysis was proposed using a single-band analysis to avoid data dimensionality and check its reliability in detecting faults, folds, foliations, and lineaments.
4. Exhaustive lineaments extraction investigations with special emphasis on spatial resolution effect by comparing nine different remote sensing datasets.
5. Delineation of hydrothermal alterations from different datasets and comparing the highly altered zones with structural results and aeromagnetic anomalies using spatial overlay analysis.
6. Microscopic investigations including petrographic study, X-ray powder diffraction (XRD), scanning electron microscopy with energy dispersive X-ray spectroscopy (SEM-EDX), and whole-rock geochemistry for major, trace, and rare earth element distribution.

Chapter 2: MATERIALS AND METHODS

2.1 Materials Used

To realize the objectives of the present study, the following materials and datasets were used:

1. Remote sensing data, diversifying information sources, and increasing the sheer amount of available remote sensing data ensure better results. Thus, the following datasets are integrated or occasionally used for comparison:
    a) **A**dvanced **S**paceborne **T**hermal **E**mission and **R**eflection **R**adiometer (ASTER)[13]
    b) Landsat-8 (L8) or Landsat **O**perational **L**and **I**mager (OLI)[14]
    c) Landsat-9 (L9) or Landsat **O**perational **L**and **I**mager-2 (OLI-2) [15]
    d) Earth Observing-1 **A**dvanced **L**and **I**mager (ALI)[16]
    e) Sentinel 2 (S2)[17]
    f) Sentinel 1 (S1)[18]
    g) **S**huttle **R**adar **T**opography **M**ission (SRTM) DEM [19]
    h) **N**ational **A**eronautics and **S**pace **A**dministration (NASA) DEM [20]
    i) ASTER –**G**lobal **D**igital **E**levation **M**odel (ASTER GDEM)[21]
    j) **A**dvanced **L**and **O**bserving **S**atellite (ALOS) with its **P**hased **A**rray **L**-type band **S**ynthetic **A**perture **R**adar (PALSAR) [22]
    k) ALOS with its **P**anchromatic **R**emote-sensing **I**nstrument for **S**tereo **M**apping (PRISM)[23]
    l) PRISMA (**PR**ecursore **I**per**S**pettrale della **M**issione **A**pplicativa or Hyperspectral Precursor of the Application Mission) hyperspectral data [24,25].
    m) **En**vironmental **M**apping and **A**nalysis **P**rogram (EnMAP) hyperspectral data[26].

All of these datasets are utilized and described in more detail in our following published papers [27,28,37–40,29–36]. The source of L8, ASTER, SRTM DEM, and ALI is the U.S. Geological Survey Earth Resources Observation and Science Center (EROS) (https://earthexplorer.usgs.gov/). NASA DEM was obtained from the USGS web-based data

(https://lpdaac.usgs.gov/) and ALOS PALSAR from the Alaska Satellite Facility (https://asf.alaska.edu/). Sentinel 1 and Sentinel 2 data were attained through the ESA open data hub. PRISMA and EnMap data were available through their official hubs on https://prisma.asi.it/missionselect/ and https://www.enmap.org/ respectively.

2. The topography and geological settings based on formerly available data (e.g., topographic, and geological maps [6–12,41–43]).
3. Airborne geophysical data. The data included in this study is blended with the airborne magnetic and gamma-ray spectrometric survey. This survey was carried out by the Aero Service Division of Western Geophysical Company of America back in 1983 [44].
4. Collecting representative rock samples including mineralized quartz veins and different alteration types for preparing thin, thick, and polished sections for further investigations.
5. Field observations of complicated lithological associations including intrusion contacts, relative age determinations, cross-cutting relationships besides other old mining activities and current random and placer mining works.

2.2 Methods

2.2.1 Image Processing Techniques

2.2.1.I False Color Composite (FCC)

FCC is a traditional image processing technique that can significantly improve image visualization by introducing suitable bands (wavelengths) into the RGB channels to create a color composite image. The selected wavelengths for each FCC depend mainly on the exposed rock units; however, SWIR bands are mostly useful in geological applications [45].

2.2.1.II Band ratio (BR) and Relative Absorption Band Depth (RBD)

The Band ratio is a robust method for distinguishing various rock and mineralogical categories by enhancing spectral differences and mitigating topographical effects[46]. It is executed by dividing the digital number values of one band by the corresponding values of another band and displaying the result as a grayscale image that reflects relative band intensities[47]. Relative Band Depth (RBD) is the proportion between the sum of the bands at the shoulders of a specified absorption peak and the band closest to the peak [48].

2.2.1.III Directed Principal Component Analysis (DPCA)

It is a powerful method for extracting features. Principal component eigenvector loadings of linked feature bands are the main focus of DPCA, sometimes referred to as feature-oriented principal component analysis[49]. The primary distinction between DPCA and PCA is that the latter uses a subset of bands to highlight a particular feature; in other words, the bands that are chosen for analysis are closely associated with the target. Bands are chosen and analyzed using DPCA based on the spectral range of each band and the target alteration type [50].

2.2.1.IV Constrained Energy Minimization Method (CEM)

CEM is a spectral mapping technique for mineral localization that primarily employs a finite impulse response filter to minimize background noise while allowing only the targeted signals to pass through [27,51]. CEM is widely used in geological and hydrothermal alteration mapping with ASTER data. The CEM algorithm was applied to the relevant ASTER SWIR bands to validate and identify the dominant hydroxyl-bearing minerals within the observed hydroxyl-altered zones, providing additional details and confirming the presence of alteration minerals.

2.2.2 Machine Learning Algorithms (MLAs)

Without a doubt, MLAs have found their way in several applications and provided outstanding results for several studies in various disciplines. MLAs could be simply defined as automated inference frameworks that could infer hidden and inherited data patterns [52]. To the best of our knowledge, the current contribution reports for the first time the findings of three well-known machine learning algorithms (Artificial Neural Network or ANN, Maximum Likelihood Classifier or MLC, and Support Vector Machine or SVM) over hybrid datasets including multispectral (S2, L8, ALI, and ASTER), radar (S1, ALOS PALSAR), and DEM derivatives (Slope, Aspect). Additionally, our results monitor the relationship between the data dimensionality and the adopted training data [29]. Additionally, with the PRISMA hyperspectral data, we used more robust algorithms like RF and XGB to prevent overfitting and computational issues associated with hyperspectral data.

2.2.2.I Data cleaning and preprocessing

Remote sensing data should be preprocessed based on its characteristics. For instance, multispectral data were atmospherically and

geometrically corrected. Speckle filtering was applied to radar data to decrease the noise. DEMs were filled and checked with the topographic maps and real elevation measurements in the field to ensure the real pixel value representations. Additionally, all the available geological maps should be georeferenced to the same coordinate system, to provide a useful tool for extracting training and testing data from our raster datasets. So, at this stage, our datasets are ready (numerical, clean, resized, and preprocessed by applying several image processing techniques and selecting their best results), now we can teach the classifier about our classes through some training data and specify some testing data to check his performance after fulfilling the task.

The input raster data to MLAs (ANN, MLC, and SVM) include Sentinel 2, ASTER, Landsat OLI, Earth-observing 1 Advanced Land Imager, Sentinel 1, ALOS PALSAR-1, ALOS PALSAR DEM, Slope, and Aspect and their combinations. These hybrid datasets are reprojected to the same coordinate system (WGS 1984, Zone 36) to ensure that every pixel in the dimensional space has the same location. Cubic convolution resampling to a pixel size of 20 meters is then performed. Combining spectral information (such as from optical sensors) with non-spectral information (such as DEMs and radar) results in extended pixel vectors created using the stacked-vector method described by Richards and Jia, (1999) [53]. On the other side and for hyperspectral data, three data inputs of PRISMA including 1-2PC (the former 2 PCs), 1-4PC (the first 4 PCs), and 234bands (all the utilized bands) are used for classification using SVM, XGB, and RF. These inputs were used with PRISMA as it is critical to introduce improved input, especially with hyperspectral remote sensing data to get reliable classification as stated by Pal and Foody, (2010) [54]. Furthermore, dimensionality-reduction methods like PCA offer a far better diagnosis for our lithological targets.

2.2.2.II Training and Testing Datasets

At this level, we have to assign two parts to the datasets (splitting). Training datasets are utilized to make our classifier learn about the data and create certain patterns that link some input features with a certain output (i.e., building a relationship between the inputs and outputs). To make learning easier, sometimes a feature extraction and selection phase is adopted. This is performed by somehow highlighting the important features that have a notable correlation with the outputs. This could be achieved through a variety of image processing techniques, such as false color combinations, principal component analysis, independent component analysis, minimum

noise fraction, etc. Their results introduced an effective reference geological map that is critical for better sampling and feature selection, which is in turn pivotal for improving classification accuracy [55]. Then the selection of training pixels, as georeferenced polygons or points for each class. It could be achieved using several software or platforms (e.g., Google Earth Engine). In our case, training and testing samples were delineated as georeferenced polygons, comprising approximately 70% to 80% for training and 30% to 20% for testing, respectively [56]. This approach ensured that area-wise training samples, ranging between 70% and 80%, were selected for each rock unit. These pixels are introduced with the data to the classifiers for the fitting process. The implemented models include Maximum Likelihood Classifier, Artificial Neural Networks, Support Vector Machine, Random Forest, and Extreme Gradient Boosting (XGBoost). Only SVM, XGB, and RF were applied with PRISMA hyperspectral data, while MLC, along with ANN, was excluded due to its higher computational power requirements and unsatisfactory results (after several trials).

2.2.2.III Maximum Likelihood Classifier (MLC)

One of the widely used, and reasonably efficient conventional supervised classifiers. It is a statistical parametric method for classifying the pixels according to their probability functions, i.e. a pixel is assigned to a certain class if it has the maximum likelihood for that class according to several equations described in detail in previous studies [29,53]**.** In a practical sense, training data is selected by the user/supervisor and then introduced (after numerical analysis) to MLC which assumes a Gaussian or normal distribution for these data. Based on a probability function that computes the probability or likelihood of each pixel being associated with a specific target, further pixels or data could be assigned to their classes. This could be achieved by giving a class membership for each pixel during the classification/generalization process. This class membership is given to the pixel based on the relative similarity or likelihood of the pixels with the previously computed class probability function (using training data). In case of signature overlapping for a certain pixel among different classes, the same criterion will be applied where the pixel is classified to the class possessing the higher probability. Thus, MLC is considered a decision criterion based mainly on statistical analysis [57].

2.2.2.IV Artificial Neural Networks (ANN)

Several researchers think about developing artificial intelligence just by mimicking the human brain, which works through an interconnected and

complicated network of neurons. That is why we could see several types of neural networks in artificial intelligence and machine learning studies trying to simulate the self-organized human brain, which has a robust performance through handling complicated, parallel and non-linear computations [58] . Consequently, several types of neural networks including Artificial Neural Networks (ANN), Recurrent Neural Networks (RNN), and Convolution Neural Networks (CNN) are developed.

In the current study, ANN was implemented to classify the lithological targets within the study area, as several studies report better results from ANN than MLC over remote sensing data [59,60]. ANN might be described as a massive processor constituted of simple processing units that have the propensity for knowledge storing [61]. From two main perspectives, ANNs imitate the human brain by 1) acquiring knowledge from the environment through a learning process, and 2) storing the acquired knowledge through synaptic weights or interneuron connection strengths [58,61]. Similar to the human brain, the neuron is the main computational unit of ANN and could be calculated through the following equation [58]:

$$v_k = \sum_{j=0}^{m} w_{kj} x_j$$

$$y_k = \varphi(v_k)$$

Eq. 1

where each neuron has a set of inputs (x1, …, xm) the connection from the input to the neuron is controlled by a synaptic weight, then connected to neuron K, and finally, the outputs are passed through an activation function for handling and limiting. Several activation functions are well-known, e.g., threshold, piecewise-linear, sigmoid, and hyperbolic, and are described in detail in previous literature [58].

2.2.2.V Support Vector Machine (SVM)

SVM is still one of the hotspots in machine learning as it provides outstanding results for almost all machine learning applications including outliers detection, nonlinear classifications, and regression. However, it was developed by Cortes and Vapnik, (1995) [62], as a binary classifier SVM that can achieve multiclass allocation efficiently. SVM basically depends on the precise allocation of the optimal separator hyperplane between two classes.

This is fulfilled by keeping the points representing the two classes as separated as possible by pushing the boundaries between them to the maximum (margin). By maximizing the latter, the peripheral points (support vectors) define the margin where the optimal hyperplane could be determined at the middle distance between these support vectors as shown in (Figure 2-1) [63]. This is the simplest case for SVM, however, in practical applications, some data points of a particular class are seen on the wrong side leading to a kind of class overlapping and misclassifications. To overcome this issue, SVM introduces a soft margin option to minimize the effect of these data points by reducing their weights. The soft margin is a good solution to minimize misclassifications, however, it is much better to keep it as small as we can to achieve the best results. Additionally, SVM could handle higher dimensional data and overcome nonlinearity by introducing a kernel that could efficiently separate the higher dimensional data [63]. Simply, the kernel could fulfill a kind of linear separation of higher dimensional data in high dimensional space. Selecting a convenient kernel and parameters plays a pivotal role in getting better results. The radial basis function (RBF) was found to be well-suited for several equivalent uses [29,30,36,64].

Generally, the kernel technique is often used to better analyze non-linear data patterns through a set of algorithms that depends mainly on a particular function [65]. The basic concept of the kernel function is transforming the original data space to a kernel space specified through a user-defined feature map. Thus, a proper kernel (e.g., radial bias, polynomial, etc.) and its suitable parameters (e.g., sigma in the RBF kernel) should be carefully specified when adopting a kernel-based classifier.

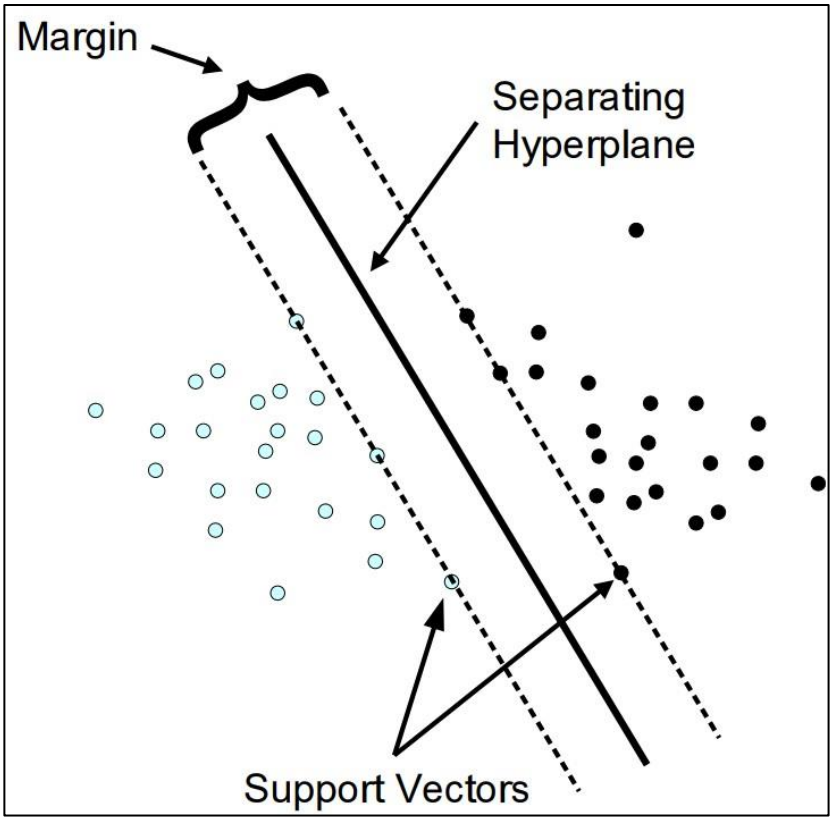


Fig. 2-1: Basics of SVM classification, after Meyer, (2015) [63].

2.2.2.VI Random Forest (RF)

Random Forest (RF) has emerged as among the most broadly embraced ensemble algorithms in the realm of remote sensing data analysis. The nomenclature itself, "forest," succinctly captures its essence: RF constitutes a collection of Classification and Regression Trees (CARTs) employed for predictive tasks [66]. Each individual tree operates autonomously to forecast a label for every data point. The amalgamation of decisions, typically through voting and averaging of class probability assignments from all trees, culminates in the final label for that particular data point. Subsequently, the algorithm transitions to processing another unlabeled data point, forecasting its corresponding label. Functioning as a bagging technique, RF utilizes approximately two-thirds of the available data (chosen at random) for training purposes, reserving the remaining third for internal validation, a mechanism to continually assess the algorithm's performance.

The optimal configuration of RF involves tuning several parameters, contingent on the field of study, the targets being predicted, and the intrinsic traits of the dataset. The number of trees, a user-defined parameter, varies across applications. Similarly, users can specify the criteria that guide tree splitting, which significantly influences predictive accuracy. Prior research findings underscore that the precision of RF predictions is more responsive to the parameters governing tree growth and splitting, compared to the number of trees in the ensemble [67–69].

Within the framework of this study, optimal results (based on a trial and error strategy; trying a wide range of parameters and checking the resultant thematic maps, besides considering previous RF research in similar applications) were achieved by setting the parameters as follows: 100 estimators, -1 job, and 500 trees. This configuration reflects an informed choice based on empirical experimentation and careful consideration of the dataset's characteristics.

2.2.2.VII The extreme gradient boosting (XGBoost)

Termed "Boosting" for its inherent nature, these algorithms offer a form of augmentation to weak learners by adjusting the weights attributed to misclassifications, progressively approaching an optimal configuration of these weights in the final outcome. This augmentation results in an overall enhancement of the final prediction, achieved by amalgamating weighted votes from successive iterations for a specific classification [70]. Boosting encompasses a range of models, including categorical boosting, gradient boosting machine, light gradient boosting machine, adaptive boosting, and XGBoost, all of which have gained recognition and found utility across diverse applications [71].

Of these, XGBoost stands out as a significant advancement beyond both bagging and previously mentioned boosting algorithms. Its innovation lies in mitigating overfitting through a regularization process, while simultaneously delivering accelerated performance through the implementation of parallel processing, utilizing the CPU's multi-threading capabilities to manage nodes more efficiently [72]. Demonstrating efficacy across various domains, XGBoost has yielded favorable outcomes in a multitude of applications. Examples include PM2.5 prediction [73], remote sensing classifications [74,75], mapping plant species diversity [76], estimating forest aboveground biomass [77], assessing flash flood hazards [78], and geological mapping [79,80].

In the context of the current research, our approach entailed adopting XGBoost with default parameters, with the sole specification being the use of "multi:softprob" as the objective. The values for n_jobs, learning_rate, max_depth, n_estimators, and booster type are as follows: 1, 0.3, 6, n_estimators, and 'gbtree'. The regularization parameters including gamma, reg_alpha, and reg_lambda, are set to 0, 0, and 1, correspondingly. The algorithm may select the optimal technique depending on the data because the tree_method is set to 'auto'. This measured choice of parameters aligns with the specific needs of our study and underscores XGBoost's robustness in handling the complexities of our dataset.

2.2.3 Structural Analysis

2.2.3.I Automatic Lineament Extraction

LINE module within PCI Geomatica software is utilized to perform this task, and several parameters are necessary to determine which pixels, edges, and curves should be considered in order to achieve a reasonable level of lineament extraction. These parameters include RADI (filter radius), GTHR (edge gradient threshold), LTHR (curve length threshold), FTHR (line fitting threshold), ATHR (angular difference threshold), and DTHR (linking distance threshold) as shown in Table 1 (Appendix). The basis of this technique is the examination of pixel images' background features [81]. For that, a vast array of threshold value combinations for the six parameters were evaluated. The most appropriate ones were chosen based on factors like direction, density, and lineament length. The correspondence between the detected lineaments and known features in the study area was the most crucial criterion.

2.2.3.II Textural analysis

Through this second-order statistical analysis, several attributes including mean, variance, homogeneity, contrast, entropy, and correlation are calculated to highlight the main structural features within the study area [82–85].

2.2.4 Airborne geophysical data processing methods

The geophysical data have been processed into reduction-to-pole (RTP) magnetic data, potassium counts (K), and equivalent thorium concentrations (eTh), as shown in Figures 2- 2a, 2- 2b, and 2- 2c respectively. These data maps have provided a clearer representation of the boundaries

between different lithologies and have allowed for more direct identification of magnetic and radiometric features in the study area. This enhanced visualization has enabled the more precise recognition of various geological structures like faults, contacts, and shear zones.

Since the primary objectives of utilizing the airborne geophysical data are to validate the observed alteration zones and create a structural framework map, the following methods are employed to achieve these goals:

a. The Center for Exploration Targeting (CET) porphyry analysis, which involves a three-stage process (detection of circular features, enhancement of boundaries, and tracing) to identify the magnetic signature associated with hydrothermally altered rocks, specifically porphyry deposits [86].

b. The eTh/K ratio, calculated from the potassium and thorium concentration maps (Figures 2- 2b, and 2- 2c), is used to detect areas with different types of hydrothermal alteration, such as potassic, phyllic, and propylitic alterations [87].

c. The 3D Euler deconvolution method [88] involves analyzing the orthogonal gradients of the potential field in horizontal (x, y) and vertical (z) directions. It's expressed as $(x - x_0)\frac{\partial t}{\partial x} + (y - y_0)\frac{\partial t}{\partial y} + (z - z_0)\frac{\partial t}{\partial z} = (B - T)N$, where N represents the structural index, B is the field's base level, and T is the magnetic field at specific x, y, and z coordinates. This approach is applied to the RTP magnetic data (Figure 2- 2a) to create a structural framework configuration for the modified regions and gauge their depths.

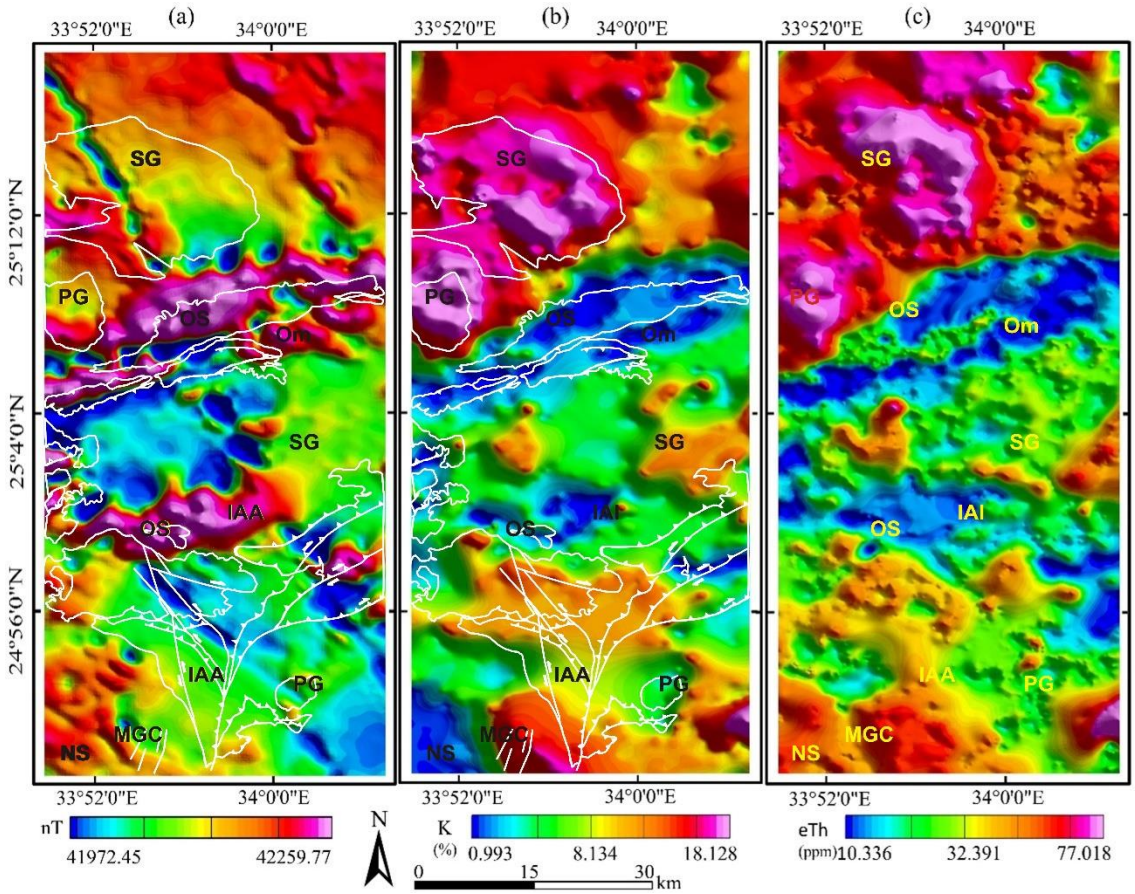


Fig. 2-2: Airborne geophysical data a) Reduction to pole (RTP) map, b) potassium concentration (K) map, c) Equivalent thorium concentration (eTh).

2.2.5 SEM-EDX

Due to the diminutive granular dimensions of the ore minerals, optical reflected light microscopy was augmented by SEM-EDX measurements, predominantly from quartz veins and alteration zones. Mineral identification relied mainly upon SEM-EDX which was conducted at the Institute of Mineralogy and Geology, University of Miskolc with the contribution of Dr. Ferenc Kristály. A SamX-controlled JEOL JXA 8600 Superprobe electron beam microprobe (utilizing a 15–20 kV accelerator voltage and 20 nA sample current) was employed, complemented by an SDD-EDX detector. Employing scanning electron microscopic methodology

(SEM), we generated backscattered electron (BSE) images. Additionally, EDX point measurements and surface element mappings were executed to perform chemical analyses on individual minerals, with a primary focus on ores, exemplified by gold.

Given the electron scattering phenomenon within the sample, when measuring grains smaller than 10 μm, the resultant X-ray spectra encompass elements from adjacent particles. Consequently, the acquired data represents amalgamated compositions of diverse grains within the excitation volume, exhibiting variations within a few micrometers in depth and radius. This variability is contingent upon the absorption characteristics of the present chemical elements. In instances involving potential polymorphism, such as in the case of carbonates, Fe- and Ti-oxides, achieving species-level identification of minerals proved elusive. Nonetheless, optical microscopy and X-ray powder diffractometry (XRPD) were instrumental in facilitating their identification.

2.2.6 Whole-rock geochemistry

To ensure utmost accuracy, the chemical analyses of the studied rocks were meticulously performed at Bureau Veritas Commodities Canada Ltd. Whole-rock major and trace element compositions were analyzed. The chosen samples were crushed and pulverized before undergoing analysis for their entire rock major, trace, and rare earth element (REE) contents. X-ray fluorescence (XRF) technique was employed to determine the chemical composition of major rock elements, as well as the abundance of Sc, Ba, and Ni. Bureau Veritas conducted the analyses using inductively coupled plasma optical emission spectrometry and mass spectrometry (ICP-OES/-MS) following protocols LF300 and LF100, part of analytical package LF200, involving sample powder fusion in lithium borate and dissolution in nitric acid. Additionally, aqua regia digestion and ICP-ES/MS (BV Mineral Laboratories method AQ200) were used to determine the levels of Ag, As, Au, Bi, Cd, Cu, Hg, Mo, Ni, Pb, Sb, Se, Tl, and Zn. By uncovering the geochemical signatures and unique characteristics of these geological samples, we aim to shed light on their origin, evolution, and their significance within the broader tectonic context. The amalgamation of these results will undoubtedly contribute to a deeper understanding of the geological processes that have shaped our study area.

Chapter 3: GEOLOGICAL SETTING

The Egyptian basement rocks make up the northernmost tip of the Nubian Shield (mostly Red Sea Hills), which in turn is a part of the ANS. The latter is considered the northern extension of the Mozambique belt, and an exemplary form of accretionary orogens and suturing [89]. As a portion of the ANS, the Egyptian basement rocks (primarily in the Eastern Desert) consist of a diverse assortment of ophiolitic components and island arc rocks, with extensive granitic intrusions [90]. As a part of ANS and the utmost southern section of the CED, the considered area is made up of imbricated slices of ophiolitic rocks that have been admixed with volcanic and sedimentary rocks from an island arc assemblage. Additionally, there are granitoid and gabbroid syn- and post-orogenic intrusions that have cut through the existing rocks and in some areas have erased the main structures. The study area's southwestern corner is covered by Phanerozoic (Cambrian – Upper Cretaceous) Nubian Sandstone. Different parts of the study area have been previously mapped in various studies that introduced different geological maps [5,6,43,7–12,41,42], which were considered a primary source for the preliminary identification of rock units. These rock units are thoroughly discussed in the upcoming section.

3.1 Ophiolitic group

The ophiolites of the considered area comprise remains or dismembered segments of an ophiolitic nappe. These allochthonous ophiolitic fragments have variable shapes and sizes, were set, and embedded in a sheared fine-grained matrix, posing, and constituting the ophiolitic mélange. In the region being studied, the dominant types of ophiolitic rocks are serpentinite (which still has some fresh peridotite remains) and metagabbro. These ophiolitic components are found close to each other within a heavily deformed matrix. The ultramafic rocks in the area have undergone widespread serpentinization. The basement rocks are mainly represented by allochthonous blocks and fragments of serpentinite and carbonatized/silicified derivatives from the Neoproterozoic ophiolitic mélange, that are tectonically emplaced within volcaniclastic metasediments. Neoproterozoic ophiolites are known from the ANS [89], and they are primarily identified as fragmented oceanic magmatic complexes made up of ultramafic rocks, metagabbroic rocks, and then primarily basaltic extrusive

rocks, with or without a sheeted dike complex and a cover of pelagic deep-sea sediments.

3.1.1 Serpentinites and talc-carbonate rocks

The study area (Barramiya-Um Salatit-Mueilha district) is well-known for its sovereign serpentinites, it could be easily known even from regional geological maps of the Eastern Desert due to its extensive areal distribution. Barramiya area serpentinites have a great sound in the Eastern Desert of Egypt as it is considered one of the largest and most pronounced outcrops. Like many ophiolitic serpentinites in the ED, serpentinites of the study area with various shapes and sizes are mixed and incorporated into a sheared matrix nearly at all the scales of observation. The serpentinite rocks are widely distributed and form conspicuous mountains (Figure 3-1) with steep slopes and beveled tops as observed in the study area. These beveled culminations exemplify the old Pre-Nubian peneplanation indicating mostly their coverage by Nubian Sandstone rocks which have already eroded. Also, serpentinites are represented as small hillocks or lenses distributed all over the study area and incorporated in the deformed matrix (Figure 3-1b, c). The eminently noticed serpentinite masses within the study area include Gabal Barramiya, Gabal Um Salatit, and Gabal Um Salim (Figure 3-1a). The sovereignty of serpentinites is represented as thrust sheets and elongated mostly in the ENE-WSW to E-W trend. A distinguished NNW dipping thrust is notable at Gabal Um Salatit even on a large scale of observation.

The serpentinite rocks located nearer to heavily distorted thrusts and shear zones have undergone listvenitization (Figure 3-1d, e) and contain sulfide minerals, such as pyrite. The remaining fragments of the less distorted ultramafic rocks are primarily made up of olivine, diopside, and orthopyroxene (hypersthene), with antigorite partially taking the place of olivine. Quartz and carbonate veins usually dissect serpentinites. Also, in sporadic occurrences and closer to the mines especially Barramiya mine silicification and ferrugination of serpentinites are observed. It is noteworthy to mention that serpentinites are often associated with talc-carbonates (creamy white colored rocks mostly exhibiting cavernous weathering) in the study area (Figure 3-1c, f).

An intimate association of serpentinites with what is called quartz-carbonate dikes have noticed (Figure 3-1e). The latter is characterized by a red to pink color, massive, hard, and sheared, and as the name suggests consists mainly of quartz and carbonate minerals (calcite and/ or ferroan

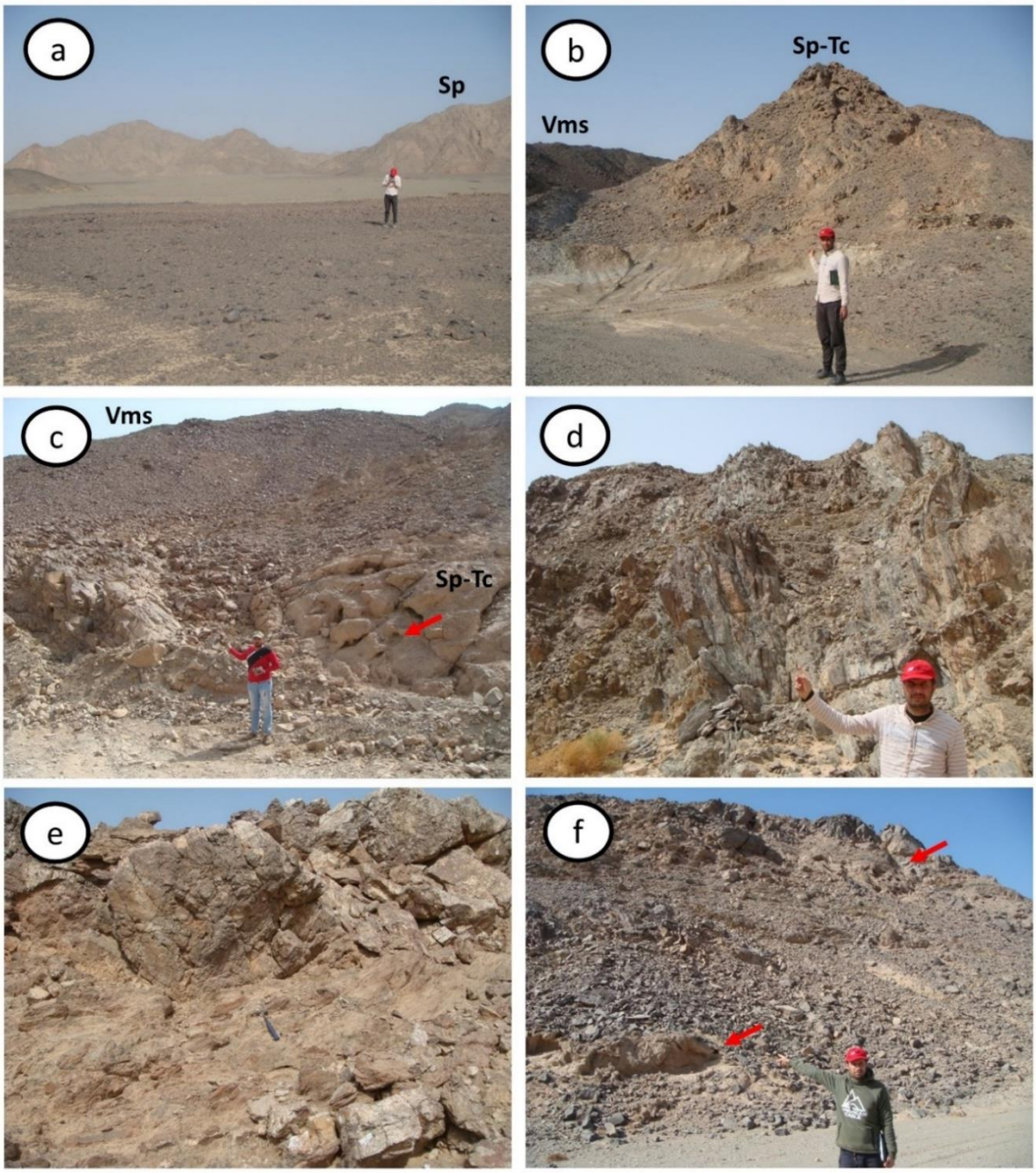


Fig. 3-1: Field photographs showing the main geological features of serpentinites (Sp) and their related rocks within the study area. (a) A panoramic view of Gabal Um Salatit serpentinite (b) Large serpentinite-talc carbonate (Tc) blocks embedded within a matrix of volcaniclastic metasediments (Vms), (c) Close-up view of serpentinite-talc carbonate blocks showing their cavernous structure (see the arrows). (d) Intensively sheared serpentinite-talc carbonate rocks, (e) Listvenization, a distinct alteration process in serpentinites, (f) alteration of serpentinites (see the arrows) to talc carbonate rocks (buff color).

dolomite and uncommonly malachite). The reddish color of this rock type is attributed to iron oxide staining. These rocks have been known as listvenite, but the usage of this word has been widened to involve an assortment of carbonatized mafic and ultramafic rocks [91]. Rocks containing carbonates (ankerite and magnesite), quartz, and fuchsite together with disseminated pyrite and chromite are restricted to the term listvenite [91]. These quartz-carbonate dikes are mostly sheared and found near the mines' site and are considered a good source for gold mineralization. These rocks are found lining the large milky quartz veins (e.g., the main lode of Barramiya goldmine). These rocks are composed mainly of quartz, calcite, ferroan dolomite, and sometimes malachite with some iron oxide staining due to oxidation of carbonate minerals [10]. It is strongly suggested that these rocks were affected by the hydrothermal solutions during the emplacement of syn-collision granites.

Serpentinites and talc-carbonate rocks are represented by the Gabal Um Salim and Barramiya-Um Salatit belt (ENE trend) that are aligned with the primary foliation of the ophiolitic mélange matrix and are mainly made up of hills composed of serpentinite, as well as small amounts of relict harzburgite, and pyroxenite [8]. Serpentinites are mainly thrust over the surrounding rocks and are mostly associated with talc/ magnesite/ chromite in the form of veinlets, nodules, or irregular pockets along these structural contacts. Additionally, listvenite is exposed within the Barramiya-Um Salatit belt and is composed mainly of carbonate minerals rich in iron and magnesium, and white mica that contains chromium and quartz [8]. According to Halls and Zhao, (1995) [91], listvenite is formed by potassic metasomatism at intermediate to low temperatures of mafic-ultramafic rocks, particularly serpentinites, and is often found in regional shear zones, which typically matches the regional geological and tectonic setting of the study area. Listvenite is formed by the alteration of tectonized serpentinite mainly through talc carbonate rock. This alteration occurs as the degree of carbonatization increases near transpressive faults.

Previous studies report other ophiolitic components within the study area. For instance, [92] reported the existence of ophiolitic metagabbro and pillow basalts within calcareous and locally carbonaceous metasediments and named the whole admixture as Muweilha-Dungash mélange. Abu El Ela, (1985) [93] described sheeted diabase blocks and pillow metabasalt in Wadi Dungash and Wadi Abu Meriewa within the study district.

3.1.2 Ophiolitic metagabbros

Ophiolitic metagabbros appear as blocks that are heterogeneous in general size and color, and they are less abundant than ultramafics (Figure 3-2a). They are found in the form of small, separate masses made up of medium to fine-grained rocks that are either mesocratic or melanocratic in color (Figure 3-2a). In certain areas, these rocks exhibit rhythmic graded layering. Additionally, the metagabbro found in the study region also exists in the form of coarse-grained cumulate rocks. Metagabbros occur either associated with the serpentinites or as discrete blocks and have scattered representation within the study area. Ophiolitic metagabbros are mostly in contact with the serpentinites through tectonic thrusting. Metagabbros underwent deformation and metamorphism, as a result of regional metamorphism (greenschist facies). One of the huge masses is located in the northern part of the map and is dissected by car tracks leading to Um Salim chromite mine. This lense-like gabbroic mass extended E-W, overthrust by Gabal Barramiya serpentinites and intruded by minor plutonic intrusions composed chiefly of granodiorites. Another minor occurrence of metagabbros is represented at the Sin El Salatit area, on the eastern flank of the car track leading to the Um Salatit area. To the south of this area, thinner metagabbroic rocks are observed in a syncline fold plunging ENE with serpentinites at the core. Also, ophiolitic metagabbros are represented on the southern flank of Idfu – Mersa Alam road at the entrance of Khuwr Abu Ashayir. Other mappable metagabbroic blocks occur in the central western part of the region under consideration between Wadi Barramiya and, Wadi Dungash as well as a few other places.

3.1.3 Ophiolitic mélange matrix

These previously mentioned ophiolitic components (serpentinites, talc-carbonate rocks, and metagabbros) are found within a mixture of quartz-sericite schists with graphite, as well as quartz-feldspathic schists (Figures 3-2 b-d) that contain metagraywackes and metasiltstone [94] in fine layers representing the ophiolitic mélange matrix within the considered area. The mélange matrix (mainly quartzofeldspathic schists) shows a well-developed preferred orientation (Figures 3- 2c, d), trending NW-SE to E-W and mostly dipping towards the north. Variable trends of the highly tectonized metasediments and schists are recorded and can be ascribed to the different orientations of the structural phases influencing these rocks. They are predominantly situated in the central portion of the study area, where

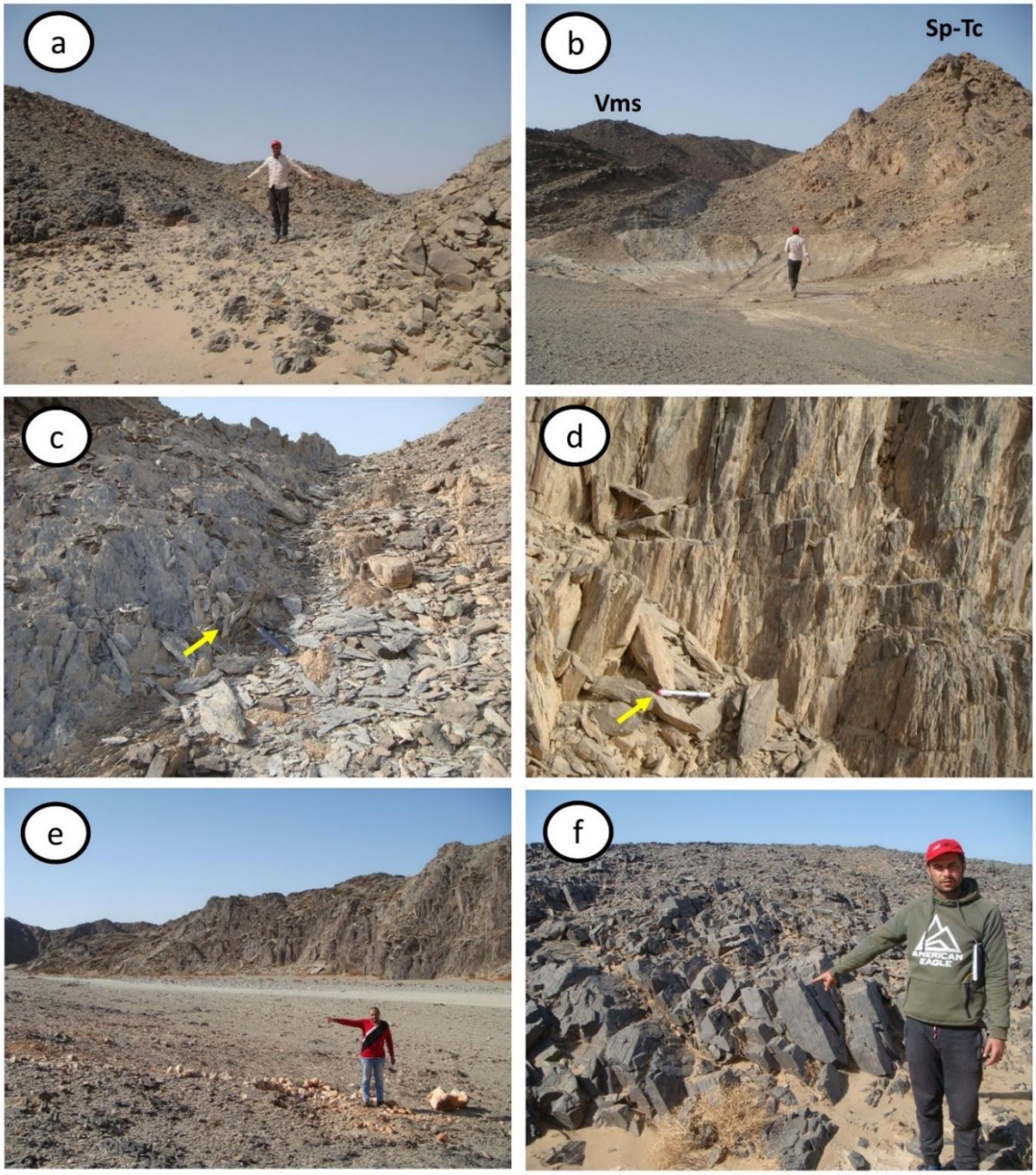


Fig. 3-2: Field photographs highlighting (a) Low-land ophiolitic metagabbros depicted as heterogeneous blocks, exhibiting subtle variations in color, (b, c, and d) Showcase the ophiolitic melange matrix (b) encompassing fragments of serpentinite-talc carbonate and (c, d) revealing intense shearing and well-developed preferred orientation of these volcaniclastic metasediments (Vms). (e) Provides a general perspective of the metavolcanics within the study area, (f) shows highly dissected basaltic meta-andesites.

they constitute lowlands enclosing numerous blocks of both serpentinites and metagabbros of unmappable sizes.

3.2 Island arc assemblage (metavolcanic/volcaniclastic rocks)

A large part of the studied terrain is covered by island arc association represented mainly by metavolcanics (Figures 3- 2e, f) exposed at the central and southwestern portion of the considered area. Additionally, it is considered the host rock for Dungash gold deposit (vein-type gold deposits in the southern sector of the considered area). Island arc assemblage within the studied terrain is represented by metamorphosed (mainly greenschist facies) basic-intermediate metavolcanics (basaltic andesite to basalt and inferior dacites), and pyroclastic tuffs/breccias [11] as shown in Figure 3-3a. One of the conspicuous exposures of these rocks is located at the southwestern portion of the study area (south of Dungash gold mine site) and is exemplified by a prominent NE-trending fold. The latter fold could be easily seen through remote sensing images, that also display structural dissection with lineaments and occasional shearing, which matches our field observations. Closer to the Dungash mine area, these rocks are mainly andesitic however, pyroclastic rocks are recorded.

These andesitic and basaltic rocks with their associated pyroclastic rocks (metatuffs) exhibit low-grade metamorphism and inessential carbonate fragments. These rocks frequently show thrust contacts with ophiolites, specifically serpentinites. Faulting, jointing, (Figure 3- 2f, Figure 3-3a, and Figure 3-3b) micro-folding, dissection by dikes, well-developed preferred orientation, and shearing were observed in these rocks in several occurrences of the study area. Metavolcaniclastic rocks usually occur as bands or lamina (with variable thickness and colors) of fine- and coarse-grained ash tuffs with some andesitic lithic fragments. In the study area, it is common to find sets of metamorphosed volcanic fragments that are exposed within the heavily deformed cores of folded rocks. These fragments are mostly dark in color and have a strong foliated or massive texture, primarily composed of mafic minerals. These rocks vary in grain size and comprise predominantly epidote, quartz, and chlorite, with smaller amounts of calcite and opaque minerals.

Regarding their petrographic characteristics, these rocks are typically made up primarily of plagioclase, epidote, chlorite, and occasionally hornblende. In certain areas, the original mineral composition has been entirely replaced by epidote, chlorite, and albite. These rocks are dominated by plagioclase that is mostly altered to sericite with a reasonable



Fig. 3-3: Field photographs showing, (a, b) highly dissected arc metavolcanics, (c) highly deformed metagabbro-diorite rocks, (d, e) highly sheared older granite intrusions, (f) post-tectonic Mueilha granite intruded into metagabbros with a distinct sharp contact.

representation of biotite and hornblende (partially replaced by chlorite and epidote), confirming the greenschist conditions. Iron oxides and kaolinized feldspars are represented within brecciated zones.

3.3 Metagabbro-diorite rocks

These rocks cut the pre-existing lithologies (ophiolitic rocks and island arc assemblages). Metagabbro-diorite rocks within the study area are deformed (Figure 3-3c), oval to sub-rounded plutons exposed mainly to the north of Dungash gold mine, and between Wadi Beizah and Wadi Barramiya. This complex is generally massive with heterogeneous grain size and as the name suggests ranges from metagabbro to diorite in composition. They crop out mainly in Wadi Um Salim and to the north of Wadi Mueilha. A subcircular mass occurred in Wadi Beizah, as well as other mappable irregular masses cropped out in the northern segment of the study site. These plutons (with metagabbro-diorite compositions) take on subcircular or irregular shapes intruding the ophiolitic, island arc metavolcanic, and metavolcaniclastic rocks. On the other hand, these metagabbro-diorite complexes are intruded by granitic masses. Coarse-grained gabbroic patches commonly occur in contact with granite. It frequently contains patches of igneous breccia where basic dikes' angular inclusions are embedded in a matrix of white igneous material. Also, dioritic breccia intrusions were found to be incorporated within a granitic host.

3.4 Granitic rocks

Generally, the granitic rocks (syn and post) constitute extensive stretches extending, north, south, and east beyond the studied area. A significant amount of gabbroic, dioritic, and metavolcanic breccia intrusions at various stages of interaction and digestion with the granitic material are present in the study area's granitic rocks as inclusions. This granitic plutonism and diapirism have a significant role in forming gold-bearing silicified shear zones. The study area (as a part of ANS), the Amesmessa and Tirek deposits in the Hoggar Shield, and the Morro do Ouro deposit in the Brasilia fold belt are among the geological shields that contain the gold-bearing silicified shear zones. These zones likely formed simultaneously with greenschist-grade metamorphism and granitoid diapirism, as suggested by [95], or as a consequence of brittle-ductile shearing and folding, as proposed by [96]. In the northern Red Sea Hills of Sudan, the formation of auriferous quartz veins was likely the result of an episode of intense shearing that

occurred after the emplacement of batholithic intrusions and regional cooling, as indicated by Almond et al. (1984) [97]. Elsamani et al. (2010) [98] suggested that gold was mobilized from island-arc volcano-magmatic sequences that were 715 million years old and subsequently deposited along structurally more favorable sites that developed after the collision of the plates.

3.4.1 Syn-orogenic granitoids

The syn-orogenic granitoids are medium-grained, grey color, quartz–diorite/granodiorite [11], and have a sheared appearance and local schistosity (Figure 3-3d, Figure. 3-3e). Sometimes, they exhibit intrusive contact with other units including the ophiolitic, island arc metavolcanic, and metavolcaniclastic rocks in addition to metagabbro-diorite complexes. Syn-tectonic granite is jointed, and dissected by felsic and mafic dikes, besides quartz veins, and shows spheroidal weathering. They occur as low-land (Figure 3-3d) cones and ridges, covering considerable areas of the research area. In the northern part, an extensive area of syn-orogenic granites is represented by Gabal El Rukham. Also, closer to the southern flank of the Idfu–Mersa Alam asphaltic road and at Talat Ghannam area there is a local representation of this rock unit. In the area between Gabal Um Salim and Wadi Beizah, these granitoids are also represented and mainly dissected by a net of valleys. In the southern part of the study area and exactly at Wadi Rud Elliqah syn-orogenic granitoids are cropped out. Other smaller occurrences are also observed around the study area with the same composition as these previously just mentioned larger representations. On the microscopic scale, these rocks have coarse-grained, equigranular hypidiomorphic texture, and mostly leucocratic with obvious plagioclase and quartz crystals. In most samples, quartz is less pronounced indicating intermediate composition.

3.4.2 Late-orogenic granites

These plutons are locally represented, exhibit buff to pinkish color, mostly without or poorly developed foliation, and intrude the ophiolitic group, island arc metavolcanic, and metavolcaniclastic rocks and metagabbro-diorite complexes, especially in the northwestern and southeastern parts of the study area. These plutons are circular to subcircular and chiefly composed of alkali-feldspar granites, granite porphyries, and scarcely albitite, as Gabal Mueilha which has a prominent sharp contact with the surroundings (Figure 3-3f) appeared even from remote sensing data and

aerial photographs. Gabal Mueilha is the main representation of post-orogenic granites within the study area and is exposed in its southern part. It has an intrusive contact with other units particularly the gabbroic mass and volcaniclastic metasediments (Figure 3-3f). Granitic rocks were subjected to extensive fieldwork due to their radiogenic importance of being favorable host rocks for rare metals. The Mueilha granite pluton forms a prominent elevated, elliptical body covering approximately 7.5 km^2, penetrating the adjacent foliated metasedimentary sequence. It slightly slopes at 15-20° outward from the granitic pluton (Figure 3-3f) indicating that the Mueilha pluton's apparent exposure is the pinnacle of a granitic magma chamber. It is also dissected by NE and NW-trending faults/fracture sets (Figure 3- 4a, Figure 3- 4b) filled by dikes and pegmatite veins (Figures 3- 4c, and d). These fractures vary from centimeters to several meters in length and can extend for kilometers within the metasediments, occasionally transitioning into vertical normal faults (Figure 3-4e). Dikes, amazonite- and quartz-rich fluorite-bearing pegmatitic veins extend from the pluton into the nearby metasediments. Locally, slightly greisenized pegmatite pockets are found near the edges of the pluton of Mueilha. While some angular to subrounded exogenic metasedimentary xenoliths can be located along the southern periphery of the granite pluton, the majority of the pluton is completely devoid of such associated xenoliths. These xenoliths do not appear to have interacted with the granite that surrounds them, suggesting either a frigid character of the granitic magma or its shallow emplacement depth. Other main representations of this rock unit in the study area include Urf Abu Hamam in the northwestern part of the study area. It is characterized by its high relief. In certain regions within the study area, such as the northern Urf Abu Hamam area, the boundaries between the late- and syn-tectonic granite masses are well-defined, with the former containing several xenoliths from the latter. Additionally, these granite masses send out offshoots into the surrounding rocks. Closer to the Barramiya mine area, some granitic bodies of variable trends intruded the serpentinites.

3.5 Dikes

Remarkably, the rocks exposed in the considered area are transected and traversed by a great number of dikes. Lithologically, these dikes exhibit various compositions ranging from mafic to felsic. In the research region, the felsic dikes frequently feature ENE-trending sets and are found close to post-



Fig. 3-4: Field photographs showing Mueilha granite and its related structural Features. The pluton is intricately dissected by (a) fracture sets, joints, and (b) faults. These tectonic elements are detected through the surrounding rocks as the fractures are filled with pegmatite veins (c, d, and e). These veins have a considered extension (c), prominent coarse quartz grains (see the arrows), and are affected mostly by steep normal faulting. (f) Mafic dikes cutting through granitic rocks.

orogenic granite outcrops. These are pink-colored porphyritic in hand specimens, with feldspar phenocrysts embedded in a groundmass of fine-grained quartz, sericite, and chlorite. Island arc Metavolcanics and metavolcaniclastic rocks are regularly cut by the mafic dikes. These dikes show signs of deformation or displacement in some spots.

As these dikes are almost the same in all rock units, they are considered as later intrusions concerning ophiolite rocks. Dikes with basaltic and dacitic composition are observed cutting granitic rocks in various trends (Figure 3-4f). Numerous dike sets are abundant in the northern and southern parts of the study area. The ENE-trending dikes are sovereign and close to the ENE-WSW Barramiya-Um Salatit belt in the study area's northern region. The NNW-trending dikes in the southern part of the area provided evidence for the tectonic evolution of the area for different tensile deformation timings and shapes.

3.6 Phanerozoic sediments

Along the western and southwestern portions of the study area, the Phanerozoic cover is represented by NSS exposures. They exhibit noticeable lithological variations and overlap unconformably with the Precambrian basement rocks and are mainly defined as Nubian Sandstone (Cambrian–Upper Cretaceous).

Chapter 4: RESULTS

4.1 Lithological mapping utilizing multisource remote sensing data (multispectral) and Machine Learning Algorithms

The content in this section has been previously published in the following articles: Shebl and Csámer [29,32]. For detailed information on this topic, please refer to the respective publications.

It should be emphasized that in this subchapter, we applied only MLC, ANN, and SVM using these multispectral datasets. However, with the increased number of bands provided by PRISMA hyperspectral data (the next subchapter), more robust algorithms, such as RF and XGB, were utilized to avoid overfitting and computational issues.

4.1.1 Classification Results

Nine lithological targets including Ophiolitic Serpentinite (Osp), Ophiolitic Metagabbro (Omg), Ophiolitic Melange (Ome), Metavolcanics (Mvs), Metagabbro-Diorite (MgD), Syn-orogenic granite (Sog), Post-orogenic granite (Pog), Nubian Sandstone (Nss), and Wadi Deposits (Wdp) are classified. The average accuracies of allocating all the lithological units using the four optical sensors by ANN, MLC, and SVM are shown in Appendix 4-1 a, b, and c respectively. By checking Appendix 4-1 and based on its statistical findings derived from over 100 classification processes, we concluded that SVM and MLC are much better than ANN. Additionally, it highlighted the best-classified rock units. The best-classified classes (more than 90% accuracy) include Ophiolitic Serpentinite (Osp), Nubian Sandstone (NSS), and Wadi Deposits (Wdp) as shown in Appendix 4-1. Also, the four multispectral datasets reasonably act as valid input for performing such kind of lithological mapping within complicated terrains. Appendix 4-1 d and 4-1 e indicate the preeminence of ALI compared to S2, ASTER, and L8 as a classification input where kappa coefficient (k) and Overall accuracies (OAs) are higher for ALI compared to the others under the same conditions (i.e., training and validation data). Boosting the optical datasets with each other or with different types of data (e.g., radar or dem derivatives) enhances the overall allocation accuracies almost for all the lithological classes. A significant enhancement is achieved when using ALI in these combinations.

For instance, boosting S2+AST+L8 with ALI significantly increases the OA above 90% as shown in Appendix 4-1 d and 4-1 e. Regarding the classifier performance, all the current results indicate the superiority of SVM over ANN and MLC for all the research experiments using different datasets (Appendix 4-1 f). Appendix 4-1 f also clearly indicates enhancing the classifier performance by increasing the participated inputs. For instance, the overall accuracies of ANN, MLC, and SVM have increased by adding ALI to S2+ASTER+L8. Investigating this kind of variation for SVM clearly indicates the role of ALI in enhancing Ome generalization from less than 55% to around 80 %, as shown in Appendix 4-1 g.

Quantitative analysis of the best classifiers (SVM, MLC) performance with the number of bands was done (Appendix 4-2a). This analysis shows that the overall accuracy gradually increases with the number of utilized bands. However, after 31 utilized bands the final OA slightly increases indicating that any additional data will be less helpful in achieving better results unless the training data have been increased. Additionally, the richness and nature of utilized data are crucial factors in increasing the overall accuracy. For example, Appendix 4-2b shows a large difference in the OA (around 9%) with the same dimensions or number of input bands (18) but for different datasets. It should also be emphasized that incorporating elevations (DEM) of the rock units significantly enhances the allocation results almost with all the datasets as shown in Appendix 4-2c. Appendix 4-2d confirms the importance of DEM compared to radar data or even its derivatives (slope and aspect). One of the best combinations in delivering reliable lithological discrimination is ALI+S2+AST+DEM (including DEM) and the average accuracies for its results with all the classified targets are seen in Appendix 4-2e. These findings were even visually compared by manifesting radar data and DEM derivatives (e.g., Slope) as shown in Appendix 4-3.

More than 100 classification processes, statistical analysis of the classifiers, datasets, and dimensionality effect were assessed to find the best results. The best results are shown in Appendix 4-4. Figure 4-1 represents the final thematic map utilizing the adopted datasets and SVM with an overall accuracy of about 91.41 % overall accuracy. This map has been validated using testing data, previous geological maps, and fieldwork.

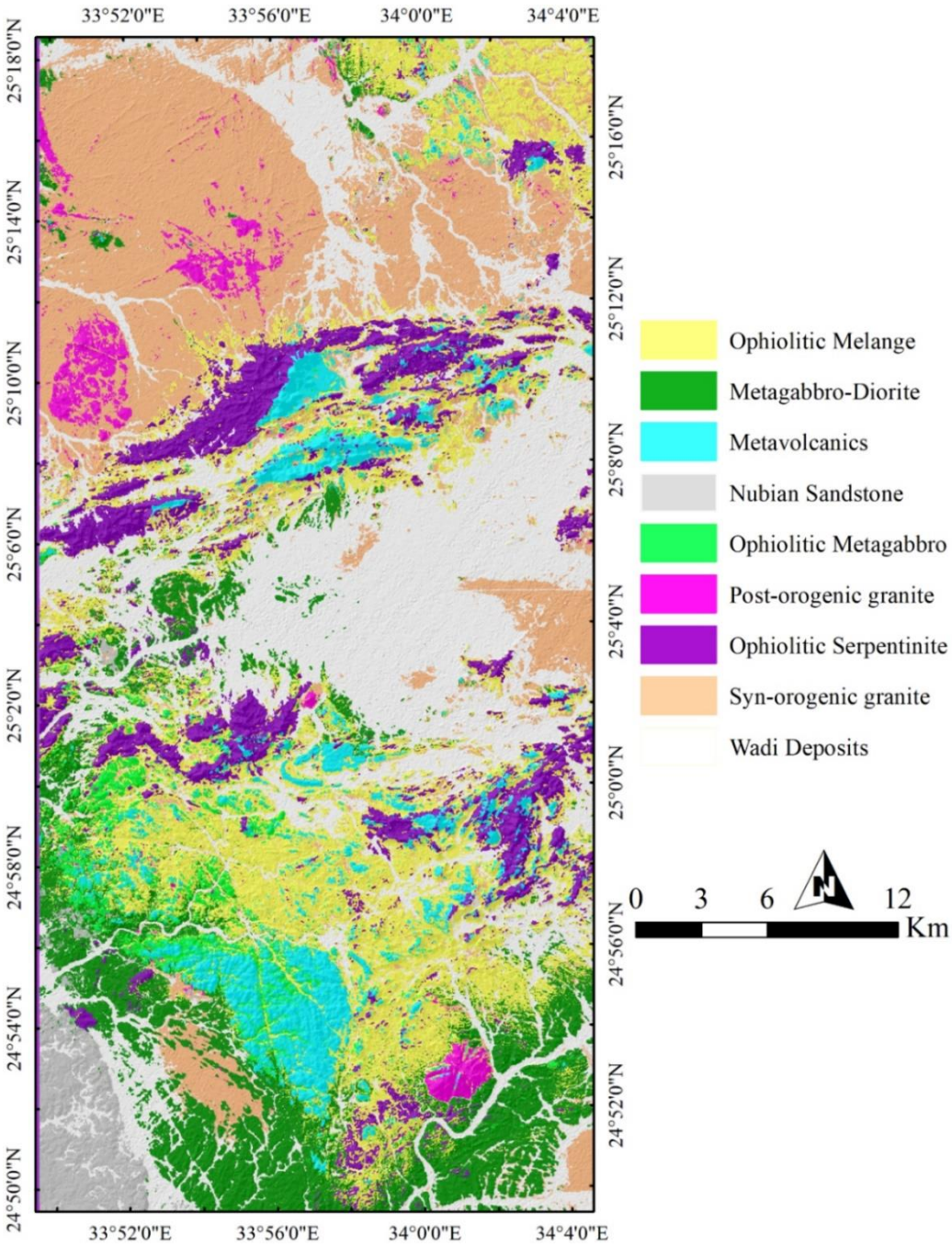


Fig. 4-1: Final lithologic map classified using ALI+S2+AST+ DEM+S1+PALSAR1+slope data and SVM.

4.2 Lithological mapping using PRISMA hyperspectral data and ensemble machine learning (Bagging and boosting)

The content in this section has been previously published in the following article: Shebl et al., (2023) [39]. For detailed information on this topic, please refer to the respective publication.

In the previous section, all the utilized optical datasets are multispectral data which provide a limited number of bands (broad wavelength bands). With this number of limited wavelengths, several features could be missed due to the lack of continuous imaging by wavelength specification. To overcome this issue, hyperspectral sensors could provide hundreds of bands resulting in higher-resolution spectral coverage (Figure 4-2). Of course, it is a kind of trade-off, to get these higher spectral details you can encounter costly sensors and images, higher data dimensionality, larger sizes, and time-consuming pre-processing and processing operations compared to multispectral data. Notwithstanding the foregoing, it is worth adopting these hyperspectral data in lithological classification due to the wealth of SWIR coverage that provides outstanding discrimination for various rocks and minerals expecting excellent results. Thus, PRISMA hyperspectral data were picked out for the current research due to its relative novelty (launched in 2019), plausible VNIR and SWIR coverage, and reasonable Signal-to-noise ratio. The only defect is the available data covers around two-thirds of the study area. Thus, It is important to note that the number of lithological targets in this chapter differs from the previous subchapter because PRISMA data was available only for a smaller part of the study area and did not cover the entire region under study.

Of course, to control all the foregoing issues related to data size and preprocessing, ensemble learning algorithms implementing both bagging and boosting techniques were applied to PRISMA data. Additionally, SVM will be applied as well for comparison and highlighting the best classifier (based on the previous subchapter results) performance for future similar studies. Table 2 (Appendix) presents the training and testing datasets utilized for training, validating, and evaluating the performance of the classifiers, along with the abbreviations representing the different lithological classes.

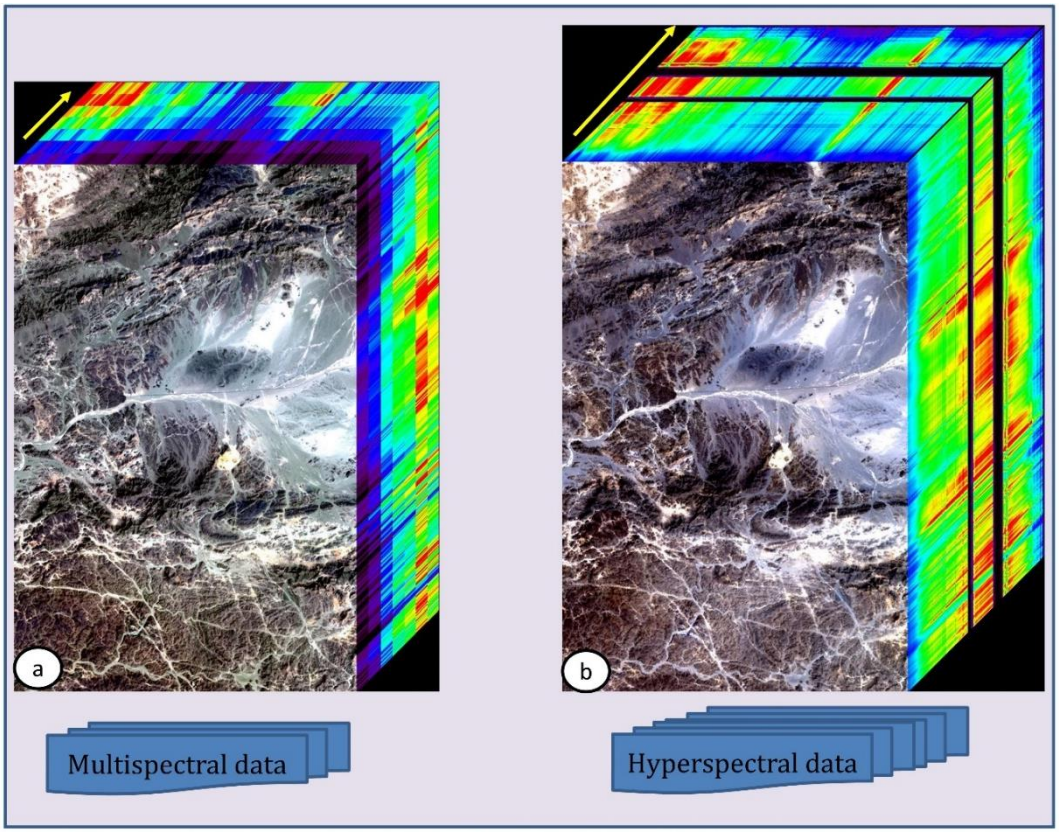


Fig. 4-2: Three dimensional cubes of the study area using a) Multispectral Landsat 9 data and b) PRISMA hyperspectral data, highlighting the higher band count (mostly highly informative) in the latter compared to the former.

In this ongoing investigation, a cloud-free, surface reflectance PRISMA was harnessed to investigate the lithological attributes of the designated research zone. The scene underwent meticulous atmospheric and geometric rectification, subsequently being resized to match the precise boundaries of the study area, thereby facilitating the extraction of significant features. Alongside the invaluable PRISMA dataset, a series of lithological maps pertaining to the study locale were meticulously reprojected and juxtaposed to intensify the depth of our geological comprehension regarding the lithological discrimination. For a comprehensive overview of the chosen data and the entire procedural framework employed in this study, a visual representation in the form of Appendix 4-5 is offered illustrating the step-by-step methodology.

4.2.1 Results

A total of nine thematic maps were generated through the application of the chosen algorithms –RF, XGB, and SVM – across three primary datasets: the complete set of bands (234b), the first two Principal Components (1-2 PC), and the preceding four Principal Components (1-4 PC). Our findings (based on the trials) revealed that the 1-2 PC dataset yielded the least satisfactory results, displaying unsatisfactory lithological allocation, as illustrated in Appendix 4-6. This was substantiated by notably lower Overall Accuracies (OAs) for all three employed algorithms. Specifically, RF, XGB, and SVM demonstrated OAs of 69.5%, 69.2%, and 71.5%, respectively. These marked decreases in OAs were chiefly attributed to several instances of misclassifications within the seven lithological classes, detailed in Table 3 (Appendix). In particular, suboptimal F1-scores were recorded for various classes: metavolcanics (0.61), metagabbro diorite (0.49), volcaniclastic metasediments (0.52), and wadi deposits (0.55). The composite F1-score for the resultant RF thematic map hovered around 0.69. Similarly, the XGB and SVM results were discouraging, each yielding an overall F1-score of approximately 0.69 and 0.71, respectively. These trends are meticulously outlined, with precision and recall metrics detailed for every lithological class in Table 3 (Appendix). Furthermore, macro-, and weighted-average recall, precision, and F1-scores were computed, consistently signaling the unsuitability of utilizing the 1-2 PC dataset from PRISMA for the classification of intricate lithologies, regardless of the employed algorithm.

A visual appraisal of the produced thematic maps from RF, XGB, and SVM, using the 1-2 PC dataset, corroborates the statistical analysis. Notably, the maps reveal the capacity to reasonably differentiate serpentinite rocks (yielding the highest F1-score), represented by the violet hue. However, the classification performance for the remaining six classes is considerably subpar, manifesting as a "salt and pepper" phenomenon across the thematic maps. An illustrative example is the substantial overlap of metavolcanics (blue) in the southwestern region with green pixels indicating metagabbro diorite rocks and talc carbonate rocks. Similarly, the elliptical mass of metagabbro-diorite at the study area's central part is often misclassified as metavolcanics (with dominant blue pixels instead of green). Despite the prevalence of errors within the 1-2 PC dataset, nuanced differences that underscore the diverse capabilities of the employed algorithms can still be discerned. For instance, granitic formations at the far northwestern corner of

the study area demonstrate more accurate classification (fewer error pixels) when processed with SVM in comparison to RF and XGB.

Considering the unsatisfactory outcomes stemming from the 1-2 PC, we took a stride forward in our research by adopting the first four informative Principal Components (1-4PC). Through rigorous experimentation, feeding these three classifiers with the 1-4PC dataset yielded discernibly improved predictions. The ensuing thematic maps, overall accuracies, precision, recall, and F1-scores (as detailed in Appendix Table 4) markedly outperformed the prior experiment (utilizing 1-2PC). Drawing upon previous geological maps, field observations, and the analytical insights from the classification assessment, RF, XGB, and SVM demonstrated a capacity to generate accurate thematic maps (depicted in Appendix 4-7) for the study area through the utilization of PRISMA data.

Remarkably, SVM emerged as the frontrunner, surpassing RF and XGB in delivering a reliable lithological map, achieving an Overall Accuracy (OA) of 90.07%, in contrast to 88.8% for RF and 89.5% for XGB. Detailed scrutiny of the classified targets confirmed remarkable lithological discrimination, a fact substantiated by the statistical analysis presented in Appendix Table 4. Notably, classes such as ophiolitic serpentinite, talc-carbonate, granitic rocks, and wadi deposits were accurately designated, seamlessly aligning with prior geological records and field investigations. For instance, serpentinite's F1-score exhibited values of about 0.91, 0.95, and 0.96 for RF, XGB, and SVM, respectively, illustrating the efficacy of the employed classifiers and the appropriateness of the 1-4 PC input data for successfully distinguishing these classes.

However, some discernible errors – both visually interpreted and statistically recorded – manifested between metavolcanics (blue) and metagabbro-diorite (green), as well as between metavolcanics and volcaniclastic metasediments (dark grey). These misclassifications can be attributed to the broad compositional range within metavolcanics, encompassing slightly metamorphosed calc-alkaline andesite-dacite volcanics, as well as related pyroclastic materials [11,32]. This intricacy occasionally leads to classifier confusion, given the limited information provided by only four bands. Similarly, volcaniclastic metasediments predominantly comprise ophiolitic mélange within the study area, signifying a heterogeneous blend of diverse rocks [99] within this class, which ultimately results in several misclassifications – particularly when juxtaposed with metavolcanics. This phenomenon is clearly evidenced by inspecting the southwestern section of the thematic maps, where green error pixels of

metagabbro-diorite appear within the metavolcanics class. Similarly, metavolcanics errors predominate within the metagabbro-diorite mass situated at the central portion of the study area.

To address the complexities inherent in distinguishing spectrally similar classes (as depicted in Appendix 4-8), an experiment was conducted, involving the application of the complete set of bands (234b) as input to the three algorithms. The objective was to evaluate their potential and performance in achieving robust generalization. As anticipated, this dataset of 234 bands notably enhanced classifier predictions, resulting in more precise thematic maps (shown in Appendix 4-9) compared to the earlier outcomes. Statistically, SVM emerged as a standout performer with an exceptional Overall Accuracy (OA) of 0.95, surpassing XGB (0.92) and RF (0.90). An in-depth evaluation considering precision, recall, and F1-scores for each class, coupled with an overarching analysis involving macro-, and weighted-average metrics (recall, precision, and F1-score), underscores the elevated performance of SVM and XGB in lithological mapping through PRISMA data (detailed in Appendix Table 5). This finding indicates that SVM and XGB outshine RF, potentially attributed to RF's inability to adequately handle non-data pixels – an issue occasionally encountered with hyperspectral data – which in turn compromises training data availability for RF classification. Appendix Table 6 outlines the strengths and limitations of Random Forest (RF), Extreme Gradient Boosting (XGB), and Support Vector Machine (SVM) classifiers, providing a comprehensive overview of their respective capabilities and constraints.

In addition to evaluating statistical accuracy, conducting visual analysis, and comparing the results with previous geological maps, we validated the thematic maps generated with our on-site investigations. Our fieldwork involved visiting over 50 field stations to meticulously study lithological contacts. Notably, we placed representative observation points onto the final thematic map (Figure 4-3), with detailed explanations provided in figures Appendix 4-10 and Appendix 4-11. These illustrations highlight a significant coincidence between the thematic maps generated and the actual exposed rock units we encountered. Furthermore, Appendix 4-12 showcases photomicrographs capturing the key lithological units present within the study area. These images serve to facilitate identification and bolster the validation process. The consistent agreement between our findings and the field observations reinforces the robustness of our approach, suggesting its viability for future lithological mapping endeavors in analogous terrains.

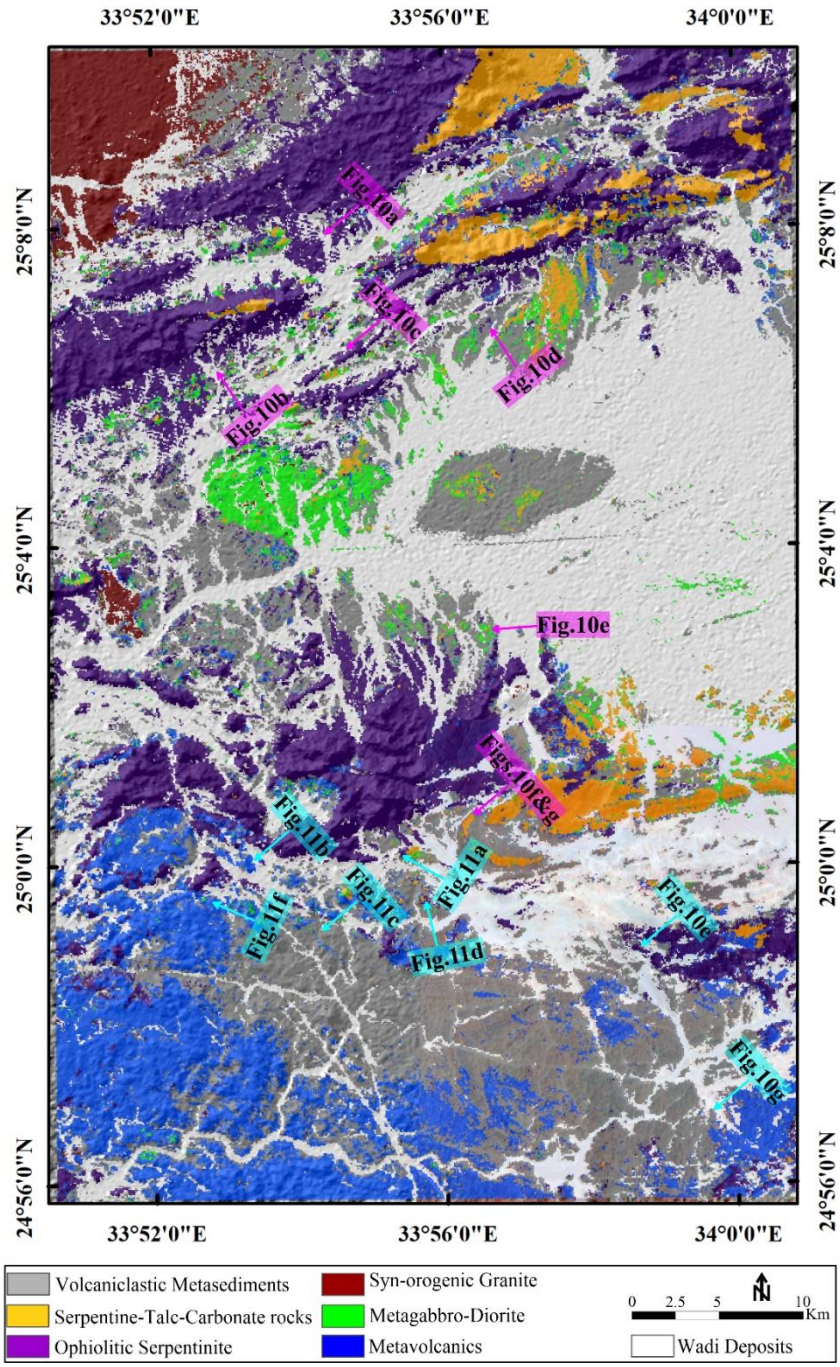


Fig. 4-3: Final lithological map of the study area using PRISMA hyperspectral data and SVM with annotations of the distribution for 14 field verification points presented and illustrated in Appendix (figures 4-10 and 4-11).

4.3 Structural analysis

The content in this section has been previously published in the following article: Shebl and Csámer, (2021) [28]. For detailed information on this topic, please refer to the respective publication.

The main goal of this thesis is to evaluate and compare diverse remote sensing data sets and determine their effectiveness in identifying lineaments for geological research. This study covers almost all available remote sensing data sources used in geological lineament extraction, including optical sensors (Landsat 8 OLI, ASTER, EO 1 ALI, Sentinel 2A), active radar data (Sentinel 1), digital elevation models (ALOS PALSAR, SRTM, NASA, ASTER V3), and manual digitizing from existing geological maps [7–9]. The flow chart methodologies for optical images, DEMs, and radar datasets are presented in Appendix 4-13, Appendix 4-14, and Appendix 4-15, respectively. These appendices show in detail the data processing and the lineament extraction method.

Lineament extraction was performed in PCI Geomatica and an ArcGIS environment. Over 200 maps from different sources were created and examined in this study to efficiently judge the best data source and best combination to detect lineaments by unifying most of the parameters (even the resolution sometimes) and making the only variable the data source.

A fully automated environment for deriving lineaments is established by combining edge detection and line-linking algorithms and digitizing existing lineaments from geological maps. The outcomes are subjected to thematic comparisons, visual interpretations, geostatistical analyses, and accuracy evaluations. Our results resolved the tectonic setting of the considered area and revealed a reasonable matching with the known tectonic model of the area (D1-D4). Additionally, the study shows that optical sensors are less efficient than DEMs with the same resolution, while Sentinel 1 radar data is more competent than optical data sources. ALOS PALSAR DEM is the most eligible data type, even more so than Sentinel 1 data. The study concludes that PALSAR DEM is effective in automatic lineament extraction, to a point where the number of extracted lineaments can deviate from the expected relationship with pixel size.

4.3.1 Results

Many outcomes were made on various levels, as shown in Figures 4-4, 4-5, and Appendix 4-16 including the optimal VNIR and SWIR bands for each form of optical data and the best data type overall for each resolution

category. The overall results are summarized in Appendix Table 7 and introduced in Figures 4-4 for simplicity. More details about the results and their interpretations are discussed by [28].

The study found that at a resolution of 30m, the best optical data sources were ASTER, EO1, and L8, while SRTM, NASA, and ASTER v3 were the best DEMs. At 20m, S2 B5 VNIR was superior to S2 B11 SWIR. At 15m, the best data sources were manually extracted lineaments, PCA1 ASTER, ASTER B3, L8 B8, and L8 PCA1. At 12.5m, ALOS PALSAR was the most effective, while at 10m, radar VH & VV were better than optical data sources. The study also found that PALSAR DEM provided superior results than using S1 radar data. This study is unique in comparing nine different data sources and considering the spatial resolution. The study found that DEMs and radar data were more effective than optical data sources for lineament extraction due to their independence from sensor characteristics and sensitivity to geomorphology without being affected by weather conditions. The study recommended the best data sources for different pixel values commonly used in geological applications to help users achieve the most potent results.

4.3.2 Accuracy Assessment using Density and Validation Analysis

Density and lineament analysis are closely related, as the former calculates the amount of a particular feature within a given area [100] and provides a clear representation of the distribution of the latter. In the current study, the creation of density maps involves using the line density tool in the ArcMap software (which assigns red colors to areas of high density and green colors to areas of low density) in 3 ways:

1- The study first overlayed manually digitized faults onto density maps (Appendix 4-17), finding that all data sources showed a reasonable fit. The best matching results were obtained from ALOSPALSAR DEM, S1 VV&VH, NASADEM, SRTM DEM, L8 b8, EO1 panchromatic band, S2 b5, and S2 b2. The resultant density map built from manually delineated lineaments showed considerable agreement with other density maps by highlighting the southern portion of the study area as a denser zone.

2- Two selected areas (Samut and Dungash) with detailed geological maps overlain by lineaments and faults were obtained after extensive field studies, confirming the accuracy of the density maps Appendix 4-18, and Appendix 4-19.

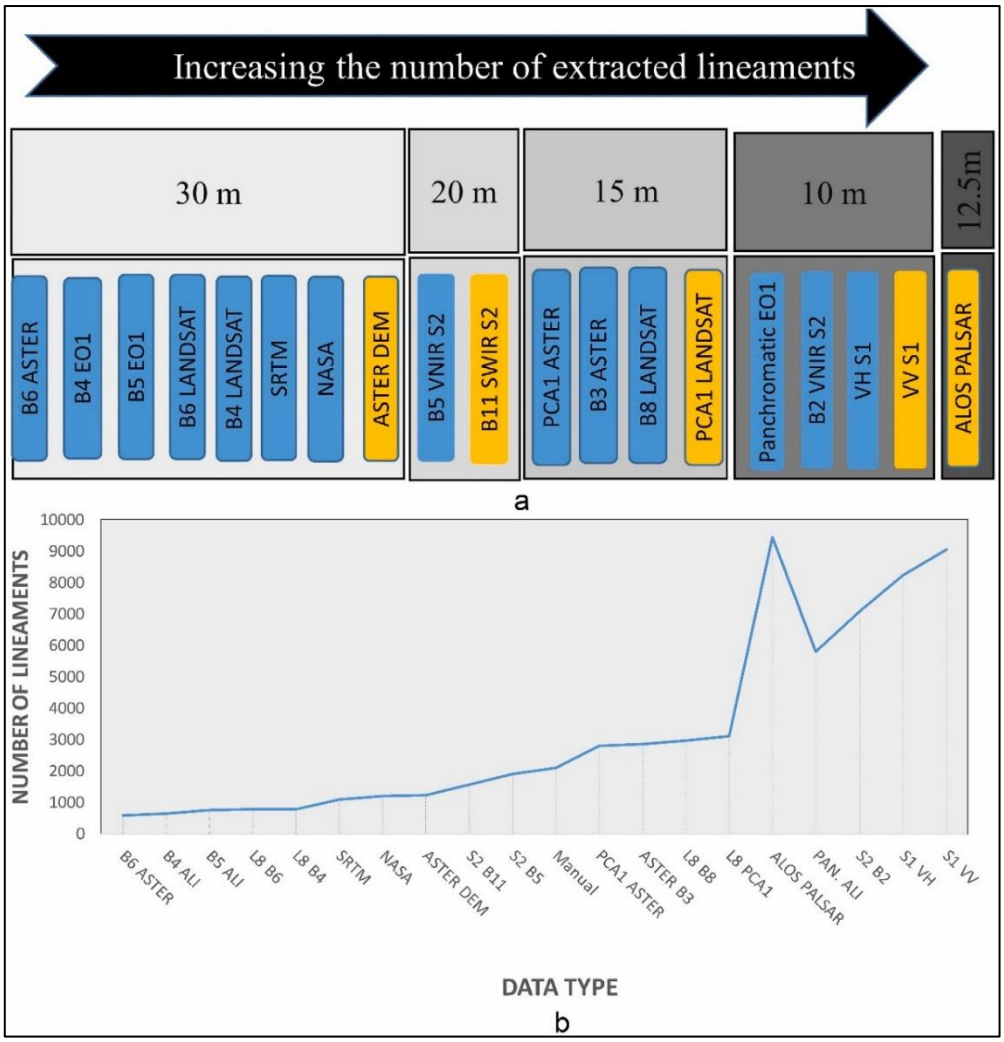


Fig. 4-4: (a) The best data types are ordered according to the ability of lineaments extracting, in each spatial resolution category (b) Ordering of the best data types, showing a directly proportional relationship of the extracted number of lineaments and pixel resolution except an odd behavior of ALOS PALSAR DEM reflecting its notability over all the used data at the study area.

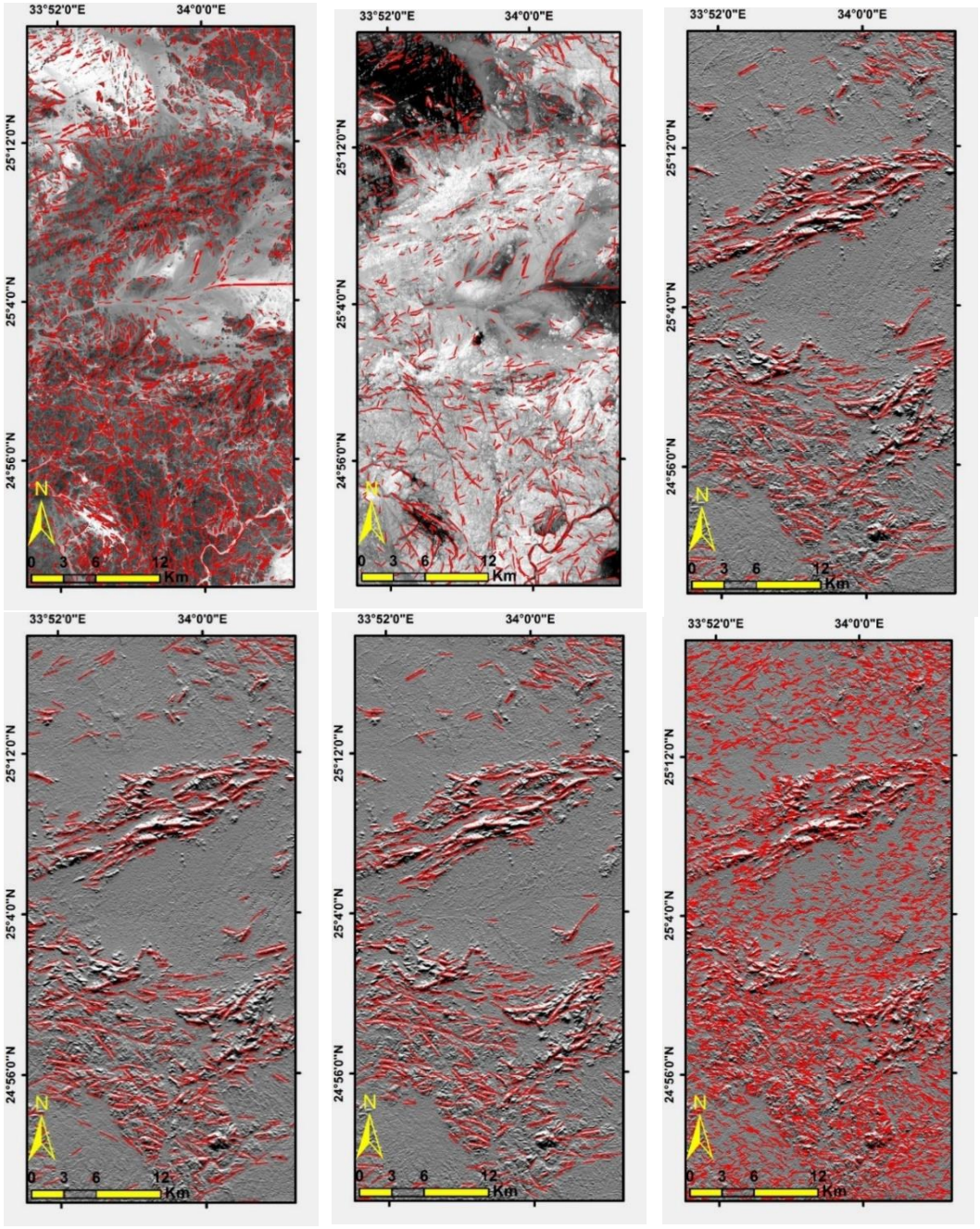


*Fig. 4-5: Grey scale images of (**a**) S2 b2, (b) PCA1 of S2 bands. Shaded relief maps at azimuth 0 and altitude 30 for (c) SRTM DEM, (d) NASA DEM, (e) ASTER GDEM and (f) ALOS PALSAR DEM, overlaid by automatically derived lineaments from each of them.*

3- The fourth verification method involved testing higher-density areas themselves to determine if the extracted lines were accurately distributed and reflected real linear features. The Gabal Mueilha area (Appendix 4-20, Appendix 4-21, and Appendix 4-22), constituted of post-orogenic alkali feldspar granite, was used to enhance and boost the study.

After analyzing the trends, it can be concluded that preferred lineament trends fall into the following categories: NNE-SSW to NNW-SSE, ENE-WSW to WNW-ESE, NE-SW, and NW-SE (Figure 4-6, Appendix 4-23, and Appendix 4-24). These trends are consistent with a recent study [9] of the structural setting of the study area, which groups deformation phases and their relevant structures into three main phases: D1, D2, and D3 [9]. D1 is responsible for NE-SW trending lines due to NNW-SSE shortening, while D2 results in NW-SE trends due to NNE-SSW shortening. D1 and D2 collectively contribute to the generation of ENE-WSW to WNW-ESE trends. Lines with NNE-SSW to NNW-SSE trends result from the D3 phase, known as E-W Oblique Convergence. The lineaments match well with the structural map for the study area, and all trends are represented.

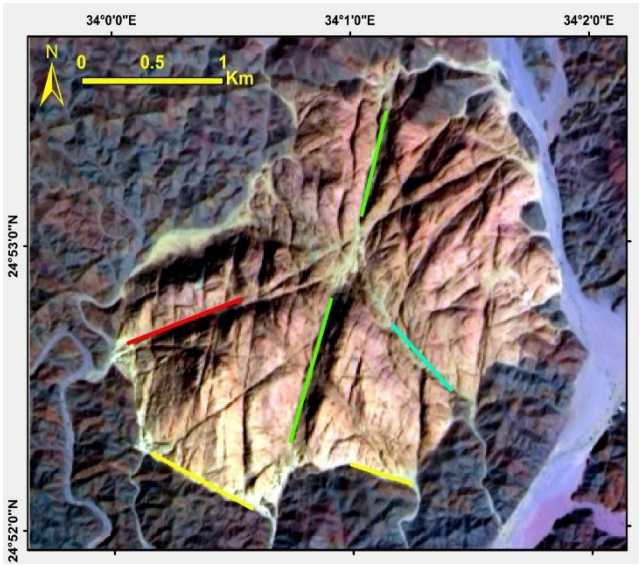


Fig. 4-6: Manifestation of the common line orientations over Gabal Mueilha, NNE-SSW to NNW-SSE trends are represented by green line, ENE-WSW to WNW-ESE trends are highlighted by yellow lines, NE-SW trend is represented by cyan color and red color for denoting NW-SE orientation. Moreover, and in a sinistral sense of displacement, the yellow lines are shifted in away manifesting the existence of NNE-SSW fault (green line).

Our results revealed that the detected lineament groups could reasonably be assigned to the deformation phases (D1-D3) based on our field observations and by comparing our detected lineaments with previous studies addressing these deformational phases [9]. It is important to emphasize that the contacts between the rock units are predominantly structurally controlled, as documented by field observations, and occasionally reasonably match some of the detected linear features as well.

4.4 Textural analysis

The content in this section has been previously published in the following article: Shebl et al., (2024) [84]. For detailed information on this topic, please refer to the respective publication.

In order to better distinguish the rock units within the research region, several band combinations were constructed. For the lithological content distinction within the research area, one of the best results is introduced by a 10 m FCC 12–6-2 in RGB. After that, this composite was pan-sharpened with a 2.5 m pixel size utilizing PRISM data to obtain a greater level of texture-related information. To improve lithological and structural mapping through a more straightforward paradigm, textural features in the study area were computed using only one band. Using band 12 as an input, the greatest results were recorded after multiple trials. Thus, two distinct spatial resolutions (10 m and 2.5 m) of band 12 are currently ready for a more thorough textural examination.

The Grey Level Co-occurrence Matrix, also known as the grey-level spatial dependence matrix [83,101], was utilized in our study to conduct a thorough textural analysis because of its effectiveness in a variety of datasets, including radar [82] and aeromagnetic [102] datasets for lithological mapping. Basically, spatial heterogeneity among nearby pixels could be used to discern textural properties. To interpret the textural features, a moving kernel (window) whose size mostly depends on the desired output is used to verify the digital values of image pixels.

4.4.1 Lithological mapping

Our outcomes, including mean, variance, homogeneity, contrast, entropy, and correlation, exhibit varying capabilities when it comes to distinguishing between different rock types in the studied region. Furthermore, the level of detail extracted largely depends on two key factors:

the spatial resolution of the input data (either 2.5m or 10m) and the size of the moving window used (ranging from 3×3, 7×7, to 11×11).

In general, our findings suggest that the most effective textural parameters for creating meaningful lithological maps are the mean, variance, and homogeneity. For example, the mean parameter, acting as a straightforward form of smoothing, can distinctly differentiate between serpentinites in dark brown shades, granitic rocks, and mining activities in bright light hues, and metavolcanics and metagabbro diorites, which exhibit a combination of cyan and yellow shades due to their diverse compositions within the study area.

The combination of mean, variance, and homogeneity significantly improves the ability to distinguish different rock types within the research area, as evidenced by Figure 4-7. When representing mean, variance, and homogeneity using a pseudocolor ramp in RGB format, distinctive patterns emerge: serpentinite rocks are distinctly highlighted in blue, metavolcanics are represented in yellow, certain types of wadi deposits and mining areas appear in red, while the pinkish hues predominantly signify the ophiolitic mélange matrix, which typically comprises volcaniclastic metasediments and metagabbros. Hence and upon a field check for the distribution of the main rock units, this study strongly recommends the adoption of an RGB composite consisting of homogeneity, mean, and variance as a standard approach for conducting comprehensive lithological mapping in future research endeavors.

In Figure 4-7, the RGB of correlation, mean, and variance are displayed and give lithological insights where the red-brown colors indicate basic rocks, however green color indicates acidic rocks or wadi deposits indicated by bright pixels. The most important is tracking these colors which may reveal minor structural features as displayed in the figure.

4.4.2 Comprehensive structural analysis

One of the key findings in our study involves the elucidation of intricate structural features, such as foliations, folding, faulting, and cross-

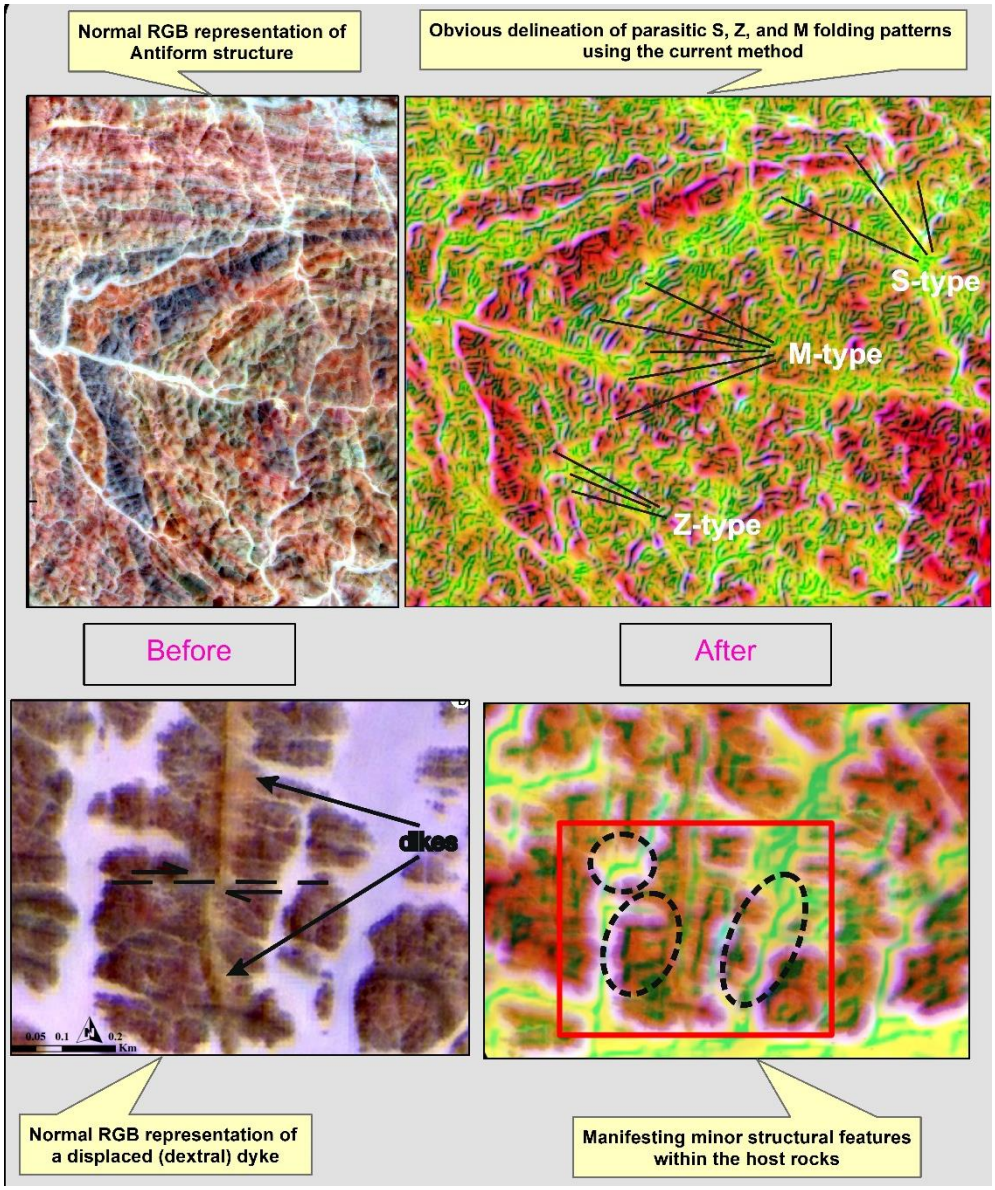


Fig. 4-7: Lithological and structural analysis using normal FCC images (left, before applying textural analysis) and an RGB of correlation, mean, and variance, respectively using textural analysis (right).

cutting relationships (Figure 4-7). Previous studies focusing on textural analysis have seldom addressed this aspect, yet it significantly enhances the precision of analyzing structurally complex terrains, approaching levels of detail comparable to on-site fieldwork.

In light of the aforementioned considerations, the application of textural-based structural analysis offers a valuable means of delineating the positions of various structural relationships. This, in turn, facilitates more refined geological interpretations, with potential applications in the identification of structurally controlled mineral deposits and other geological phenomena.

4.5 Integrating Remote Sensing and Geophysics for Mineralized Zone Delineation

The content in this section has been previously published in the following articles: Shebl et al., (2023)[37]; and Shebl and Csámer, (2021) [31]. For detailed information on this topic, please refer to the respective publications.

This part aims to unveil potentially mineralized zones by integrating hydrothermal alteration patterns and structural framework via remote sensing and geophysical data characterization (Figure 4-8). The findings regarding the primary hydrothermal alteration pattern (outlined in Appendix Tables 8, and 9) indicated that the composite images generated by ASTER using color ratios (4/7, 2/1, 4/3), Sentinel 2 (11/12, 4/2, 1/8), Landsat OLI (6/7, 4/2, 6/5), and ALI (8/9, 4/1, 8/6) demonstrate considerable visual similarity. This resemblance is particularly evident in the representation of hydroxyl-bearing alteration (highlighted in the red channel), which closely resembles the patterns depicted in Appendix 4- 25a, 4- 25b, 4- 25c, and 4- 25d.

Upon comparison with geological maps, it becomes apparent that hydroxyl-bearing alterations predominantly occur within serpentinite formations. Metavolcanic formations show signs of influence from iron oxides and minerals containing hydroxyl groups. Typically, iron oxides are denoted by blue and green colors and are primarily concentrated within ophiolitic mélange regions, which include volcaniclastic metasediments, weathered syn-tectonic granites, and quaternary deposits.

4.5.1 Relative Band Depths (RBDs)

It is important to emphasize that RBDs can highlight a broad range or group of hydrothermal alteration minerals, but they cannot definitively identify a specific mineral, unlike spectral localization techniques, such as

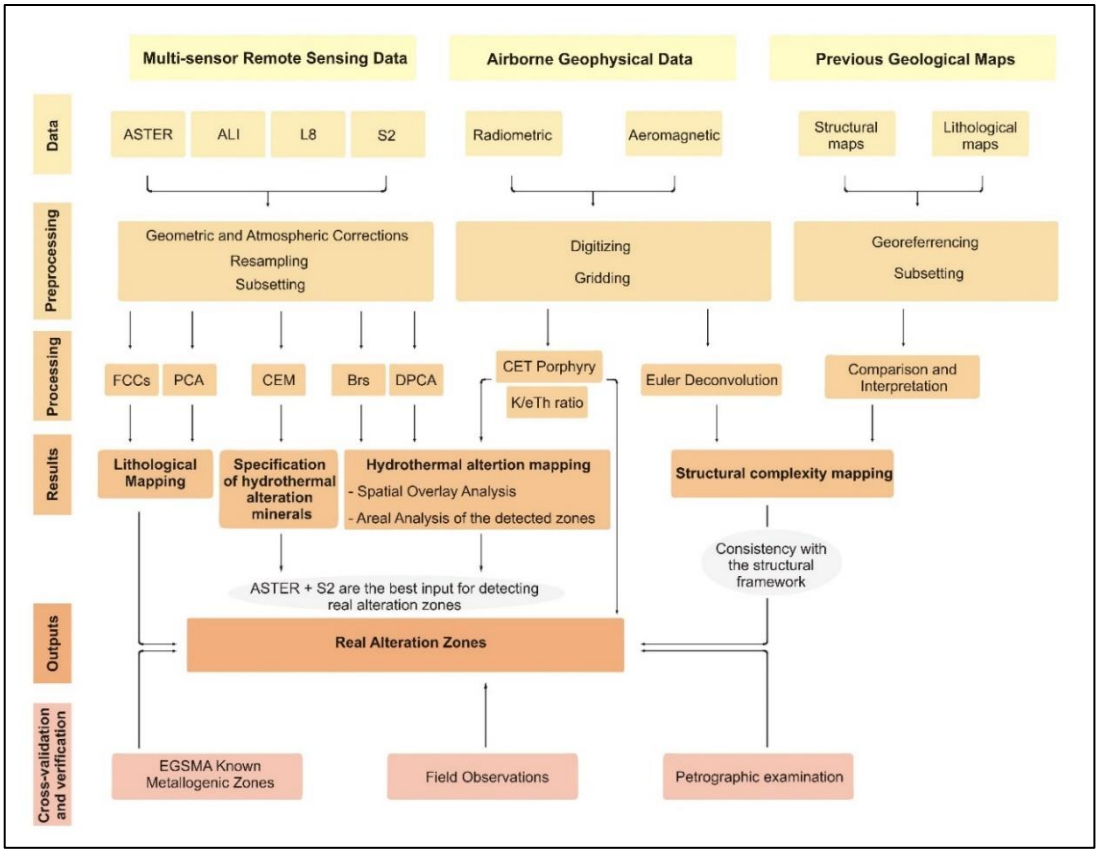


Fig 4-8: Flowchart showing the adopted methodology utilized in the current study.

constrained energy minimization (CEM). For example, RBD can indicate the presence of phyllosilicate clay minerals (such as alunite, kaolinite, or pyrophyllite [103], but they cannot pinpoint a particular mineral like CEM, which can identify a single mineral based on its unique spectral signature in terms of reflectance or absorption.

When applying the RBD method to ASTER data, the outcomes reveal the distribution of various minerals, including phyllosilicate clay minerals (alunite, kaolinite, pyrophyllite), Al/Fe-OH compounds, Mg-Fe-OH compounds, and Si-OH minerals, as depicted in Appendix 4- 25e, 4- 25f, 4- 25g, and 4- 25h. These minerals are reasonably assigned based on the exposed rock types. For instance, the concentration of alunite, kaolinite, and pyrophyllite is primarily observed on extensively weathered granitic rocks in the northern portion of the study area. Similarly, minerals enriched in Al/Fe-OH (mainly sericite, muscovite, illite, and smectite) are linked to syn-tectonic

granite and iron-rich Nubian Sandstone. On the other hand, chlorite and epidote minerals correlate closely with serpentinite formations. Si-OH minerals are widespread across the ophiolitic mélange, metavolcanic rocks, and serpentinite formations.

4.5.2 DPCA

Within Appendix Table 10, various types of alterations are presented based on the contribution of input bands or band ratios to the eigenvector matrix in DPCA. Examining the magnitude and eigenvector loadings extracted through DPCA has proven highly valuable for identifying groups of alteration minerals within the four datasets. To illustrate, in ASTER's DPCA involving bands 1, 3, 4, and 7, the initial DPC does not provide specific information about any hydrothermal alteration type, as all eigenvector loadings for the four input bands are negative (Appendix Table 10). In contrast, DPC 4 exhibits robust positive loadings for B7 (0.96) and minor positive or negative loadings for bands 1, 3, and 4. Consequently, DPC 4 (Appendix 4- 26a) effectively highlights the intended target from this combination, which pertains to hydroxyl-bearing minerals.

For Landsat 8, DPC 1 lacks distinctive information due to the prevalence of positive loadings across all input bands. DPC 3 (Appendix 4-26b) surpasses DPC 2 and DPC 4 in distinguishing hydroxyl-bearing minerals due to its significant loadings for band 7 (0.67) relative to the other components (Appendix Table 10). In the context of Sentinel 2 findings, DPC 1 does not yield unique insights due to dominant negative loadings for all input bands. DPC 2 displays moderate loadings for nearly all alteration mineral groups, thus failing to strongly emphasize any of them. DPC 3 could reasonably highlight iron oxides due to their negative loadings in band 2 and positive ones in band 8a; however, pinpointing hydroxyl-bearing minerals is challenging due to weak loadings in bands 11 and 12. DPC 4 (Appendix 4-26c) successfully distinguishes hydroxyl-bearing minerals owing to their robust loadings in bands 11 and 12. Similarly, ALI's DPC 3 (Appendix 4- 26d) stands out as the most effective in highlighting OH-enriched minerals due to its high loadings in band 9, especially compared to the same band's loadings in other components.

These outcomes align closely with previous studies [104–106] that emphasized the presence of altered anomalies within the noisiest components (typically the third or fourth). The current research further establishes that the most effective DPCs for revealing hydroxyl-bearing

minerals are ASTER DPC 4, Sentinel 2 DPC 4, Landsat 8 DPC 3, and ALI DPC 3. Similarly, when analyzing the eigenvector matrix to discern rocks rich in iron oxides, the most informative components are ASTER DPC 2 (Appendix 4- 26e), Landsat 8 DPC 3 (Appendix 4- 26f), Sentinel 2 DPC 3 (Appendix 4- 26g), and ALI DPC 3 (Appendix 4- 26h). Notably, for Sentinel 2, Landsat 8, and ALI, the key wavelength (around 0.48 μm) for distinguishing iron oxides exhibits strong loadings in DPC 3. Even though this wavelength is absent in ASTER, DPC 2 proves to be the optimal component, displaying the highest loading (0.71) in band 1.

4.5.3 DPCA applied to Band Ratios

DPCA was also employed to analyze band ratio indices that provide valuable information for identifying alteration types, as discussed by [49]. In the case of ASTER data, the selected inputs were 2/1, 4/2, (5 + 7)/6), and ((7 + 9)/8), to emphasize rocks containing ferric/ferrous oxides, Al/Fe-OH, and Mg-Fe-OH. In DPC 3, rocks containing ferrous oxides (as shown in Figure 4- 9a) could be effectively delineated, attributed to the significant contribution of the B2/B1 ratio input (0.99), when compared to the other inputs. DPC 4 was capable to distinguishing rock units enriched with ferric iron (Figure 4- 9 b), primarily due to strong negative loadings in B4/B2.

Our findings indicated that DPC 1 (Figure 4- 9c) is notably effective in discerning Al/Fe-OH enriched minerals ((5 + 7)/6) from those enriched in Mg-Fe-OH ((7 + 9)/8). This underscores the remarkable capability of ASTER data to not only detect hydroxyl-bearing minerals but also classify them as either Al/Fe-OH or Mg-Fe-OH minerals, showcasing the superiority of ASTER data due to its Short-Wave Infrared (SWIR) bands. Furthermore, through the Constrained Energy Minimization (CEM) technique, certain minerals within these categories can be identified and specified.

The outcomes of Sentinel 2's DPCA highlighted the effectiveness of DPC 3 (Figure 4- 9d) in identifying rocks enriched with OH-bearing minerals, primarily due to the prominent contribution of the 11/12 band ratio (0.98). DPC 4 (depicted in Figure 4- 9e) demonstrated clear differentiation between rocks containing ferrous (11/4) and ferric (11/8a) elements, with reasonable negative loadings (-0.52) for the former compared to strong positive loadings (0.82) for the latter.

Analyzing the DPCA results for Landsat 8 data revealed the superiority of DPC 3 (Figure 4- 9f) in distinguishing rocks enriched with OH-bearing minerals, driven by the significant contribution of the 6/7 band ratio

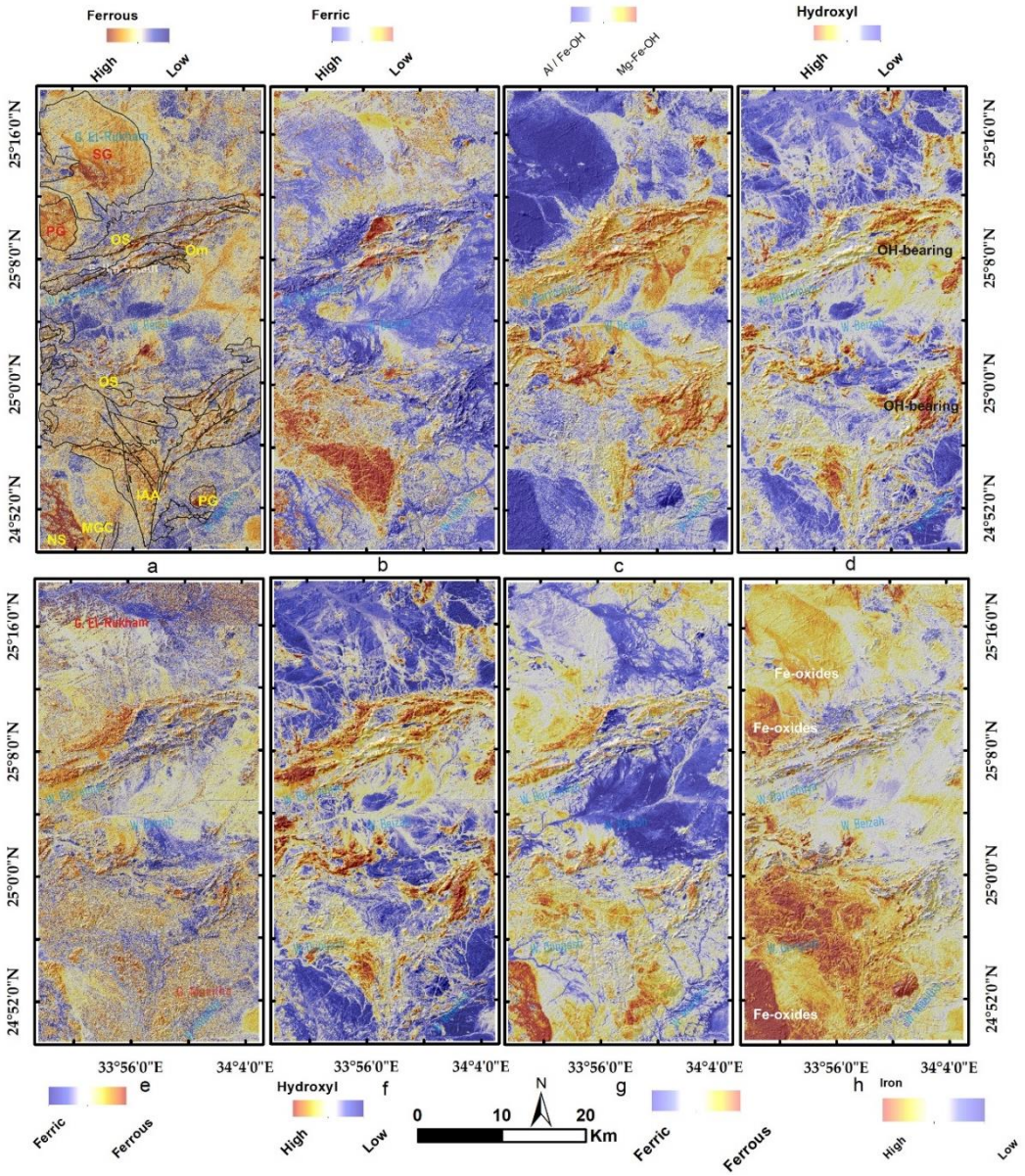


Fig. 4-9: Pseudocolor ramps representing rule images of (a) ASTER DPC3, (b) ASTER DPC4, (c) ASTER DPC1, (d) Sentinel 2 DPC3 (e) Sentinel 2 DPC4, (f) Landsat 8 DPC4, (g) Landsat 8 DPC4 and (h) ALI DPC4 showing lithological units affected by various types of hydrothermal alterations within the study area.

(0.99). The distinction between ferrous (6/4) and ferric (6/5) elements was achieved through the loadings of DPC 4 (Figure 4- 9g). Similarly, ALI data successfully differentiates rocks enriched with OH-bearing minerals through DPC 3, while simultaneously highlighting iron oxides within DPC 4 (Figure 4- 9h).

4.5.4 Constrained Energy Minimization (CEM)

The present study employs the CEM method to approximate the identification of alteration minerals within the SWIR range, using ASTER data (Figure 4-10). Nevertheless, before determining the spatial extents of the recognized hydrothermal alteration anomalies, a comprehensive review of airborne geophysical data was conducted to ascertain the validity of these detected zones. This analysis encompassed findings such as the reduction-to-pole (RTP) map, potassium concentration (K) map, and equivalent thorium concentration (eTh) map.

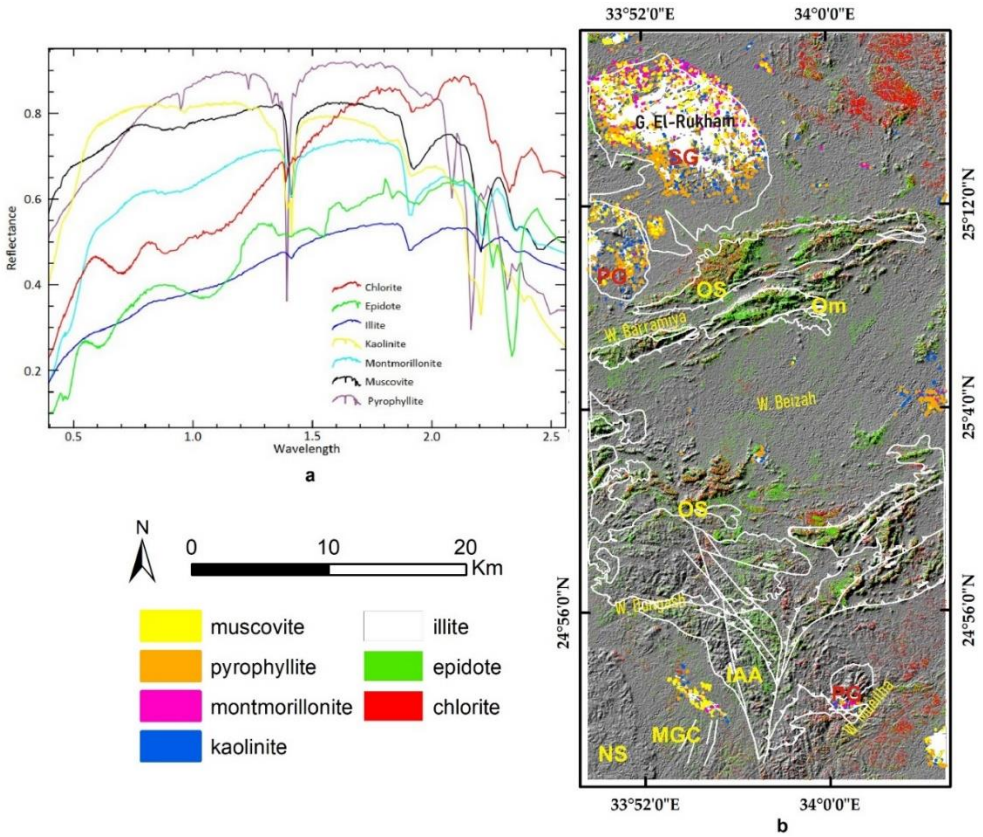


Fig. 4-10: (a) Spectral curves (from USGS spectral library) of the minerals utilized in CEM analysis and (b) their distribution within the study area.

4.5.5 Geophysical data findings

Through integrating magnetic and radiometric data, which are mainly employed to depict magnetic and radiometric characteristics linked to hydrothermal alteration zones, we were able to verify the presence of shear zones and related structures that generally align with the previously mentioned hydrothermal alterations across all interpreted maps of the surveyed area. This collaboration also facilitated the estimation of the depths of these features.

In terms of aeromagnetic data, a series of algorithms were applied to the RTP magnetic map within the framework of CET porphyry analysis. This approach aimed to locate circular or semi-circular structures resembling porphyry intrusions, which are often associated with hydrothermal alteration. These intrusions and/or their inner alteration zones tend to exhibit high magnetic anomalies, while the outer zones display lower magnetic properties. In the initial stages, circular features and their central points within the study region were highlighted using the Circular Feature Transform (CFT) technique (Figure 4-11a). Subsequently, the Amplitude Contrast Transform (ACT) was employed to define the boundaries of the identified circular intrusions (Figure 4-11b). The outcomes of the CET and ACT were leveraged to outline the detected porphyry-like features (Figure 4-11c).

Aeroradiometric data presented in the form of equivalent concentrations of potassium and thorium proved valuable for distinguishing between various lithologies within the study area. For example, ophiolitic serpentine formations tend to exhibit low values in potassium (K) and thorium (eTh) concentration maps, while the highest values are typically associated with syn-orogenic granitoids. Furthermore, the map displaying the highest values of K/eTh ratio (Figure 4-11d) and characterized by a pink color effectively highlights regions of hydrothermal alteration.

Upon visual inspection of Figures 4-11a, 4-11b, 4-11c, and 4-11d, it becomes evident that extensively altered areas are identifiable, particularly in connection with ophiolitic serpentine formations oriented in an ENE-WSW direction over Gabal Um Salatit, and Gabal Um Salim (known as the Baramiya-Mubarak shear zone). A more comprehensive explanation of this phenomenon follows in the subsequent section.

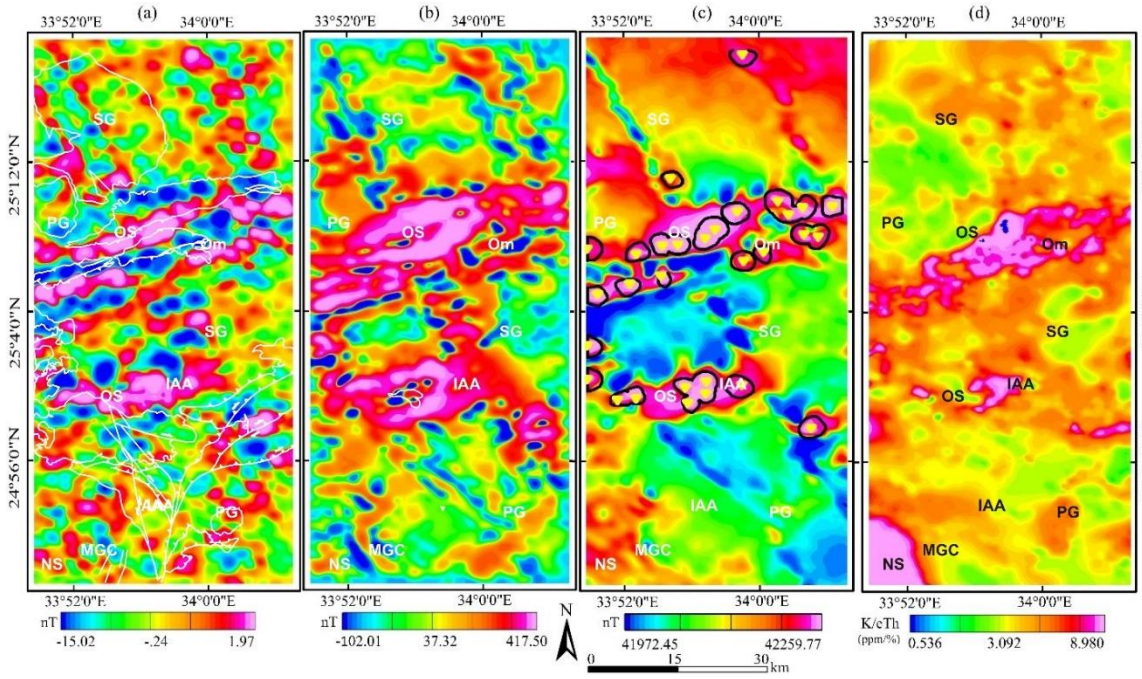


Fig. 4-11: Hydrothermal alteration maps a) Circular feature transform, b) Amplitude contrast transform, c) Boundary tracing of detected hydrothermal intrusions overlaid on RTP map, d) K/eTh ratio map.

4.5.6 Field verification and petrographic investigations

The primary outcome of our investigation emphasizes how ASTER and Sentinel 2 data may be used more effectively in collaboration for better characterization of hydrothermal alteration zones. Our findings agreed with investigations using aircraft magnetic and radiometric data, known mineralized zones, and earlier research. Fieldwork was also conducted to confirm the hydrothermal alteration zones identified by the four datasets (Appendix 4- 27, Appendix 4- 28, and Appendix 4- 29), which are shown in Figure 4- 12a to demonstrate the effectiveness of the combined ASTER and Sentinel 2 (Figure 4- 12b) in identifying real hydrothermal alteration zones within the study area. Figures 4- 12, and 4- 13 show that there is a strong correlation between the observed alterations and our field findings. Our field investigation uncovered various hydrothermal alteration minerals or previously mined zones, demonstrating how our research has contributed to

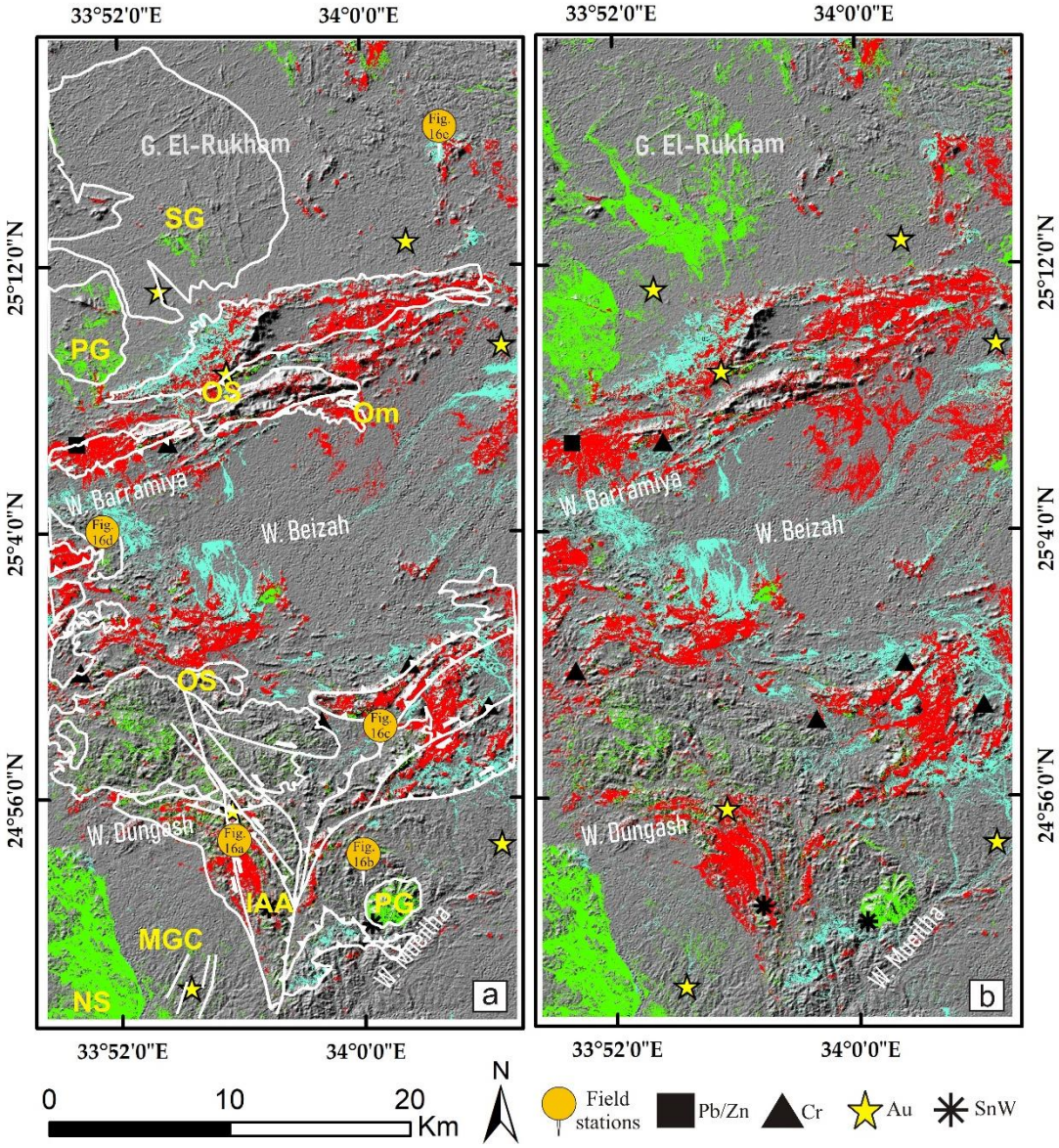


Fig. 4-12: The areal distribution of rocks enriched with hydroxyl-bearing minerals (red), iron oxides (green), and ferrous oxides (cyan) derived utilizing (a) the four sensors, and (b) ASTER and Sentinel 2. A great similarity is noticed revealing the potency and reliability of applying the combined sensor results in confirming hydrothermal alteration (see the location of the mineralized spots within or in between the detected altered zones). Also, the locations of each field photo highlight the consistency of the detected alteration zones with our field investigations.

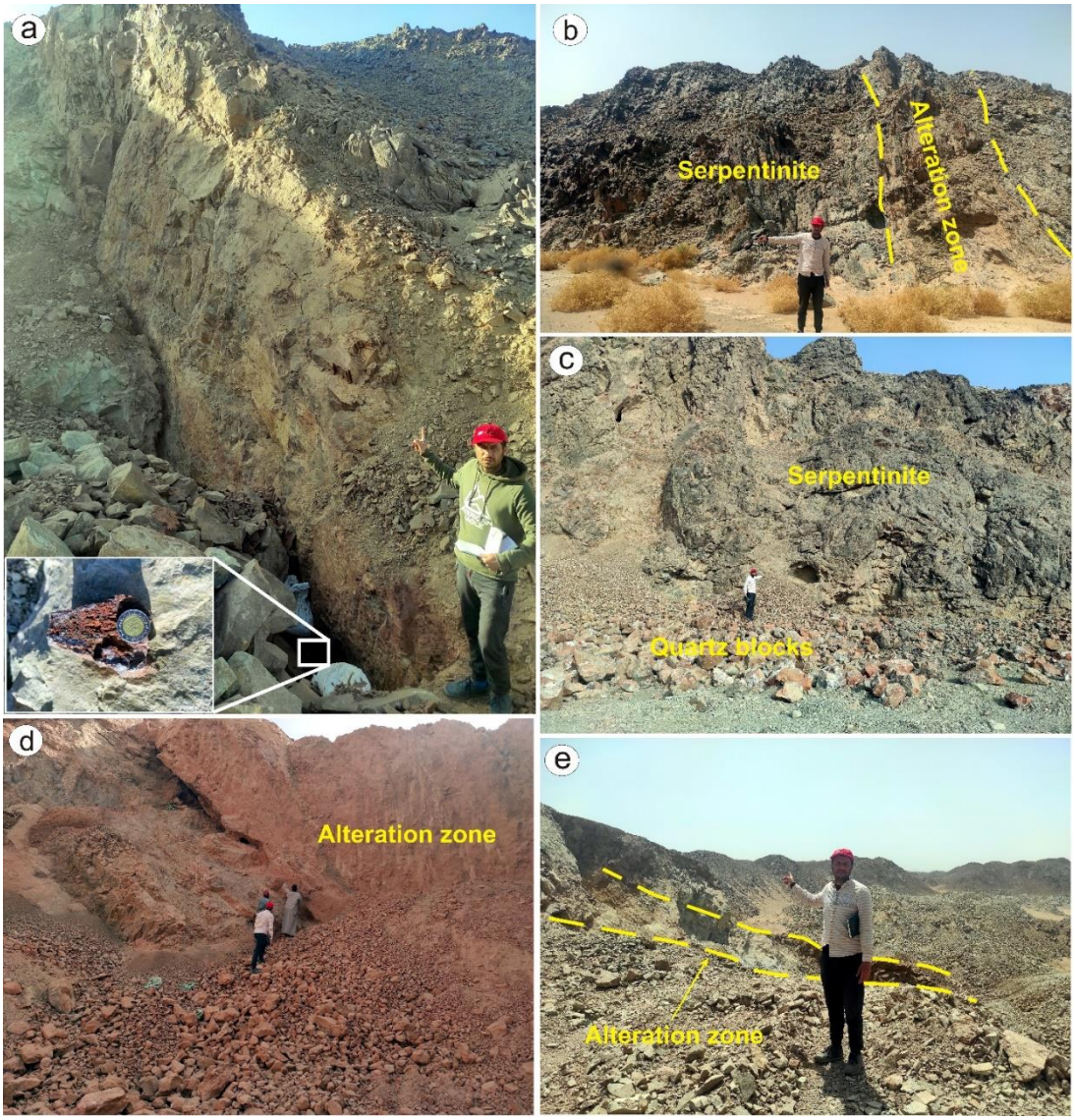


Fig. 4-13: Field photos showing shear-related hydrothermal alterations of (a) Serpentinites exhibiting greenish field tint enclosing excavated gold mineralized quartz vein by random (artesian) miners. Note the reddish ferrous tarnish on the contact surface between the quartz and the host serpentinites. (b) Talc-carbonate zone with a pale whitish buff color associated with the darker serpentinites. (c) Falling down blocks and scree from little quartz stock invading the serpentinites. (d) Huge argillic-ferric alteration zone, several tens of meters across, in serpentinites leading to brick red deposits that are mined by the random (artesian) miners with rather low 1-2 ppm gold according to their estimation. (e) Intensive random mining in the alluvial and highly fractured loose (greenish propylitic altered) serpentinites was done by the random (artesian) miners using the loaders and guided by the metal detectors.

understanding the hydrothermal alteration zones in the study area and the best datasets for their delineation.

Based on the geological context highlighted in the previous chapters, the El Rukham-Mueilha district is characterized by a diverse combination of lithologies. These encompass the suprastructural Neoproterozoic Pan-African nappe assemblage, featuring fragmented masses of ophiolitic mélange and island arc association, alongside syn to post-orogenic intrusive rocks. These geological units, situated within the Barramiya-Mubarak area [107], have undergone extensive alterations prompted by magmatic fluids, leading to hematization (Figure 4- 13a), serpentinization (Figures 4- 13 b, and 4- 13c), argillic (Figure 4- 13 d), and propylitic alterations (Figure 4- 13e). These distinct forms of alteration are intrinsically tied to magmatic activity that coincided with the development of ophiolites and island arc association. These geological processes were concomitant with multi-phase magmatism, facilitating the circulation of hydrothermal fluids and thereby enabling the dissolution of parent rocks.

The nappe assemblage stands out as the predominant lithology, encompassing serpentinites (as depicted in Figure 4- 13), a metagabbro-diorite complex, and metavolcanics enveloped within a matrix of low-grade metasedimentary rocks. Serpentinite, indicative of low-temperature metamorphic/hydrous alterations of igneous ultramafic rocks, is evident, whereas the metavolcanics predominantly exhibit andesitic composition. Our findings are strongly aligned with this pattern, pinpointing hydroxyl-bearing alteration zones primarily in serpentinite rocks within the study area, notably exemplified by Gabal Um Salim and Gabal Um Salatit (as shown in Figure 4- 12). The island arc metavolcanics, largely comprising andesite, also exhibit signs of hydrothermal alterations, particularly prominent in the southwestern region around Wadi Dungash (Figure 4- 12). Notably, the petrographic analysis reveals heavily altered plagioclase and hornblende phenocrysts, transformed into epidote, iron oxides, or chlorite. These are embedded within a fine-grained groundmass composed of plagioclase, hornblende, quartz, and mica, imparting a porphyritic texture (depicted in Figures 4- 14a, 4- 14b, 4- 14c, and 4- 14e).

This lithological sequence is subsequently intruded by multi-stage magmatism, encompassing both syn-orogenic and post-orogenic granites. While syn-orogenic granitoids are chiefly exposed in Gabal El-Rukham, post-orogenic granite sporadically emerges within the research area, exemplified by Mueilha granite. The syn-orogenic granites exhibit a dioritic composition characterized by plagioclase, hornblende, quartz, and epidote, with iron

oxides representing the altered state of hornblende (Figures 4- 14d, and 4-14f).

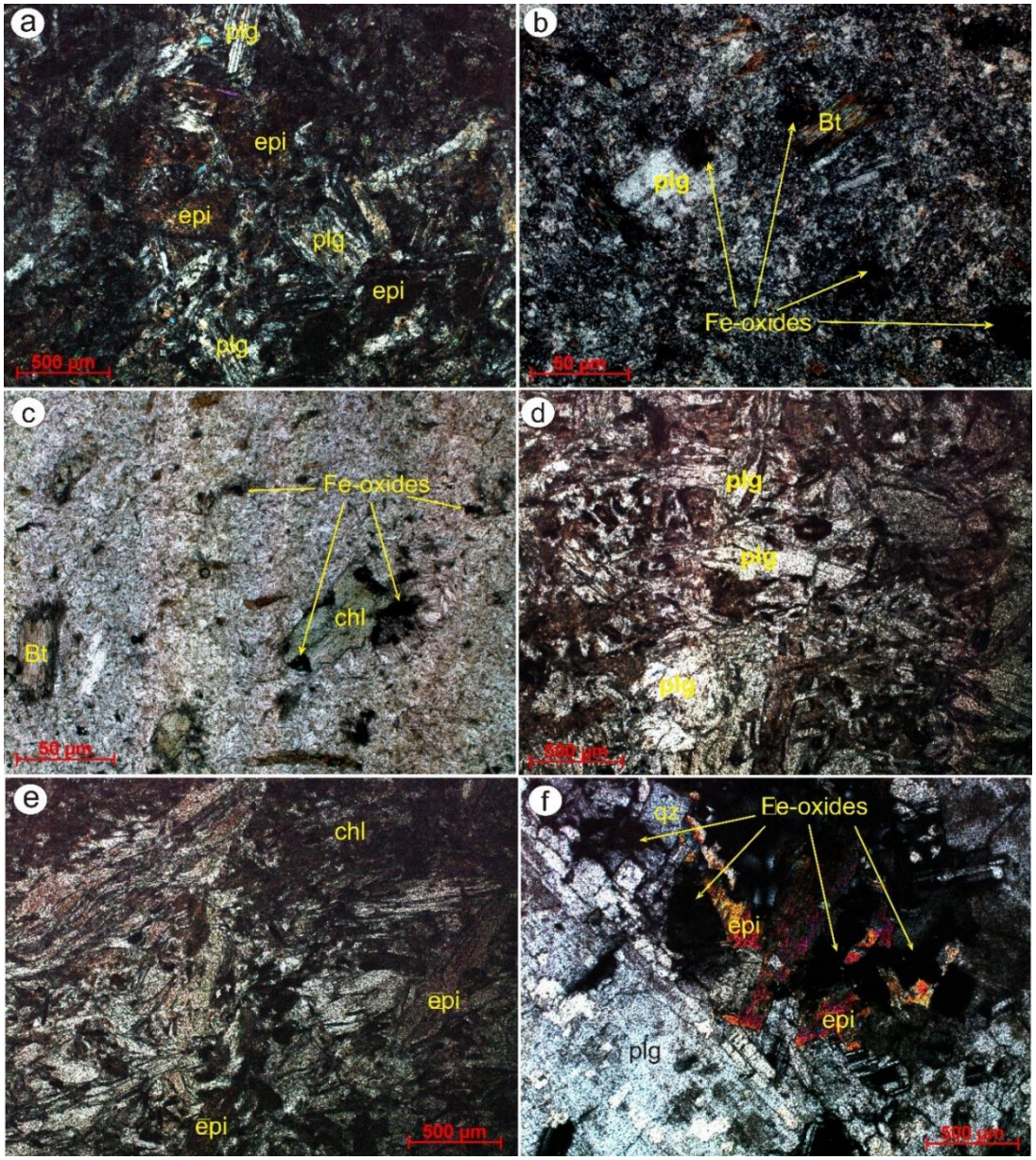


Fig. 4-14: Thin-section photomicrographs showing the effect of hydrothermal alterations (a) within plagioclase (sericitized) and epidote (xN), (b) altered biotite and plagioclase phenocrysts (xN), and (c) iron oxides with altered biotite and chlorite phenocrysts (ppl) in altered metavolcanics exhibiting porphyritic texture. Depiction of typically hydrothermal alteration related minerals including (d) altered plagioclase (ppl), (e) chlorite (xN), and (e and f) epidote (xN) within highly deformed lithologies. Abbreviations, Qz: quartz, Pl: plagioclase, Bt: biotite, Chl: chlorite, Epi: epidote.

4.6 Petrographic and geochemical characterization of the rock units

4.6.1 Petrographic investigations, XRD analysis, SEM-EDX, and Geochemical analysis

In this chapter, we delve into a comprehensive analysis of the lithologies exposed in our research area, shedding light on their petrography, opaque mineralogy, and geochemistry. The current thesis reports our lab investigations and analytical results applied to the exposed rock units, veins, and hydrothermal alteration zones in terms of petrography, XRD, opaque mineralogy, and geochemical analysis. These techniques are mainly utilized for the verification of remote sensing results besides supplementing the fieldwork in resolving the geological and tectonic setting of the considered area. Adopting multiscale investigations (remote sensing → fieldwork → hydrothermal alterations delineation → petrographic investigations → opaque mineralogy → XRD → geochemical analysis) in mineral explorations has become more popular in recent years in mineral potentiality mapping [34]. Each rock unit will be discussed in the following part.

This chapter includes a description of the main petrographic characteristics of mineralogy and textures for the various lithologies cropping out in the considered area. Thin sections of representative rock samples were prepared from the various rock exposures to identify the different rock types. The main rock types in Um Salatit-Mueilha area are represented by ophiolitic group association (serpentinites, metagabbros, and ophiolitic mélange), island arc metavolcanics (mainly metaandesites), metagabbro-diorite complex, older, and younger granites, and post-granitic dikes.

4.6.2 Petrographic characteristics

Each rock unit has undergone meticulous examination using a transmitted polarized light microscope. The key characteristics of the investigated rock units are presented in Table 1:

Table 1: Summary of the petrographic characteristics of various rock types from the study area

Serpentinite		
Color	Texture	Rock-forming Minerals
greenish-gray to blackish-green	Pseudomorphic mesh and bastite textures	Antigorite, chrysotile, talc, chlorite, carbonates, iron oxides, chromite, and sulfides
Key characteristics (Figures 4-15 a:f and 4-16 a)		
Antigorite: Colorless to pale green fibrous or lamellar aggregates Chrysotile: Colorless veinlets with low relief and weak to moderate interference colors Chlorite: Large aggregates, often an alteration product Talc: Occurs as discrete minute grains and is frequently found as dispersed aggregate pockets Carbonates: Predominant and fine-grained, frequently present Listvaenite: Contains significant carbonate content, with well-represented silica and serpentine minerals		
Ophiolitic metagabbro (hornblende metagabbro)		
Color	Texture	Rock-forming Minerals
greyish green speckled with white	ophitic and subophitic	Plagioclase, hornblende, tremolite-actinolite, clinozoisite, calcite, sericite, chlorite sericite, epidote, opaques (iron oxide), quartz and apatite
Key characteristics (Figure 4-16 b)		
Plagioclase: has an andesine composition (An37) and is sometimes highly saussuritized.		
Mélange matrix (Quartz-feldspathic schists)		
Color	Texture	Rock-forming Minerals
diverse range	Schistose	Quartz, plagioclase, sericite, and iron oxides
Key characteristics (Figure 4-16 c:f)		
It is composed of polymict assemblages, including dismembered ophiolitic blocks, Plagioclase: is subhedral and subprismatic medium-grained crystals with an intermittent appearance of twinning due to the sericitization effect Quartz: exhibits wavy extinction because of deformational events (shearing)		

Island arc metavolcanics (Meta-Basaltic Andesite)		
Color	Texture	Rock-forming Minerals
dark green to dark gray	Porphyritic and glomeroporphyritic	plagioclase, hornblende, augite sericite, chlorite, opaques, biotite, quartz, titanite and epidote
Key characteristics (Figure 4-17 a, b, and b)		
Plagioclase: labradorite composition (An51-56) partly deformed and intensively saussuritized Hornblende: prismatic crystals of pale green color and shows pleochroism Pyroxenes: augite, which is altered completely or partially to pale green fibrous tremolite-actinolite and hornblende. Chlorite: (as an alteration product of hornblende and biotite) forms anhedral to subhedral fan-shaped crystal aggregates of green color and shows faint pleochroism		
Island arc metavolcanics (Meta-Andesite)		
Color	Texture	Rock-forming Minerals
grey to greenish-gray color	porphyritic	plagioclase, hornblende, quartz biotite, chlorite, epidote, sericite titanite, calcite apatite, and opaques
Key characteristics (Figure 4-17 a, b, and b)		
Plagioclase: is present in two generations; xenocrysts and fine laths in the groundmass Plagioclase: ranging from oligoclase to andesine (An27-34) Hornblende: shows distinct pleochroism and is quite altered to chlorite and epidote Quartz: anhedral and shows undulose extinction (phenocrysts or groundmass microcrystals) Secondary silica (quartz) occurs as micro veins invade the rock Chlorite: shows pale green color and pleochroism from pale green to colorless		
Metagabbro-Diorite complex (ranges from gabbro, diorite to quartz diorite)		
Color	Texture	Rock-forming Minerals
whitish grey to grey	hypidiomorphic and sub-idioblast granular	plagioclase, hornblende, pyroxene, biotite, quartz, chlorite, sericite, calcite, few tremolite-actinolite iron oxide, apatite, zircon, and titanite
Key characteristics (Figure 4-17 d, e, and f)		

Plagioclase: thick flattened crystals and is commonly andesine in composition (An36 - An42)
Hornblende: has green (and brown) color with faint pleochroism
Biotite: is strongly pleochroic and shows varying degrees of alteration to chlorite.
Quartz: occurs as xenoblast crystals, filling the interstitial spaces between other crystals and shows weak undulose extinction
The rock underwent regional metamorphism under greenschist facies conditions, resulting in the common replacement of calcic plagioclase with saussurite

Syn-orogenic or older granite (tonalites-granodiorites)

Color	Texture	Rock-forming Minerals
grey	hypidiomorphic granular	plagioclases, quartz, hornblende, ± biotite and k-feldspar, saussurite, chlorite, calcite, kaolinite, and epidote, opaque minerals, and apatite

Key characteristics (Figure 4-18 a: d)

Plagioclases: are the main component and are mostly saussuritized. Some plagioclases are corroded by quartz and are severely altered to clay minerals and calcite.
Quartz: coarse undeformed crystals, whereas the deformed ones show undulose extinction
Hornblende: exhibits green color and strongly pleochroic
Chlorite: occurs either as an alteration product of mafics or results from the hydrothermal solutions that affect the grey granites

Post-orogenic or younger granite (alkali feldspar granite)

Color	Texture	Rock-forming Minerals
red to pink	hypidiomorphic granular and myrmekitic textures	quartz, perthitic k- feldspar, plagioclases, muscovite, and a few biotite, hornblende, Sericite, kaolinite apatite, zircon, garnet and opaque minerals

Key characteristics (Figure 4-18 e, and f, and 4-19)

Quartz: occurs as interstitial anhedral crystals and shows wavy extinction
K-feldspars: are represented by orthoclase and microperthite.
Orthoclase: is relatively kaolinized and it can be replaced by microcline.
Microcline: cross-hatching twinning and occasionally replaces plagioclases and orthoclase.
Plagioclases: (An. 6-13) Plagioclases show albite twinning and are relatively sericitized. Plagioclases are replaced by K-feldspar and quartz.
Hornblende: is colorless to yellowish green.
Chlorite (with no pleochroism) and epidote are alteration minerals.

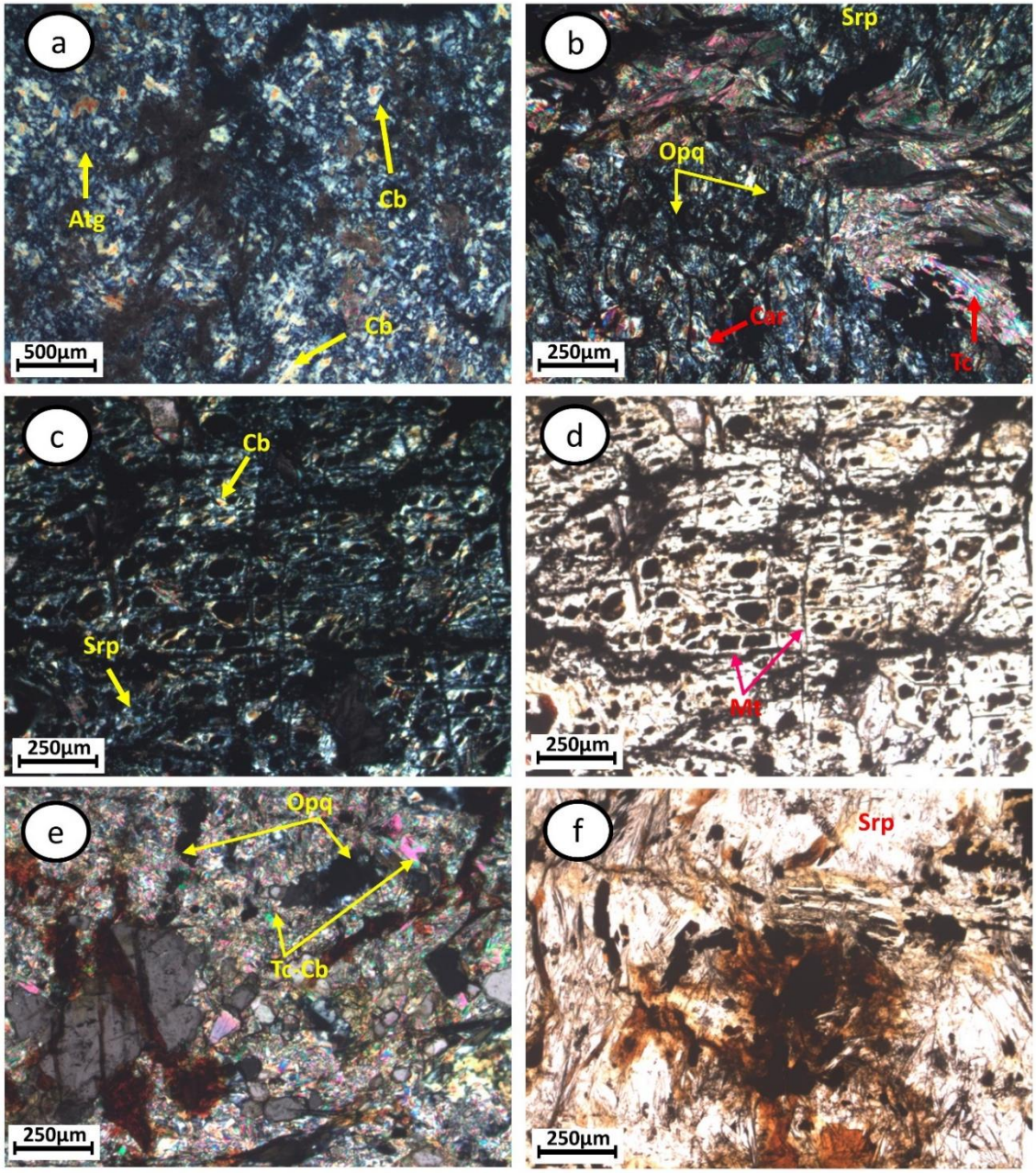


Fig. 4-15: Photomicrographs showing petrographic textures and features in serpentinite. a) Bundles of Antigorite (Atg) represented by flakes exhibiting interpenetrating textures forming the main constituent of serpentinites with occasional replacement of antigorite by carbonates b), talc-carbonate (third-order color) associated with serpentinite, c, and d) the pseudomorphic textures, such as mesh serpentine replacements of olivine or pyroxene by antigorite and carbonates, leaving magnetite in the cleavage e) antigorite replacement by carbonates, f) The chromian spinel, vermicular in shape, with iron oxides. All photos are taken in cross-polarized transmitted light (CN), except panel (c)is under plane-polarized light (PPL). (Srp: serpentine, Ant: antigorite, Opq:opaques, Cb: carbonate,Tc: talc, Mt: magnetite).

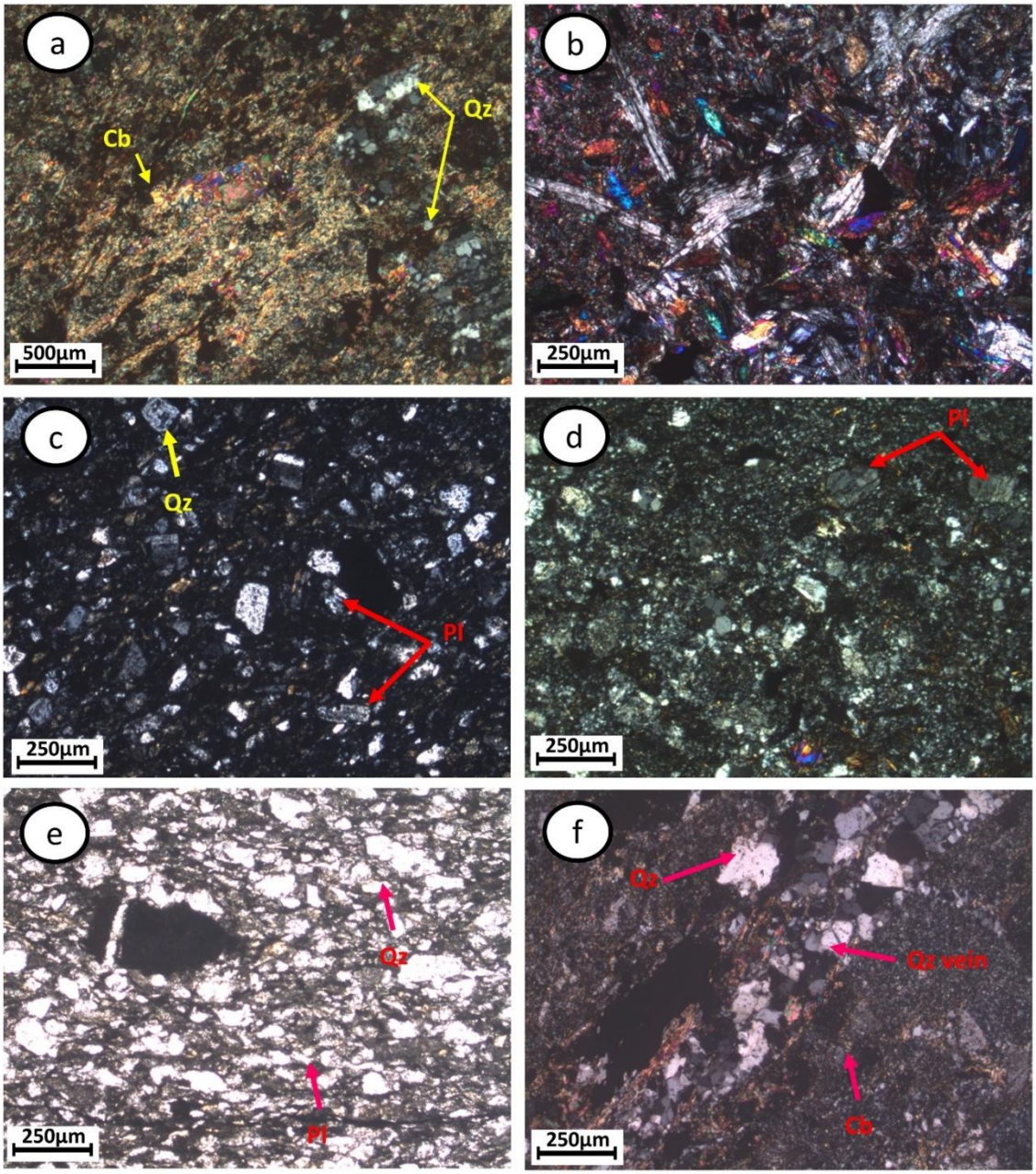


Fig. 4-16: Photomicrographs showing various petrographic textures in (a) serpentinite and listvenites when viewed between crossed nicols (CN) and (b)ophiolitic metagabbro. Photomicrographs of (c and d) highlight the main petrographic characteristics of the ophiolitic mélange matrix. The mélange matrix contains metagreywacke, occasionally displaying a weak schistosity (e). (f) volcaniclastic metasediments with prominent quartz crystals are cut by a quartz vein, set within a fine-grained carbonate-rich schistose matrix. All photos are taken in cross-polarized transmitted light (CN), except panel (c) is under plane-polarized light (PPL). (Cb: carbonate, Tc: talc, Pl: plagioclase, Qz: quartz).

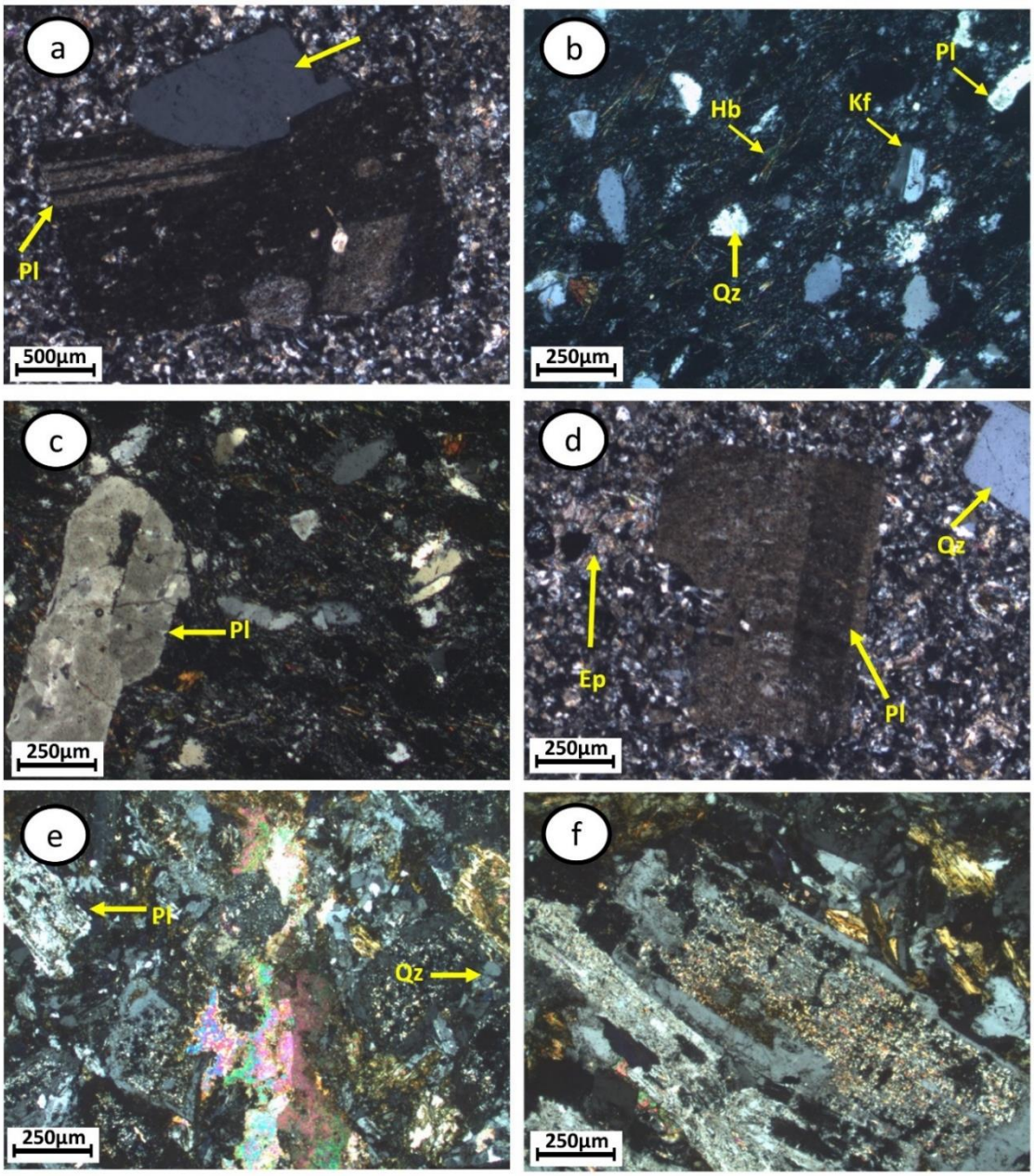


Fig. 4-17 (a, b, and c) Photomicrographs showing the primary petrographic characteristics of metavolcanics demonstrating porphyritic textures, predominantly composed of plagioclase and quartz phenocrysts embedded in a finely grained groundmass. These metavolcanic rocks are mainly meta-andesites and contain minerals like plagioclase, chlorite, epidote, hornblende, and alkali-feldspars in their groundmass. (d, e, and f) Photomicrographs revealing the key petrographic features of metagabbro-diorite rocks and showing (d) Subophitic texture characterized by plagioclase laths and clinopyroxenes, (e) Occasional quartz grains within a highly altered quartz meta-gabbro-diorite, (f) Highly sassuritized plagioclase, resulting from hydrothermal alteration of the original plagioclase feldspar. All photos are taken in cross-polarized transmitted light (CN). (Pl: plagioclase, Qz: quartz, Cpx: clinopyroxene, Ep: epidote, Mt: magnetite)

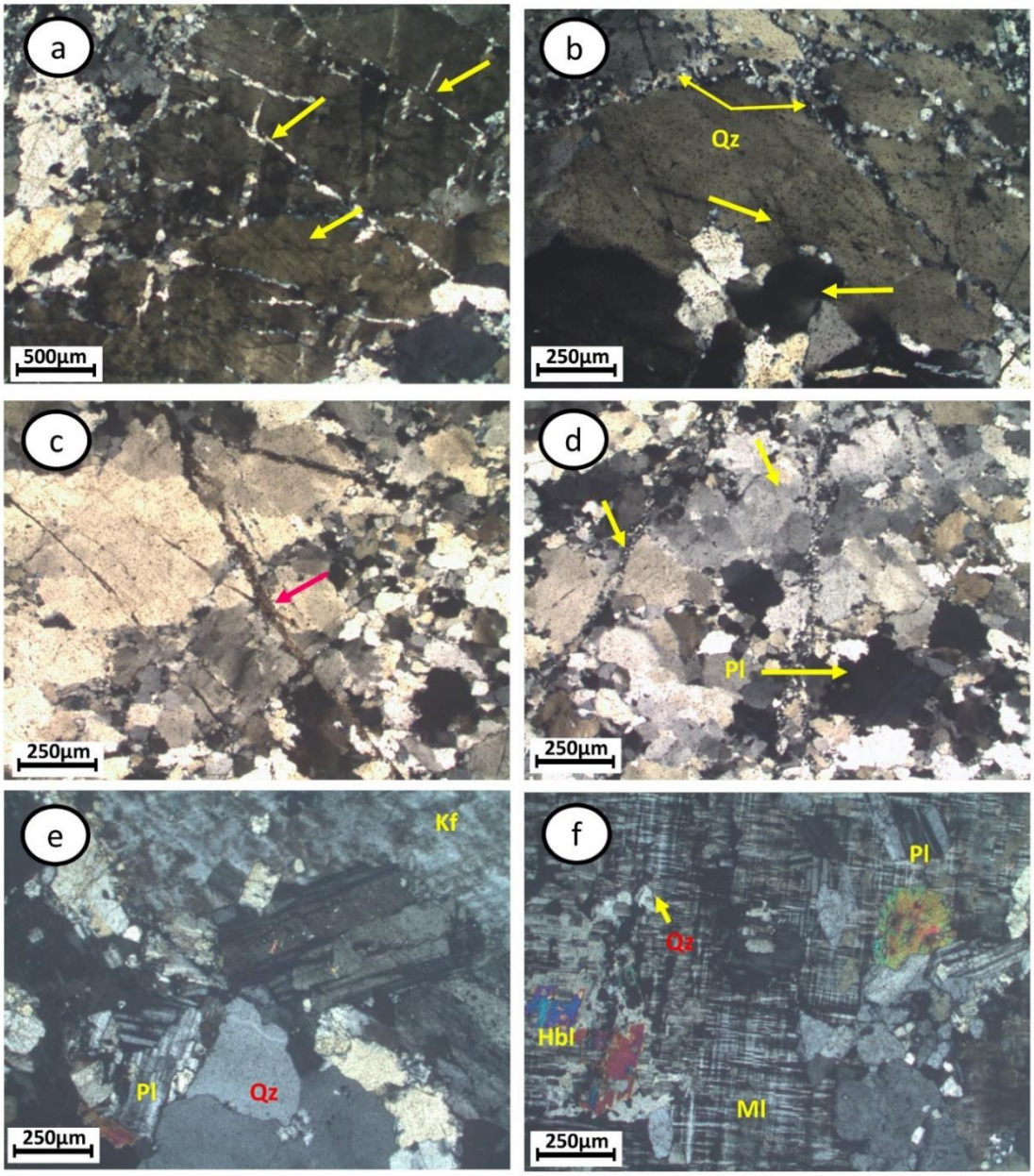


Fig. 4-18: (a-d) Photomicrographs depicting the highly altered and micro-faulted synorogenic granodiorite. (a) The rock displays multiple microfractures (indicated by arrows) cutting across its structure, subsequently filled with (b) Quartz micro veinlets (also indicated by arrows) and (c) oxides (marked by arrows). (d) Strained quartz grains with wavy extinction are observed alongside micro faulting along the quartz veinlets. (e and f) photomicrographs of the Mueilha post-orogenic granite showing (e) a hypidiomorphic texture composed of plagioclase (albite/oligoclase), quartz, and K-feldspar (predominantly perthite) in varying proportions, and (f) a Microcline crystal exhibiting cross-hatched twinning with plagioclase and quartz inclusions. All photos are taken in cross-polarized transmitted light (CN). (Pl: plagioclase, Qz: quartz, Ml: microcline, Kf: potash feldspar, Hbl: hornblende).

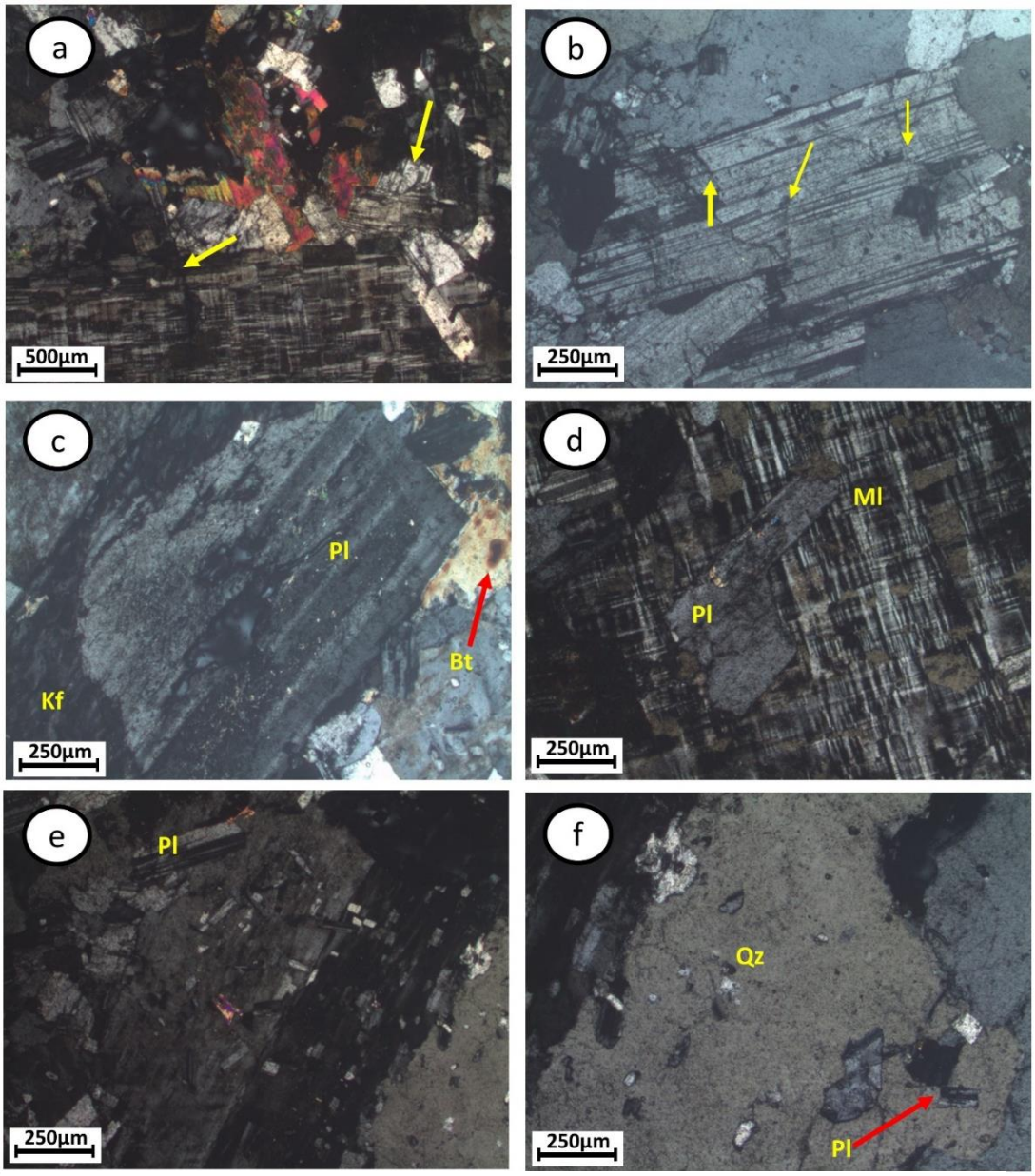


Fig. 4-19 (a) The coarse-grained red granite displays a reduced medium-grained albite/oligoclase framework with some degree of (b) strain evident in broken exsolution lamellae within the larger mineral grains. (c) The coarse-grained albite/oligoclase crystals are variably overgrown by large K-feldspar. Additionally, a brown flake of biotite is present, exhibiting numerous dark brown circular pleochroic halos, which are considered diagnostic features of biotite affected by radioactivity. This radioactivity is typical of mueilha granite, a rare-metal bearing granite that contains zircon. (d, e, f) Albite/oligoclase inclusions are found within alkali feldspar, represented by (d) Microcline, (e) Carlsbad orthoclase, and (f) quartz megacrysts, showing thin, fine, dusty halos. All photos are taken in cross-polarized transmitted light (CN). (Pl: plagioclase, Qz: quartz, Ml: microcline,Kf: potash feldspar, Bt: biotite).

4.6.3 X-ray diffraction (XRD) investigations

A potent method for crystallography and mineral identification is X-ray diffraction (XRD). The basic concept of XRD depends on the interaction between incident X-ray and the crystals of a certain mineral. X-rays interact with the atoms in the crystal lattice as they travel through crystalline materials, scattering in various ways. A diffraction pattern is created due to the crystal's lattice scattering X-rays, and it is indicative of the crystal's structure. This pattern is made up of peaks that are related to certain angles (Bragg angles), and the interatomic distances in the crystal. These angles and distances are characteristic and unique for each mineral. Thus, a mineral will create a different XRD pattern since each mineral has a different crystal structure. This mineral can be identified by comparing the experimental XRD pattern with a database of known mineral patterns [108].

In the current study, XRD analysis was performed through careful sample selection and preparation. All the selected samples underwent processes of crushing, grinding, and finally pulverizing by using hand tools (hammer, steel percussion mortar, agate mortar) to prevent mechanical damage to the clay minerals. XRD analyses were conducted on fifteen samples, primarily consisting of serpentinites, hydrothermal alteration zones, and metagabbros, in order to identify their mineral composition. A diverse range of minerals was identified within the studied samples. These minerals include muscovite, smectite, illite, smectite, kaolinite, chlorite, quartz, K-feldspar, plagioclase, calcite, dolomite, ankerite, siderite, magnesite, epidote, talc, serpentine, hematite, goethite, amphibole, and rutile (Figure 4-20).

The samples and mineralized alteration zones contain ore minerals predominantly composed of iron oxides, namely hematite, and goethite, present within fissures, fractures, and the altered wall rock. Goethite is typically observed as an alteration product resulting from the transformation of iron-bearing minerals like pyrite and magnetite. Additionally, chlorite, with higher iron content, is frequently observed replacing ferromagnesian minerals rich in iron [109].

In the current study, Appendix 4-30 displays the geographic distribution of the selected sample sites chosen for XRD analyses. The subsequent findings, presented in Figure 4-20, are systematically arranged along a north-to-south direction according to their positions in the Appendix 4-30. This arrangement facilitates a comprehensive comparison between the obtained results and the exposed lithologies found within the study area.

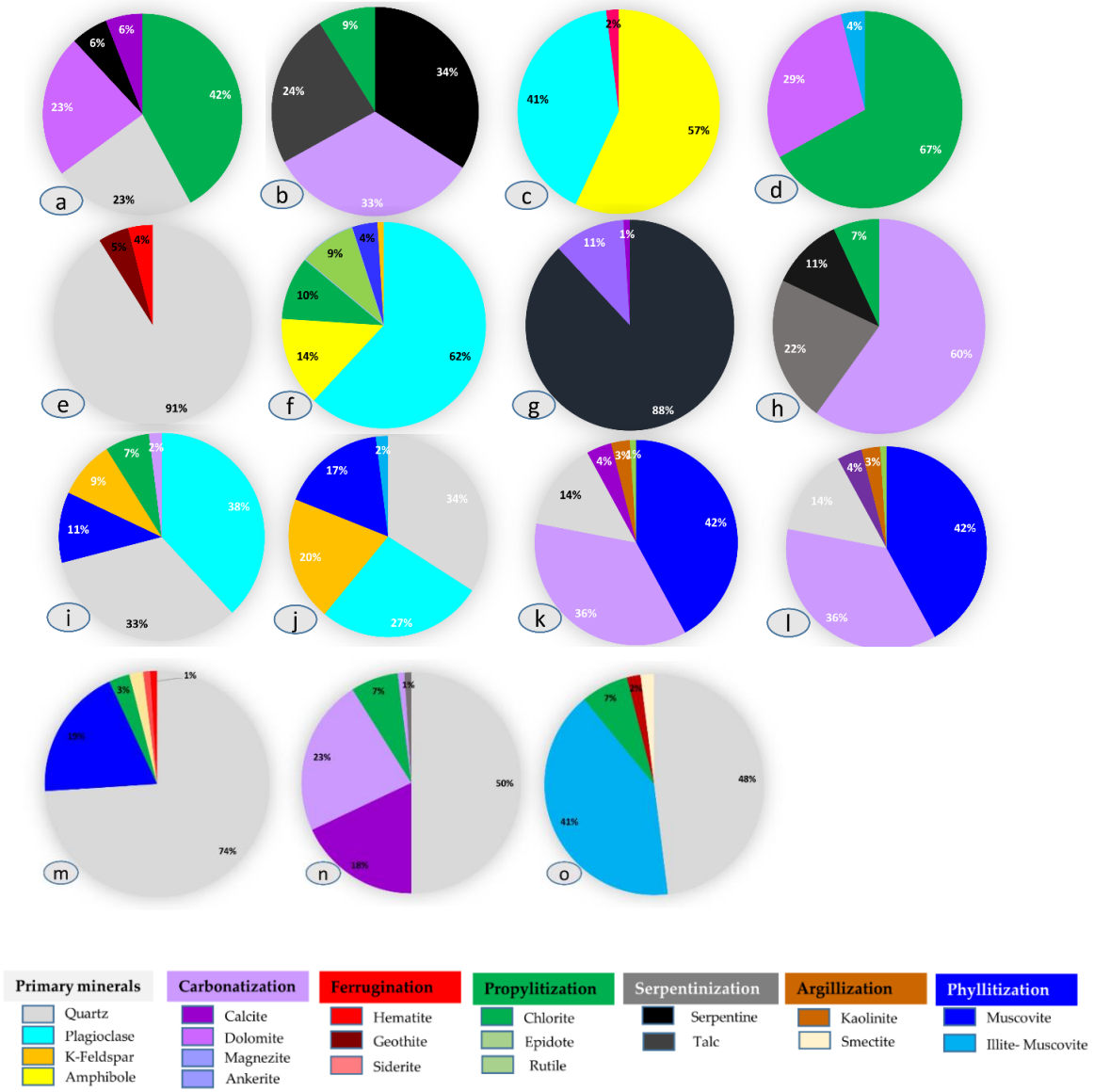


Fig. 4-20: Pie graphs showcasing mineral percentages within the samples of (a) CED-98, (b)CED-92, (c)CED-83, (d) CED-87, (e)CED-6, (f) CED-14, (g)CED-16, (h)CED-17, (i) CED-24, (j)CED-34, (k)CED-33, (l)CED-42, (m), (n) CED-47 and (o) CED-71 as unveiled through XRD analysis. Samples are arranged from north to south according to their respective locations on the map.

Through XRD analysis, the selected samples were meticulously examined, shedding light on both essential and accessory minerals.

Of notable significance, the analysis prominently identified clay minerals and various sheet silicates that are closely associated with hydrothermal alteration zones. For instance, in Figure 4-20a, the dominant minerals observed in the sample encompass chlorite, dolomite, calcite, quartz, and serpentinites. These mineral proportions harmoniously correspond with our on-site observations that identified highly altered zones in this location. The alteration pattern primarily exhibits characteristics of propylitic alteration, evidenced by the predominance of chlorite, and carbonate alteration, highlighted by the abundance of calcite and dolomite, as deduced from the XRD analysis. Remarkably, these alterations are notably evident in the highly jointed serpentinite rocks. Figure 4-20b offers an insightful representation of Gabal Um Salatit serpentinite, a prominent rock unit within the mountainous terrain of the study area. Supported by complementary petrographic examinations, XRD analysis unveils the fundamental composition of these rocks, revealing their core constituents as serpentine minerals (primarily antigorite) augmented by a notable presence of magnesite. Additionally, minor constituents of talc and chlorite are observed, indicating alteration products.

Figure 4-20c depicts the metamorphic andesitic nature of metabasalt, with a clear dominance of amphibole and plagioclase as the fundamental mineral constituents, a correlation that impeccably aligns with findings from both fieldwork and petrographic analysis. These metavolcanic rocks are interspersed among various serpentinite masses within the surveyed regions. Serpentinite and its associated alterations are pervasive, ranging from colossal mountains to diminutive blocks. In certain instances, they encompass uranium-gold-bearing marbles or extensively transformed chlorite-rich rocks (depicted in Figure 4-20d). This diverse array of rocks is embedded within volcaniclastic metasediments predominantly composed of quartz (as evidenced in Figures 4-20 e and 4-20f).

Similarly, even within the southern extent of the study area (beneath the transversely traversing Idfu – Marsa Alam Road at approximately 25°50' N latitude), numerous serpentinite outcrops are observable. In these formations, the serpentine mineral content, primarily antigorite, is notably elevated, constituting approximately 88% of the mineral composition. However, minor representations of magnesite and carbonates (calcite) are discernible, as depicted in Figure 4-20g. The transformative effects are showcased in Figure 4-20h, elucidating escalated concentrations of

magnesite, talc, and chlorite. Figures 4-20 i, j, k, l, and m illustrate subordinate fluctuations in the mineral constituents of schistose volcaniclastic metasediments and metavolcanics, with quartz, plagioclase, and muscovite as the predominant minerals. Other minerals, chiefly chlorite, are indicative of low-grade metamorphism. Additional lesser occurrences of smectite, illite, kaolinite, K-feldspar, calcite, dolomite, ankerite, siderite, hematite, goethite, amphibole, and rutile are perceptible depending on the specific rock location and its original composition as shown in Appendix 4-30.

Furthermore, in addition to elucidating the primary essential minerals and their minor modifications across the aforementioned samples, a focused analysis was conducted on two specimens extracted from zones of alteration where haphazard mining activities were extensive. Figures 4-20 n predominantly illustrate a manifestation of listvenitization that has occurred within serpentinite rock formations. These particular samples exhibit the distinctive presence of microcrystalline quartz veins, which contributes to an approximate 50% quartz content within the sample. Nonetheless, the process of listvenitization is substantiated by significantly elevated concentrations of carbonates and chlorite. Figure 4-20 o pertains to a specific locale situated to the north of the Gabal Mueilha pluton (Appendix 4-30), where an alteration zone has been extensively excavated. Our meticulous XRD analysis disclosed a prevalence of phyllitic, propylitic, and argillic alterations, as indicated by the presence of chlorite, illite, and muscovite visually and depicted in Figure 4-20 o. It is imperative to underscore that the sampling locations are impeccably aligned with the outcomes of our remote sensing investigations, which had initially indicated the occurrence of various alteration types at these specific stations.

4.6.4 SEM-EDX

SEM-EDX images were utilized to confirm the petrographic analysis and to identify the ores and their associated minerals within the study area. Several samples, mainly from quartz veins or alteration zones, were checked. Our analysis revealed the existence of several ores, including scheelite, molybdenite, apatite, marcasite, hematite, magnetite, and gold.

Quartz and calcite: These minerals formed the main matrix of several ore minerals formed within quartz veins. Calcite is found as abundant minor veins cutting the main quartz veins, as shown in Figure 4-21. Within this matrix, several grains of Scheelite (Figure 4-21) were detected in CED 22. An elemental composite map (thumbnail image in Figure 4-22) was built to

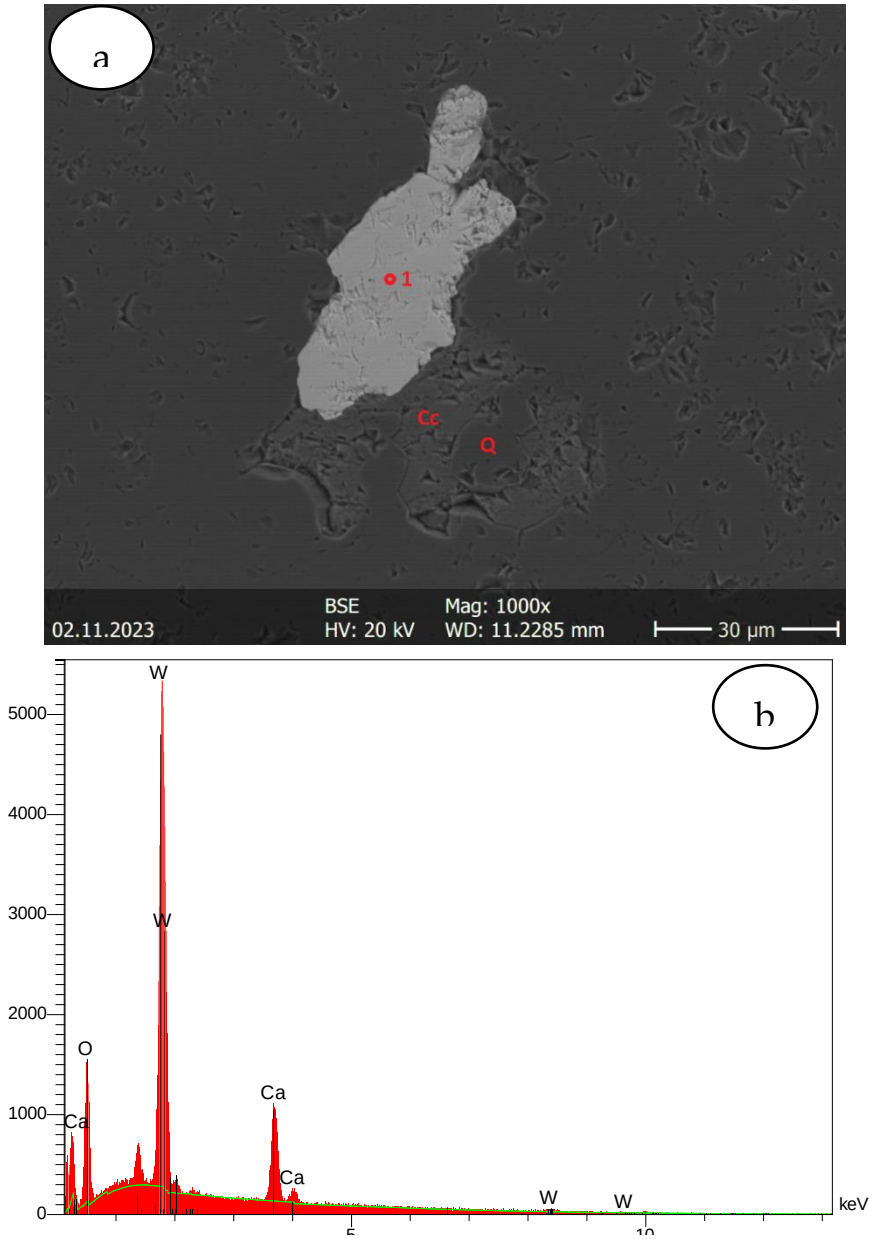


Fig. 4-21: (a) BSE image showing scheelite grain and (b) their SEM-EDX spectra. Cc for calcite and Q for quartz.

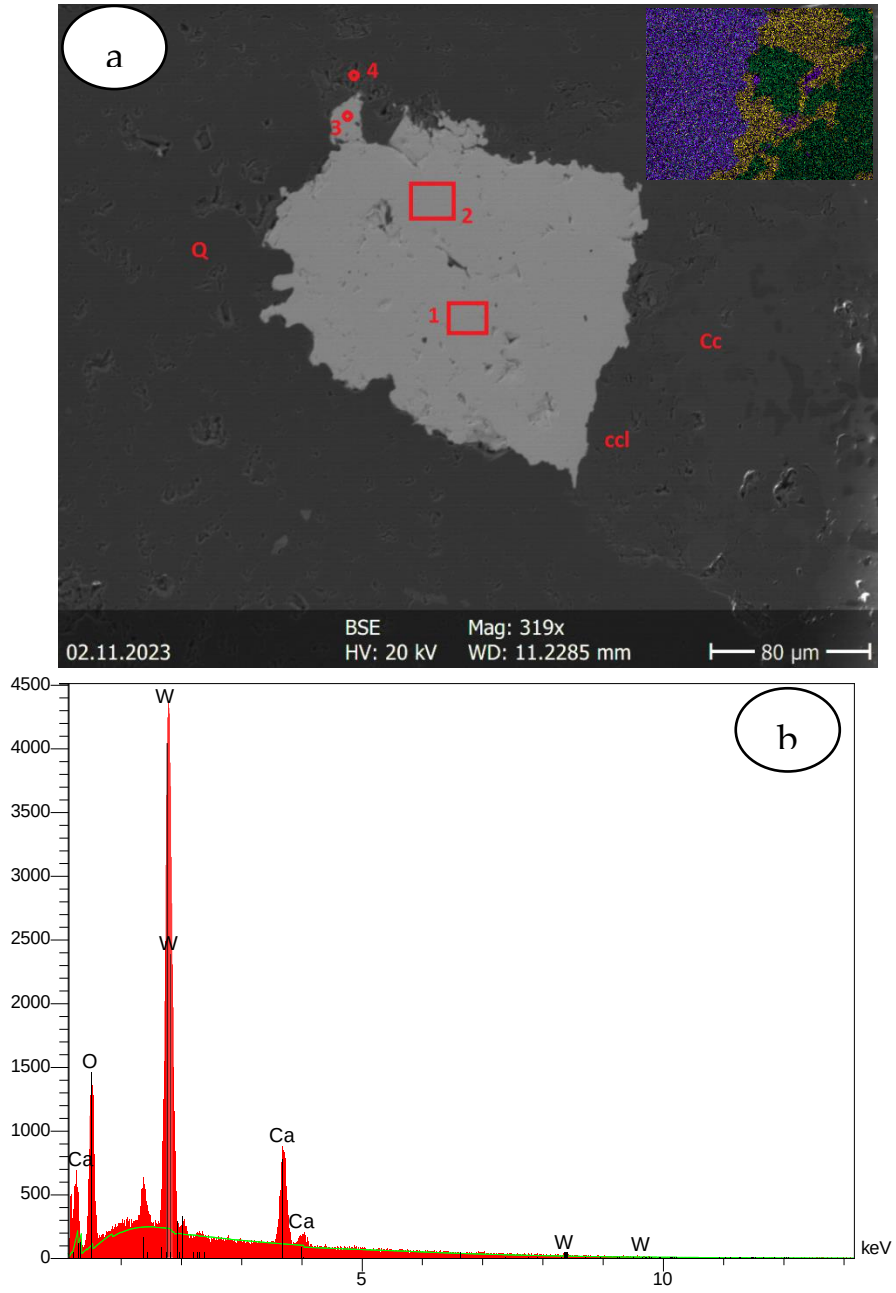


Fig. 4-22: (a) BSE image showing scheelite grain with a thumbnail (top-right corner) elemental image showing the abundances of Mg (Yellow), Ca (green), and W (Purple)and (b) their SEM-EDX spectra for point 1. CCl for clinochlore, Cc for calcite and Q for quartz.

highlight the abundances of Mg (yellow), Ca (green), and W (purple). Scheelite or calcium tungstate ($CaWO_4$), together with some inclusions of quartz with dominant Mg-bearing calcite were seen. Clinochlore ($Mg_5Al(AlSi_3O_{10})(OH)_8$) is very common either in the background Figure 4-22 or as inclusions within Scheelite (Figure 4-23a).

In other locations within the same sample, inclusions of clinochlore were found within scheelite (Figure 4-23*a*). Iron sulfide euhedral crystals mainly marcasite (prismatic or orthorhombic), were detected in the same sample (Figure 4-23*a*). Our investigation reveals the prevalence of quartz and calcite in most of the examined samples. Calcite is identified as a mineral that typically fills pores during later stages of formation (late-stage-pore filling mineral), sometimes occurring in pure form and at other times containing magnesium. Sheelite is also present, albeit not located within cracks. Apatite is observed within the cracks alongside magnesium-rich chlorite, which approaches the endmember composition of magnesium. Furthermore, lamellar iron sulfide, appearing as prismatic crystals, was encountered, possibly identified as marcasite or pyrrhotite. In several parts of the sample, Mg-free calcite and Mg-rich chlorite are found in contact. This indicates a gap between the formation of calcite and chlorite; otherwise, Mg should be found in both of them.

Molybdenite (Figure 4-23*b*), a mineral composed of molybdenum disulfide (MoS_2), is predominantly located within the quartz rather than within the cracks. Geochemical analysis indicates a high Mo content in the sample, a finding supported by the abundance of molybdenite crystals observed during SEM investigations. This is one of the main benefits of integrating various techniques to validate our results and endorse our findings. Molybdenite's association with quartz, rather than cracks, is noted, along with the presence of Ni-bearing phases. This observation suggests a potential association between Molybdenite and scheelite within pegmatitic phases. Furthermore, Molybdenite exhibits a directional orientation and is primarily linked with cavity-filling calcite, with no chlorite detected in its vicinity.

Special consideration was given to gold in such quartz veins. Examinations conducted using transmitted and reflected light on quartz veins and veinlets revealed that they were composed mainly of quartz and calcite. Sparse gold grains were found within these veins, along with secondary iron oxides like hematite and goethite, as well as unaltered sulfides such as pyrites.

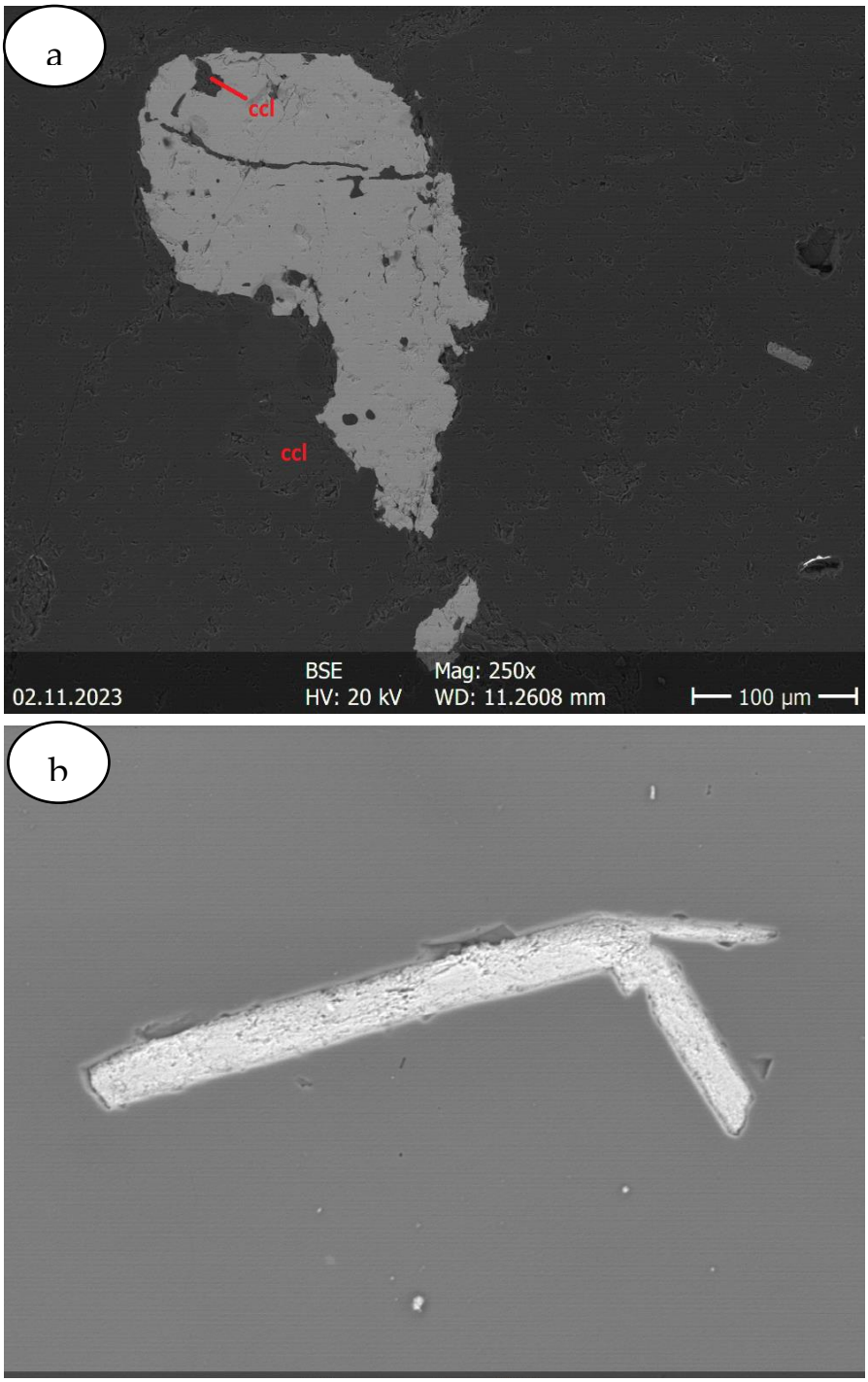


Fig. 4-23: (a) BSE image showing inclusions of CCl within scheelite grain and (b) Molybdenite. CCl for clinochlore, Cc for calcite and Q for quartz.

Examination through SEM revealed diverse shapes of the gold grains, often appearing as anhedral (Figure 4-24) to subhedral (Figure 4-25), and equidimensional subrounded grains (Figure 4-26). For instance, the presence of these small, rounded gold grains (Figure 4-26) suggests the possibility of localized gold dissolution under supergene conditions. These grains were found as separate entities within the microcavities and microfractures of quartz veins and veinlets, as well as filling the gaps between quartz crystals (Figures 4-24 and 4-25). Tiny gold grains were also detected as ultramicroscopic inclusions, ensnared within secondary iron oxides, and filling the microfractures (Figure 4-24). Additionally, they were observed to develop near the edges of these iron oxides (Figure 4-24). This is thought to result from the slow remobilization of gold from pre-existing gold-bearing pyrites over short distances [110,111]. Moreover, gold experienced dissolution, remobilization, and subsequent redeposition within the microcavities and microfractures of quartz veins.

4.6.5 Whole-rock geochemistry

This part deals with the geochemical classification, tectonic implications, and characteristics of the studied rock units. Twenty-six representative samples (Appendix 4-31), underwent geochemical analysis, encompassing major oxides, trace elements, and rare earth elements.

4.6.5.I Harker variation diagrams

The investigation of major oxide variations concerning SiO_2 content has been conducted on the studied samples of the Um Saltit-Mueilha area through Harker diagrams (Appendix 4-32). The latter illustrates the major oxide composition in the function of the SiO_2 content. Each major element and silica are represented as weight percentages (Wt.%) of major oxides. A compositional gap of around 5-10% silica is discernible between metagabbros-metadiorites (green) and granitic rocks (blue). In a general sense, samples originating from metagabbros-metadiorites tend to possess lower silica concentrations (ranging from 47.97 % to 58.14% by weight). This wide range of silica reflects the diverse composition that ranges from metagabbro, metadiorite, and quartz-metadiorite. On the other side, granitoid rocks exhibit higher silica concentrations ranging from 65.16 Wt.% for granodiorites to 75.94 Wt.% for younger granites.

Generally, and through all the studied samples, younger granites have the highest amount of silica (75.94 Wt.%) and serpentinites encompass

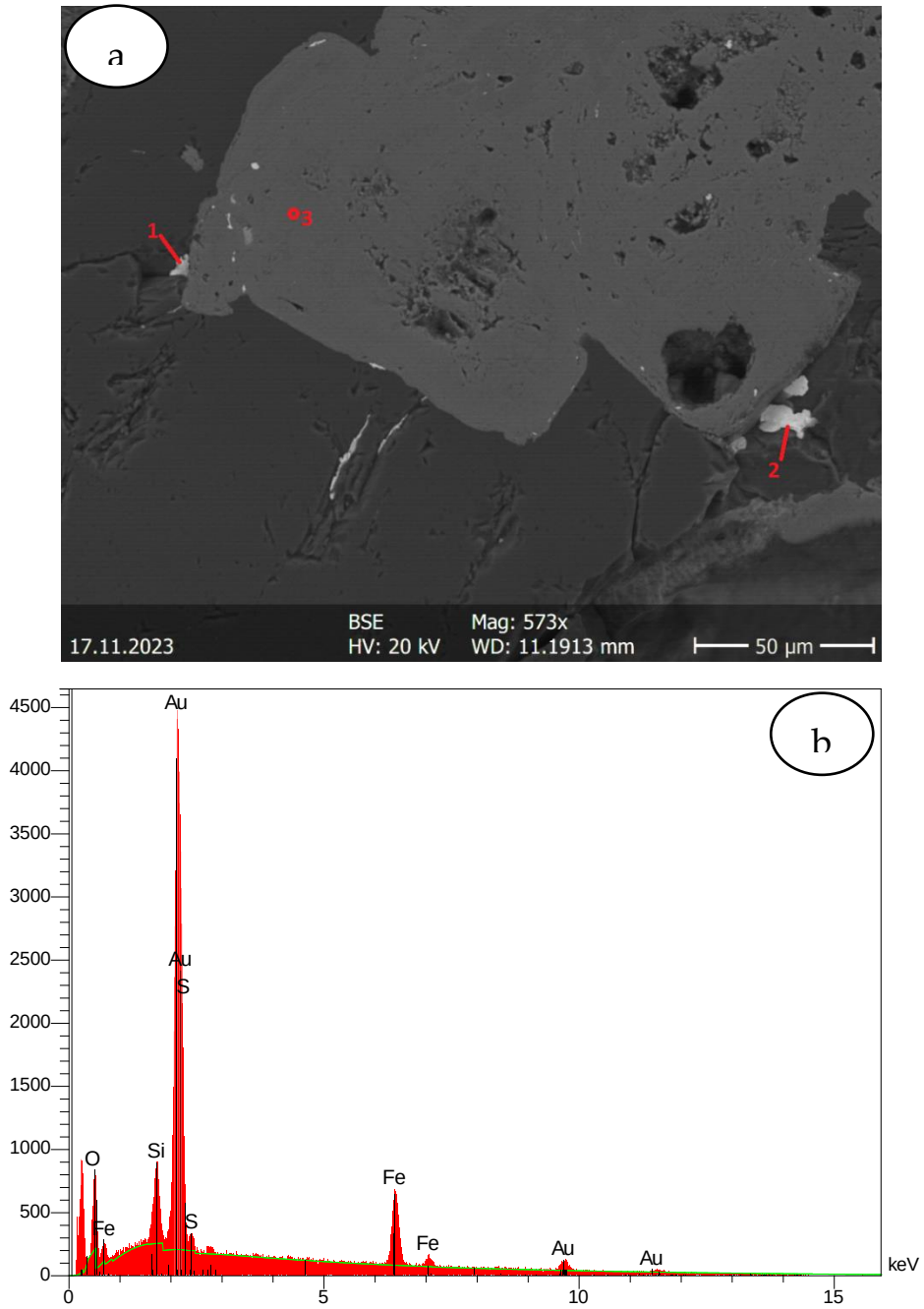


Fig. 4-24: (a) BSE image showing several anhedral gold grains and (b) their SEM-EDX spectra.

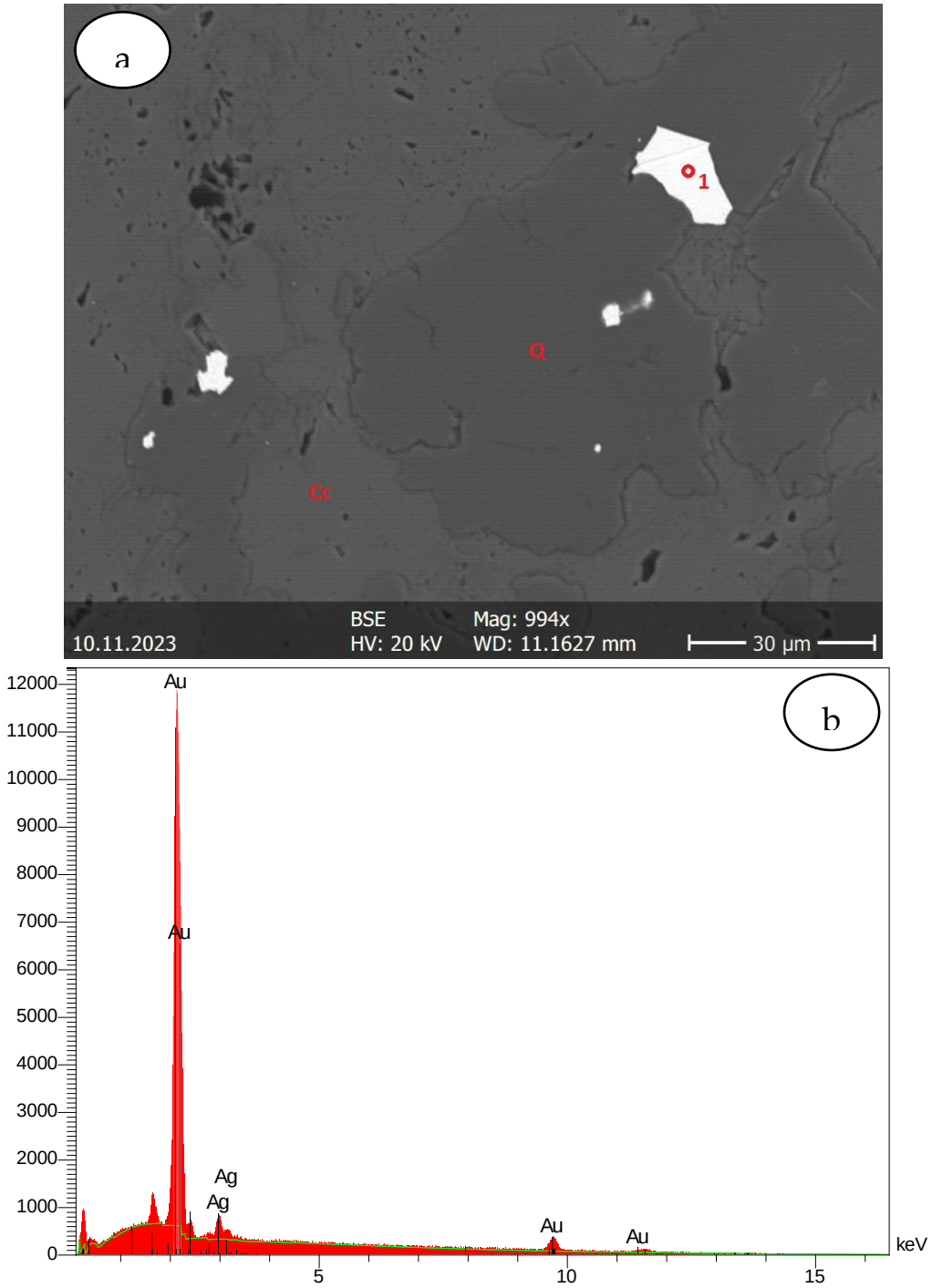


Fig. 4-25: (a) BSE image and (b) SEM-EDX spectra of subhedral electrum (83% gold and 17% silver without any oxygen). Q for quartz and cc for calcite.

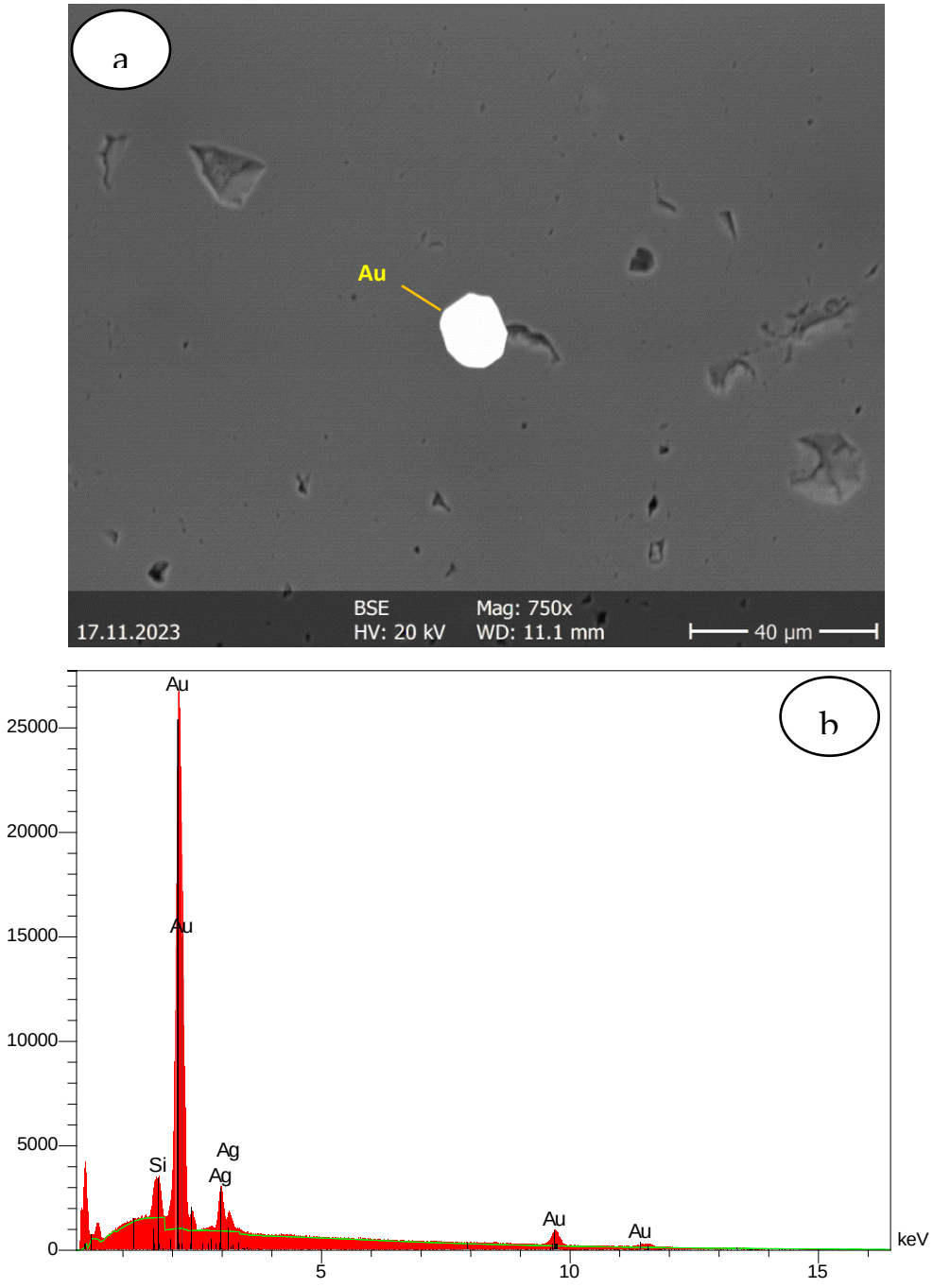


Fig. 4-26: (a) BSE image showing equidimensional gold grain and (b) their SEM-EDX spectra.

the lowest range (35.64- 40.52 Wt.%) of silica values. In between, gabbroic rocks, basic and intermediate metavolcanics are represented as shown in Appendix 4-32. These metavolcanics exhibit a wide range of silica content due to their compositional variations (mainly basic to intermediate with some acidic dikes as well). A discernible yet imperfect correlation between major oxides and SiO_2 is evident. This discrepancy might be ascribed to the major oxides' susceptibility to alteration and metamorphism-induced mobility.

In the granitic rocks samples (blue), the decline in major oxide concentrations with increasing silica content is likely attributed to the fractionation of crystalized plagioclase (contributing to Al_2O_3 and CaO variations), apatite, and ilmenite (affecting TiO_2, P_2O_5, and FeO concentrations). Furthermore, the process of iron oxide utilization in the crystallization of hornblende and biotite could contribute to this trend.

Metagabbro-metadiorites demonstrate a relatively modest increase in Fe_2O_3 content (ranging from 3.15 Wt.% to 9.13 Wt.%), MgO (ranging from 1.56 Wt.% to 8.86 Wt.%), and CaO (ranging from 3.39 Wt.% to 8.86 Wt.%). These rocks exhibit lower Na_2O (ranging from 2.14 Wt.% to 4.37 Wt.%) and K_2O (ranging from 0.46 Wt.% to 1.54 Wt.%). Serpentinite rocks possess the highest MgO content (ranging from 35.02 Wt.% to 38.09 Wt.%) when compared to other rock types.

Appendix 4-33 illustrate the relationship between concentrations of trace elements and the weight percentage of SiO_2. These graphical representations use data that depict the concentrations of trace elements in units of parts per million (ppm). A clear and consistent pattern could not be discerned among the samples under investigation for most of the elements, however, some relationships could be identified for a certain rock type. For instance, the elements Sr and Zr demonstrate a subtle decline in their concentrations within granitic rocks (blue) as the SiO_2 content increases. This trend suggests that the presence of Sr and Zr is inversely correlated with higher SiO_2 levels. Notably, the content of Sr is commonly linked to the process of plagioclase fractionation in the context of granitic magma. This is very clear by comparing the silica content (75.94 Wt.%, the highest among all the samples) and Sr (6.8 Wt.%, the lowest among all the samples) content for the Mueilha younger granite sample. Furthermore, the element Ba exhibits a wide concentration range from 1 to 1120 ppm, coinciding with an elevation in silica content. This behavior is indicative of Ba's role as a compatible element in felsic magma [112], reflecting the process of alkali-feldspar fractionation from a molten state. It is worth highlighting that these

observations are particularly relevant when discussing the Mueilha granite (silica 75.94 Wt.%, Sr 6.8 Wt.%, and Ba 16 ppm).

4.6.5.II Rock classification

De la Roche et al. (1980) [113] introduced a systematic method for classifying volcanic and plutonic igneous rocks. This categorization depends mainly on the ratios of cations. The binary diagram, known as the R1-R2 classification, is devised, where R1 is calculated as [5Si-11 (Na + K) – 2 (Fe + Ti)], and R2 is given by (Al + 2Mg + 6Ca). Employing the R1-R2 classification framework, metavolcanic rock varieties are mainly grouped into andesitic and andesite-basalt types with minor representations of dacitic and rhyolitic rocks (Figure 4-27a).

Metavolcanics found in the study region exhibit a wide range of chemical and mineralogical compositions, encompassing both acidic and intermediate metavolcanic rocks along with their associated pyroclastic materials. These findings are in harmony with the findings of [11]. This study highlighted that these metavolcanics constitute a collection of mildly altered calc-alkaline volcanic formations, primarily consisting of andesite-dacite compositions. This assemblage gives rise to a diverse range of lithofacies, including interconnected pyroclastic volcanic tuffs and breccias.

Meanwhile, the plutonic rock samples are situated within the regions corresponding to gabbros, diorites, alkali-granite, and granodiorite-tonalite compositions (Figure 4-27b). These results are in great harmony with other multiscale findings (remote sensing, field, petrography, and XRD analysis).

4.6.5.III Alkalinity

The Alkalis-Silica ($Na_2O + K_2O$ versus SiO_2) binary diagram, as crafted by Cox et al., (1979) [114], still stands out as a highly advantageous classification tool for igneous rocks. The studied metavolcanics fall under the subalkaline umbrella, predominantly aligning with the andesite to basaltic classification (Figure 4-28a). On the other hand, the scrutinized plutonic specimens represent another subalkaline rock series and are categorized as diorite, gabbro, granodiorite (quartz diorite), and granite (Figure 4-28b). In certain instances, samples are positioned in the high silica content (>75%) granite sector representing alkali feldspar Mueilha granite.

As per the comprehensive alkali-silica diagrams crafted by Middlemost, (1994) [115], the examined specimens are graphed within their

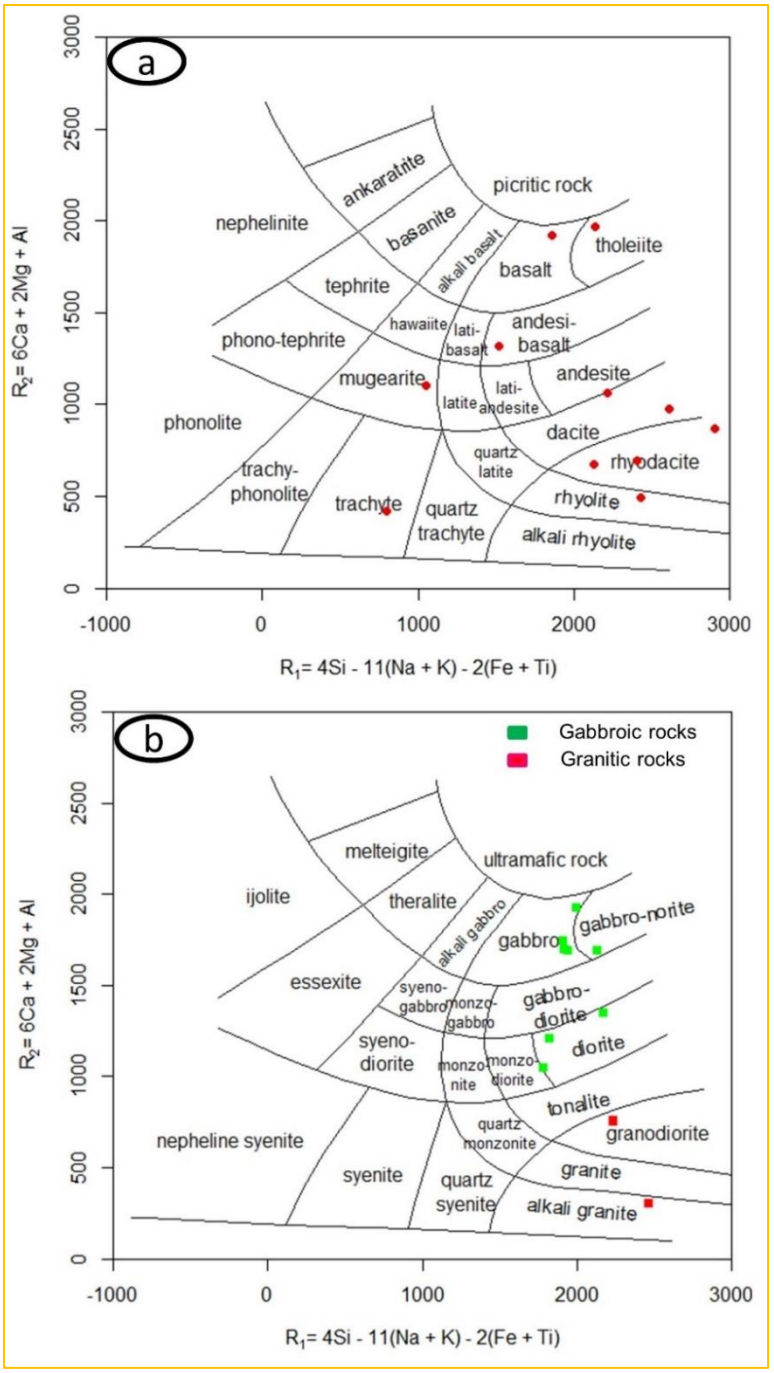


Fig. 4-27: R1 and R2 classification of (a) metavolcanics and (b) plutonic rocks within the study area after la Roche et al, (1980).

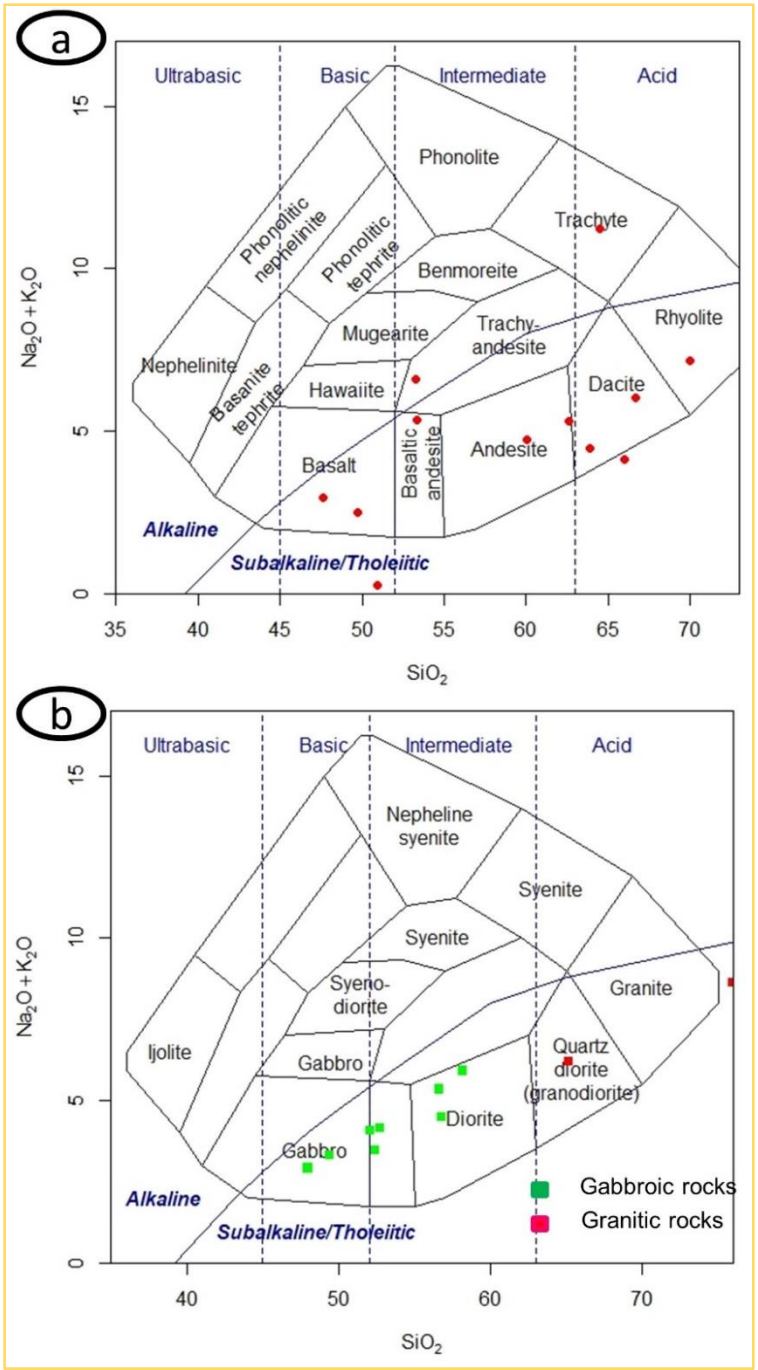


Fig. 4-28: Total Alkalis Silica classification diagram of the studied (a) metavolcanics and their related rocks and (b)plutonic rocks after Cox et al., (1979).

corresponding fields. This chemical analysis facilitates the categorization of the studied plutonic samples into various rock types, including gabbro, gabbro-diorite, diorite, granodiorite, and granite (Figure 4-29a). Notably, the alkali content emerges as a key differentiator, giving rise to two distinct clusters:

1. Subalkaline rocks encompassing gabbro and gabbro-diorite, characterized by an alkaline content of less than 5 wt. %.

2. Alkaline rocks, including diorite and granitic formations, boast an alkaline content exceeding 5 wt. % of Na_2O+K_2O (Figure 4-29a).

As per the methodology introduced by Streckeisen and Le Maitre [116], which utilizes a Q` [100*Q/(Q+Or+Ab+An)] versus ANOR [100×An/(Or+An)] binary diagram (Figure 4-29b), the classification of plutonic igneous rocks was undertaken. In this context, all examined samples have been placed within specific zones. Notably, the samples have been categorized as Zone 2: Alkali-feldspar granite (mainly representing Mueilha granite), Zone 5a: Tonalite (mainly representing the older granite rocks that range from granodiorite to tonalite), and Zone 10a: Quartz diorite (mainly representing the metagabbro-diorite rocks)

Also, The Alkalis-FeO^t-MgO (AFM) discrimination diagram, as a widely employed tool for subalkaline rocks to differentiate tholeiitic from calc-alkaline rock series, has been applied to all the analyzed samples (Figure 4-30a). AFM analysis revealed that most of the analyzed samples possess a calc-alkaline nature with a few metavolcanic samples hinting at a tholeiitic tendency. Furthermore, the granite rocks tend to exhibit a higher propensity for alkali-rich compositions, while the serpentinites and metagabbros showcase a notable presence of MgO (Figure 4-30a).

Igneous rock classification is commonly conducted using the total alkali-silica diagram. However, due to the susceptibility of LILEs (Large Ion Lithophile Elements) to movement, an alternative approach has been adopted for classifying these samples. This entails employing the Th–Co diagram proposed by [117], which accounts for immobile elements. In this regard, the rocks are predominantly assigned to the calc-alkaline series, with a minor presence of the high K-calc alkaline series, notably exemplified by acidic metavolcanics and their equivalent Mueilha granite. Similarly, several of the metavolcanic rocks fall within the classification of tholeiitic basalts to andesites (Figure 4-30b).

Application of the Th–Co diagram to the studied samples reveals a transition from tholeiitic to calc-alkaline affinities. Notably, the lowermost part exhibits tholeiitic characteristics, spanning a compositional range mainly

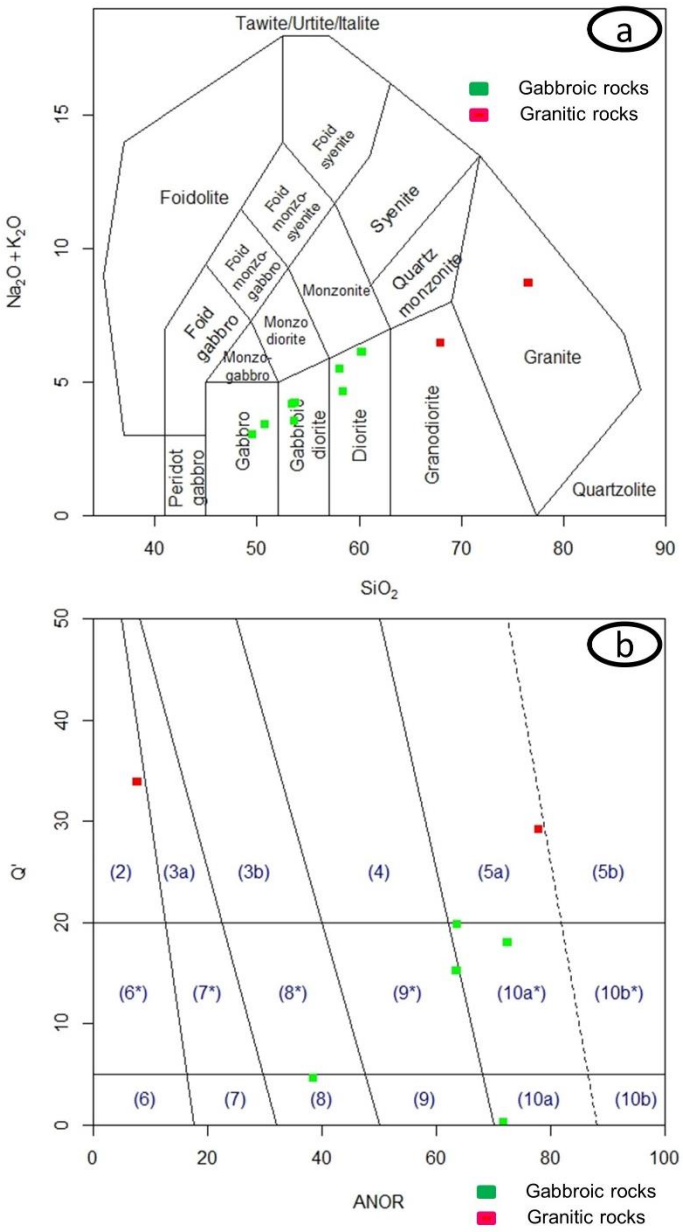


Fig. 4-29: (a) Total Alkali vs Silica (TAS) diagram based on Middlemost's classification (1994), and (b) 2-Q'ANOR diagram as proposed by Streckeisen and Le Maitre, (1979), illustrating the sample classifications. (2 alkali-feldspar granite, 3a syenogranite, 3b monzogranite, 4 granodiorite, 5a tonalite, 5b calcic tonalite, 6 alkali-feldspar quartz-syenite, 7* quartz syenite, 8* quartz monzonite, 9* quartz monzodiorite, 10a* quartz diorite, 10b* quartz gabbro, 6 alkali-feldspar syenite, 7 syenite, 8 monzonite, 9 monzogabbro, 10a diorite, 10b gabbro.*

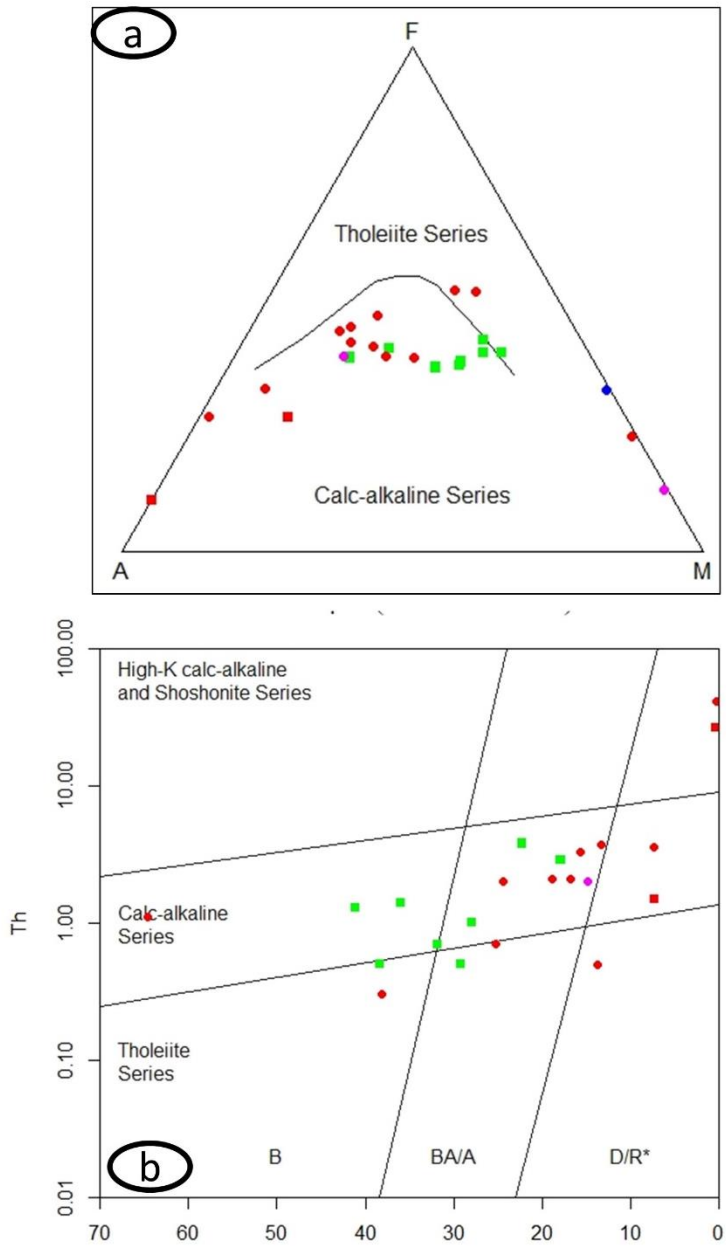


Fig. 4-30: (a) presents an AFM ternary diagram (after Irvine and Baragar (1971)) depicting the analyzed rock samples. A= Al_2O_3 wt. %; F= FeO(t) wt. % M= MgO wt. %; granite and metavolcanics (red); metagabbro-diorite (green) and serpentinite (purple). Notably, the proximity of specific points to the diagram corners is noteworthy; for instance, the red point (CED-64, representing Mueilha granite) is situated closely to the A corner, while the purple point (CED-16, signifying serpentinites) is found near the M corner. (b) The Th-Co classification diagram, after Hastie et al. (2007), depicts our samples mainly as calc-alkaline series. Rock types like basalt (B), basaltic andesite/andesite (BA/A), dacite/rhyolite (D/R).

from basaltic andesites to basalts. Contrarily, the middle part exhibit calc-alkaline tendencies, encompassing basalts, basaltic andesites (for the red metavolcanics), and their equivalent metagabbro-diorite (for the green plutonic rocks), along with serpentinites (depicted in purple). Remarkably, these outcomes closely mirror the conclusions drawn from the preceding diagrams (Figure 4-30b).

4.6.5.IV Trace and rare earth element geochemistry

Thompson et al., (1982) [118] carried out computations involving a chondrite-normalized spider diagram, aiming to compare the dynamic melting of mantle peridotite (Iherzolite) with actual compositions of oceanic basalt. This approach sought to evaluate the potential enrichment or depletion of Light Rare Earth Elements (LREE) in relation to Heavy Rare Earth Elements (HREE), typically visualized through a vector multivariate plot.

In this present study, our samples have been visualized through vector multivariate plots (depicted in Figure 4-31). These plots reveal a consistent and notable trend of significant enrichment in LREE, paired with evident depletion in HREE for the majority of the analyzed samples. This pronounced LREE enrichment is often attributed to the contamination of magma by rock materials originating from the continental crust, a phenomenon frequently observed in island arcs and beneath subduction zones.

Upon closer scrutiny of the investigated metavolcanics (illustrated in Figure 4-31a) and their associated rocks, occasional variations emerge. These discrepancies could potentially stem from hydrothermal alterations or the effects of the metamorphic processes that have impacted these rocks within the study area. Furthermore, a comprehensive analysis of a specific quartz vein (indicated by the blue line) within the study region indicates a noticeable depletion of both LREE and HREE.

In contrast, an examination of plutonic rocks, primarily characterized by metagabbros-metadiorites (depicted in green) and metagranitic rocks (shown in red), along with serpentinites (purples), showcases a relatively typical pattern for these rock types (depicted Figure 4-31b). Furthermore, our findings underscore the enrichment of Mueilha granite rocks with key elements such as thorium (Th), niobium (Nb), tantalum (Ta), potassium (K), lanthanum (La), and uranium (U) – a correlation that is also supported by geophysical data. These observations point to a highly evolved geological setting or a heightened fractionation nature inherent to these rocks. This

distinctive trait subsequently justifies the designation of these rocks as rare-metal-bearing granites.

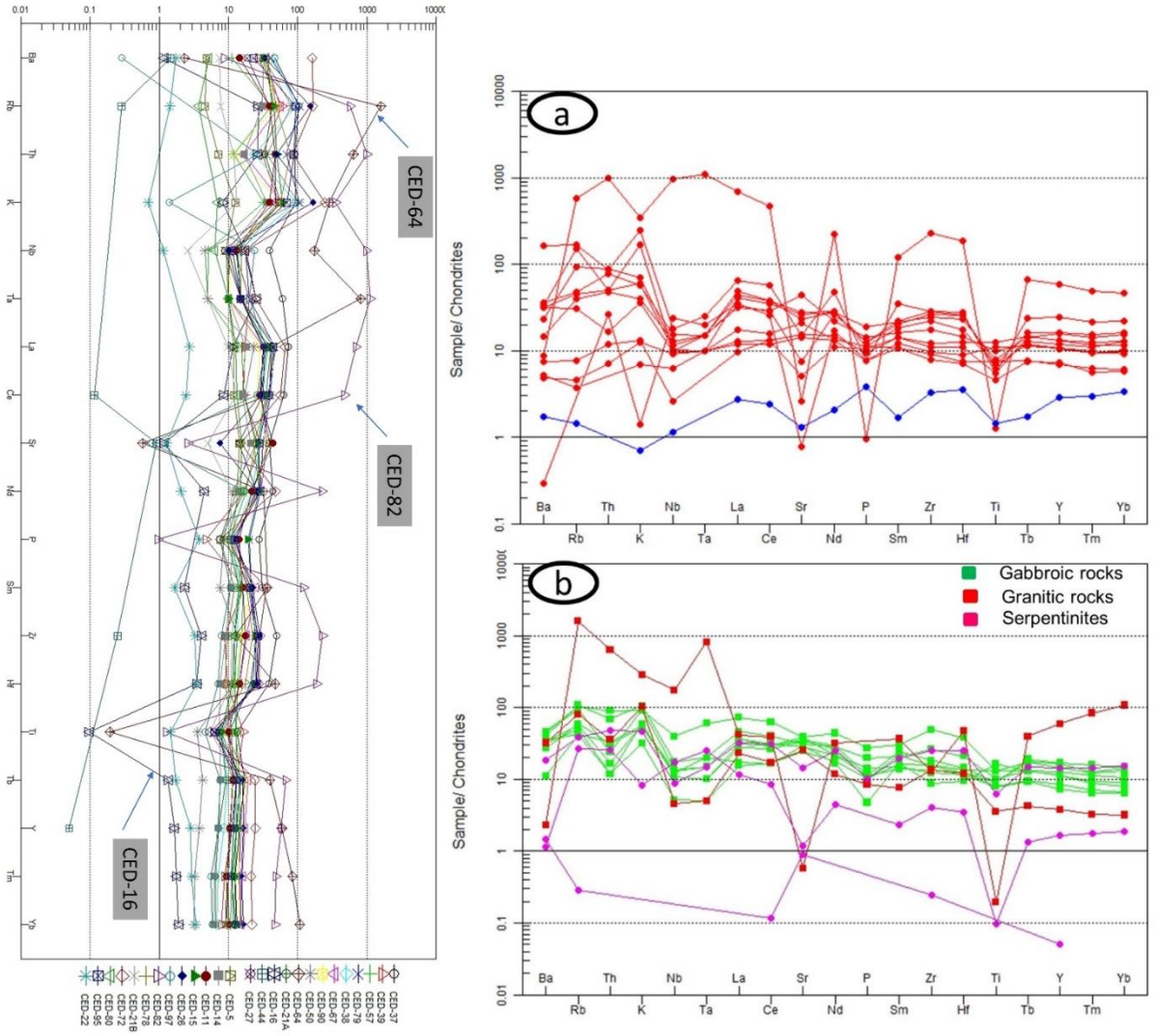


Fig. 4-31: Chondrite-normalized REE patterns of the studied samples according to Thompson et al., (1982). Chondrite-normalized REE patterns of the studied (a) metavolcanics and (b) plutonic rocks and serpentinites (Thompson et al., 1982). The blue-colored sample in subfigure (a) represents a quartz vein geochemical analysis within the study area.

4.6.5.V Tectonic setting

Pearce and Cann, (1973) [120] introduced a series of distinctive diagrams, grounded in geochemical analysis of Ti, Zr, Sr, and Y, serving as robust tools for tectonic setting differentiation. These diagrams are considered preliminary reasonable tools in categorizing volcanic rock types into distinct categories, namely Continental Arc Basalts (CAB), Within-Plate Basalts (WPB), Mid-Oceanic Ridge Basalt (MORB), and Intra-Continental Alkaline Basalts (IAT). The utilization of these diagrams yields that most of the studied Metavolcanics are mainly with Continental Arc Basalts (Figure 4-32).

Moreover, an effective approach for distinguishing Island Arc Volcanics (VIA), Mid-Oceanic Ridge Basalt (MORB), and Within-Plate Basalts (WPB) rests upon the Ti-Zr binary diagram, as proposed by Pearce, (1982) [121]. As shown in Figure 4-32, the analysis of the examined metavolcanics predominantly aligns with the Island Arc Volcanics category, with a few samples residing within MORB.

Additionally, the Zr/5-2Nb-Y Ternary discrimination diagram, introduced by Meschede, (1986) [122], emerges as another valuable tool for differentiating Within-Plate Basalts (WPB), Volcanic Arc Basalts (VAB), and Mid-Oceanic Ridge Basalt (MORB). This diagram also offers distinctions within alkali and tholeiitic basalts, as well as E-type and N-type MORB. Figure 4-33 exemplifies that the geochemical analyses of the examined metavolcanics predominantly align with Volcanic Arc Basalts (zones C&D). However, a subset of samples deviates from the defined fields due to their Zr content.

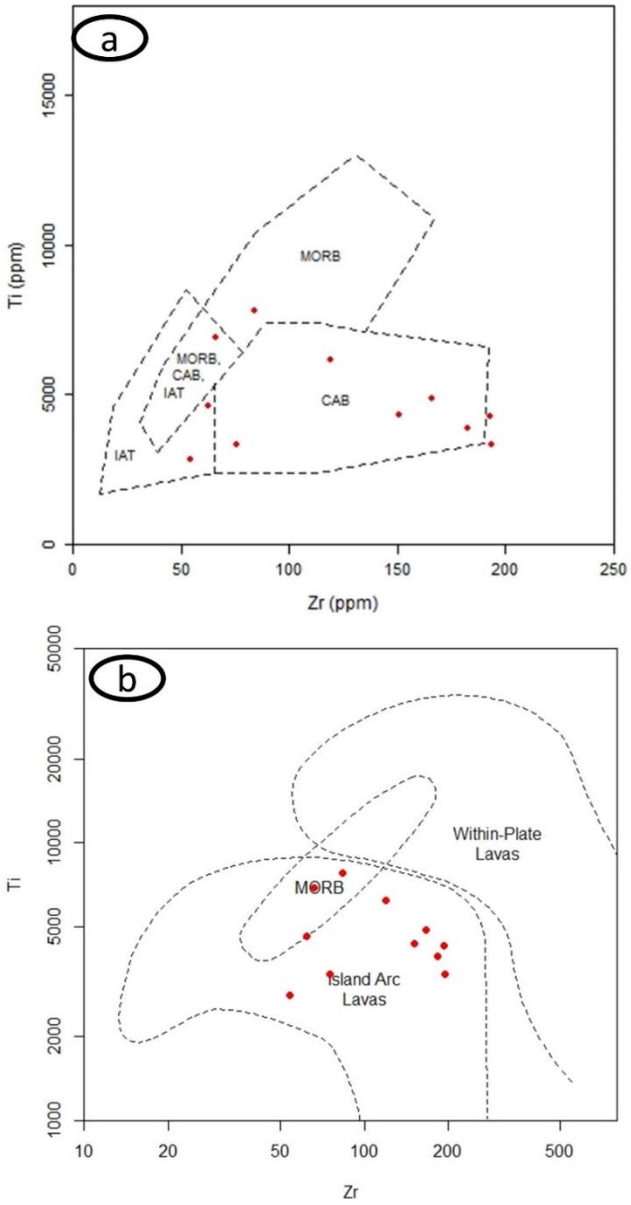


Fig. 4-32: (a) Ti-Zr binary diagram (Pearce and Cann, 1973) and (b) Ti-Zr diagram (Pearce, 1982) of the studied metavolcanics.

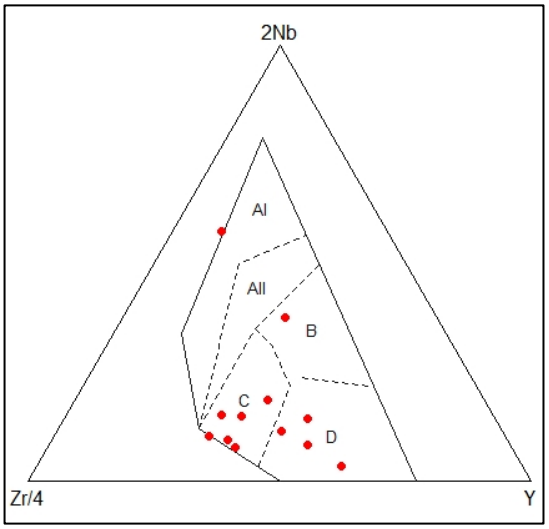


Fig. 4-33: The Zr/5-2Nb-Y discrimination diagram of the studied metavolcanics (after Meschede, 1986). AI: Corresponding to within-plate alkali basalts. AII: Representing a combination of within-plate alkali basalts and within-plate tholeiites. B: Reflecting E-type mid-ocean ridge basalts (MORB). C: Encompassing within-plate tholeiites and volcanic-arc basalts. D: Characterizing N-type MORB as well as volcanic-arc basalts.

Chapter 5: DISCUSSION

5.1 Lithological mapping advancements

The current research implemented several datasets (multispectral and hyperspectral) and MLAs (ANN, MLC, RF, XGB, and SVM) to enhance the lithological mapping of the studied terrain. Visual scrutiny of the thematic maps confirms their heightened accuracy (by increasing the number of input bands) when contrasted with the earlier results, with the "salt and pepper" effect notably diminished, particularly in the case of SVM. Our finding introduced a solid base for specifying lithological targets hosting various ores. For instance, a reasonable identification of mineralized Fe-Ti-rich gabbroic rocks from the Southeastern Desert of Egypt was evident by applying SVM over integrated sentinel 2 data and DEM [38].

Thus, it is imperative to underscore that the findings of this study hold substantial potential to advance mineral prospectivity mapping, employing MLAs to bolster lithological mapping—a critical component for identifying mineral deposits—utilizing multispectral and hyperspectral data. This study contributes an enhanced lithological map, which, when combined with meticulous structural mapping and precise identification of alteration zones, can notably aid in pinpointing mineral deposits [27,31,34–36]. These advances in mapping methodologies contribute to a more efficient approach to discovering potential mineral resources.

In the larger context, the algorithms chosen for this study (e.g., RF, XGB, and SVM) exhibit substantial promise for future mineral potentiality mapping across various datasets, owing to their capacity to process high-dimensional data, produce robust outcomes, and assess feature importance. These algorithms have the potential to evaluate the significance of specific geological features – such as geochemical data, lithology, geological structures, and topographical characteristics – in mineral exploration programs within distinct regions. Furthermore, these algorithms could be employed to predict new occurrences of minerals like gold, by training the model with known gold mineralization occurrences in a particular area. Numerous studies have demonstrated the efficacy of RF, XGB, and SVM in targeting gold mineralization. For instance, Xu et al., (2019) [123] emphasized the significance of alteration zone mapping and SVM in extracting gold metallogenic predictions. Similarly, Abdolmaleki et al., (2020) [124] developed a mineral perspective map by merging geological, geochemical,

and geophysical datasets using SVM. Additionally, utilizing random forests for remote sensing data analysis, and extracting target features crucial for mineral exploration, have been highlighted [55]. Zhang et al., (2022) [71] emphasized the effective classification model provided by XGB in establishing three-dimensional (3D) mineral prospectivity maps, using geological data to build a 3D model based on metallogenic systems and geological anomaly theories.

It should be emphasized that the studied methods are suitable for detecting other metals and are surely valid in arid terrains. For instance, remote sensing data were applied to detect copper alterations in several arid terrains including Iran [125,126], the Tibetan plateau[127,128], and Egypt [129]. Furthermore, the integration of remote sensing and geophysical data has been employed to identify various metal and ore deposits, such as iron oxide-copper-gold (IOCG) deposits and hydrothermal nickel deposits[130].

5.2 Structural analysis enhancements using lineament extraction.

Considering the paramount significance of lineaments across a multitude of applications and the availability of efficient automated extraction techniques, this Ph.D. research delved into the extraction of lineaments from various data sources, including DEMs, optical satellite imagery, and radar satellite data. Remarkably, our study revealed intriguing insights. For instance, when comparing the performance of different data sources, the ALOS PALSAR DEM (12.5m resolution) outperformed all the other datasets in lineament extraction. The superiority of DEMs over optical data can be attributed to their independence from sensor characteristics, as previously highlighted in the work of Sahoo and Jain, (2018) [131]. Radar data's superiority in lineament extraction can be attributed to its resilience against the adverse effects of weather conditions, as elucidated by Adiri et al. [132].

As a result, the combination of DEM and radar data, such as the PALSAR DEM, surpasses Sentinel 1 – a choice often favored by researchers – by a margin that could potentially exceed the established correlation between pixel size and the quantity of extracted lineaments. In conclusion, the study recommends the optimal data types, primarily dependent on the number of extracted lineaments and pixel size. These recommended data types are commonly utilized in geological applications across a broad range of pixel values (ranging from 10 to 30 meters). This guidance aims to cater to the needs of the majority of geological studies and assist users in achieving the most

promising results by selecting the most effective data type for their specific requirements.

It is important to note that regardless of the technique or data source used, manual line segment extraction—or at least a visual inspection of automatically derived line segments—remains essential. Automatic lineament extraction can significantly reduce time and effort, minimize estimation errors, and enhance objectivity rather than subjectivity. However, combining automatic methods with manual approaches is beneficial. Manual methods are particularly adept at assigning full chronological sequences between derived lineaments, a task that is challenging for automatic techniques. Additionally, the method of illumination direction based on DEMs may result in varied amounts and lengths of linear features, which must be considered in the analysis. Moreover, the best results from such analysis are often obtained in arid terrains.

5.3 Structural analysis enhancements using textural analysis.

Based on the information presented [84], employing this textural-based structural analysis approach enables the identification of various structural relationships by applying several filters (e.g., correlation). Correlation data should be adopted as it estimates the linear dependencies and allows robust identification of several structural features. The delineation of these relationships can be tailored to suit the specific objectives and scale of future studies, ultimately leading to improved geological interpretations. These interpretations, in turn, can prove invaluable in applications such as the detection of mineral deposits influenced by structural factors. As a result, this investigation offers a simplified tool for identifying several noteworthy structural features, including:

1. Analyzing dikes (as shown in Figure 4-7) and their interactions with surrounding rock units, including cross-cutting relationships and their impact on adjacent rock formations (as depicted in Figure 4-7).
2. Examining foliations (illustrated in Figure 4-7), including their orientations and what they reveal about the response of foliated rocks to deformational events.
3. Recognizing structures resembling folds (seen in Figure 4-7).
4. Identifying different types of displacements, which are indicative of faults within various rock types (as illustrated in Figure 4-7).

All of these findings were compared with previous work on the study area [9,11] and checked on the field. Textural interpretations are more complicated than interpreting optical (multispectral or hyperspectral) combination results, but they are nevertheless important for thorough geological investigation [133]. Since it examines the information from multiple angles, including tonal intensities and the spatial importance of the image pixels, rather than just the spectral fingerprints [101]. Hence, textural analysis is expected to yield a significant quantity of information (mostly pertaining to the deep or inherited structure of the image pixels) in comparison to optical data processing alone. The textural analysis's binary pixel properties, which give each pixel local variability and spatial regularity, are considered the strength point of that kind of analysis [83]. Thus, the utilized technique has proven its efficiency over other data sets including gravity [134], aeromagnetic [102], TerraSAR-X [135,136], and airborne polarimetric TopSAR [137].

Overall, our research findings (structural features) were compared to prior studies conducted in the study area. Notably, our analysis of the study area aligns closely with the extensive fieldwork carried out by Zoheir et al., (2019) [9], where they proposed three main phases of deformation (D1, D2, and D3). Our analysis successfully identified various deformational features that can be attributed to these phases.

5.4 Prospective mineralization identification

The results of CEM, combined with additional validation methods (Figure 4-8), indicate that the majority of pixels highlighted for minerals like muscovite, illite, kaolinite, pyrophyllite, montmorillonite, epidote, and chlorite are concentrated within the previously identified zones rich in hydroxyl-bearing minerals (Figure 4-20). Furthermore, concentrations of chlorite and epidote are observed in proximity to serpentinite rock formations. Clay minerals, such as montmorillonite, illite, and kaolinite, along with muscovite, are primarily limited to weathered granitic rocks or sediment deposits found in wadis. These recognized hydrothermal alteration anomalies were comparable with airborne geophysical anomalies (including RTP, K map, and eTh-map) conducted to ascertain the validity of these detected zones. These anomalies are also compared with the structural complexity pattern within the study area.

Fowler, (2001) [138] hypothesized that certain structural discontinuities in the Central Eastern Desert, like significant transpressional

and transtensional shear zones, along with moderately inclined thrusts, played a role in facilitating the entry of syn-tectonic granitoid intrusions. Many of these intrusions are connected to hydrothermal activity and the formation of mineralizations, as discussed in works by [139–141].

Of these various structures, the northwest-oriented transpressional Najd-style system, together with its Barramiya-Mubarak conjugate shear zone that extends remarkably to the northeast, as well as the secondary and tertiary extensional shears, have a significant link to ore deposits, particularly those containing gold. This connection with gold mineralization is established through studies by [5,142,143]. The presence of gold mineralization is observed in various distinct rock types, encompassing ophiolitic serpentinite, arc metavolcanics, gabbroic, and granitoid rocks. Locally within the research area, the Baramiya-Mubarak shear zone is identified at Gabal Um Salatit, consisting of ophiolitic rocks and displaying a dextral shift in the ENE-WSW direction (Figure 5-1). Even though this shear zone and its secondary fractures do not explicitly cause mineralization, they offer a conduit for the alteration of hydrothermal fluids, which primarily contribute to the detected hydrothermal features in the ongoing research.

The aeromagnetic RTP map is utilized to carry out the 3D Euler deconvolution approach in order to more effectively aid in mapping structural characteristics (Essential components for hydrothermal modifications) of the examined zone and determine their depths. The approach was applied to contacts, dikes, and faults, respectively, with structural indices of 0, 0.5, and 1. The primary tectonic trends in the region are shown to be oriented in the NW-SE and ENE-WSW directions. Figure 5-2 shows the depths that were discovered. The prevalent depths were determined using statistical analysis.

Most of the depths are between 0 and 600 meters, indicating shallow sources, while the depths beyond 1500 meters point to moderate and deep dikes and fault-like structures. To recapitulate, the shear zone and other magnetic structures (contacts, dikes, and faults), which primarily serve as the pathways for hydrothermal fluids, were clearly enhanced by the RTP aeromagnetic data coupled with the Euler deconvolution and provided an estimate for their depths.

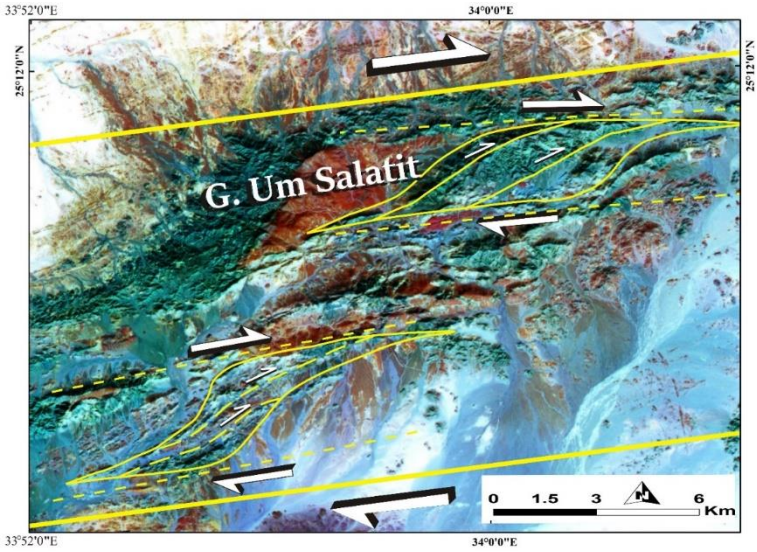


Fig. 5-1: ASTER FCC 7/3/1 in RGB showing the dextral shear zone [9], [15] along G. Um Salatit.

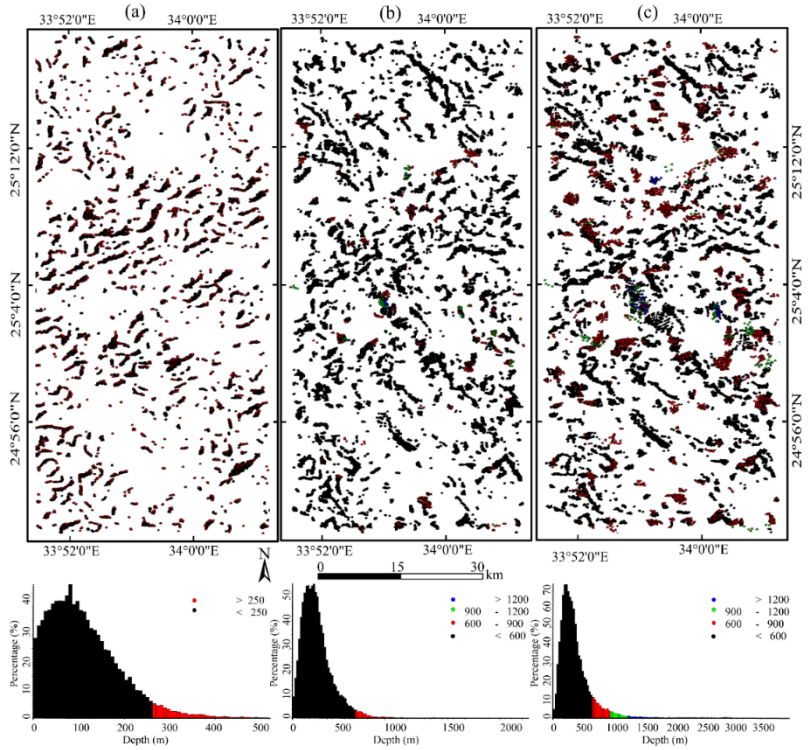


Fig. 5-2: structural features and their depths by Euler deconvolution for, (a) Contact SI=0.0, (b) dikes SI=0.5, c) faults SI=1.0.

Drawing from our meticulous laboratory analysis, the genesis of these hydrothermal alteration zones, which hold the promise of mineralization, can be attributed to the intricate interplay of lithological diversity and structural intricacies. These dynamic patterns facilitate enhanced pathways for hydrothermal fluids, fostering a mature Setting for diverse metasomatic processes to take effect. Heat-releasing occurrences, like igneous intrusions or hydrothermal solutions introduced into cooler country rocks, will lead to both heat dissipation into the nearby surroundings and the migration of volatile and mobile constituents, playing a role in metasomatic effects. Hence, metasomatism can be described as the phenomenon in which elements are swapped between fluids and neighboring rocks [144]. More precisely, alkali metasomatism encompasses the migration of alkali ions - Na and K - from a fluid phase formed during the solidification of an igneous mass, into neighboring rocks.

5.5 Mueilha's Rare-Metal bearing granite

The mineralogical composition of the Gabal Mueilha rocks exposed within the study area is affected by alkali metasomatism changes. This can be noticed both texturally and mineralogically by the presence of perthitic textures [144] and muscovite. Perthitic textures of feldspar may be indicative of alkali metasomatism. The substitution of Na for K in feldspars is evident through the occurrence of irregular albite inclusions within the K-feldspar host. Microclinisation also shows features such as the generation of microcline and micas.

Based on the geochemical characteristics and petrographic conclusions derived from the study of Mueilha granitic rocks, our investigation places special emphasis on the utilization of aero-radiometric data to identify their radioactive content. In Figures 5-3, 5-4, and 5-5, a conspicuous presence of elevated levels of potassium (K), equivalent thorium (eTh), and equivalent uranium (eU) within the Mueilha granitic pluton is clearly discernible. These heightened concentrations are vividly depicted as a deep black coloration in the radiometric ternary map and coincide with a notably low magnetic intensity observed in the RTP map. Such distinctive characteristics are commonly associated with rare-metal-bearing granites. Therefore, based on these findings, the study strongly advocates for further in-depth analysis of these rocks and an exploration of their feasibility for potential economic purposes.

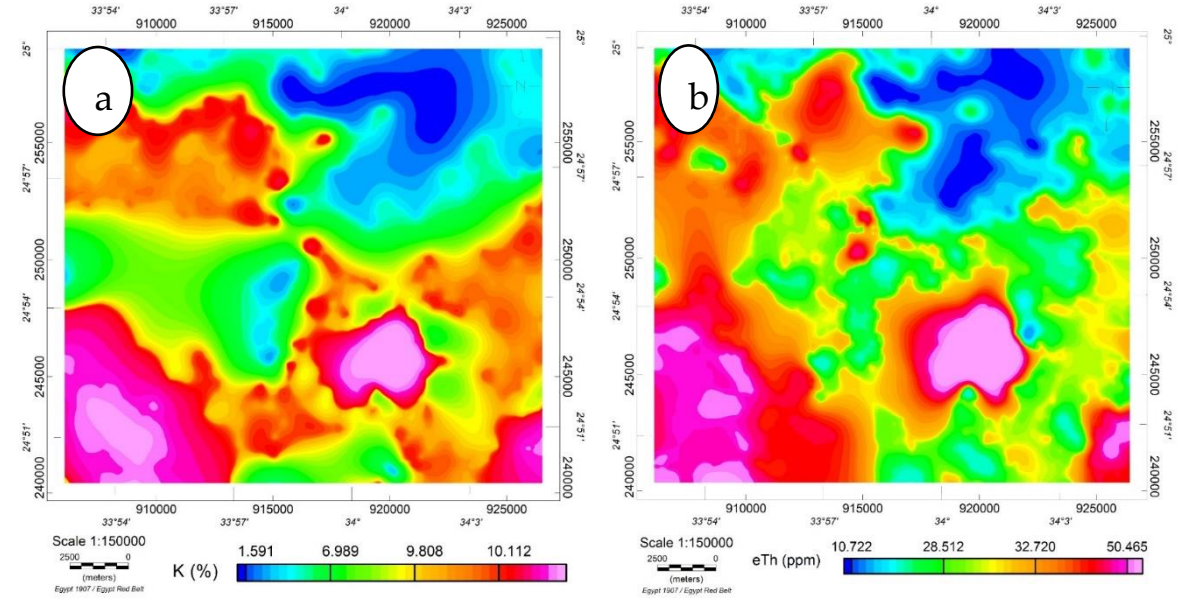


Fig. 5-3: Spectrometric gamma-ray results: (a) potassium concentration, (b) Equivalent thorium

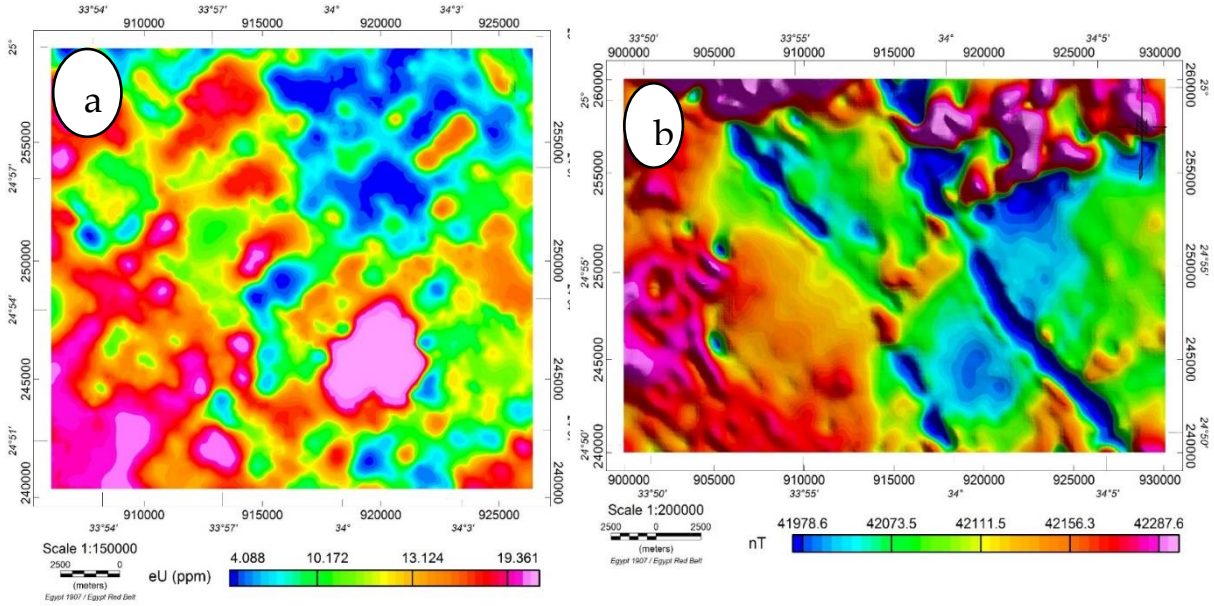


Fig. 5-4: (a) Equivalent uranium concentration map, (b) RTP magnetic map.

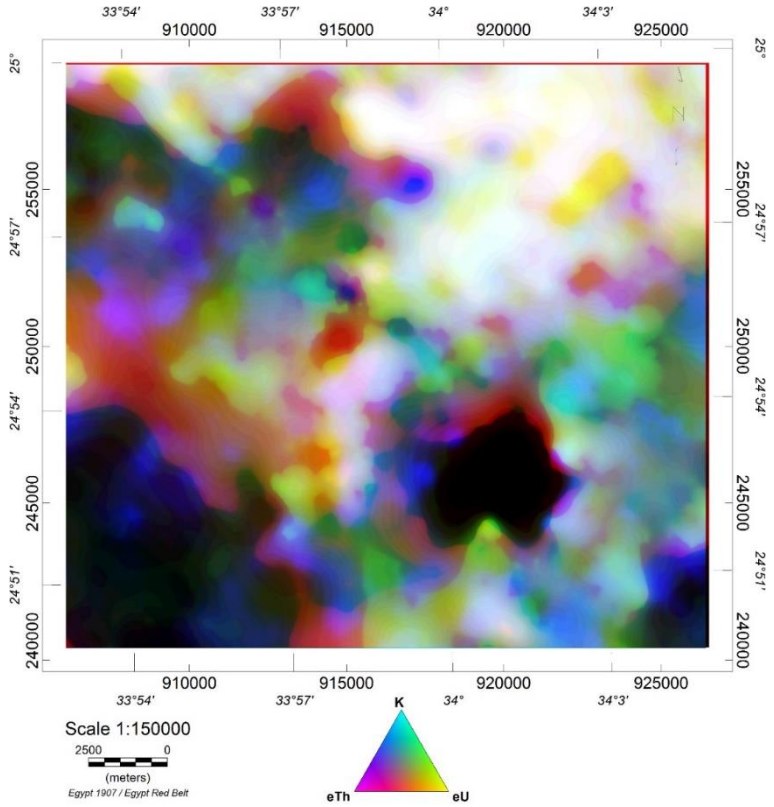


Fig. 5-5: (a) Radiometric ternary map. The black area (e.g., Mueilha) shows the highest concentration of K, eTh, and eU.

5.6 Orogenic Gold Mineralization

The integrated analysis of precise lithological mapping, meticulous structural assessments, and comprehensive geophysical insights, including radiometric and magnetic data, has identified specific zones as prime targets for gold exploration within the study area. This method effectively discerned the alteration zones within the study area. These alteration zones, which accompany mineralized quartz veins, exhibit compositions ranging from carbonate-chlorite and quartz-sericite to carbonate-quartz-sericite, along with evident hematitic-limonitic stains.

Our field survey encompassed visits to these zones, where collected samples underwent scrutiny through SEM-EDX measurements. The latter uncovered a prevalence of gold mineralization in numerous samples, alongside a diverse spectrum of other ores, such as iron oxides (magnetite, hematite), scheelite ($CaWO_4$), marcasite, pyrrhotite, pyrite, molybdenite, W-bearing rutile, and baddeleyite (zirconium oxide), primarily within quartz

veins. The quartz veins and veinlets observed in the study area are the product of metamorphic hydrothermal processes. Their gold-bearing fluids stemmed from the dehydration and decarbonation of ophiolitic mélange rocks of the region. The prevailing nature of hydrothermal gold-bearing quartz veins in the study area is likely epithermal rather than mesothermal, as also suggested by other studies [145].

Gold, the primary focus of our study, was discerned in several veins, manifesting in different forms, including electrum (a naturally occurring gold-silver alloy) or pure gold grains in Figures 5-6, 5-7, and 5-8. Electrum, as illustrated in Figure 5-6, was predominantly found within quartz, veins. Additionally, a void-filling late-stage calcite was identified surrounding quartz and gold grains.

Chapter 6: CONCLUSIONS

Utilizing more than 10 remote sensing datasets, magnetic and radiometric geophysical data, fieldwork, petrographic investigations, opaque mineralogy, XRD, SEM, and geochemical analysis, several conclusions were drawn from the current study. We introduced an updated lithological map of the study area utilizing different machine learning algorithms. In arid terrains, our research opens the door for further research by emphasizing the efficiency of incorporating DEMs in lithological mapping and highlighting ASTER and Sentinel 2 data as the best multispectral data for lithological and hydrothermal alteration mapping compared to the utilized datasets. Additionally, our research confirmed the eligibility of SVM, RF, and XGB in such lithological mapping tasks using PRISMA hyperspectral data.

These algorithms were provided with several processed images using various remote sensing techniques including FCCs, PCA, DPCA, MNF, ICA, and BRs. These methods aid in discriminating between rock units and provide a reference lithological map for capturing training and testing data. Our results revealed a wide range of lithological units including igneous, metamorphic and sedimentary rocks. Spectral analysis of EnMap data revealed high concentrations of aluminum (Al) and iron (Fe) in the Nubian Sandstone, providing insights into the presence of bauxite ores in the southwestern corner of the study area.

As the structural complexity is considered one of the main criteria for mineral deposits, lineament extraction, textural analysis, Circular Feature Transform (CFT), and Amplitude Contrast Transform (ACT) were applied to remote sensing and magnetic data revealing the main structural features within the study area and highlighting three phases of deformation (D1, D2, and D3).

Regarding hydrothermal alteration zones, the study concluded that the area is severely affected by iron- and hydroxyl-bearing alterations. The airborne gamma-ray data were also integrated to identify such alteration zones. Petrographic and XRD analysis of such alteration zones revealed a wide range of alterations including carbonatization (calcite, dolomite, ankerite, and magnesite), ferrugination (hematite, goethite, and siderite), propylitization (chlorite, and epidote), serpentinization (serpentine, and talc), argillization (kaolinite, and smectite), and phyllitization (muscovite and illite). SEM analysis investigations revealed the existence of several ores, including scheelite, molybdenite, apatite, marcasite, hematite, magnetite, and gold.

The range of gold shapes includes anhedral to subhedral forms, elongated structures, and equidimensional subrounded grains. These grains were discovered as individual entities within microcavities or as ultramicroscopic inclusions within secondary iron oxides and were also observed to form near the edges of these iron oxides.

Besides gold, insights for bauxite at NSS, a conspicuous presence of elevated levels of potassium (K), equivalent thorium (eTh), and equivalent uranium (eU) within the Mueilha granitic pluton is clearly discernible, indicating Gabal Mueilha as a rare-metal bearing granite.

It should be emphasized that our results are most applicable and should be interpreted with a focus on arid terrains. It is noteworthy that a remarkable consistency among the results obtained from the integrated techniques was observed across various levels. For example, even in laboratory studies, samples where scheelite was detected using SEM exhibited higher tungsten (W) content in our geochemical analysis. Likewise, all samples where gold was identified using SEM were corroborated by the findings of the geochemical analysis. Similarly, the results obtained from remote sensing data and geophysical techniques, further validate the findings of our research.

REFERENCES

1. Stern, R.J. Arc-assembly and continental collision in the Neoproterozoic African orogen: implications for the consolidation of Gondwanaland. *Annu. Rev. Earth Planet. Sci.* **1994**, *22*, 319–351.
2. Johnson, P.R. An Expanding Arabian-Nubian Shield Geochronologic and Isotopic Dataset: Defining Limits and Confirming the Tectonic Setting of a Neoproterozoic Accretionary Orogen. *undefined* **2014**, *8*, 3–33, doi:10.2174/1874262901408010003.
3. Greiling, R.O.; Abdeen, M.M.; Dardir, A.A.; El Akhal, H.; El Ramly, M.F.; El Din Kamal, G.M.; Osman, A.F.; Rashwan, A.A.; Rice, A.H.N.; Sadek, M.F. A structural synthesis of the Proterozoic Arabian-Nubian Shield in Egypt. *Geol. Rundschau 1994 833* **1994**, *83*, 484–501, doi:10.1007/BF01083222.
4. Finger, F.; Helmy, H.M. Composition and total-Pb model ages of monazite from high-grade paragneisses in the Abu Swayel area, southern eastern desert, Egypt. *Mineral. Petrol. 1998 623* **1998**, *62*, 269–289, doi:10.1007/BF01178032.
5. Abd El-Wahed, M.A. Oppositely dipping thrusts and transpressional imbricate zone in the Central Eastern Desert of Egypt. *J. African Earth Sci.* **2014**, *100*, 42–59, doi:10.1016/J.JAFREARSCI.2014.06.010.
6. Hamdy, M.M.; Aly, G.A. Preliminary results of a first record of gold and uranium in marble from central eastern desert, egypt: A witness for (syn- and post-?) metamorphic mineralization in metasediments. *Arab. J. Geosci.* **2011**, *4*, 25–43, doi:10.1007/S12517-009-0054-0/FIGURES/9.
7. Gad, S.; Kusky, T. Lithological mapping in the Eastern Desert of Egypt, the Barramiya area, using Landsat thematic mapper (TM). *J. African Earth Sci.* **2006**, *44*, 196–202, doi:10.1016/j.jafrearsci.2005.10.014.
8. Zoheir, B.; Lehmann, B. Listvenite–lode association at the Barramiya gold mine, Eastern Desert, Egypt. *Ore Geol. Rev.* **2011**, *39*, 101–115, doi:10.1016/J.OREGEOREV.2010.12.002.
9. Zoheir, B.; El-Wahed, M.A.; Pour, A.B.; Abdelnasser, A. Orogenic gold in transpression and transtension zones: Field and remote sensing studies of the barramiya–mueilha sector, Egypt. *Remote Sens.* **2019**, *11*, 2122.
10. Osman, A. The mode of occurrence of gold-bearing listvenite at El Barramiya gold mine, Eastern desert, Egypt. *Middle East Res. Centre. Ain Shams Univ. Earth Sci. Ser.* **1995**, *9*, 93–103.

11. Zoheir, B.; Weihed, P. Greenstone-hosted lode-gold mineralization at Dungash mine, Eastern Desert, Egypt. *J. African Earth Sci.* **2014**, *99*, 165–187.
12. Helba, H.A.; Khalil, K.I.; Abou, N.M.F. Alteration Patterns Related to Hydrothermal Gold Mineralizaition in Meta-andesites at Dungash Area, Eastern Desert, Egypt. *Resour. Geol.* **2001**, *51*, 19–30, doi:10.1111/j.1751-3928.2001.tb00078.x.
13. Yamaguchi, Y.; Kahle, A.B.; Tsu, H.; Kawakami, T.; Pniel, M. Overview of advanced spaceborne thermal emission and reflection radiometer (ASTER). *IEEE Trans. Geosci. Remote Sens.* **1998**, *36*, 1062–1071.
14. Morfitt, R.; Barsi, J.; Levy, R.; Markham, B.; Micijevic, E.; Ong, L.; Scaramuzza, P.; Vanderwerff, K. Landsat-8 Operational Land Imager (OLI) Radiometric Performance On-Orbit. *Remote Sens.* **2015**, *7*, 2208–2237, doi:10.3390/rs70202208.
15. Masek, J.G.; Wulder, M.A.; Markham, B.; McCorkel, J.; Crawford, C.J.; Storey, J.; Jenstrom, D.T. Landsat 9: Empowering open science and applications through continuity. *Remote Sens. Environ.* **2020**, *248*, 111968, doi:https://doi.org/10.1016/j.rse.2020.111968.
16. Mendenhall, J.A.; Bernotas, L.A.; Bicknell, W.E.; Cerrati, V.J.; Digenis, C.J.; Evans, J.B.; Forman, S.E.; Hearn, D.R.; Hoffeld, R.H.; Lencioni, D.E.; et al. Earth Observing-1 Advanced Land Imager: instrument and flight operations overview. *Massachusetts Inst. Technol. Lincoln Lab. Proj. Rep. EO-1* **2000**, *1*, 121.
17. Drusch, M.; Del Bello, U.; Carlier, S.; Colin, O.; Fernandez, V.; Gascon, F.; Hoersch, B.; Isola, C.; Laberinti, P.; Martimort, P.; et al. Sentinel-2: ESA's Optical High-Resolution Mission for GMES Operational Services. *Remote Sens. Environ.* **2012**, *120*, 25–36, doi:https://doi.org/10.1016/j.rse.2011.11.026.
18. Potin, P.; Rosich, B.; Grimont, P.; Miranda, N.; Shurmer, I.; O'Connell, A.; Torres, R.; Krassenburg, M. Sentinel-1 mission status. In Proceedings of the Proceedings of EUSAR 2016: 11th European conference on synthetic aperture radar; 2016; pp. 1–6.
19. Farr, T.G.; Kobrick, M. Shuttle Radar Topography Mission produces a wealth of data. *Eos, Trans. Am. Geophys. Union* **2000**, *81*, 583–585.
20. Crippen, R.; Buckley, S.; Agram, P.; Belz, E.; Gurrola, E.; Hensley, S.; Kobrick, M.; Lavalle, M.; Martin, J.; Neumann, M.; et al. NASADEM global elevation model: Methods and progress. *Int. Arch. Photogramm. Remote Sens. Spat. Inf. Sci.* **2016**, *41*, 125–128.
21. Tachikawa, T.; Hato, M.; Kaku, M.; Iwasaki, A. Characteristics of

ASTER GDEM version 2. In Proceedings of the 2011 IEEE international geoscience and remote sensing symposium; 2011; pp. 3657–3660.
22. Rosenqvist, A.; Shimada, M.; Ito, N.; Watanabe, M. ALOS PALSAR: A pathfinder mission for global-scale monitoring of the environment. *IEEE Trans. Geosci. Remote Sens.* **2007**, *45*, 3307–3316.
23. Takaku, J.; Tadono, T.; Tsutsui, K. Generation of high resolution global DSM from ALOS PRISM. *Int. Arch. Photogramm. Remote Sens. Spat. Inf. Sci.* **2014**, *40*, 243–248.
24. Candela, L.; Formaro, R.; Guarini, R.; Loizzo, R.; Longo, F.; Varacalli, G. The PRISMA mission. In Proceedings of the 2016 IEEE international geoscience and remote sensing symposium (IGARSS); 2016; pp. 253–256.
25. Loizzo, R.; Daraio, M.; Guarini, R.; Longo, F.; Lorusso, R.; DIni, L.; Lopinto, E. Prisma Mission Status and Perspective. *Int. Geosci. Remote Sens. Symp.* **2019**, 4503–4506, doi:10.1109/IGARSS.2019.8899272.
26. Kaufmann, H.; Segl, K.; Guanter, L.; Hofer, S.; Foerster, K.-P.; Stuffler, T.; Mueller, A.; Richter, R.; Bach, H.; Hostert, P.; et al. Environmental mapping and analysis program (EnMAP)-Recent advances and status. In Proceedings of the IGARSS 2008-2008 IEEE International Geoscience and Remote Sensing Symposium; 2008; Vol. 4, pp. IV--109.
27. Shebl, A.; Abdellatif, M.; Elkhateeb, S.O.; Csámer, Á. Multisource Data Analysis for Gold Potentiality Mapping of Atalla Area and Its Environs, Central Eastern Desert, Egypt. *Miner. 2021, Vol. 11, Page 641* **2021**, *11*, 641, doi:10.3390/MIN11060641.
28. Shebl, A.; Csámer, Á. Reappraisal of DEMs, Radar and optical datasets in lineaments extraction with emphasis on the spatial context. *Remote Sens. Appl. Soc. Environ.* **2021**, *24*, 100617, doi:10.1016/J.RSASE.2021.100617.
29. Shebl, A.; Csámer, Á. Stacked vector multi-source lithologic classification utilizing Machine Learning Algorithms: Data potentiality and dimensionality monitoring. *Remote Sens. Appl. Soc. Environ.* **2021**, 100643, doi:10.1016/J.RSASE.2021.100643.
30. Shebl, A.; Abdellatif, M.; Hissen, M.; Ibrahim Abdelaziz, M.; Csámer, Á. Lithological mapping enhancement by integrating Sentinel 2 and gamma-ray data utilizing support vector machine: A case study from Egypt. *Int. J. Appl. Earth Obs. Geoinf.* **2021**, *105*, 102619, doi:10.1016/J.JAG.2021.102619.
31. Shebl, A.; Csámer, Á. Lithological, structural and hydrothermal alteration mapping utilizing remote sensing datasets: a case study

around Um Salim area, Egypt. *IOP Conf. Ser. Earth Environ. Sci.* **2021**, *942*, 012032, doi:10.1088/1755-1315/942/1/012032.

32. Shebl, A.; Kusky, T.; Csámer, Á. Advanced land imager superiority in lithological classification utilizing machine learning algorithms. *Arab. J. Geosci. 2022 159* **2022**, *15*, 1–13, doi:10.1007/S12517-022-09948-W.
33. Shebl, A.; Abdelaziz, M.I.; Ghazala, H.; Araffa, S.A.S.; Abdellatif, M.; Csámer, Á. Multi-criteria ground water potentiality mapping utilizing remote sensing and geophysical data: A case study within Sinai Peninsula, Egypt. *Egypt. J. Remote Sens. Sp. Sci.* **2022**, *25*, 765–778.
34. El-Desoky, H.M.; Shebl, A.; Abdel-Rahman, A.M.; Fahmy, W.; El-Awny, H.; El-Sherif, A.M.; El-Rahmany, M.M.; Csámer, Á. Multiscale mineralogical investigations for mineral potentiality mapping of Ras El-Kharit-Wadi Khashir district, Southern Eastern Desert, Egypt. *Egypt. J. Remote Sens. Sp. Sci.* **2022**, *25*, 941–960, doi:10.1016/J.EJRS.2022.09.001.
35. Badawi, M.; Abdelatif, M.; Shebl, A.; Makroum, F.; Shalaby, A.; Nemeth, N. Mapping Structurally Controlled Alterations Sparked by Hydrothermal Activity in the Fatira-Abu Zawal Area, Eastern Desert, Egypt. *Acta Geol. Sin. - English Ed.* **2022**, doi:10.1111/1755-6724.15019.
36. Abdelkader, M.A.; Watanabe, Y.; Shebl, A.; El-Dokouny, H.A.; Dawoud, M.; Csámer, Á. Effective delineation of rare metal-bearing granites from remote sensing data using machine learning methods: A case study from the Umm Naggat Area, Central Eastern Desert, Egypt. *Ore Geol. Rev.* **2022**, *150*, 105184, doi:10.1016/J.OREGEOREV.2022.105184.
37. Shebl, A.; Abdellatif, M.; Badawi, M.; Dawoud, M.; Fahil, A.S.; Csámer, Á. Towards better delineation of hydrothermal alterations via multi-sensor remote sensing and airborne geophysical data. *Sci. Rep.* **2023**, *13*, 7406.
38. Shebl, A.; El-Desoky, H.M.; Abdel-Rahman, A.M.; Fahmy, W.; El-Awny, H.; El-Sherif, A.; El-Rahmany, M.M.; Csámer, Á. Impact of DEMs for Improvement Sentinel 2 Lithological Mapping Utilizing Support Vector Machine: A Case Study of Mineralized Fe-Ti-Rich Gabbroic Rocks from the South Eastern Desert of Egypt. *Minerals* **2023**, *13*, 826.
39. Shebl, A.; Abriha, D.; Fahil, A.S.; El-Dokouny, H.A.; Elrasheed, A.A.; Csámer, Á. PRISMA hyperspectral data for lithological mapping in the Egyptian Eastern Desert: Evaluating the Support Vector Machine, Random Forest, and XG Boost Machine Learning Algorithms. *Ore Geol.*

Rev. **2023**, 105652.
40. Shebl, A.; Hamdy, M. Multiscale (microscopic to remote sensing) preliminary exploration of auriferous-uraniferous marbles: A case study from the Egyptian Nubian Shield. *Sci. Rep.* **2023**, *13*, 9173, doi:10.1038/s41598-023-36388-7.
41. Hagag, W.; Abdelnasser, A. High resolution mapping of alteration zones in Daghbag and Bakriya gold occurrences (Central Eastern Desert, Egypt) using field, mineralogical-geochemical, and remote sensing data. *Arab. J. Geosci.* **2021**, *14*, 1–26.
42. Harraz, H.Z.; Hamdy, M.M.; El-Mamoney, M.H. Multi-element association analysis of stream sediment geochemistry data for predicting gold deposits in Barramiya gold mine, Eastern Desert, Egypt. *J. African Earth Sci.* **2012**, *68*, 1–14, doi:https://doi.org/10.1016/j.jafrearsci.2012.03.009.
43. El-Bedawi, M.A.; Hassan, Y.M.; Zaki, M.E.; Arnous, M.M. *Results of prospecting-evaluation work carried out at Barramiya gold ore deposit (1979--1981). Geological Survey Egypt*; 1983;
44. Aero-Service Final operational report of airborne magnetic/radiation survey in the Eastern Desert, Egypt. For the Egyptian General Petroleum Corporation (EGPC) and the Egyptian Geological Survey and Mining Authority (EGSMA) 1984.
45. Pour, A.B.; Hashim, M. ASTER, ALI and Hyperion sensors data for lithological mapping and ore minerals exploration. *Springerplus* **2014**, *3*, 130.
46. Rowan, L.C.; Mars, J.C. Lithologic mapping in the Mountain Pass, California area using Advanced Spaceborne Thermal Emission and Reflection Radiometer (ASTER) data. *Remote Sens. Environ.* **2003**, *84*, 350–366, doi:10.1016/S0034-4257(02)00127-X.
47. Sabins Jr, F.F.; Ellis, J.M. *Remote sensing: Principles, interpretation, and applications*; Waveland Press, 2020;
48. Mars, J.C.; Rowan, L.C. Regional mapping of phyllic-and argillic-altered rocks in the Zagros magmatic arc, Iran, using Advanced Spaceborne Thermal Emission and Reflection Radiometer (ASTER) data and logical operator algorithms. *Geosphere* **2006**, *2*, 161–186.
49. Jain, R. Feature-Oriented Principal Component Selection (FPCS) for delineation of the geological units using the integration of SWIR and TIR ASTER Data. In *Recent Remote Sensing Sensor Applications-Satellites and Unmanned Aerial Vehicles (UAVs)*; IntechOpen, 2021.
50. Loughlin, W.P. Principal component analysis for alteration mapping.

Photogramm. Eng. Remote Sensing **1991**, *57*, 1163–1169.
51. Ren, H.; Du, Q.; Chang, C.-I.; Jensen, J.O. Comparison between constrained energy minimization based approaches for hyperspectral imagery. In Proceedings of the IEEE Workshop on Advances in Techniques for Analysis of Remotely Sensed Data, 2003; 2003; pp. 244–248.
52. Witten, I.H.; Frank, E.; Geller, J. Data Mining: Practical Machine Learning Tools and Techniques with Java Implementations. *SIGMOD Rec.* **2002**, *31*, 76–77, doi:10.1145/507338.507355.
53. Richards, J.A.; Jia, X. *Remote sensing digital image analysis*; 1999; ISBN 9783540251286.
54. Pal, M.; Foody, G.M. Feature selection for classification of hyperspectral data by SVM. *IEEE Trans. Geosci. Remote Sens.* **2010**, *48*, 2297–2307, doi:10.1109/TGRS.2009.2039484.
55. Kuhn, S.; Cracknell, M.J.; Reading, A.M. Lithologic mapping using Random Forests applied to geophysical and remote-sensing data: A demonstration study from the Eastern Goldfields of Australia. *Geophysics* **2018**, *83*, B183–B193, doi:10.1190/geo2017-0590.1.
56. Kumar, C.; Chatterjee, S.; Oommen, T.; Guha, A. Automated lithological mapping by integrating spectral enhancement techniques and machine learning algorithms using AVIRIS-NG hyperspectral data in Gold-bearing granite-greenstone rocks in Hutti, India. *Int. J. Appl. Earth Obs. Geoinf.* **2020**, *86*, 102006, doi:10.1016/J.JAG.2019.102006.
57. Mustapha, M.R.; Lim, H.S.; Jafri, M.Z.M. Comparison of neural network and maximum likelihood approaches in image classification. *J. Appl. Sci.* **2010**, *10*, 2847–2854.
58. Mas, J.F.; Flores, J.J. The application of artificial neural networks to the analysis of remotely sensed data. *http://dx.doi.org/10.1080/01431160701352154* **2007**, *29*, 617–663, doi:10.1080/01431160701352154.
59. Kavzoglu, T.; Mather, P.M. Pruning artificial neural networks: An example using land cover classification of multi-sensor images. *http://dx.doi.org/10.1080/014311699211796* **2010**, *20*, 2761–2785, doi:10.1080/014311699211796.
60. Frizzelle, B.G.; Moody, A. Mapping continuous distributions of land cover: A comparison of maximum-likelihood estimation and artificial neural networks. *Photogramm. Eng. Remote Sensing* **2001**, *67*, 693–706.
61. Haykin, S. Neural networks: a comprehensive foundation. 1999. *Mc Millan, New Jersey* **2010**, 1–24.

62. Cortes, C.; Vapnik, V. Support-vector networks. *Mach. Learn.* **1995**, *20*, 273–297, doi:10.1007/bf00994018.
63. Meyer, D. Support Vector Machines * The Interface to libsvm in package e1071. **2015**.
64. Bachri, I.; Hakdaoui, M.; Raji, M.; Teodoro, A.C.; Benbouziane, A. Machine Learning Algorithms for Automatic Lithological Mapping Using Remote Sensing Data: A Case Study from Souk Arbaa Sahel, Sidi Ifni Inlier, Western Anti-Atlas, Morocco. *ISPRS Int. J. Geo-Information 2019, Vol. 8, Page 248* **2019**, *8*, 248, doi:10.3390/IJGI8060248.
65. Ding, X.; Liu, J.; Yang, F.; Cao, J. Random radial basis function kernel-based support vector machine. *J. Franklin Inst.* **2021**, *358*, 10121–10140, doi:10.1016/J.JFRANKLIN.2021.10.005.
66. Breiman, L. Random Forests. *Mach. Learn. 2001 451* **2001**, *45*, 5–32, doi:10.1023/A:1010933404324.
67. Belgiu, M.; Drăgu, L. Random forest in remote sensing: A review of applications and future directions. *ISPRS J. Photogramm. Remote Sens.* **2016**, *114*, 24–31, doi:10.1016/J.ISPRSJPRS.2016.01.011.
68. Ghosh, A.; Fassnacht, F.E.; Joshi, P.K.; Kochb, B. A framework for mapping tree species combining hyperspectral and LiDAR data: Role of selected classifiers and sensor across three spatial scales. *Int. J. Appl. Earth Obs. Geoinf.* **2014**, *26*, 49–63, doi:10.1016/J.JAG.2013.05.017.
69. Kulkarni, V.Y.; Sinha, P.K. Pruning of random forest classifiers: A survey and future directions. *Proc. - 2012 Int. Conf. Data Sci. Eng. ICDSE 2012* **2012**, 64–68, doi:10.1109/ICDSE.2012.6282329.
70. Elith, J.; Leathwick, J.R.; Hastie, T. A working guide to boosted regression trees. *J. Anim. Ecol.* **2008**, *77*, 802–813, doi:10.1111/J.1365-2656.2008.01390.X.
71. Zhang, Y.; Liu, J.; Shen, W.; Zhang, Y.; Liu, J.; Shen, W. A Review of Ensemble Learning Algorithms Used in Remote Sensing Applications. *Appl. Sci. 2022, Vol. 12* **2022**, *12*, 8654, doi:10.3390/APP12178654.
72. Chen, T.; Guestrin, C. Xgboost: A scalable tree boosting system. In Proceedings of the Proceedings of the 22nd acm sigkdd international conference on knowledge discovery and data mining; 2016; pp. 785–794.
73. Joharestani, M.Z.; Cao, C.; Ni, X.; Bashir, B.; Talebiesfandarani, S. PM2.5 Prediction Based on Random Forest, XGBoost, and Deep Learning Using Multisource Remote Sensing Data. *Atmos. 2019, Vol. 10* **2019**, *10*, 373, doi:10.3390/ATMOS10070373.
74. Bhagwat, R.U.; Uma Shankar, B. A novel multilabel classification of

remote sensing images using XGBoost. *2019 IEEE 5th Int. Conf. Converg. Technol. I2CT 2019* **2019**, doi:10.1109/I2CT45611.2019.9033768.

75. Jafarzadeh, H.; Mahdianpari, M.; Gill, E.; Mohammadimanesh, F.; Homayouni, S. Bagging and Boosting Ensemble Classifiers for Classification of Multispectral, Hyperspectral and PolSAR Data: A Comparative Evaluation. *Remote Sens. 2021, Vol. 13,* **2021**, *13*, 4405, doi:10.3390/RS13214405.
76. Zhao, Y.; Yin, X.; Fu, Y.; Yue, T. A comparative mapping of plant species diversity using ensemble learning algorithms combined with high accuracy surface modeling. *Environ. Sci. Pollut. Res.* **2022**, *29*, 17878–17891, doi:10.1007/S11356-021-16973-X/FIGURES/6.
77. Li, Y.; Li, C.; Li, M.; Liu, Z. Influence of Variable Selection and Forest Type on Forest Aboveground Biomass Estimation Using Machine Learning Algorithms. *For. 2019, Vol. 10,* **2019**, *10*, 1073, doi:10.3390/F10121073.
78. Ma, M.; Zhao, G.; He, B.; Li, Q.; Dong, H.; Wang, S.; Wang, Z. XGBoost-based method for flash flood risk assessment. *J. Hydrol.* **2021**, *598*, 126382, doi:10.1016/J.JHYDROL.2021.126382.
79. Elbegue, A.A.; Allek, K.; Zeghouane, H. Geological mapping using extreme gradient boosting and the deep neural networks: application to silet area, central Hoggar, Algeria. *Acta Geophys.* **2022**, *70*, 1581–1599, doi:10.1007/S11600-022-00814-7/TABLES/5.
80. Parsa, M. A data augmentation approach to XGboost-based mineral potential mapping: An example of carbonate-hosted ZnPb mineral systems of Western Iran. *J. Geochemical Explor.* **2021**, *228*, 106811, doi:10.1016/J.GEXPLO.2021.106811.
81. Zhumabek, Z.; Assylkhan, B.; Alexandr, F.; Dinara, T.; Altynay, K. Automated lineament analysis to assess the geodynamic activity areas. *Procedia Comput. Sci.* **2017**, *121*, 699–706, doi:https://doi.org/10.1016/j.procs.2017.11.091.
82. Ghosh, T.; Hazra, S.; Kumar Das, A. Potential of ALOS-2 PALSAR-2 StripMap data for lithofacies identification and geological lineament mapping in vegetated fold-thrust belt of Nagaland, India. *Adv. Sp. Res.* **2022**, *69*, 1840–1862, doi:10.1016/J.ASR.2021.09.007.
83. Li, N.; Frei, M.; Altermann, W. Textural and knowledge-based lithological classification of remote sensing data in Southwestern Prieska sub-basin, Transvaal Supergroup, South Africa. *J. African Earth Sci.* **2011**, *60*, 237–246, doi:10.1016/J.JAFREARSCI.2011.03.002.
84. Shebl, A.; Badawi, M.; Dawoud, M.; Abd El-Wahed, M.; El-Dokouny,

H.A.; Csámer, Á. Novel comprehensions of lithological and structural features gleaned via Sentinel 2 texture analysis. *Ore Geol. Rev.* **2024**, *168*, 106068, doi:https://doi.org/10.1016/j.oregeorev.2024.106068.
85. Liesenberg, V.; Gloaguen, R. Evaluating SAR polarization modes at L-band for forest classification purposes in eastern Amazon, Brazil. *Int. J. Appl. Earth Obs. Geoinf.* **2012**, *21*, 122–135, doi:10.1016/j.jag.2012.08.016.
86. Macnae, J. Applications of geophysics for the detection and exploration of kimberlites and lamproites. *J. Geochemical Explor.* **1995**, *53*, 213–243.
87. Shives, R.B.K.; Charbonneau, B.W.; Ford, K.L. The detection of potassic alteration by gamma-ray spectrometry—recognition of alteration related to mineralization. *Geophysics* **2000**, *65*, 2001–2011.
88. Reid, A.B.; Allsop, J.M.; Granser, H.; Millett, A.J. t; Somerton, I.W. Magnetic interpretation in three dimensions using Euler deconvolution. *Geophysics* **1990**, *55*, 80–91.
89. Abdelsalam, M.G.; Stern, R.J. Sutures and shear zones in the Arabian-Nubian Shield. *J. African Earth Sci.* **1996**, *23*, 289–310, doi:10.1016/S0899-5362(97)00003-1.
90. Shackleton, R.. Contrasting structural relationships of Proterozoic ophiolites in Northeast and Eastern Africa. *Contrasting Struct. relationships Proterozoic ophiolites Northeast East. Africa* **1988**.
91. Halls, C.; Zhao, R. Listvenite and related rocks: perspectives on terminology and mineralogy with reference to an occurrence at Cregganbaun, Co. Mayo, Republic of Ireland. *Miner. Depos.* **1995**, *30*, 303–313, doi:10.1007/BF00196366/METRICS.
92. El Gaby, S.; List**, F.K.; Tehrani**, R. The basement complex of the Eastern Desert and Sinai. *Geol. Egypt* **1990**, 175–184, doi:10.1201/9780203736678-10.
93. Abu El Ela, F.F. Ophiolitic mélange of the Abu Mireiwa District, Central Eastern Desert, Egypt. *Unpubl. PhD Thesis, Assuit Univ. Egypt* **1985**.
94. El Shazly, E.M. The geology of the Egyptian region, The ocean basins and margins. *J. East. Mediterr. Plenum Press. New York, London* **1977**, *4*.
95. Goldfarb, R.J.; Baker, T.; Dubé, B.; Groves, D.I.; Hart, C.J.R.; Gosselin, P. Distribution, Character, and Genesis of Gold Deposits in Metamorphic Terran. *One Hundredth Anniv. Vol.* **2005**, doi:10.5382/AV100.14.
96. Reinhardt, M.C.; Davison, I. Structural and lithologic controls on gold

deposition in the shear zone-hosted Fazenda Brasileiro Mine, Bahia State, Northeast Brazil. *Econ. Geol.* **1990**, *85*, 952–967, doi:10.2113/GSECONGEO.85.5.952.
97. Almond, D.C.; Ahmed, F.; Shaddad, M.Z. Setting of gold mineralization in the northern Red Sea Hills of Sudan. *Econ. Geol.* **1984**, *79*, 389–392, doi:10.2113/GSECONGEO.79.2.389.
98. Elsamani, Y.; Almuslem, A.A.; Tokhi, M. El Geology and Geotectonic Classification of Pan-African Gold Mineralizations in the Red Sea Hills, Sudan. *http://dx.doi.org/10.1080/00206810109465064* **2010**, *43*, 1117–1128, doi:10.1080/00206810109465064.
99. Kusky, T.; Wang, J.; Wang, L.; Huang, B.; Ning, W.; Fu, D.; Peng, H.; Deng, H.; Polat, A.; Zhong, Y.; et al. Mélanges through time: Life cycle of the world's largest Archean mélange compared with Mesozoic and Paleozoic subduction-accretion-collision mélanges. *Earth-Science Rev.* 2020, *209*.
100. Lachaine, G. *Structures géologiques et linéaments, Beauce (Québec): apport de la télédétection*; Université de Sherbrooke., 1999; ISBN 0612617785.
101. Haralick, R.M. Statistical and structural approaches to texture. *Proc. IEEE* **1979**, *67*, 786–804, doi:10.1109/PROC.1979.11328.
102. Eldosouky, A.M.; Elkhateeb, S.O. Texture analysis of aeromagnetic data for enhancing geologic features using co-occurrence matrices in Elallaqi area, South Eastern Desert of Egypt. *NRIAG J. Astron. Geophys.* **2018**, *7*, 155–161, doi:10.1016/J.NRJAG.2017.12.006.
103. der Meer, F.D.; der Werff, H.M.A.; Van Ruitenbeek, F.J.A.; Hecker, C.A.; Bakker, W.H.; Noomen, M.F.; Van Der Meijde, M.; Carranza, E.J.M.; De Smeth, J.B.; Woldai, T. Multi-and hyperspectral geologic remote sensing: A review. *Int. J. Appl. Earth Obs. Geoinf.* **2012**, *14*, 112–128.
104. Liu, L.; Zhou, J.; Jiang, D.; Zhuang, D.; Mansaray, L.R.; Zhang, B. Targeting mineral resources with remote sensing and field data in the Xiemisitai area, West Junggar, Xinjiang, China. *Remote Sens.* **2013**, *5*, 3156–3171.
105. Hu, B.; Xu, Y.; Wan, B.; Wu, X.; Yi, G. Hydrothermally altered mineral mapping using synthetic application of Sentinel-2A MSI, ASTER and Hyperion data in the Duolong area, Tibetan Plateau, China. *Ore Geol. Rev.* **2018**, *101*, 384–397.
106. Singh, A.; Harrison, A. Standardized principal components. *Int. J. Remote Sens.* **1985**, *6*, 883–896.
107. Badawi, M.A.; Makroum, F.M.A.; Shalaby, A.; Nemth, N. GEOLOGY

AND PETROGRAPHY OF MUBARAK AREA, CENTRAL EASTERN DESERT, EGYPT. *Geosci. Eng.* **2021**, *9*, 5–16, doi:10.33030/GEOSCIENCES.2021.14.005.
108. Moore, D.M.; Reynolds Jr, R.C.; others *X-ray Diffraction and the Identification and Analysis of Clay Minerals.*; Oxford University Press (OUP), 1989;
109. Fleet, M.E.; Deer, W.A.; Howie, R.A.; Zussman, J. Rock-forming minerals: micas.; 2003.
110. Oberthür, T.; Weiser, T.; Amanor, J.A.; Chryssoulis, S.L. Mineralogical siting and distribution of gold in quartz veins and sulfide ores of the Ashanti mine and other deposits in the Ashanti belt of Ghana: genetic implications. *Miner. Depos.* **1997**, *32*, 2–15.
111. Hilmy, M.E.; Osman, A. Remobilization of gold from a chalcopyrite-pyrite mineralization Hamash gold mine, Southeastern Desert, Egypt. *Miner. Depos.* **1989**, *24*, 244–249.
112. Deng, G.; Kang, J.; Nan, X.; Li, Y.; Guo, J.; Ding, X.; Huang, F. Barium isotope evidence for crystal-melt separation in granitic magma reservoirs. *Geochim. Cosmochim. Acta* **2021**, *292*, 115–129, doi:https://doi.org/10.1016/j.gca.2020.09.027.
113. De la Roche, H. de; Leterrier, J. t; Grandclaude, P.; Marchal, M. A classification of volcanic and plutonic rocks using R1R2-diagram and major-element analyses—its relationships with current nomenclature. *Chem. Geol.* **1980**, *29*, 183–210.
114. Cox, K.G.; Bell, J.D.; Pankhurst, R.J. Compositional variation in magmas. In *The interpretation of igneous rocks*; Springer, 1979; pp. 12–41.
115. Middlemost, E.A.K. Naming materials in the magma/igneous rock system. *Earth-science Rev.* **1994**, *37*, 215–224.
116. Streckeisen, A.L.; LeMaitre, R.W. Chemical approximation to modal QAPF classification of the igneous rocks: Neus Jahrbuch fur Mineralogie, v. 136. **1979**.
117. Hastie, A.R.; Kerr, A.C.; Pearce, J.A.; Mitchell, S.F. Classification of altered volcanic island arc rocks using immobile trace elements: development of the Th--Co discrimination diagram. *J. Petrol.* **2007**, *48*, 2341–2357.
118. Thompson, R.N.; Dickin, A.P.; Gibson, I.L.; Morrison, M.A. Elemental fingerprints of isotopic contamination of Hebridean Palaeocene mantle-derived magmas by Archaean sial. *Contrib. to Mineral. Petrol.* **1982**, *79*, 159–168.
119. Cann, J.R. Rb, Sr, Y, Zr and Nb in some ocean floor basaltic rocks. *Earth*

Planet. Sci. Lett. **1970**, *10*, 7–11.
120. Pearce, J.A.; Cann, J.R. Tectonic setting of basic volcanic rocks determined using trace element analyses. *Earth Planet. Sci. Lett.* **1973**, *19*, 290–300.
121. Pearce, J. Trace Element Characteristics of Lavas from Destructive Plate Boundaries. In *Andesites: Orogenic Andesites and Related Rocks*; R.S. Thorpe, Ed.; John Wiley and Sons, Inc., New York, New York, 1982; pp. 252–548.
122. Meschede, M. A method of discriminating between different types of mid-ocean ridge basalts and continental tholeiites with the Nb◎ 1bZr◎ 1bY diagram. *Chem. Geol.* **1986**, *56*, 207–218.
123. Xu, K.; Wang, X.; Kong, C.; Feng, R.; Liu, G.; Wu, C. Identification of hydrothermal alteration minerals for exploring gold deposits based on SVM and PCA using ASTER data: A case study of Gulong. *Remote Sens.* **2019**, *11*, 3003.
124. Abdolmaleki, M.; Rasmussen, T.M.; Pal, M.K. Exploration of IOCG mineralizations using integration of space-borne remote sensing data with airborne geophysical data. *Int. Arch. Photogramm. Remote Sens. Spat. Inf. Sci.* **2020**, *43*, 9–16.
125. Shirazi, A.; Shirazy, A.; Karami, J. Remote sensing to identify copper alterations and promising regions, Sarbishe, South Khorasan, Iran. *Int. J. Geol. Earth Sci.* **2018**, *4*, 36–52.
126. Pour, B.A.; Hashim, M.; Marghany, M. Using spectral mapping techniques on short wave infrared bands of ASTER remote sensing data for alteration mineral mapping in SE Iran. *Int. J. Phys. Sci* **2011**, *6*, 917–929.
127. Yao, F.; Xu, X.; Yang, J.; Geng, X. A Remote-Sensing-Based Alteration Zonation Model of the Duolong Porphyry Copper Ore District, Tibet. *Remote Sens.* **2021**, *13*, 5073.
128. Wu, C.; Dai, J.; Zhou, A.; He, L.; Tian, B.; Lin, W.; Zhao, T.; Bai, L. Mapping alteration zones in the Southern section of Yulong copper belt, Tibet using multi-source remote sensing data. *Front. Earth Sci.* **2023**, *11*, 1164131.
129. Abuzied, S.M.; Ibrahim, S.K.; Kaiser, M.F.; Seleem, T.A. Application of remote sensing and spatial data integrations for mapping porphyry copper zones in Nuweiba area, Egypt. *Int. J. Signal Process. Syst* **2016**, *4*, 102–108.
130. Dutra, L.F.; Louro, V.H.A.; Monteiro, L.V.S. The southern IOCG and hydrothermal nickel mineralization trend of the Carajás Mineral

Province: Airborne geophysical and remote sensing evidences for structural controls and hydrothermal signature. *J. Appl. Geophys.* **2023**, *213*, 105016.

131. Sahoo, R.; Jain, V. Sensitivity of drainage morphometry based hydrological response (GIUH) of a river basin to the spatial resolution of DEM data. *Comput. Geosci.* **2018**, *111*, 78–86, doi:https://doi.org/10.1016/j.cageo.2017.10.001.
132. Adiri, Z.; El Harti, A.; Jellouli, A.; Lhissou, R.; Maacha, L.; Azmi, M.; Zouhair, M.; Bachaoui, E.M. Comparison of Landsat-8, ASTER and Sentinel 1 satellite remote sensing data in automatic lineaments extraction: A case study of Sidi Flah-Bouskour inlier, Moroccan Anti Atlas. *Adv. Sp. Res.* **2017**, *60*, 2355–2367, doi:https://doi.org/10.1016/j.asr.2017.09.006.
133. Dentith, M. Textural filtering of aeromagnetic data. *Explor. Geophys.* **1995**, *26*, 209–214, doi:10.1071/EG995209.
134. Cooper, G.R.J. The textural analysis of gravity data using co-occurrence matrices. *Comput. Geosci.* **2004**, *30*, 107–115, doi:10.1016/J.CAGEO.2003.08.001.
135. Mahmoud, A.; Elbialy, S.; Pradhan, B.; Buchroithner, M. Field-based landcover classification using TerraSAR-X texture analysis. *Adv. Sp. Res.* **2011**, *48*, 799–805, doi:10.1016/J.ASR.2011.04.005.
136. Pradhan, B.; Hagemann, U.; Shafapour Tehrany, M.; Prechtel, N. An easy to use ArcMap based texture analysis program for extraction of flooded areas from TerraSAR-X satellite image. *Comput. Geosci.* **2014**, *63*, 34–43, doi:10.1016/J.CAGEO.2013.10.011.
137. Radford, D.D.G.; Cracknell, M.J.; Roach, M.J.; Cumming, G. V. Geological Mapping in Western Tasmania Using Radar and Random Forests. *IEEE J. Sel. Top. Appl. Earth Obs. Remote Sens.* **2018**, *11*, 3075–3087, doi:10.1109/JSTARS.2018.2855207.
138. Fowler, T.J. Pan-African granite emplacement mechanisms in the Eastern Desert, Egypt. *J. African Earth Sci.* **2001**, *32*, 61–86, doi:https://doi.org/10.1016/S0899-5362(01)90019-3.
139. Helmy, H.M.; Kaindl, R.; Fritz, H.; Loizenbauer, J. The Sukari Gold Mine, Eastern Desert—Egypt: structural setting, mineralogy and fluid inclusion study. *Miner. Depos.* **2004**, *39*, 495–511, doi:10.1007/s00126-004-0426-z.
140. Zoheir, B. Transpressional zones in ophiolitic mélange terranes: Potential exploration targets for gold in the South Eastern Desert, Egypt. *J. Geochemical Explor.* **2011**, *111*, 23–38,

doi:https://doi.org/10.1016/j.gexplo.2011.07.003.
141. Killick, D. Gold and Gold Mining in Ancient Egypt and Nubia. *Azania Archaeol. Res. Africa* **2013**, *48*, 539–541, doi:10.1080/0067270X.2013.852381.
142. Loizenbauer, J.; Wallbrecher, E.; Fritz, H.; Neumayr, P.; Khudeir, A.A.; Kloetzli, U. Structural geology, single zircon ages and fluid inclusion studies of the Meatiq metamorphic core complex: Implications for Neoproterozoic tectonics in the Eastern Desert of Egypt. *Precambrian Res.* **2001**, *110*, 357–383, doi:https://doi.org/10.1016/S0301-9268(01)00176-0.
143. Abu-Alam, T.; Monsef, M.A. El; Grosch, E. Shear-zone hosted gold mineralization of the Arabian–Nubian Shield: devolatilization processes across the greenschist–amphibolite-facies transition. *Geol. Soc. London, Spec. Publ.* **2019**, *478*, 287–313, doi:10.1144/SP478.13.
144. Harlov, D.E.; Austrheim, H.; Pirajno, F. Effects of metasomatism on mineral systems and their host rocks: alkali metasomatism, skarns, greisens, tourmalinites, rodingites, black-wall alteration and listvenites. *Metasomatism Chem. Transform. Rock Role fluids Terr. Extraterr. Process.* **2013**, 203–251.
145. Darwish, M.A.G. Scanning electron microscopy and energy-dispersive X-ray investigations of gold grains in quartz veins from the Seiga gold mine, south Egypt. *Microchem. J.* **2012**, *102*, 38–48.

ACKNOWLEDGEMENTS

First and foremost, I would like to express my deepest gratitude to **Allah**, the Almighty, for granting me the strength and perseverance to successfully complete my PhD.

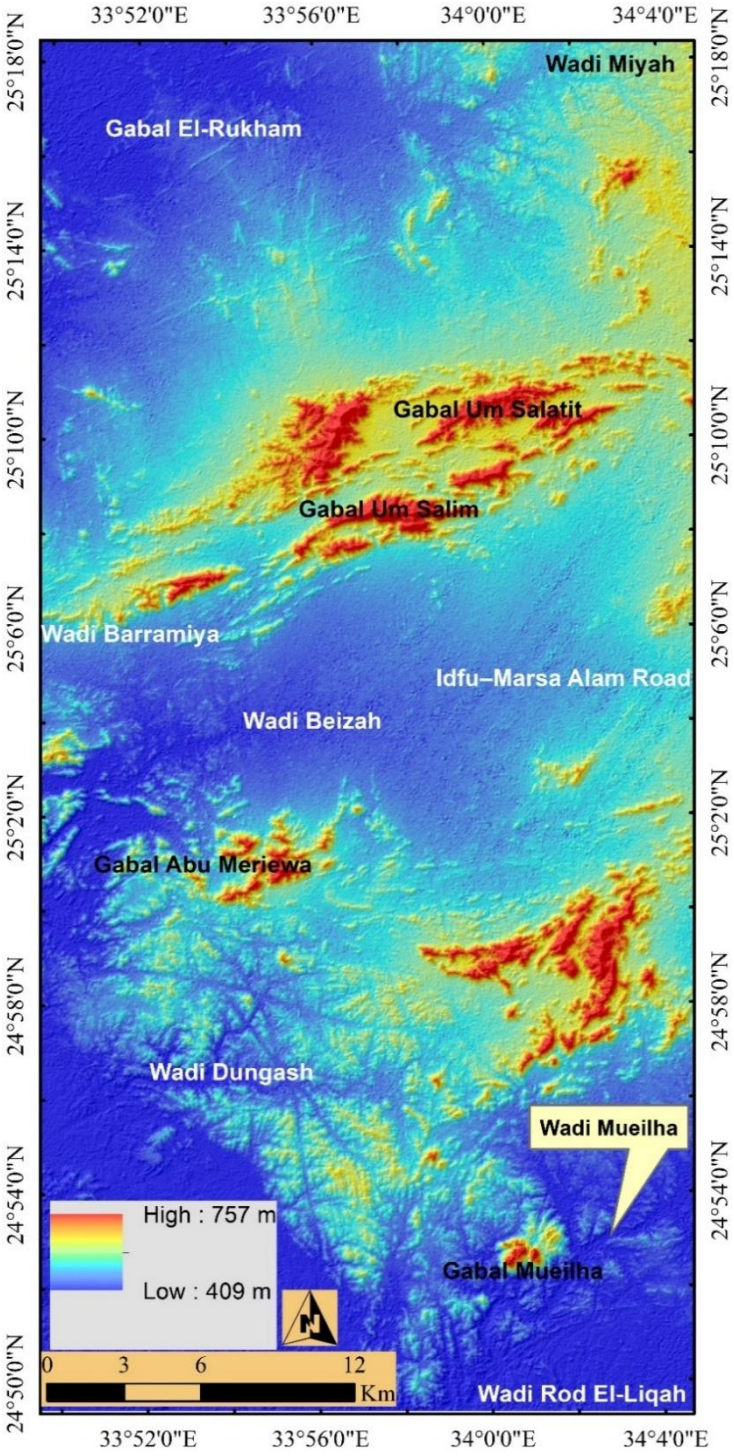
To my cherished family, thank you for your unwavering support. **To my wife, Ola,** your encouragement has been the cornerstone of my achievements. You are my beloved partner in every success. Special thanks to **my children, Yusuf and Anas**, for accompanying me in Debrecen and adding another wonderful dimension to my journey. **To my dear mother**, your constant support and prayers have been invaluable. May Allah bless and protect you. My heartfelt gratitude extends to **Yousuf, Eman, and Mofeda** for their unwavering support throughout this journey.

To my esteemed supervisor, **Dr. Árpád Csámer**, words cannot express my appreciation for your guidance and support. You have been more than a supervisor; you have been an honest advisor and a close friend, always ready to assist and facilitate any challenges related to my research. I would also like to extend special thanks to **Diana** for her help, particularly on the day of my pre-defense. Your assistance is deeply appreciated.

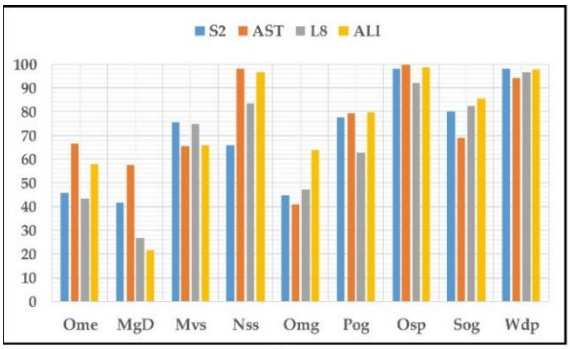
I would like to thank **my professors and colleagues** who assisted me in the fieldwork. Your help is highly appreciated.

APPENDICES

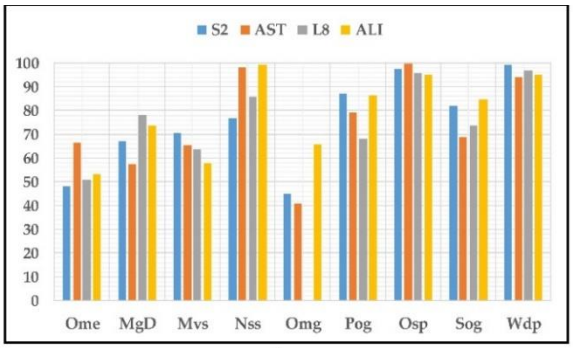
Figures



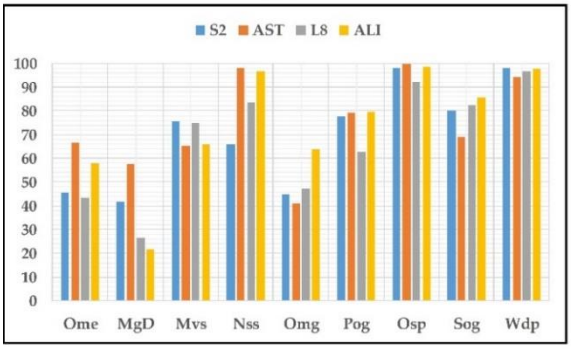
Appendix 1-1: ALOS PALSAR DEM showing the main topographical features within the study area



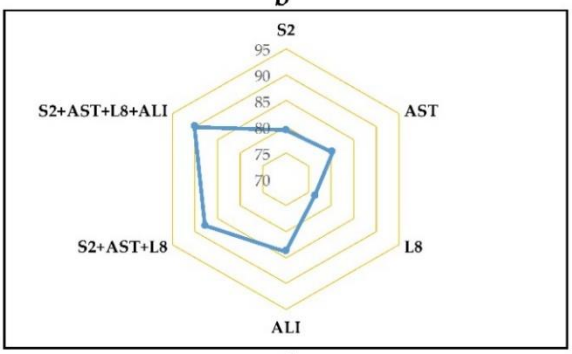
a



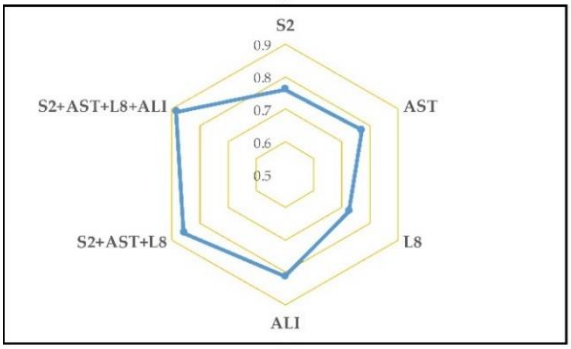
b



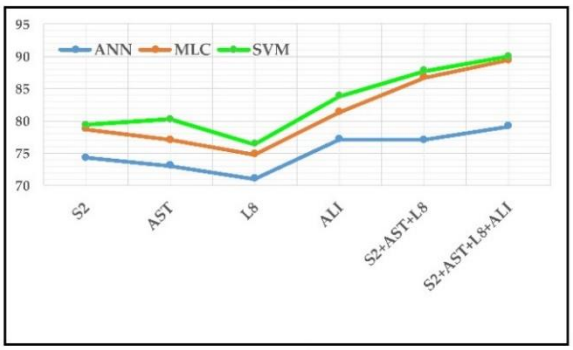
c



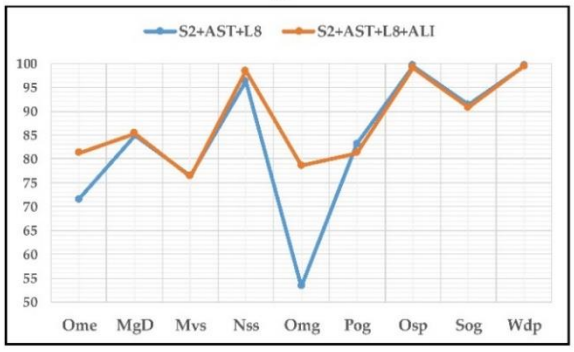
d



e

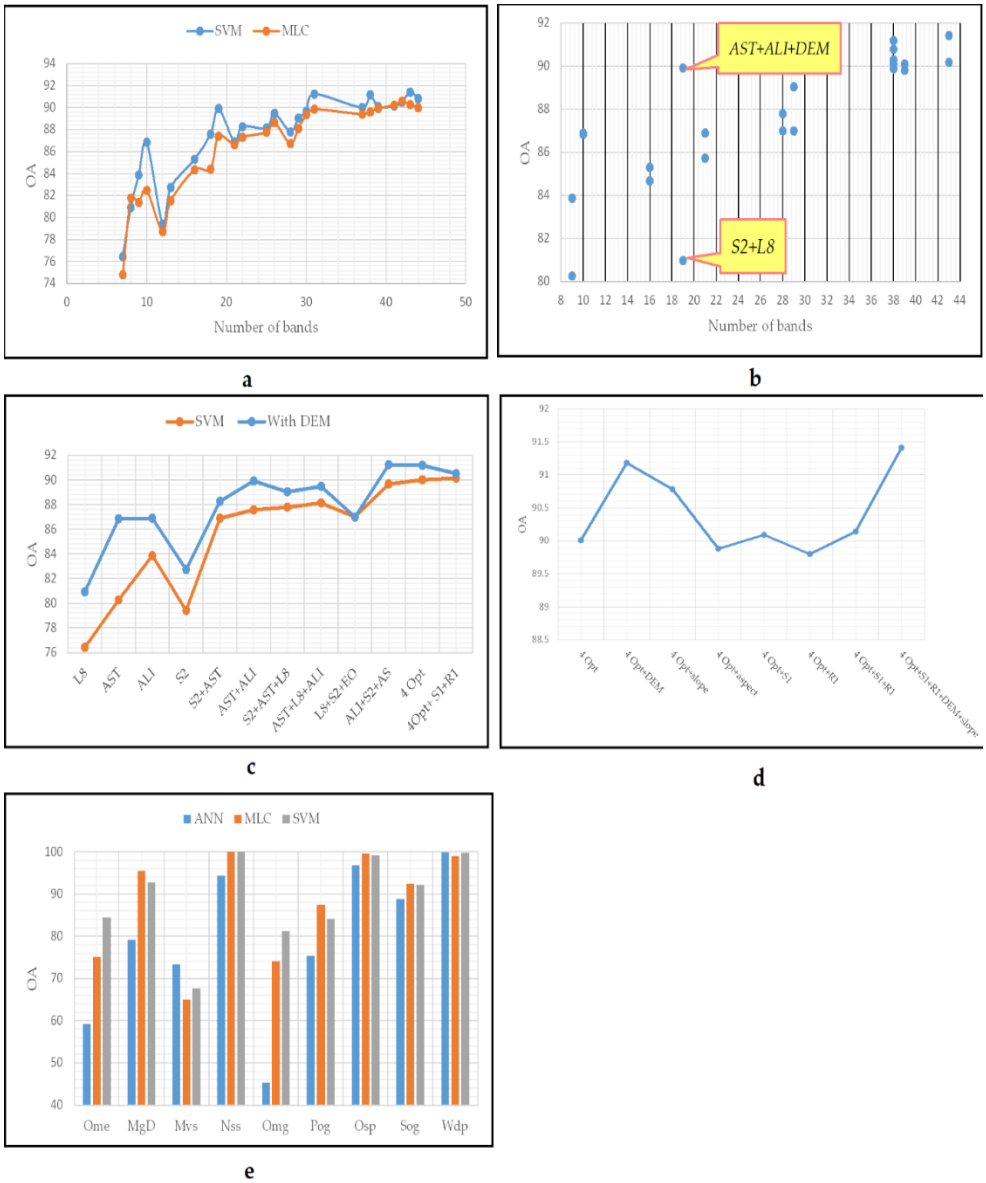


f

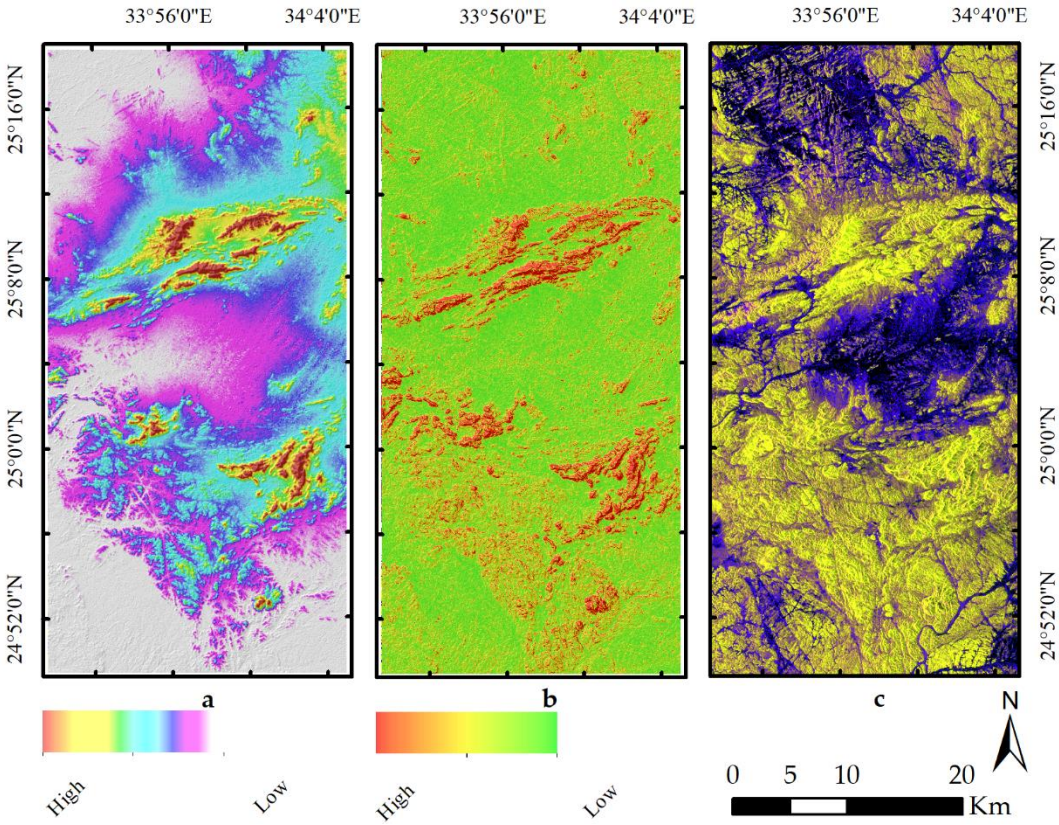


g

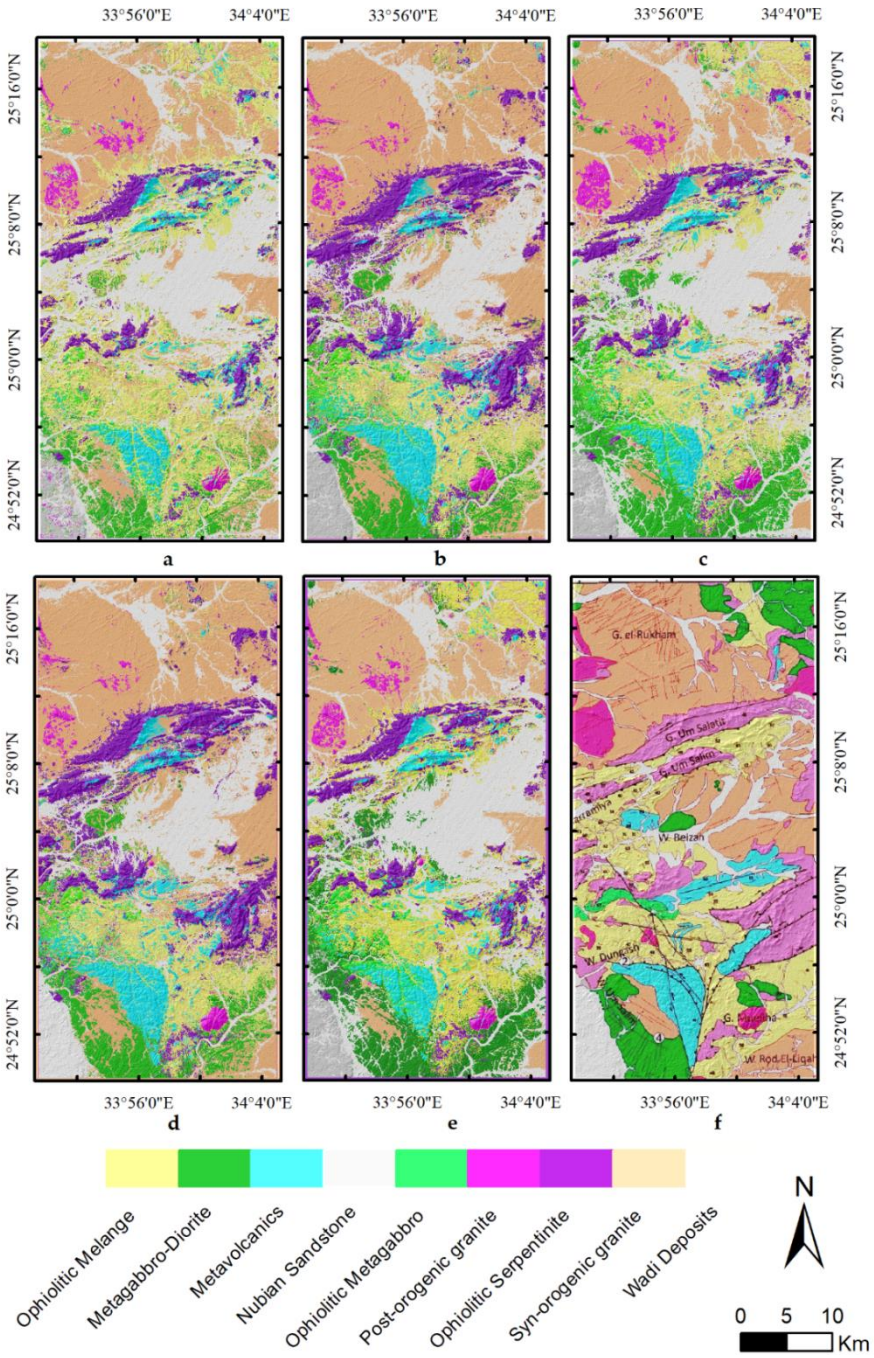
Appendix 4 -1: accuracies of the lithologic units classified by: (a) ANN; (b)MLC; and (c) SVM. overall accuracies (d); and kappa coefficients (e); for the utilized datasets after SVM classification. (f) manifest SVM good performance over ANN and MLC and shows OA increase by merging the different sensors. (g) ALI raised the classification accuracy of Ome and Omg when added to S2+AST+L8 combination.



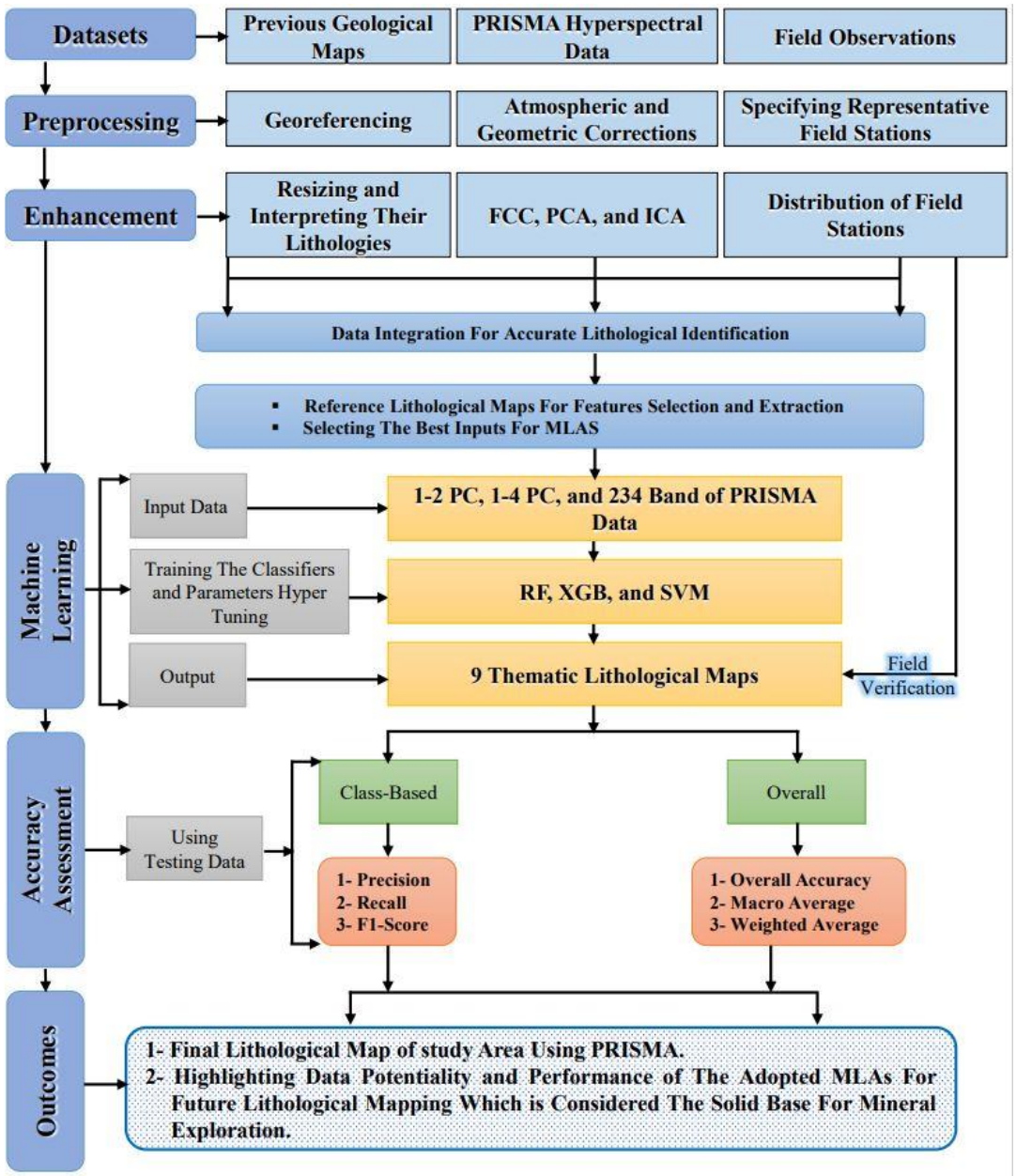
Appendix 4-2: (a) The effect of increasing data dimensionality on classification accuracy. Beyond 31 participated band, the OA excess is barely perceptible; (b) various OA results for different datasets having the same dimensions, differences could reach about 9% (between S2+L8 and AST+ALI+DEM); (c) DEM influence in boosting the classification OA; (d) Topographical and radar data impact on categorization OA; (e) Average accuracies of the information classes, classified by ANN, MLC, and SVM, from ALI+S2+AST+DEM.



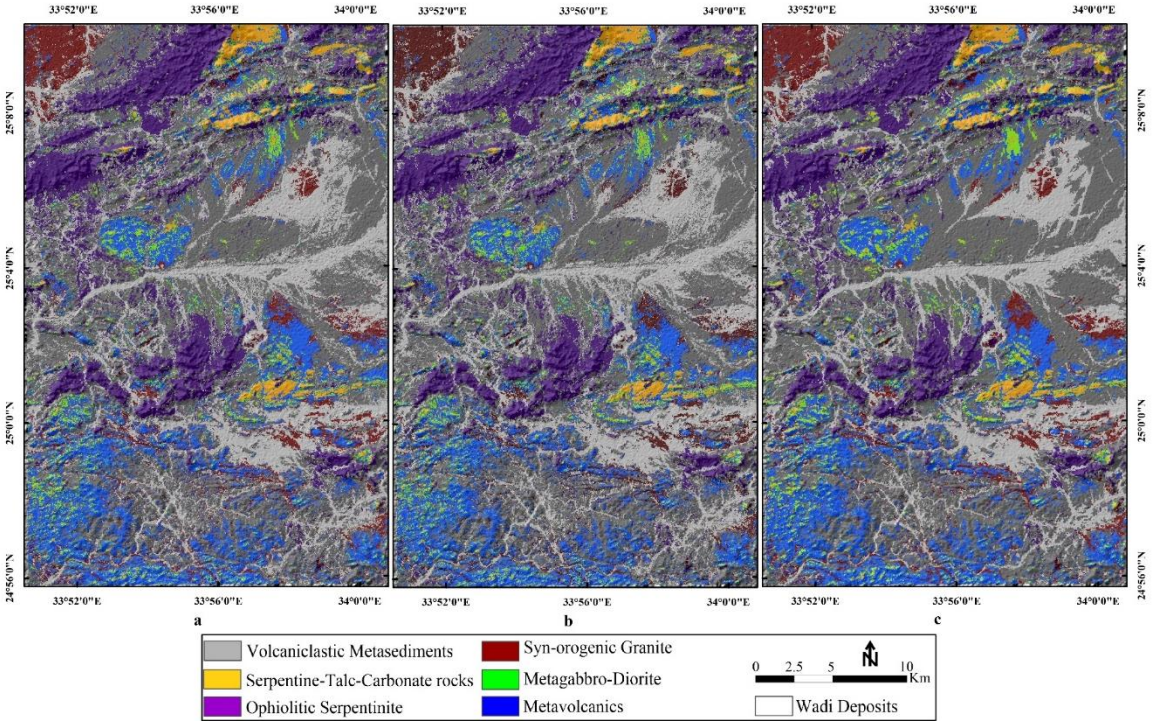
Appendix 4-3 : Reasonable lithological discrimination from (a) DEM (approximately brown Osp, green to cyan Mvs, white Wdp, and pink Sog) compared to; (b) Slope and; (c) RGB (HH, HV, HH/HV) ALOS PALSAR 1 combination.



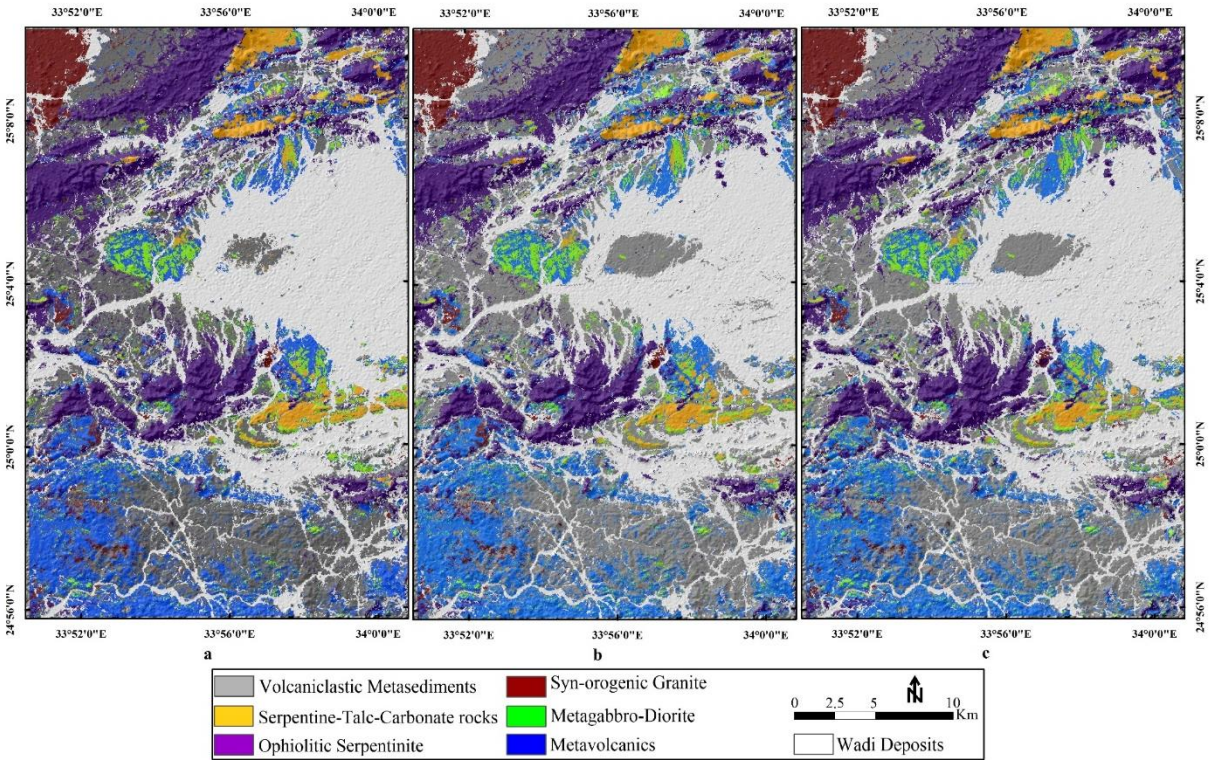
Appendix 4-4: Lithological classification outputs utilizing ALI+S2+AST+DEM data from (a) ANN; (b) MLC and (c) SVM. (d) and (e) are the results of generalization over ALI+S2+AST+ DEM+S1+PALSAR1+slope data utilizing MLC and SVM, respectively. (f)Geological map for comparison.



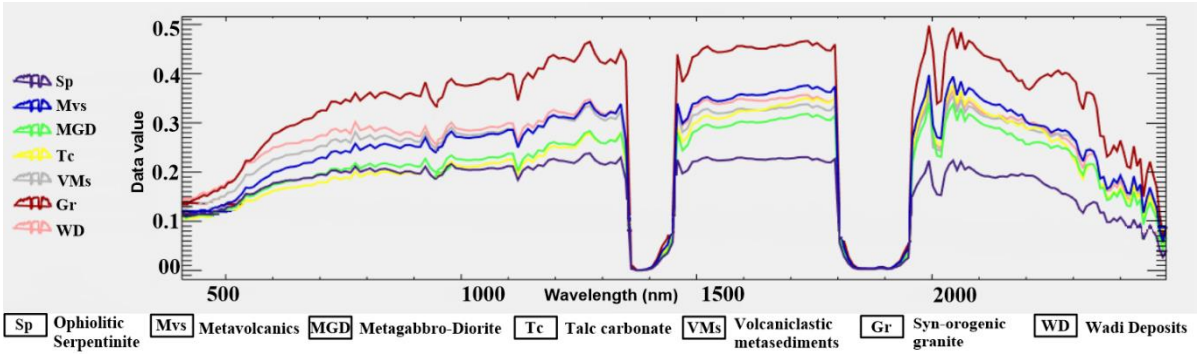
Appendix 4-5: Flow chart showing the methodology adopted in the current study.



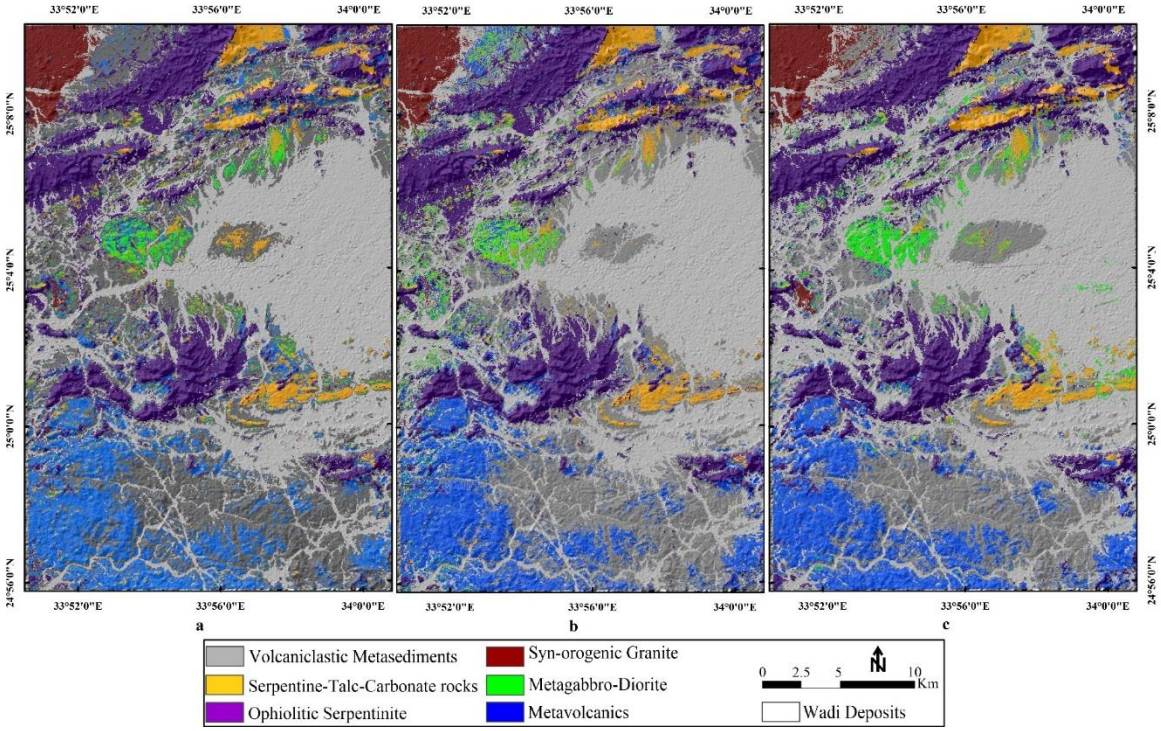
Appendix 4-6: Resultant lithological maps using 1-2pc and a) RF, b) XGB, and c) SVM.



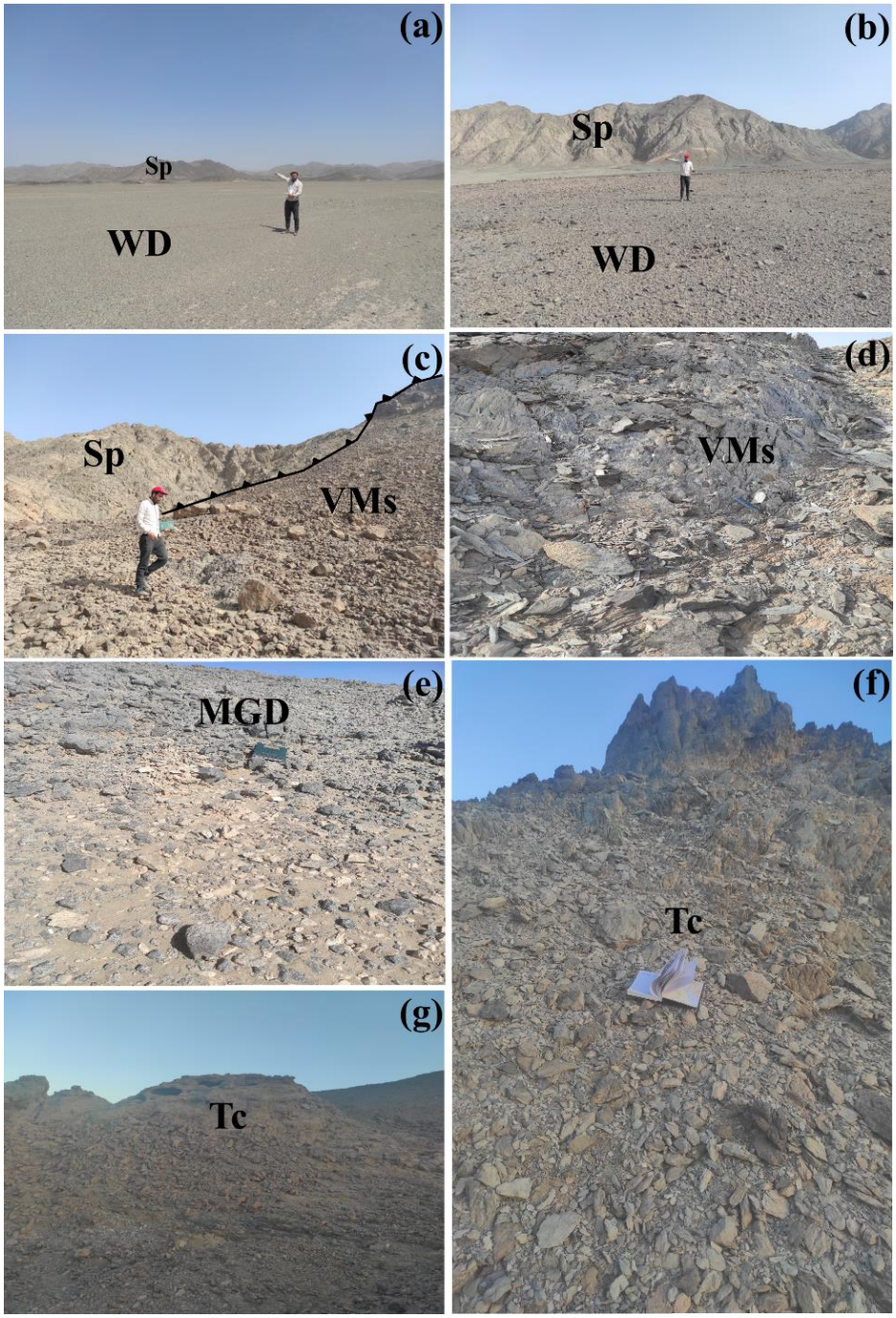
Appendix 4-7: Resultant lithological maps using 1-4pc and a) RF, b) XGB, and c) SVM.



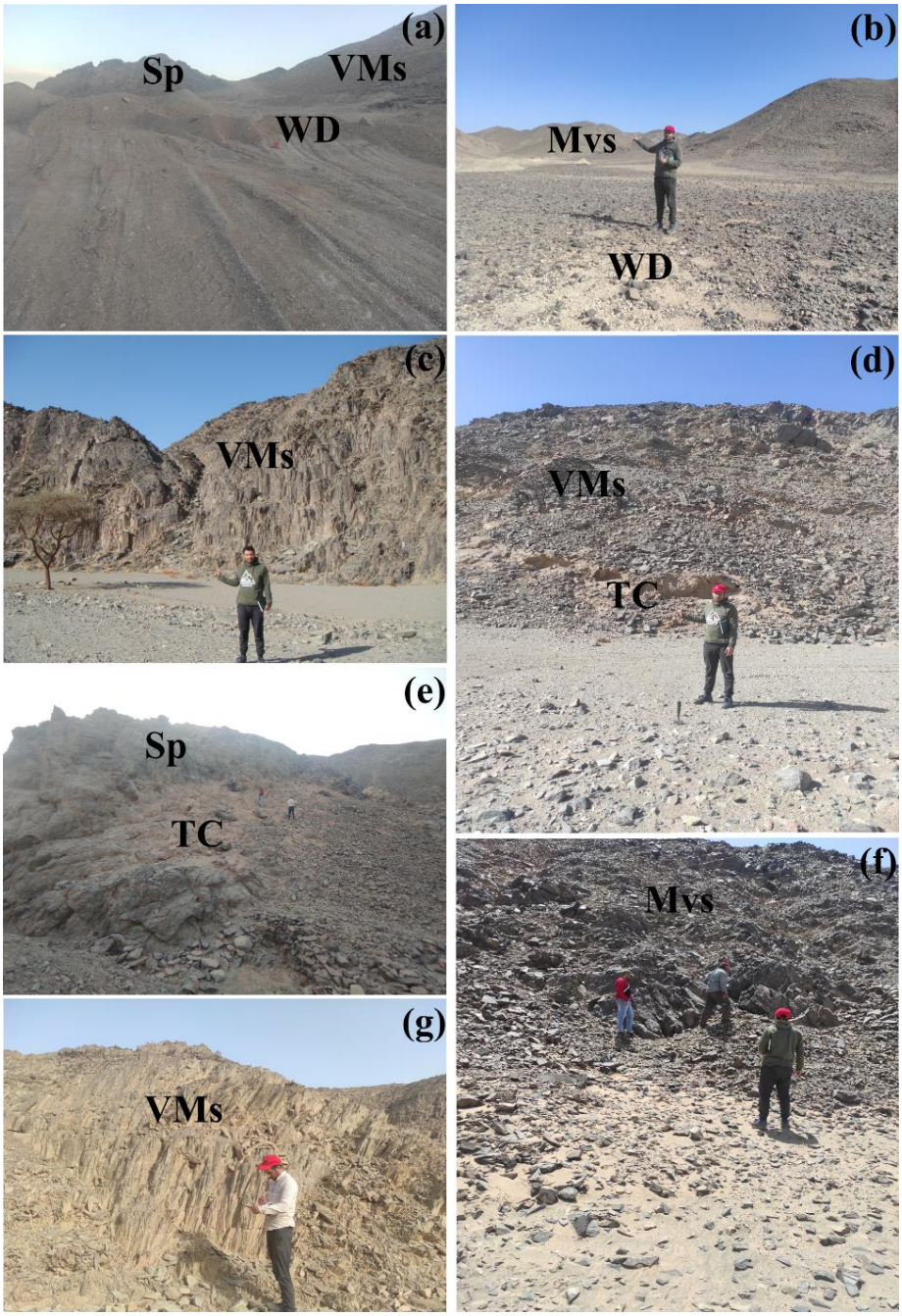
Appendix 4-8: Spectral separability of the lithological targets using PRISMA data.



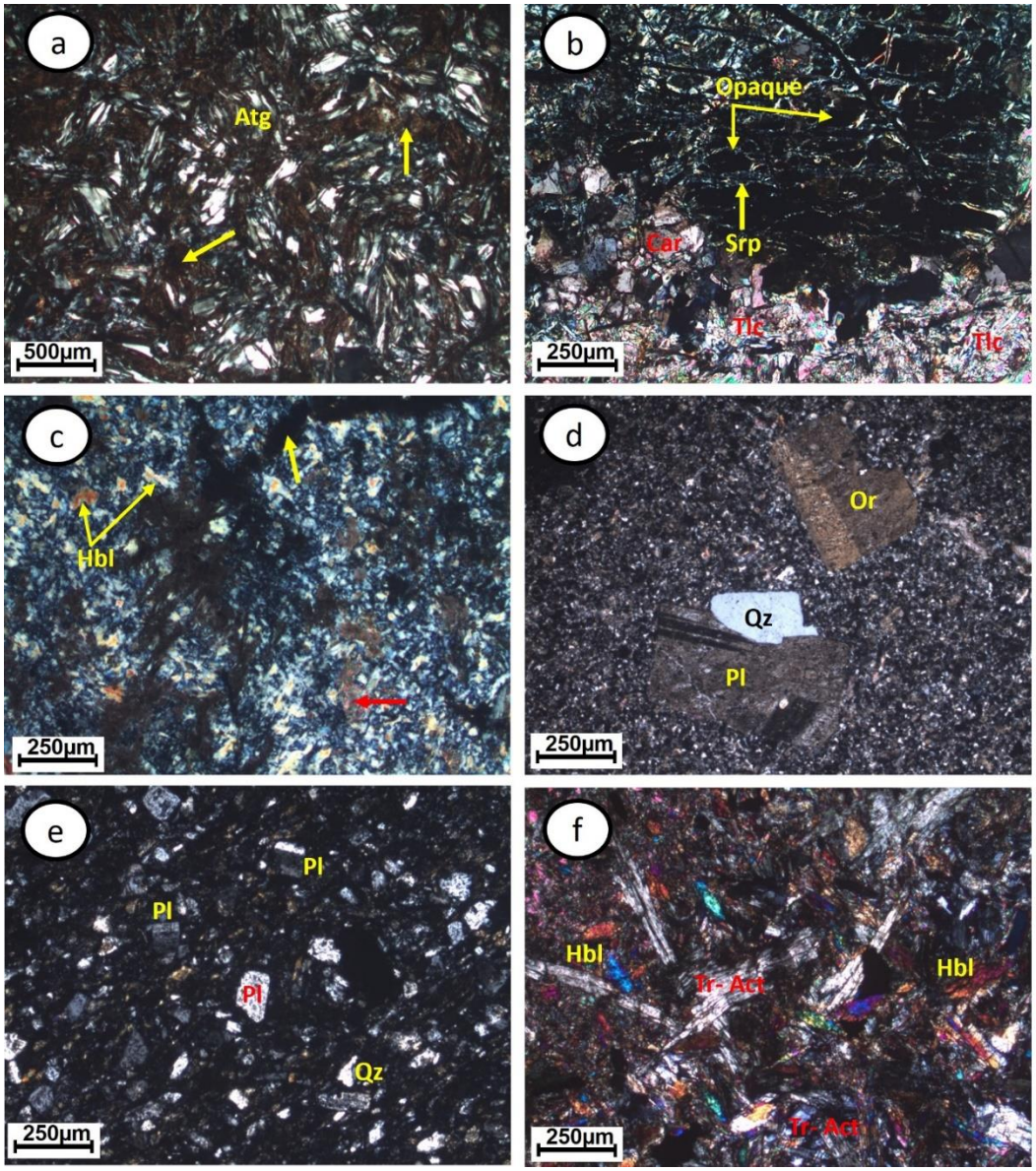
Appendix 4-9: Resultant lithological maps using PRISMA data a) RF, b) XGB, and c) SVM.



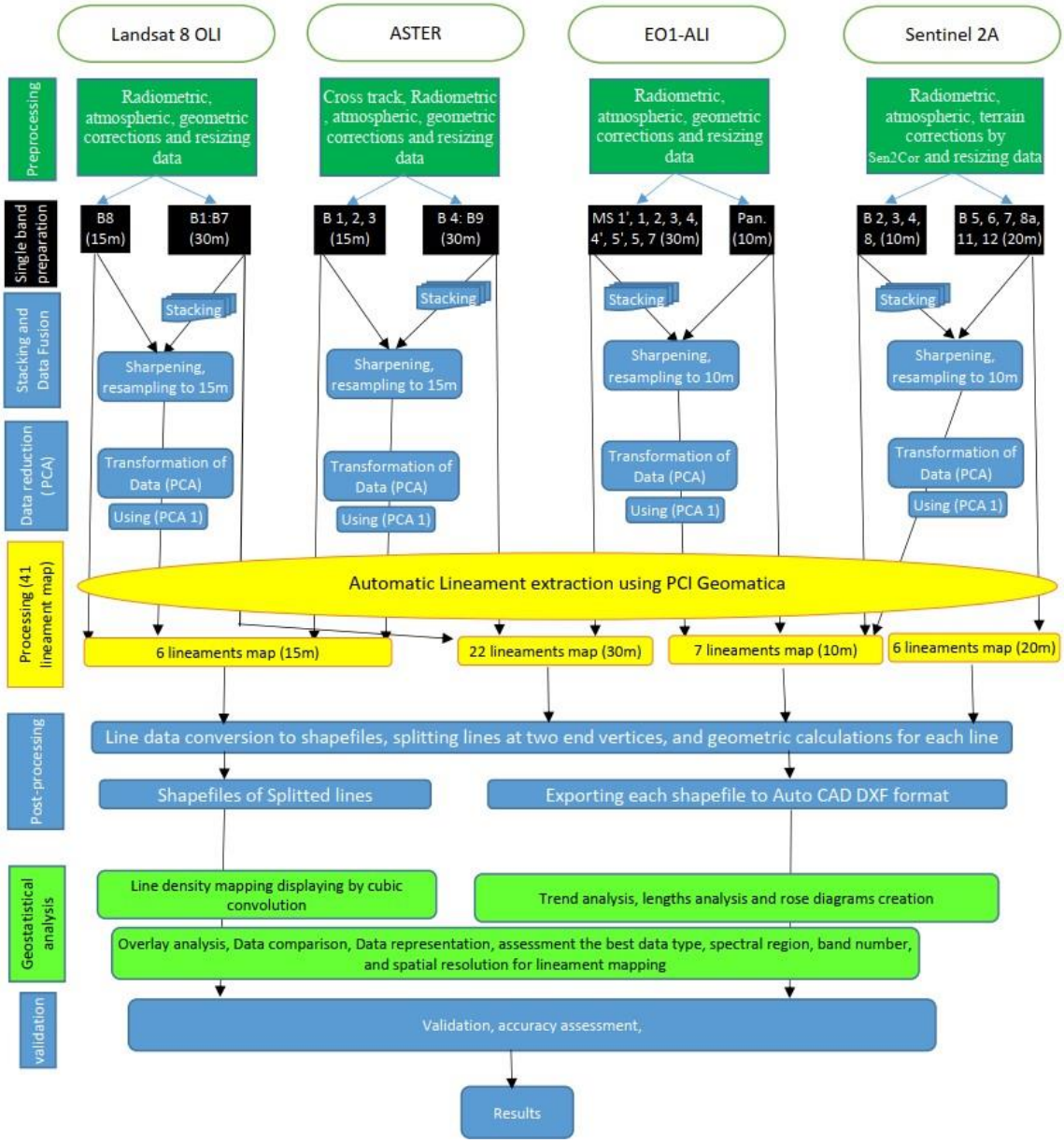
Appendix 4-10: Field photographs showing a) Wadi deposits and Gabal Um Salatit serpentinites at the background, b) Wadi deposits and Gabal Um Salim serpentinites, c) thrusting contact between serpentinites and volcaniclastic metasediments, d) highly deformed volcaniclastic metasediments, e) metagabbro diorite, and f) and g) talc carbonate rocks.



Appendix 4-11: Field photographs showing a) Wadi deposits (WD), volcaniclastic metasediments (VMs), and serpentinites (Sp), b) Wadi deposits (Wd) and Metavolcanics (MVs), c) highly deformed volcaniclastic metasediments (VMs), d) small blocks of Talc carbonate rocks (Tc) within highly deformed volcaniclastic metasediments representing the ophiolitic mélange, e) serpentinites (Sp) and their related Talc carbonate rocks (Tc), f) Metavolcanic (MVs) tuffs and, g) Nearly vertical volcaniclastic metasediments (VMs).



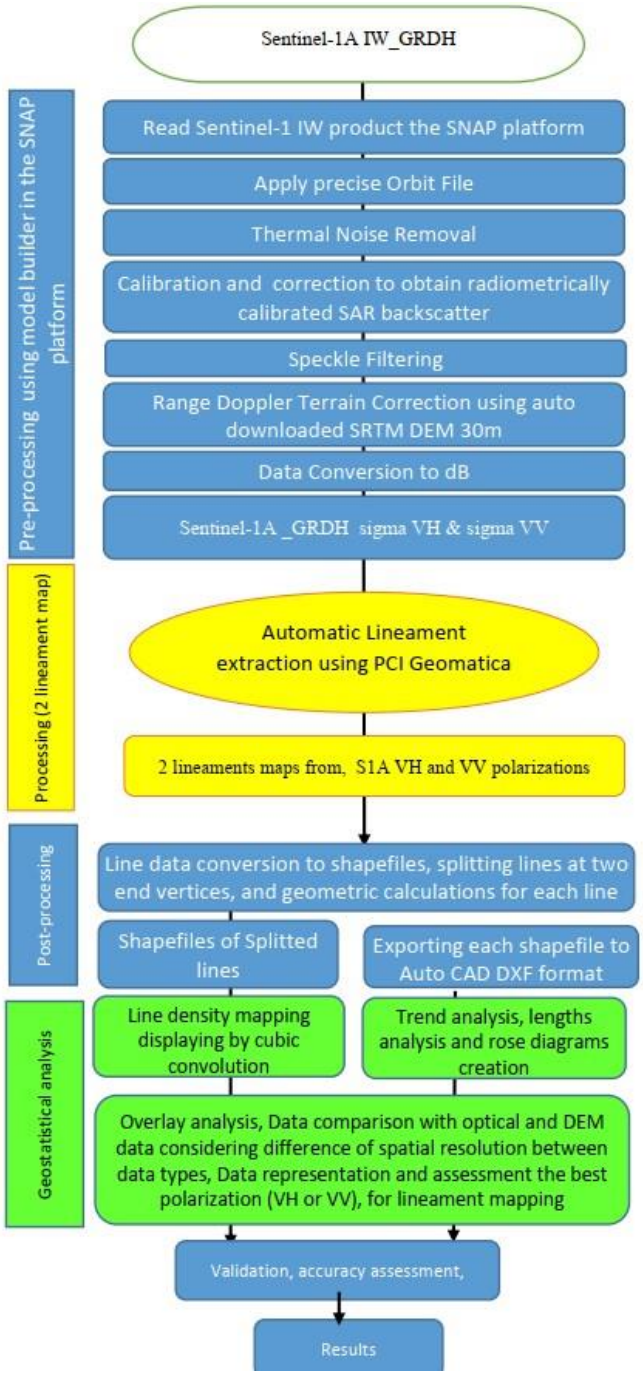
Appendix 4-12: Photomicrograph representing ophiolitic Serpentinite and their associated talc carbonates and shows a) Veins of carbonate minerals (see the arrows) cut through antigorite aggregates of fibrolamellar structure in serpentinite, C.N., and b) Opaque minerals (magnetite or chromite) resulting from the alteration of cracked olivine and /or orthopyroxene into fine-grained serpentine minerals which replaced by talc and carbonate minerals, C.N. Photomicrographs of metavolcanics showing c) metaandesite consists of fine-grained plagioclase and hornblende and dissected by veinlets of carbonate and opaque minerals, C.N., d) metarhyolite shows a porphyritic texture and consists of quartz, orthoclase and plagioclase phenocrysts in a groundmass of the same constituents, and e) Andesitic metatuffs shows plagioclase with few quartz crystal fragments embedded in a fine-grained andesitic groundmass, C.N. f) Tremolite-actinolite replaces hornblende and pyroxene in metagabbro, C.N.



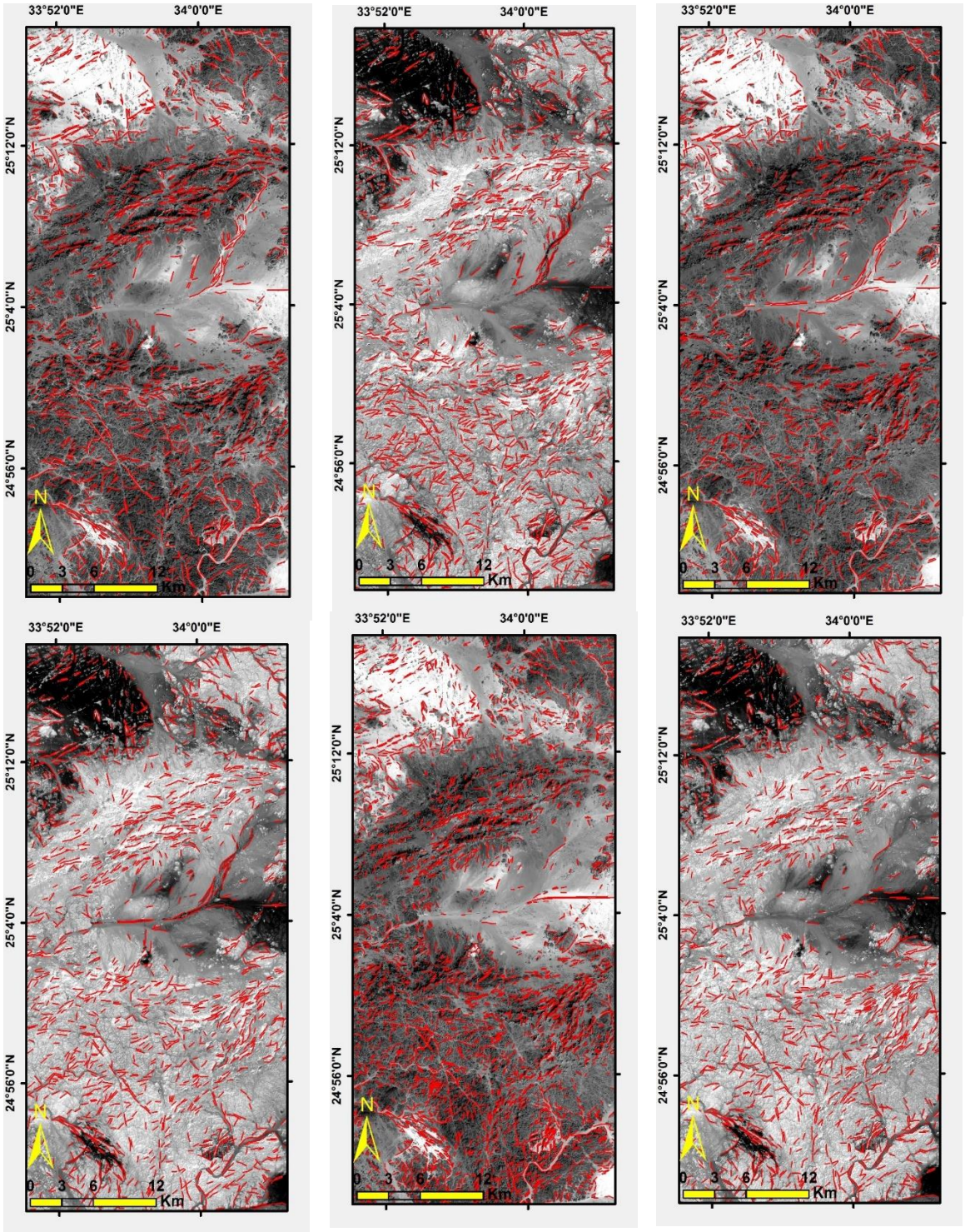
Appendix 4-13: The methodology flowchart of optical multi spectral datasets utilized in current study.



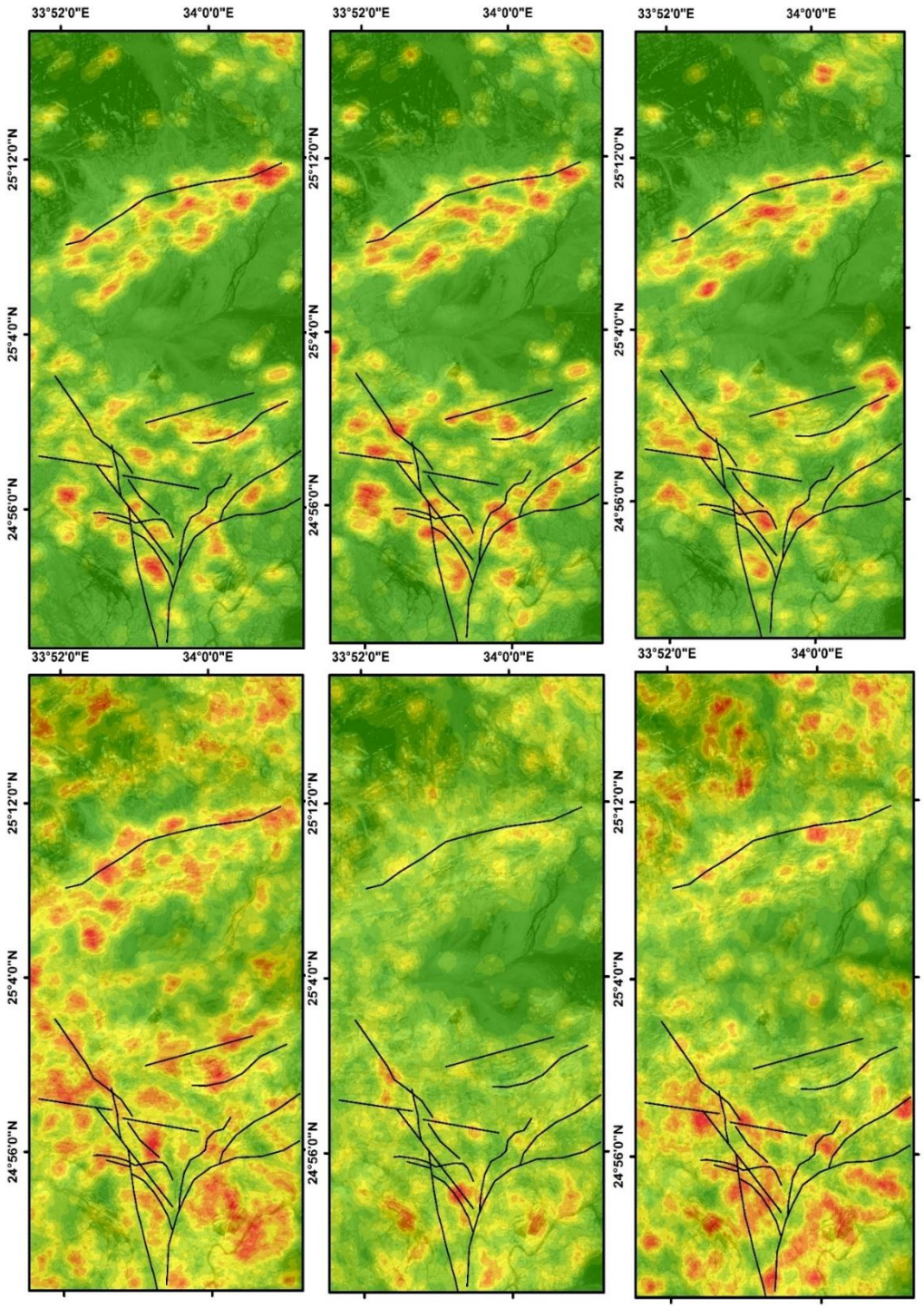
Appendix 4-14: The methodology flowchart of DEMs utilized in current study.



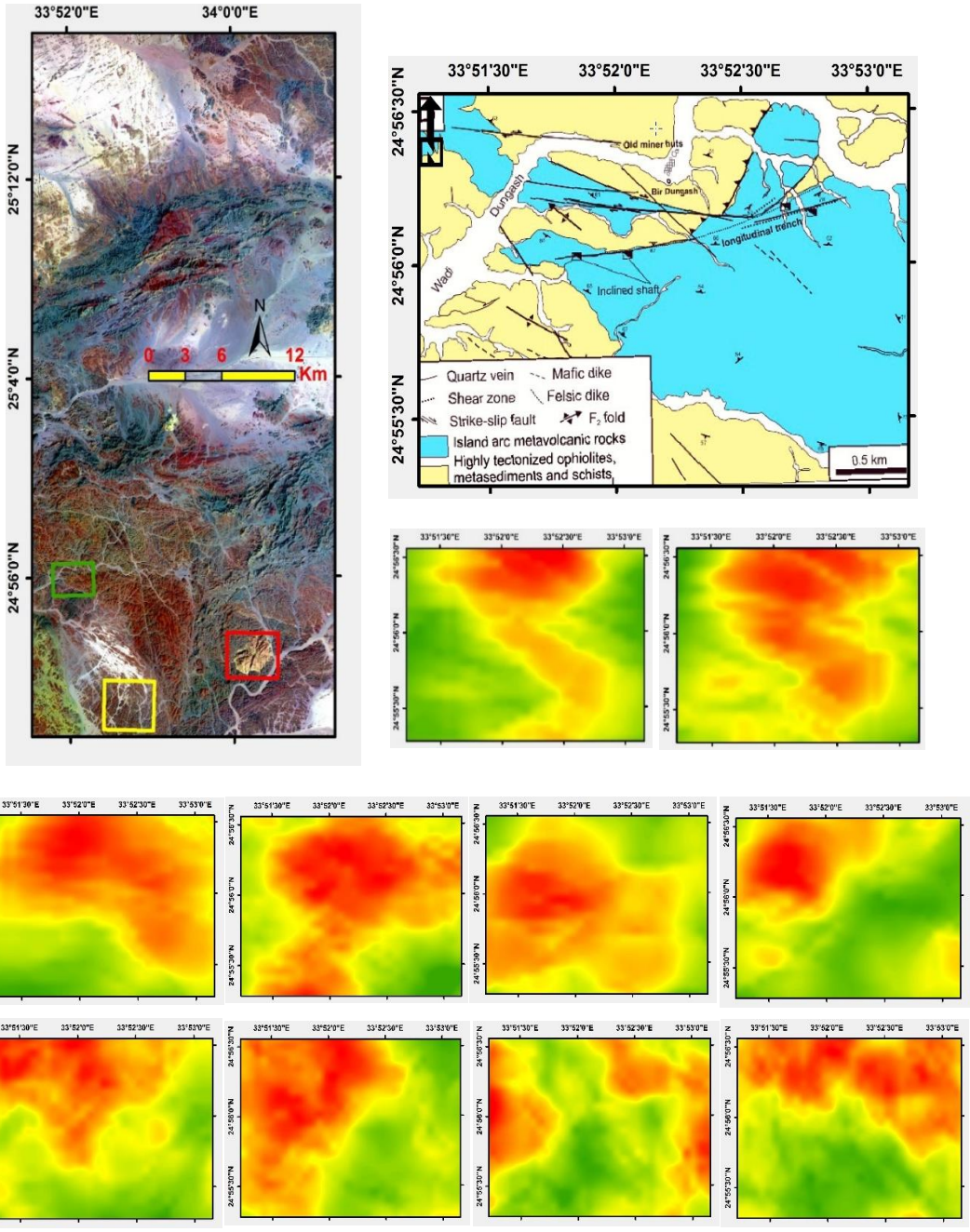
Appendix 4-15: The methodology flowchart of Sentinel 1 data utilized in the current study.



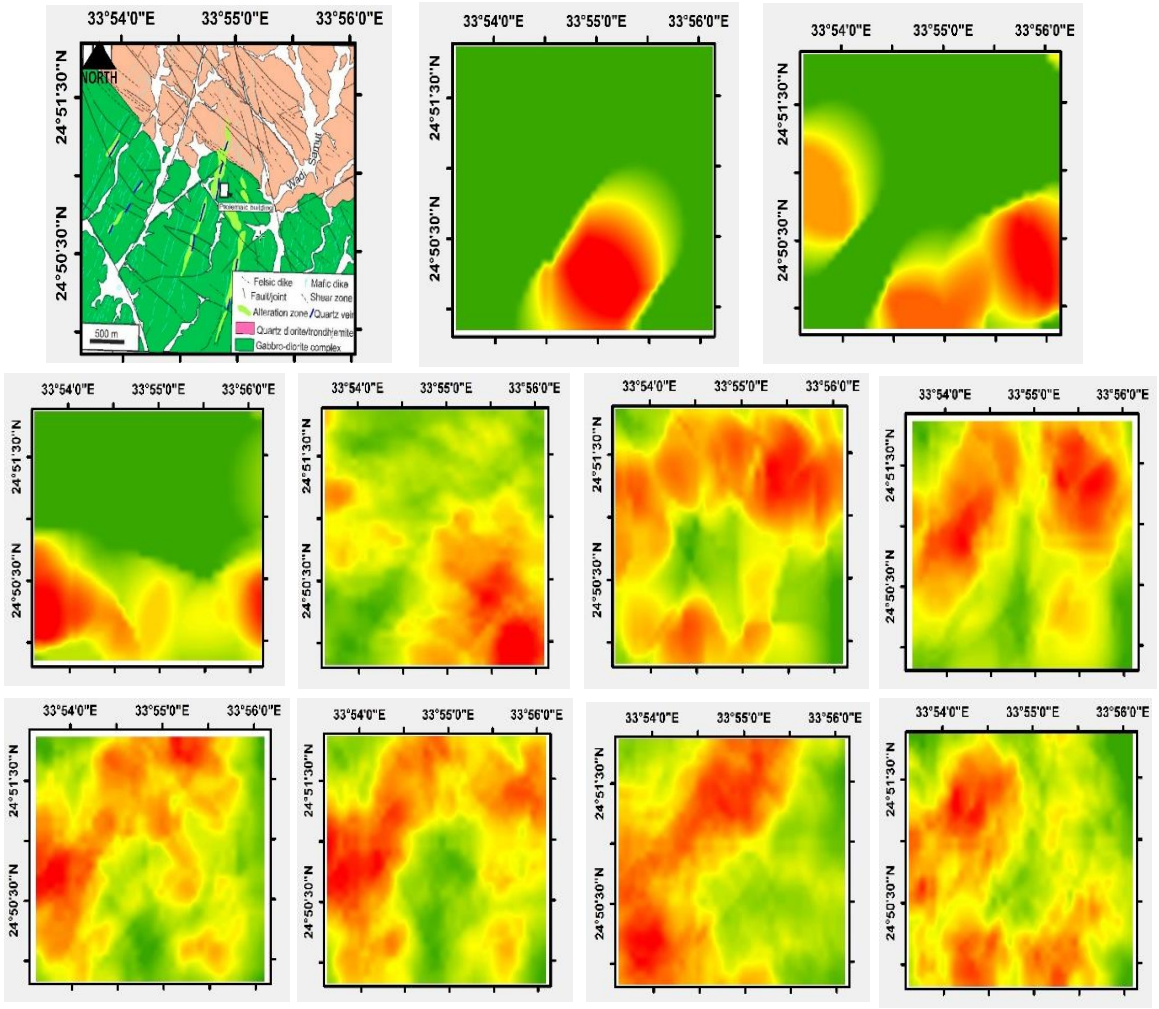
Appendix 4-16*:* Grey scale images of (**a**) L8 b8, (b) PCA1 of L8 bands, (c) ASTER b3, (d) PCA1 of ASTER bands, (e) Panchromatic EO1 and (f) PCA1 of EO1 bands superimposed by automatically derived lineaments from each of them.



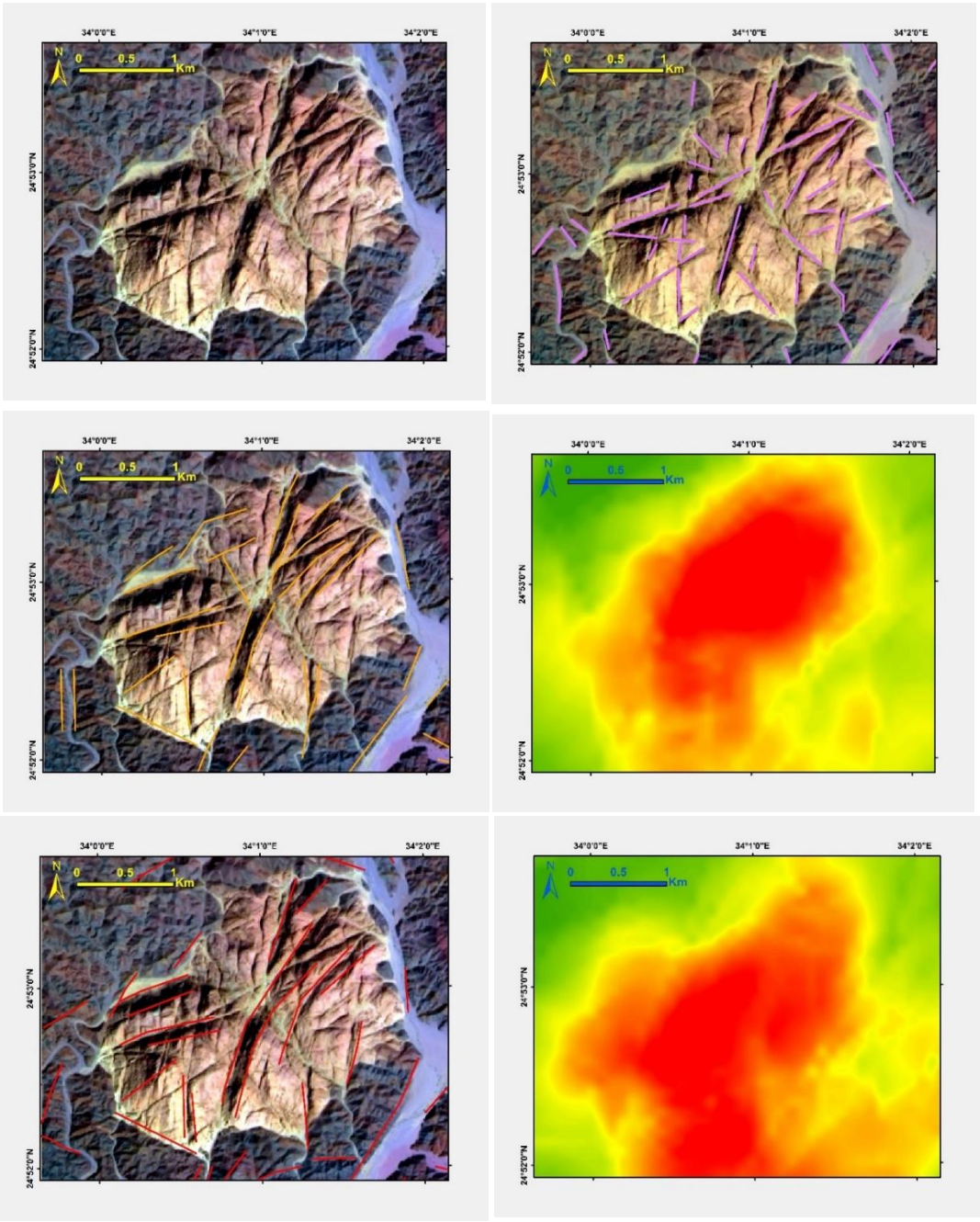
Appendix 4-17: The density maps of lineaments extracted from 30m DEMs (**a**) SRTM, (**b**) NASA, (**c**) ASTER v3, 12.5m data (**d**) ALOS PALSAR, 10m pixel size of (**e**) S1 VH, and (**f**) S1 VV, overlain by manually digitized faults from geological map.



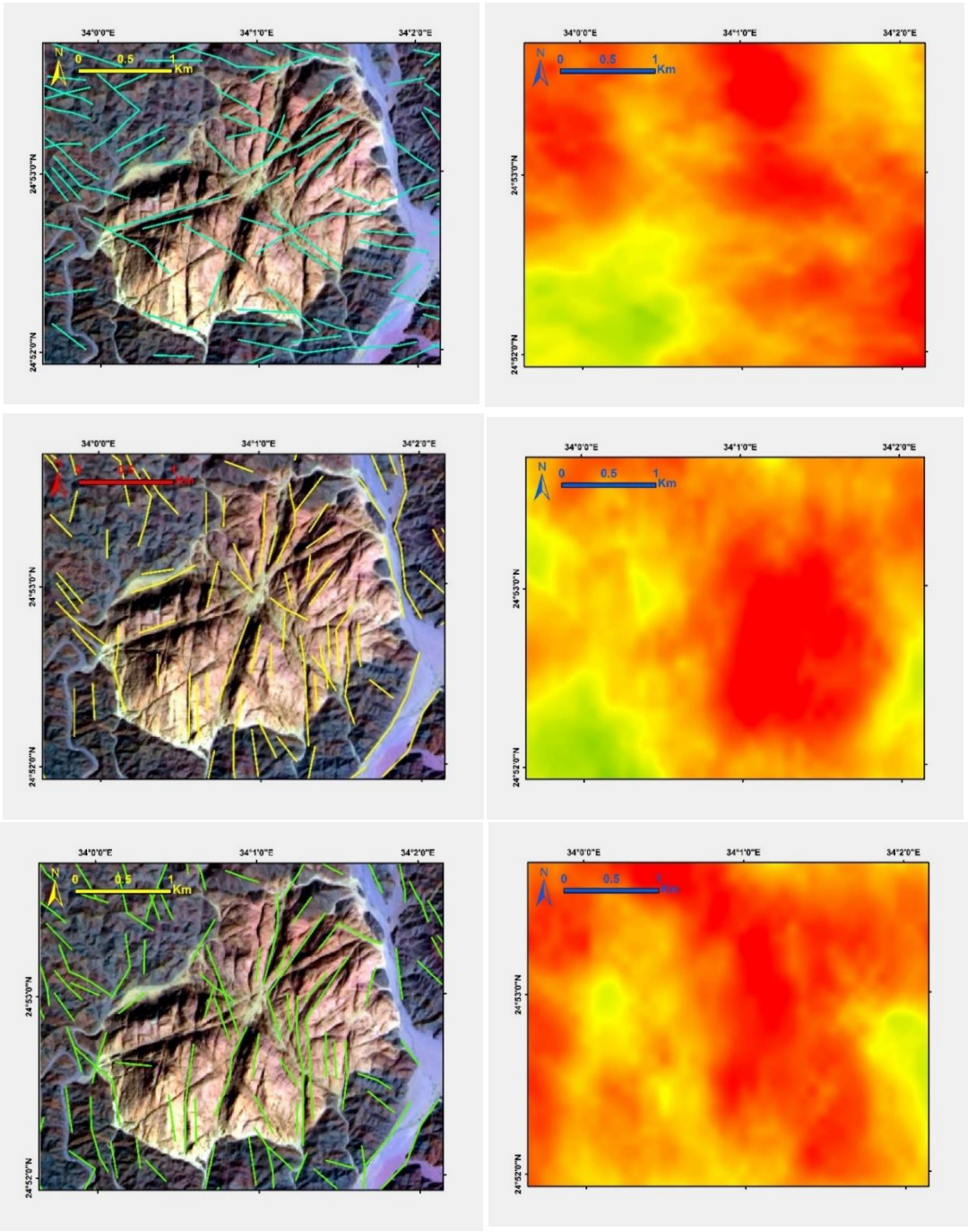
Appendix 4-18*:* (a) 752 RGB L8 composite as a location map for the three selected test areas (green box is Dungash, yellow box is Samut and red box is Mueilha). The coincidence between lineaments over (b) Dungash geologic map() and density maps of lineaments derived from (c) SRTM, (d) NASA, (e) ASTER v3, 12.5m data (f) ALOS PALSAR, 20 m (g) S2 b5, 15 m (h) L8 b8, , 10m pixel size of (i) panchromatic EO1, (j) S2 b2 , (k) S1 VH, and (l) S1 VV, is evident. More specifically, the northern part of the geologic map is highly dissected with linear structures that is well-reflected as higher density red areas nearly from all the various data sources implemented in this study.



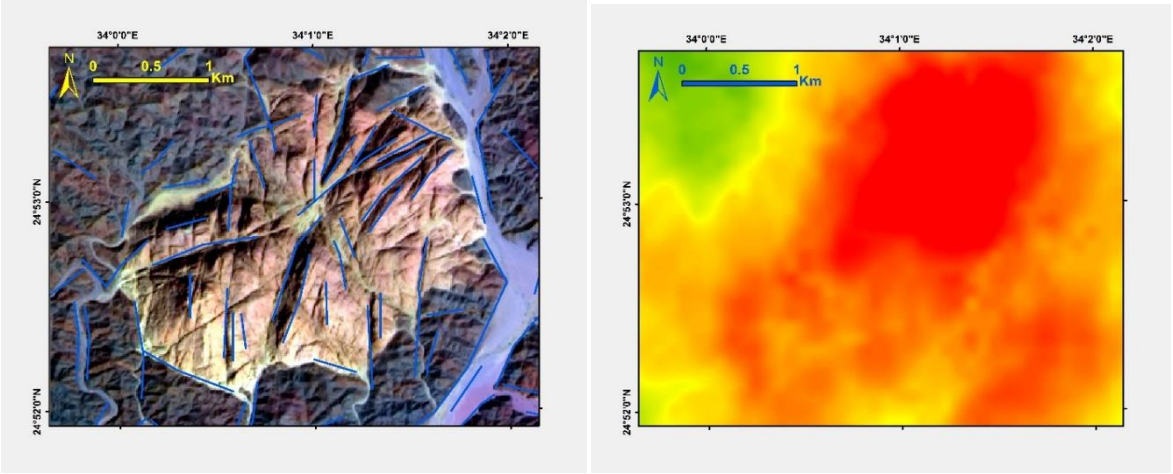
Appendix 4-19: The coincidence between lineaments over (a) Samut geologic map() and density maps of lineaments derived from (**b**) SRTM, (**c**) NASA, (**d**) ASTER v3, 12.5m data (**e**) ALOS PALSAR, 20 m (**f**) S2 b5, 15 m (**g**) L8 b8, , 10m pixel size of **(h**) panchromatic EO1, (**i**) S2 b2 , (**j**) S1 VH, and (**k**) S1 VV, is evident. Moreover, 30m resolution DEMs have a poor power to extract lines in low elevation areas as shown in the northern parts of (b, c, and d), however all the optical and radar data extract lineaments efficiently and achieved a reasonable matching percent with lineaments over the geologic map.



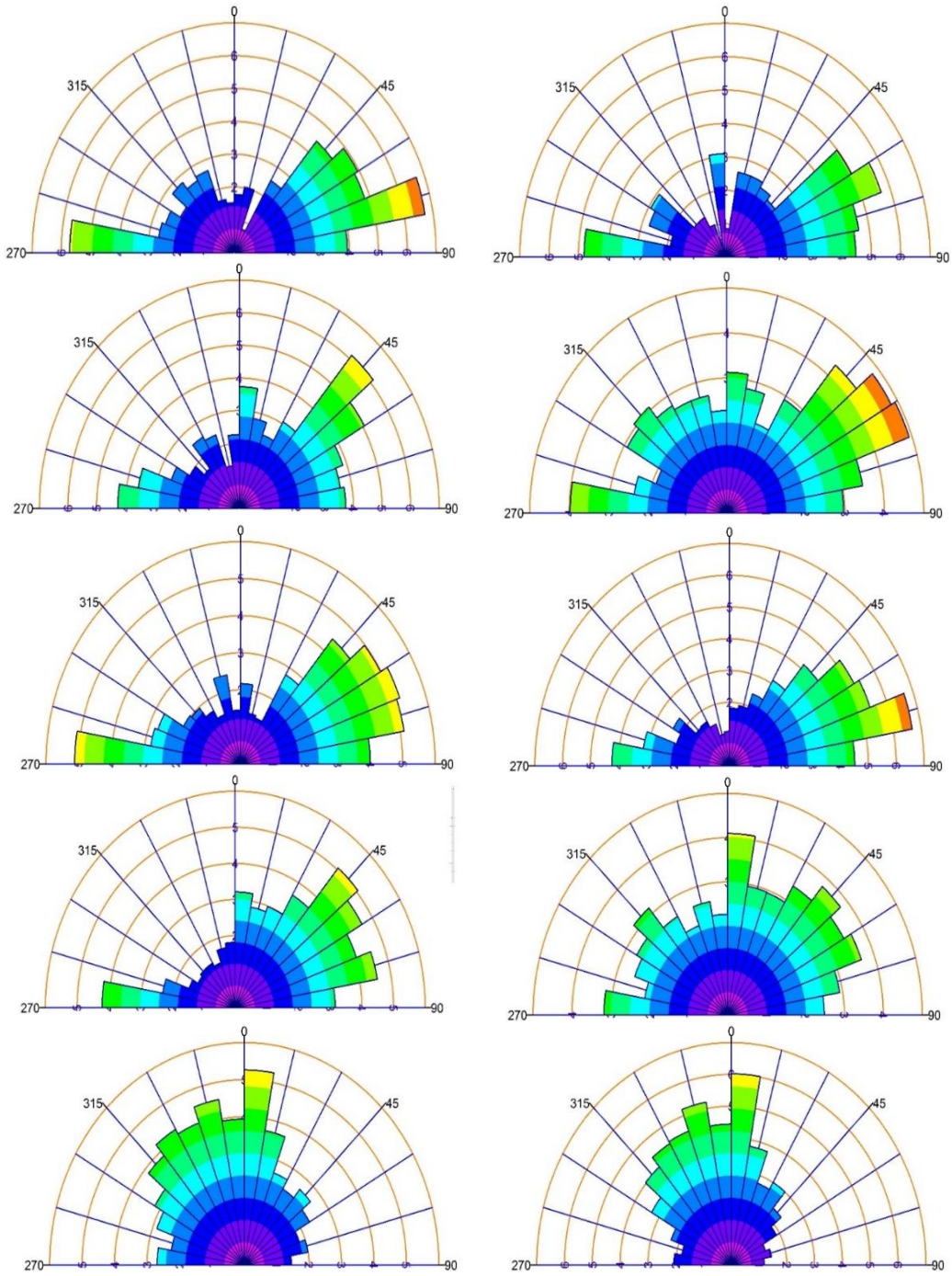
Appendix 4-20: (a) EO1 pan-sharpened 10m RGB 752 of Gabal Mueilha perfectly showing variably trending lineaments, (b) manually digitized lines over Gabal Mueilha. Automatically extracted lineaments from (c) L8 b8 and its density (d), and from (e) ASTER b3 and its density (f), dropped over the area showing outstanding matching with the real visually interpreted lines.



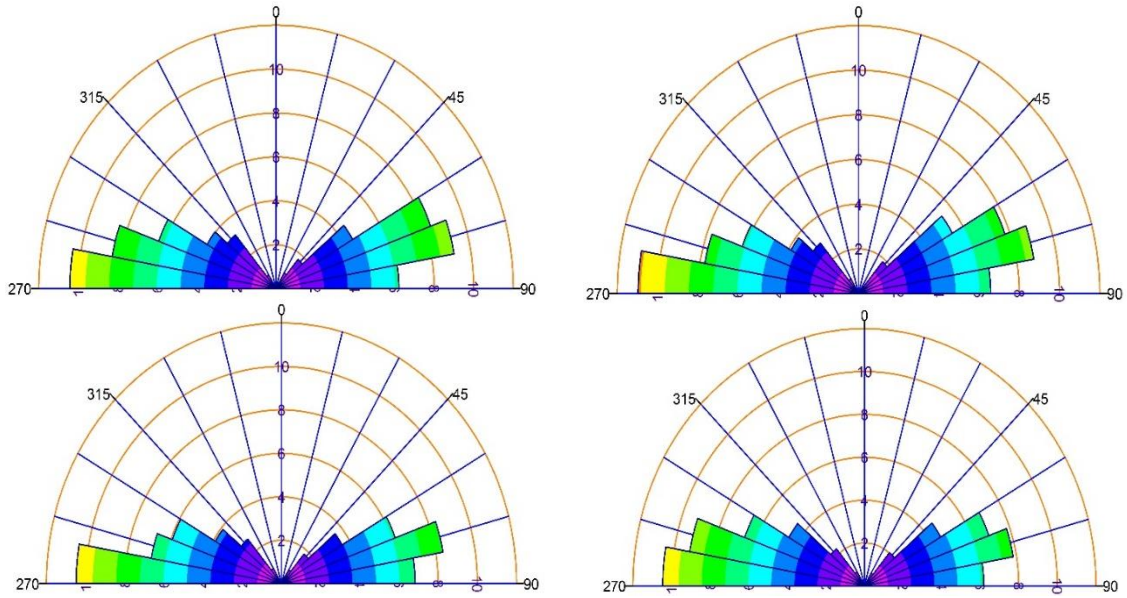
Appendix 4-21: (a) Automatically extracted lineaments from (a) ALOS PALSAR DEM and its density (b), and from (c) S1 VH and its density (d), (e) S1 VV and its density (f), dropped over the area showing outstanding matching with the real visually interpreted lines as well as dominance of red color in density maps (high density areas).



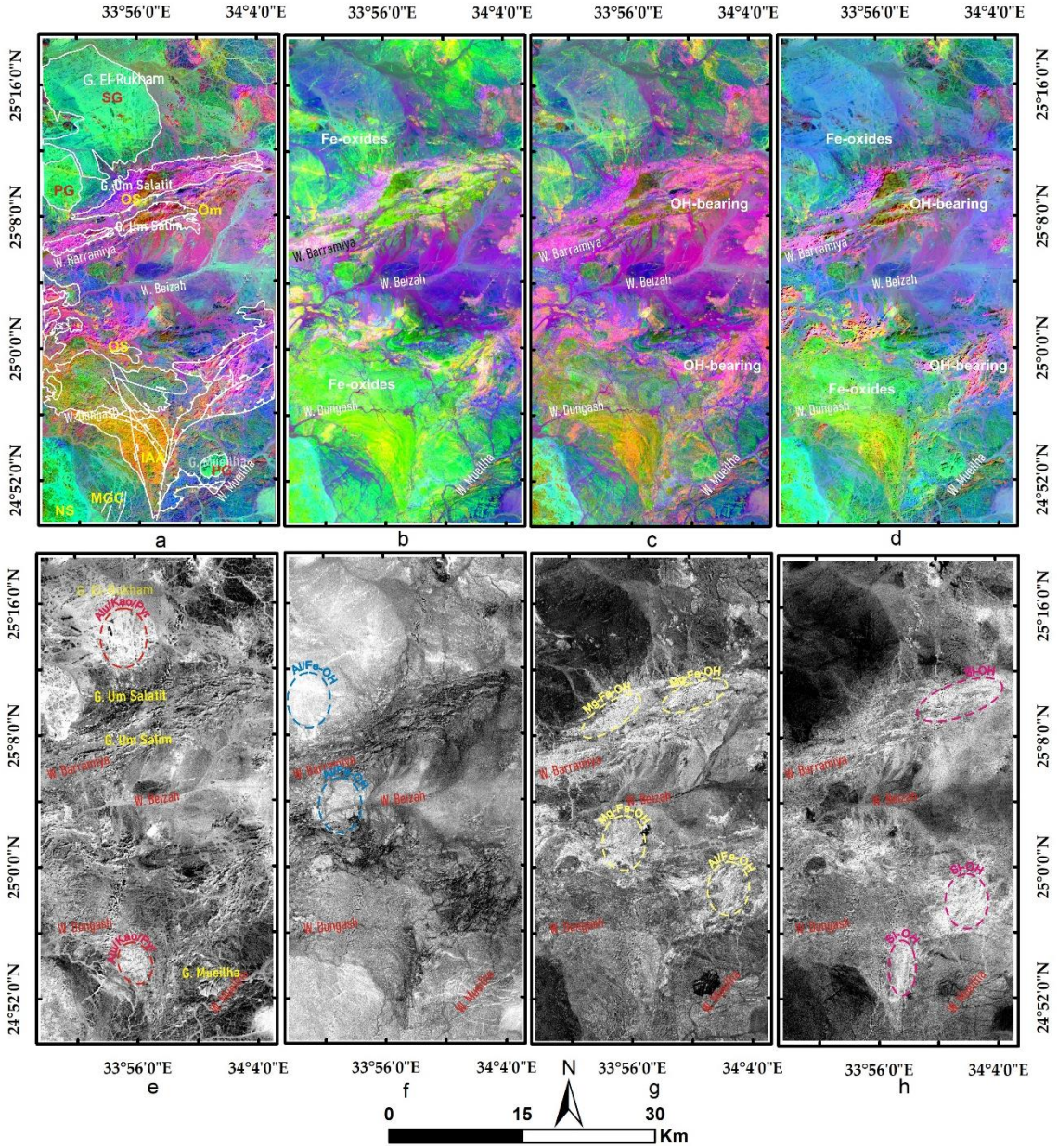
Appendix 4-22: **a**) Automatically extracted lineaments from (a) S2 b2 and its density (b), dropped over the area showing outstanding matching with the real visually interpreted lines.



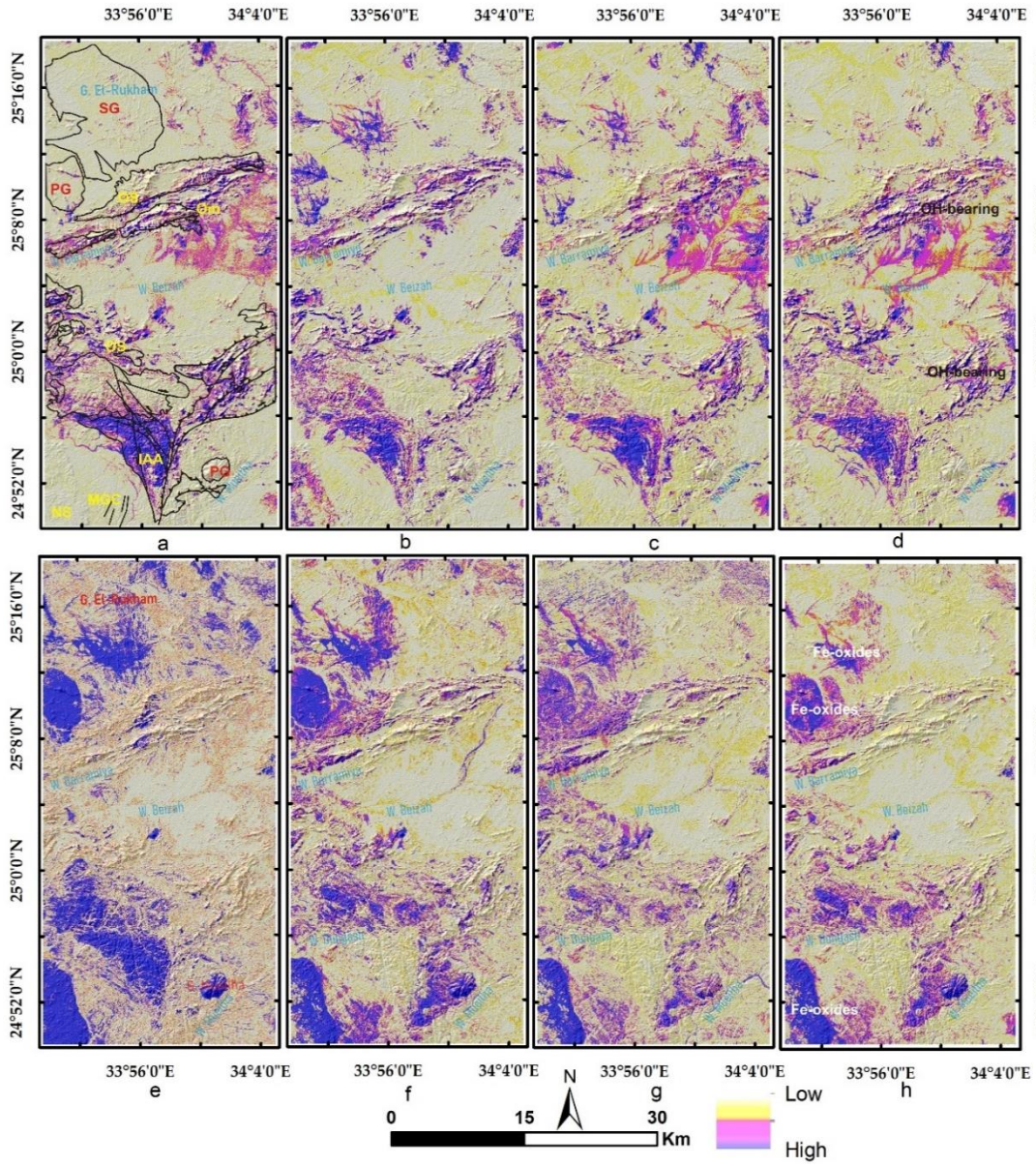
Appendix 4-23: Rose diagrams showing the orientations of lineaments extracted at 30m from (a) L8 b4, (b) ASTER b6, (c) EO1 b5, at 20 m from (d) S2 b5, at 30m from (e) L8 b8, (f) ASTER b3, and at 10m from (g) panchromatic band of EO1, (h) S2 b2, (i) S1 VH, and (j) S1 VV.



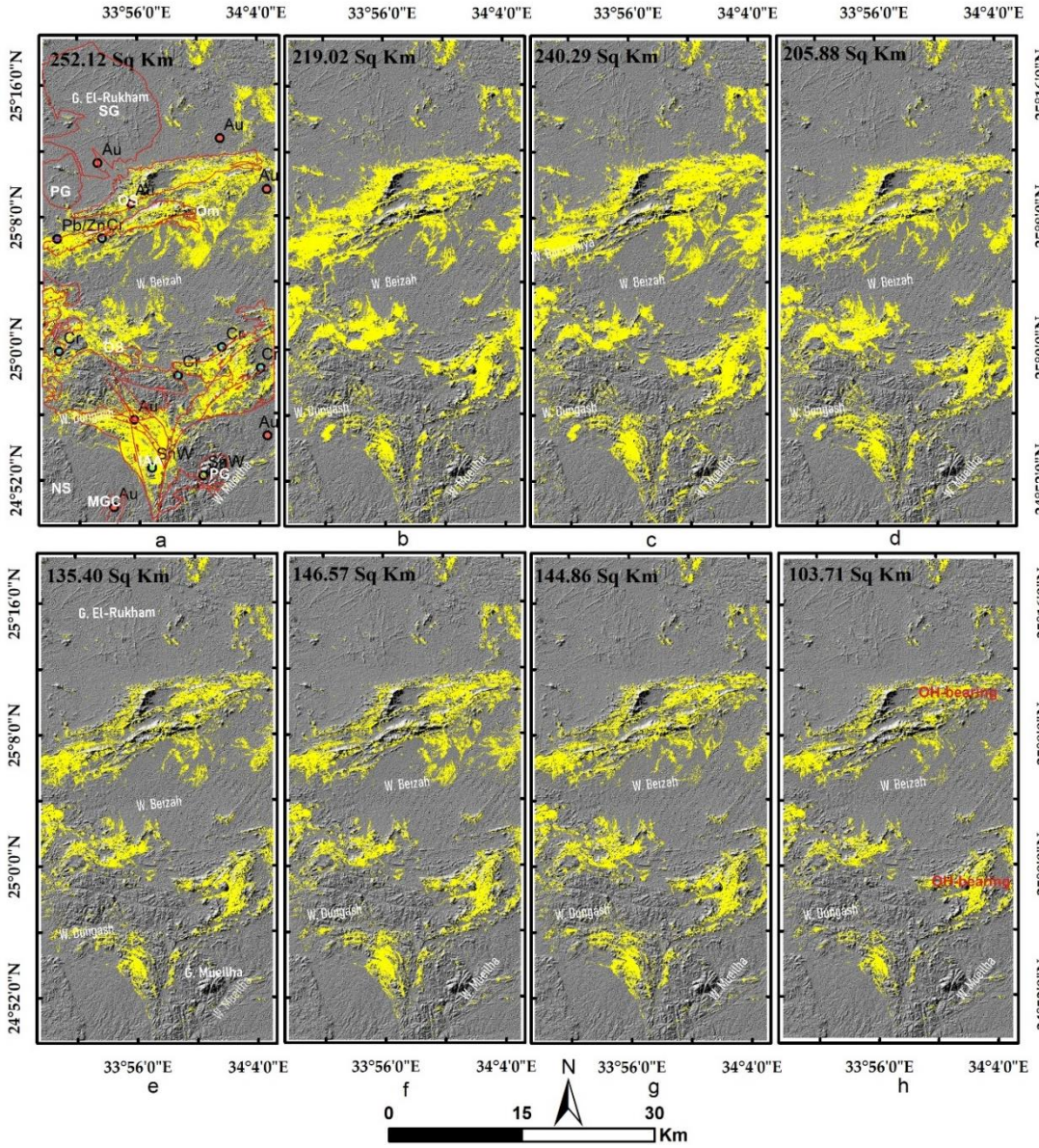
Appendix 4-24: Rose diagrams showing the orientations of lineaments extracted at azimuth (0) and altitude (30) from (a) SRTM, (b) NASA, (c) ASTER v3, and (d) ALOS PALSAR DEMs.



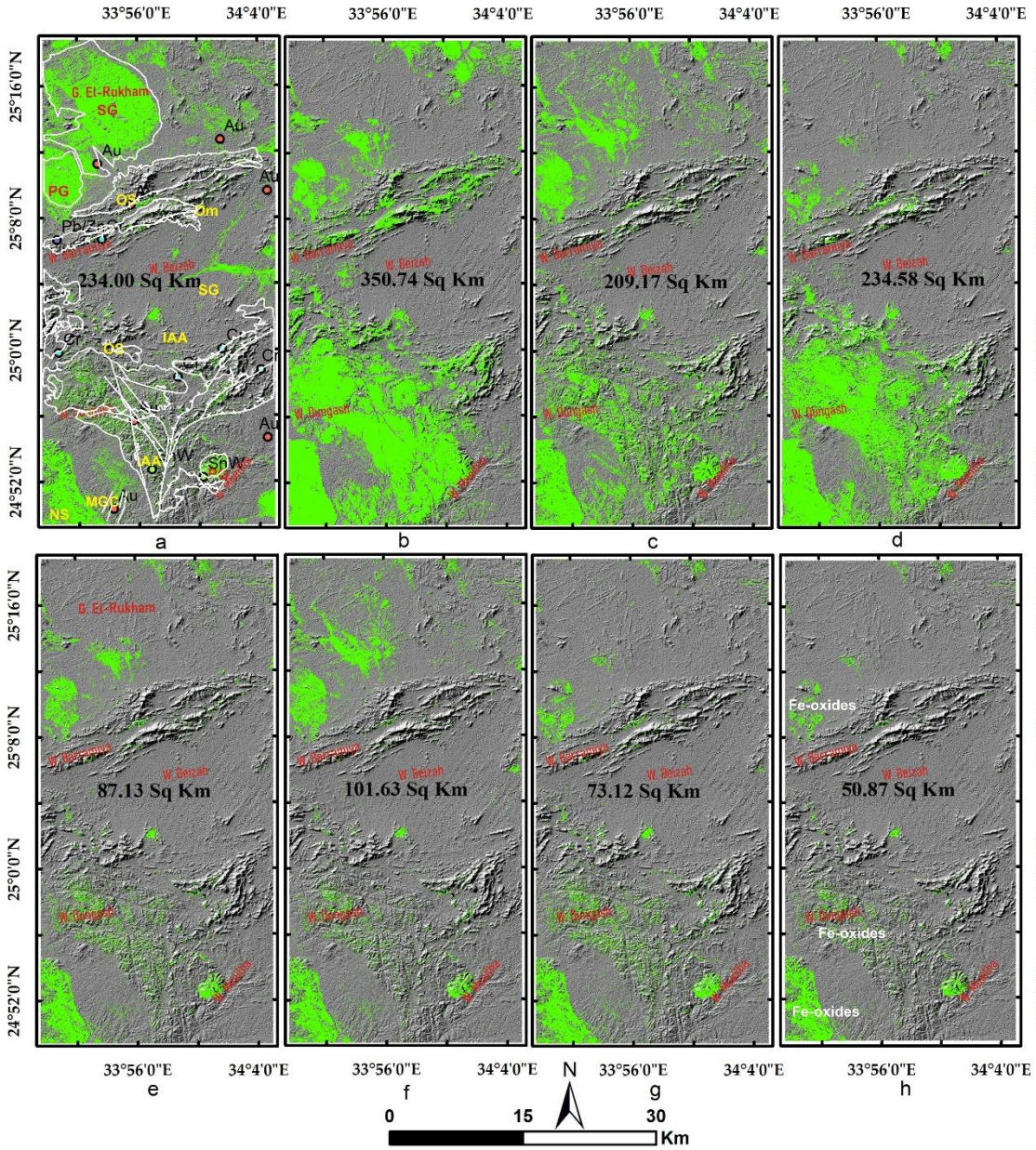
Appendix 4-25: Depiction of the general hydrothermal alterations using combinations of (a) ASTER, (b) Landsat 8, (c) Sentinel 2 and (d) ALI. Relative absorption band depth (RBD) results for highlighting (e) Alunite/Kaolinite/Pyrophyllite, (f) Al/Fe-OH, (g) Mg-Fe-OH and (h) Si-OH bearing rocks as bright pixels.



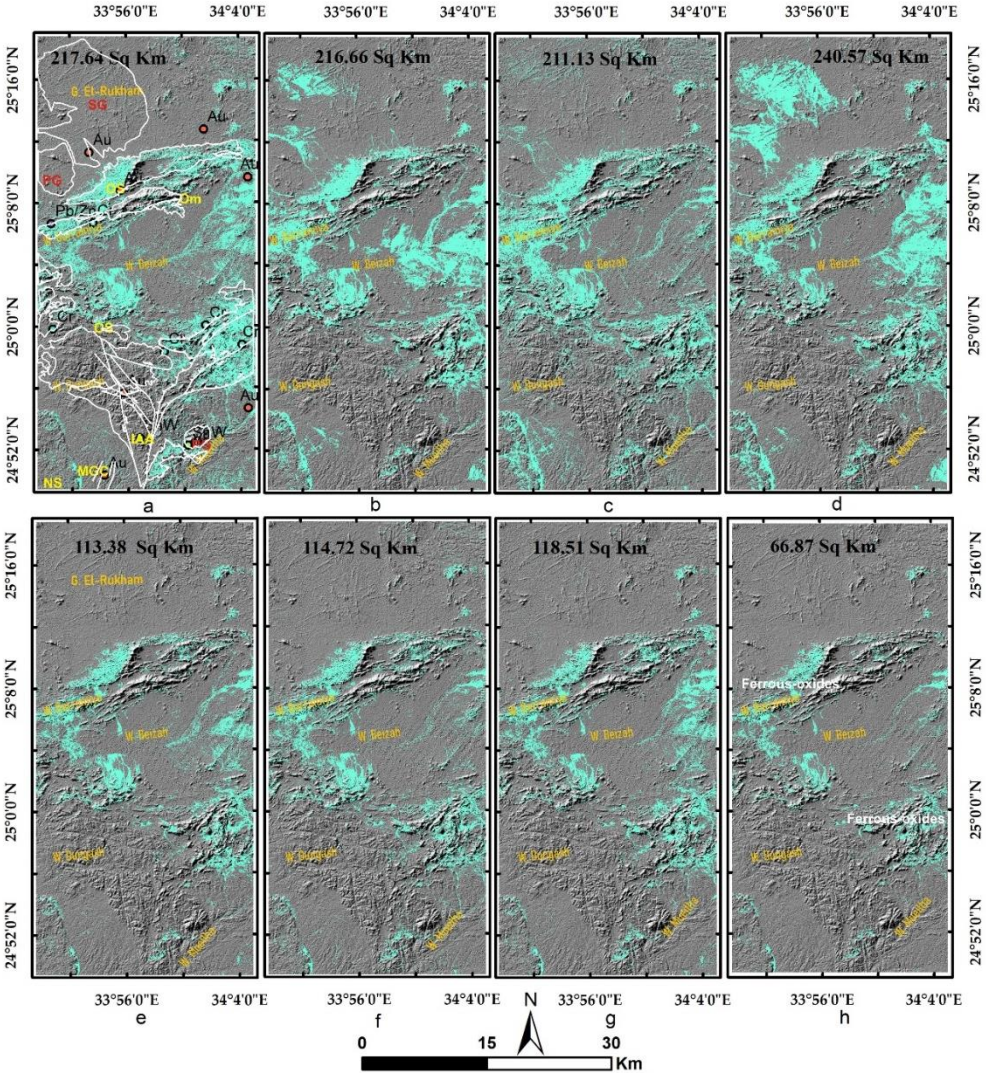
Appendix 4-26: Pseudocolor ramps representing rule images of (a) ASTER DPC4, (b) Landsat 8 DPC3, (c) Sentinel 2 DPC4 and (d) ALI DPC3 showing rocks enriched with hydroxyl-bearing minerals. Pseudocolor ramps representing rule images of (e) ASTER DPC2, (f) Landsat 8 DPC3, (g) Sentinel 2 DPC3 and (h) ALI DPC3 showing iron oxides' bearing rocks.



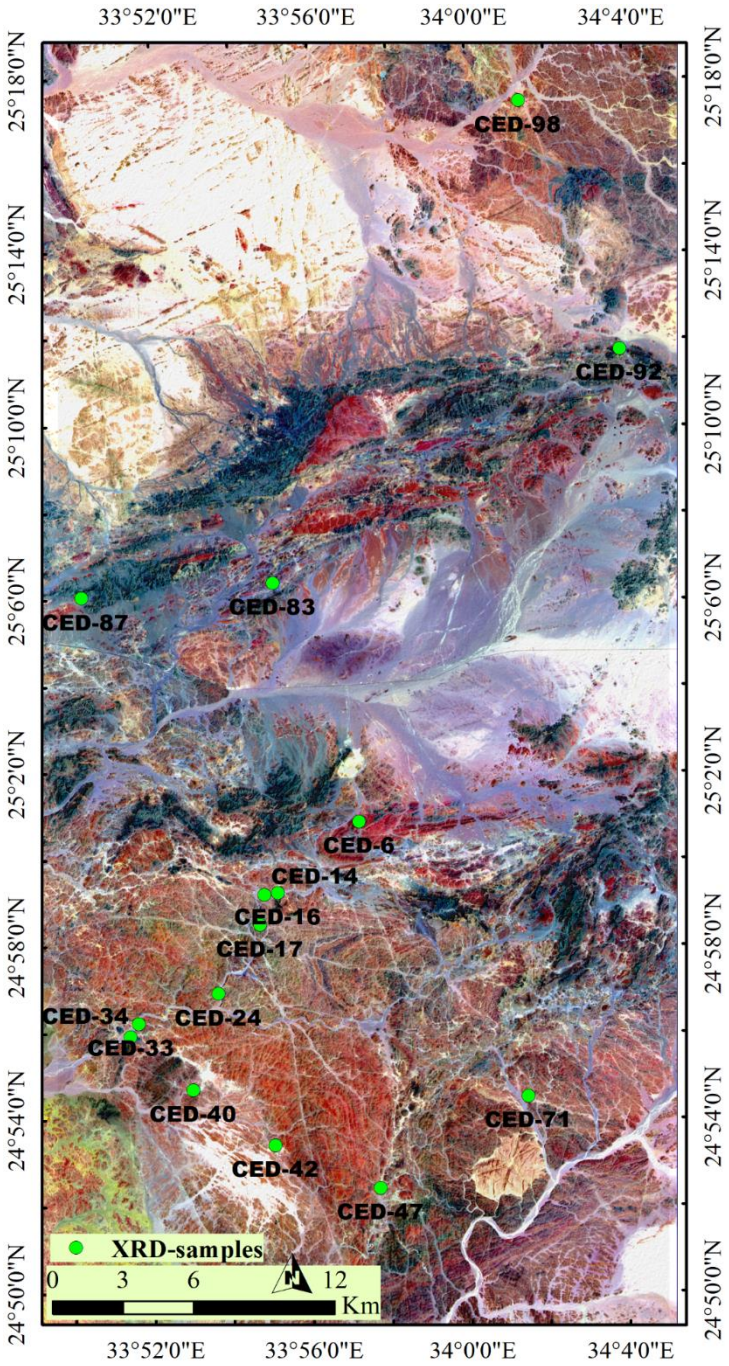
Appendix 4-27: Areal differences of the rocks enriched with hydroxyl-bearing minerals (yellow color) detected utilizing (a) ASTER, (b) Landsat 8, (c) Sentinel 2, and (d) ALI. Intersected results using (e) ASTER and Landsat 8, (f) ASTER and Sentinel 2, (g) ASTER and ALI, and (h) the four sensors dropped over shaded relief map.



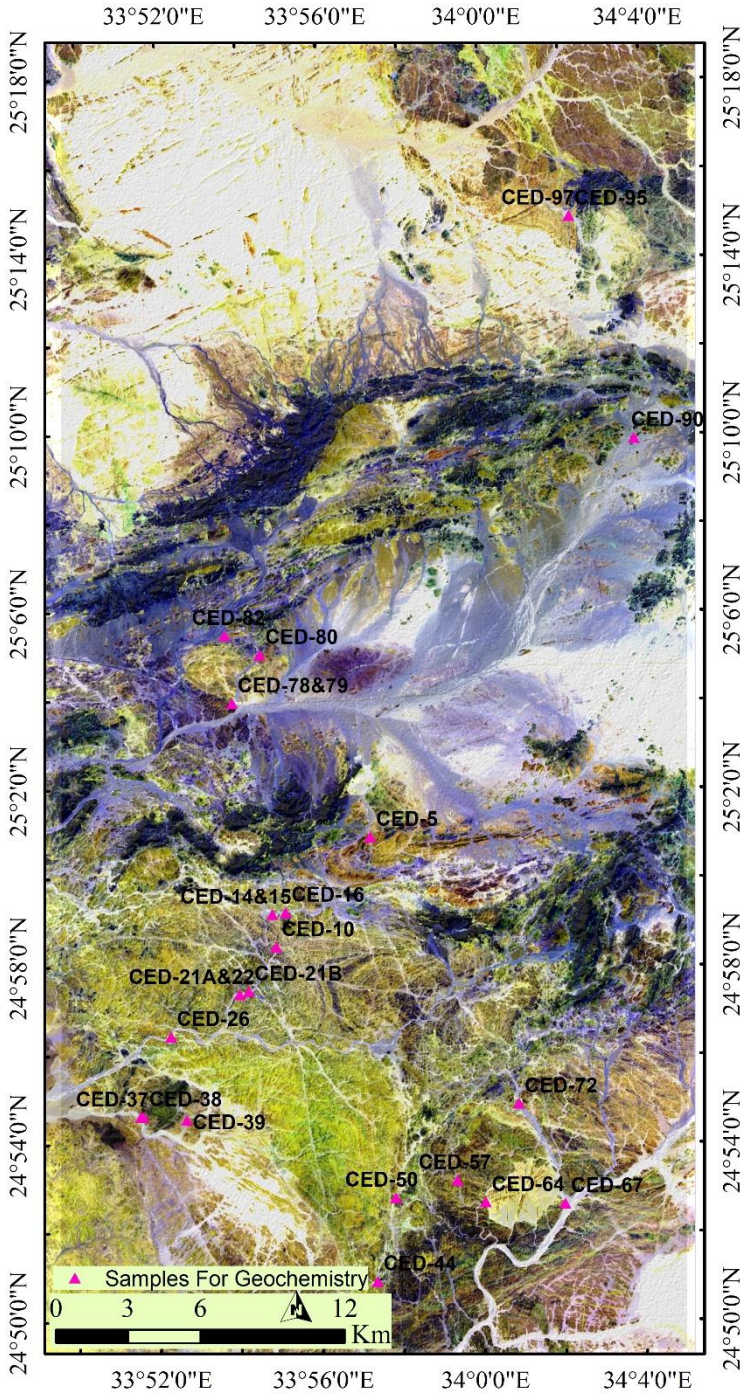
Appendix 4-28: Areal differences of iron oxides-bearing rocks (green color) detected utilizing (a) ASTER, (b) Landsat 8, (c) Sentinel 2, and (d) ALI. Intersected results using (e) ASTER and Landsat 8, (f) ASTER and Sentinel 2, (g) ASTER and ALI, and (h) the four sensors dropped over shaded relief map.



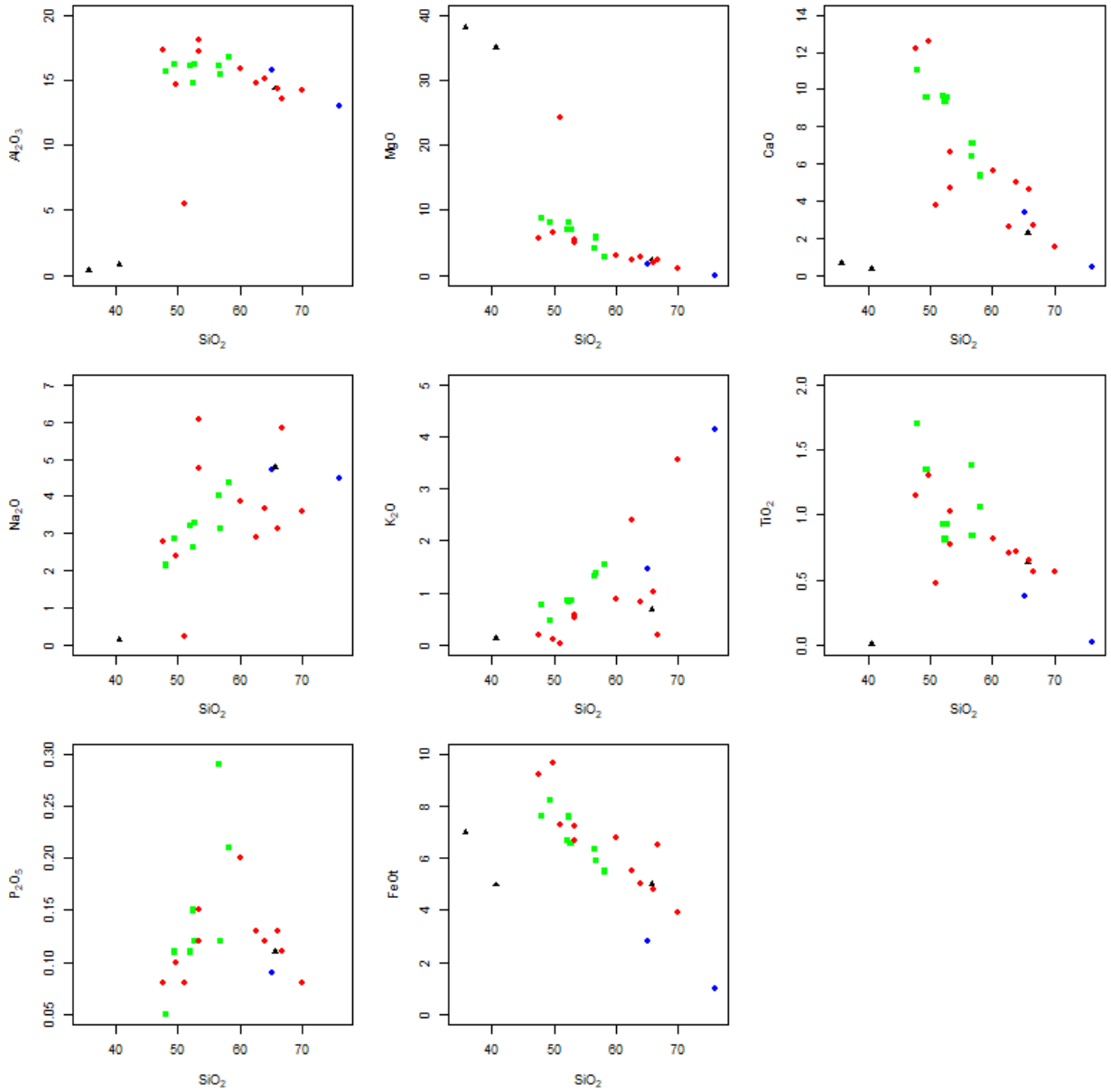
Appendix 4-29: Areal differences of ferrous oxides' bearing rocks (cyan color) detected utilizing (a) ASTER, (b) Landsat 8, (c) Sentinel 2, and (d) ALI. Intersected results using (e) ASTER and Landsat 8, (f) ASTER and Sentinel 2, (g) ASTER and ALI, and (h) the four sensors dropped over shaded relief map.



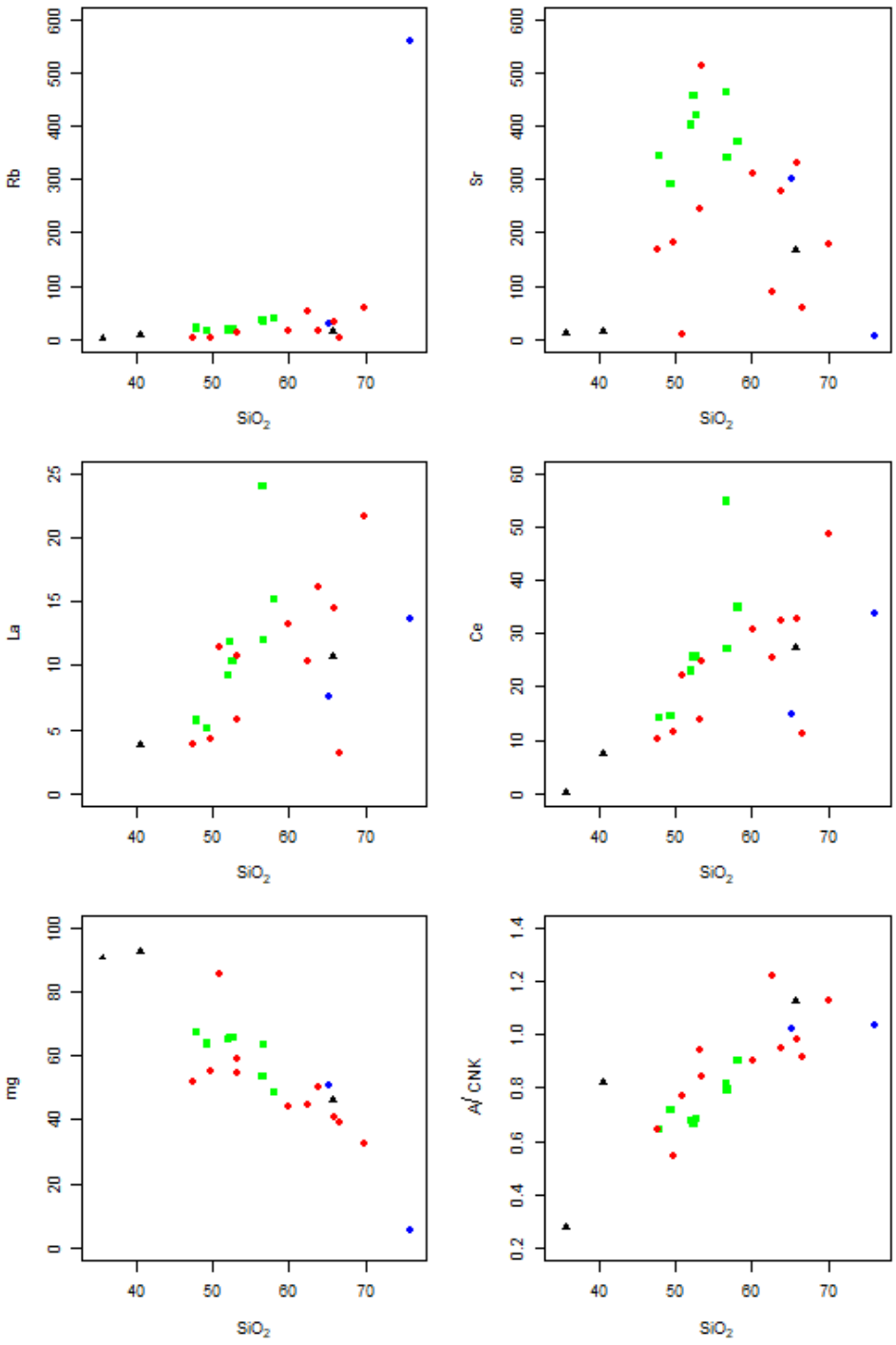
Appendix 4-30: RGB Representation of FCC 12-6-2 showing the Distribution of the analyzed samples through XRD.



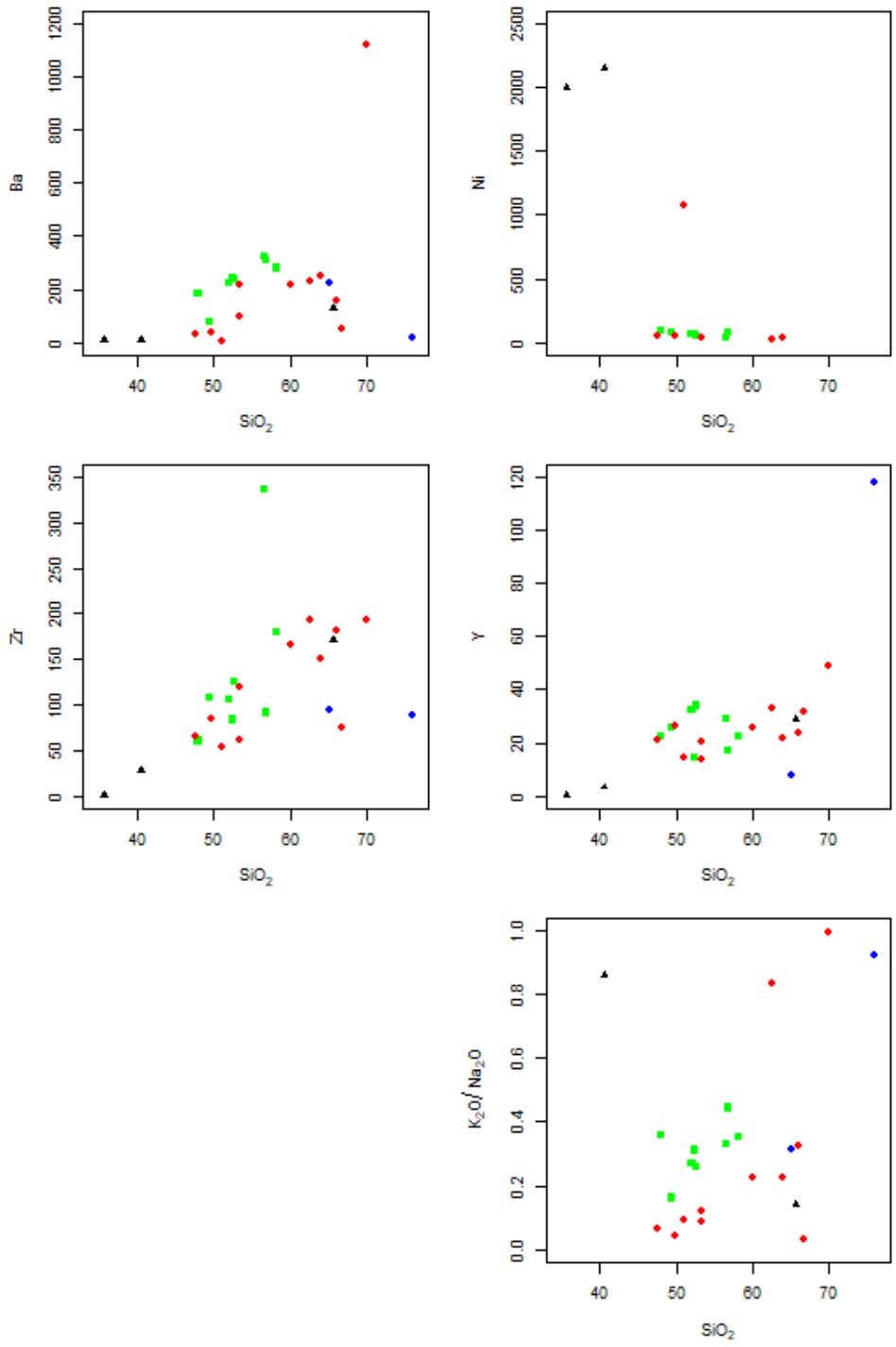
Appendix 4-31: RGB Visualization of FCC 12-11-2 highlighting the distribution of samples with geochemical analysis.



Appendix 4-32: Harker variation diagram of some major oxides versus SiO2 for the studied rocks. metagabbro (green), metavolcanics(red), serpentinite (black) and granite (blue).



Appendix 4-33: Trace elements Harker variation diagrams for the analyzed rocks.



Appendix 4-33: Continued.

Tables

Table 1: The values and practical tasks for the LINE module parameters.

Edge detection	RADI	to detect contours efficiently	10	pixels
	GTHR	to determine the pixels value considered as edges	50	-
Curve extraction	LTHR	To omit shorter curves having number of pixels lower than LTHR value	30	pixels
	FTHR	To generate polylines fitting FTHR value	3	pixels
	ATHR	Linking polylines with end point angle coinciding with ATHR	15	degree
	DTHR	Joining polylines whose endpoints respect DTHR value	20	pixels

Table 2: Training and testing data, and abbreviations of the lithological classes.

Lithological Unit	**Training pixels**	**Testing pixels**
Ophiolitic Serpentinite (Sp)	718	343
Talc carbonate (Tc)	470	197
Metavolcanics (Mvs)	627	253
Metagabbro-Diorite (MGD)	189	99
Volcaniclastic metasediments (VMs)	633	293
Syn-orogenic granite (Gr)	615	248
Wadi Deposits (WD)	617	288

Table 3: Confusion matrices, overall and class-based statistics for RF, XGB, and SVM using 1-2pc PRISMA data.

RF	Sp	Tc	Mvs	MGD	VMs	Gr	WD	tot	precision	recall	f1-score
Sp	280	0	0	0	2	0	8	290	0.965517	0.816327	0.884676
TC	0	155	6	13	0	0	0	174	0.890805	0.786802	0.83558
MVs	1	37	163	44	21	7	1	274	0.594891	0.644269	0.618596
MGD	1	5	20	41	1	0	0	68	0.602941	0.414141	0.491018
VMs	52	0	43	1	180	0	114	390	0.461538	0.614334	0.527086
GR	1	0	11	0	22	232	19	285	0.814035	0.935484	0.870544
WD	8	0	10	0	67	9	146	240	0.608333	0.506944	0.55303
total	343	197	253	99	293	248	288	1721	OA= 0.695		
Overall Assessment	Accuracy								0.695526	0.695526	0.695526
	Macro average								0.705437	0.674043	0.682933
	Weighted Average								0.714219	0.695526	0.69888

XGB	Sp	Tc	Mvs	MGD	VMs	Gr	WD	tot	precision	recall	f1-score
Sp	277	0	0	0	2	0	8	287	0.965157	0.80758	0.879365
TC	0	154	9	12	0	0	0	175	0.88	0.781726	0.827957
MVs	1	38	162	46	21	5	1	274	0.591241	0.640316	0.614801
MGD	3	5	19	41	1	0	0	69	0.594203	0.414141	0.488095
VMs	54	0	39	0	186	0	117	396	0.469697	0.634812	0.539913
GR	3	0	14	0	23	227	18	285	0.796491	0.915323	0.851782
WD	5	0	10	0	60	16	144	235	0.612766	0.5	0.550669
total	343	197	253	99	293	248	288	1721	OA= 0.692		
Overall Assessment	Accuracy								0.69204	0.69204	0.69204
	Macro average								0.701365	0.670557	0.67894
	Weighted Average								0.711474	0.69204	0.695308

SVM	Sp	Tc	Mvs	MGD	VMs	Gr	WD	tot	precision	recall	f1-score
Sp	272	0	0	0	0	0	7	279	0.97491	0.793003	0.874598
TC	0	158	2	30	0	0	0	190	0.831579	0.80203	0.816537
MVs	2	34	183	25	21	3	1	269	0.680297	0.72332	0.701149
MGD	1	5	8	44	0	0	0	58	0.758621	0.444444	0.56051
VMs	64	0	43	0	199	0	126	432	0.460648	0.679181	0.548966
GR	2	0	10	0	17	244	22	295	0.827119	0.983871	0.898711
WD	2	0	7	0	56	1	132	198	0.666667	0.458333	0.54321
total	343	197	253	99	293	248	288	1721	OA= 0.715		
Overall Assessment	Accuracy								0.715863	0.715863	0.715863
	Macro average								0.742834	0.69774	0.70624
	Weighted Average								0.742318	0.715863	0.716966

Table 4: Confusion matrices, overall and class-based statistics for RF, XGB, and SVM using 1-4pc PRISMA data.

RF	Sp	Tc	Mvs	MGD	VMs	Gr	WD	tot	precision	recall	f1-score
Sp	295	0	0	0	0	0	9	304	0.970395	0.860058	0.911901
TC	0	191	5	0	0	0	0	196	0.97449	0.969543	0.97201
MVs	4	6	197	24	3	0	1	235	0.838298	0.778656	0.807377
MGD	0	0	3	75	1	0	0	79	0.949367	0.757576	0.842697
VMs	6	0	40	0	269	0	5	320	0.840625	0.918089	0.877651
GR	0	0	0	0	0	230	1	231	0.995671	0.927419	0.960334
WD	38	0	8	0	20	18	272	356	0.764045	0.944444	0.84472
total	343	197	253	99	293	248	288	1721		OA= 0.888	
Overall Assessment				Accuracy					0.888437	0.888437	0.888437
				Macro average					0.904699	0.879398	0.888099
				Weighted Average					0.897252	0.888437	0.889341

XGB	Sp	Tc	Mvs	MGD	VMs	Gr	WD	tot	precision	recall	f1-score
Sp	319	1	0	0	0	0	7	327	0.975535	0.930029	0.952239
TC	0	187	9	0	0	0	0	196	0.954082	0.949239	0.951654
MVs	2	8	195	22	8	1	0	236	0.826271	0.770751	0.797546
MGD	0	1	5	77	1	0	0	84	0.916667	0.777778	0.84153
VMs	2	0	36	0	267	0	8	313	0.853035	0.911263	0.881188
GR	0	0	0	0	0	224	1	225	0.995556	0.903226	0.947146
WD	20	0	8	0	17	23	272	340	0.8	0.944444	0.866242
total	343	197	253	99	293	248	288	1721		OA= 0.895	
Overall Assessment				Accuracy					0.89541	0.89541	0.89541
				Macro average					0.903021	0.883819	0.891078
				Weighted Average					0.900405	0.89541	0.895841

SVM	Sp	Tc	Mvs	MGD	VMs	Gr	WD	tot	precision	recall	f1-score
Sp	329	0	2	0	0	0	6	337	0.976261	0.959184	0.967647
TC	0	191	9	2	0	0	0	202	0.945545	0.969543	0.957393
MVs	1	3	193	19	7	0	1	224	0.861607	0.762846	0.809224
MGD	0	3	6	78	1	0	0	88	0.886364	0.787879	0.834225
VMs	2	0	35	0	262	0	8	307	0.85342	0.894198	0.873333
GR	0	0	0	0	0	237	1	238	0.995798	0.955645	0.975309
WD	11	0	8	0	23	11	272	325	0.836923	0.944444	0.887439
total	343	197	253	99	293	248	288	1721		OA= 0.907	
Overall Assessment				Accuracy					0.907612	0.907612	0.907612
				Macro average					0.907988	0.896248	0.900653
				Weighted Average					0.909303	0.907612	0.907134

Table 5: Confusion matrices, overall and class-based statistics for RF, XGB, and SVM using all (234b) PRISMA bands

RF	Sp	Tc	Mvs	MGD	VMs	Gr	WD	tot	precision	recall	f1-score
Sp	110	0	0	0	0	0	1	111	0.990654	0.861789	0.921739
TC	0	79	2	4	0	0	0	85	0.951807	0.88764	0.918605
MVs	4	10	147	7	1	0	0	169	0.875	0.835227	0.854651
MGD	0	0	0	13	0	0	0	13	1	0.708333	0.829268
VMs	4	0	23	0	149	0	3	179	0.818681	0.851429	0.834734
GR	0	0	0	0	0	217	1	218	0.990909	0.995434	0.993166
WD	5	0	4	0	25	2	152	188	0.811828	0.961783	0.880466
total	123	89	176	24	175	219	157	963	OA= 0.900		
Overall Assessment	Accuracy								0.900312	0.900312	0.900312
	Macro average								0.91984	0.871662	0.890376
	Weighted Average								0.905812	0.900312	0.900588

XGB	Sp	Tc	Mvs	MGD	VMs	Gr	WD	tot	precision	recall	f1-score
Sp	115	0	0	0	0	0	1	116	0.991379	0.934959	0.962343
TC	0	82	0	2	0	0	0	84	0.97619	0.921348	0.947977
MVs	3	7	158	7	1	1	0	177	0.892655	0.897727	0.895184
MGD	0	0	0	15	0	0	0	15	1	0.625	0.769231
VMs	0	0	14	0	152	0	2	168	0.904762	0.868571	0.886297
GR	0	0	0	0	0	214	0	214	1	0.977169	0.988453
WD	5	0	4	0	22	4	154	189	0.814815	0.980892	0.890173
total	123	89	176	24	175	219	157	963	OA= 0.924		
Overall Assessment	Accuracy								0.924195	0.924195	0.924195
	Macro average								0.939972	0.886524	0.905665
	Weighted Average								0.929582	0.924195	0.924281

SVM	Sp	Tc	Mvs	MGD	VMs	Gr	WD	tot	precision	recall	f1-score
Sp	115	0	0	0	0	0	1	116	0.991228	0.918699	0.953586
TC	0	89	0	1	0	0	0	90	0.988889	1	0.994413
MVs	0	0	163	0	2	0	0	165	0.987879	0.926136	0.956012
MGD	0	0	0	22	0	0	0	22	1	0.916667	0.956522
VMs	1	0	13	0	154	0	2	170	0.914286	0.914286	0.914286
GR	0	0	0	0	0	218	0	218	1	1	1
WD	7	0	0	1	19	1	154	182	0.865169	0.980892	0.919403
total	123	89	176	24	175	219	157	963	OA= 0.955		
Overall Assessment	Accuracy								0.955348	0.955348	0.955348
	Macro average								0.963921	0.950954	0.956317
	Weighted Average								0.958079	0.955348	0.955716

Table 6: Strengths and limitations of RF, XGB, and SVM.

	RF	XGB	SVM
Advantages	Robust to overfitting problem	ability to alleviate overfitting effectively	Ability to handle high dimensionality data using relatively few training samples
	mostly ensures better performance	high computational efficiency	it provides a trade-off between time-efficiency and accuracy
	Errors can be ignored, even if overfitting or underfitting decision trees are present.	Handling missing data	Ability to manage small training data sets effectively
	RF classifier is relatively insensitive to mislabelled training data	Feature importance	SVM is one of the most memory-efficient methods,
Disadvantages	Less interpretable	Slow training time	Black-box model
	Sensitive to spatial autocorrelation of the training classes and to the proportions of the different classes within the training samples.	Limited interpretability	Computationally expensive
	Instabilities and Computationally expensive	Sensitivity to hyperparameters	Overfitting risk

Table 7. The spectral characteristics for the utilized bands of the optical datasets, and its extracted number of lineaments

Resolution (m)	Spectral Range	Optical Datasets	band	Wave length range (µm)	Central Wavelength (µm)	Lineaments number	Best wavelength
30m	VNIR	Landsat 8	1	0.433 - 0.453	0.442	706	L8 b4 (0.654)
			2	0.450 - 0.515	0.483	686	
			3	0.525 - 0.600	0.561	768	
			4	0.630 - 0.680	0.654	789	
			5	0.845 - 0.885	0.864	753	
		EO-1 ALI	1P	0.433 - 0.453	0.443	535	
			1	0.450 - 0.515	0.482	578	
			2	0.525 - 0.605	0.565	613	
			3	0.630 - 0.690	0.660	599	
			4	0.775 - 0.805	0.790	629	
			4P	0.845 - 0.890	0.867	627	
	SWIR	Landsat 8	6	1.560 - 1.660	1.609	784	L8 b6 (1.609)
			7	2.100 - 2.300	2.203	725	
		ASTER	4	1.600 - 1.700	1.650	576	
			5	2.145 - 2.185	2.165	539	
			6	2.185 - 2.225	2.205	582	
			7	2.235 - 2.285	2.260	423	
			8	2.295 - 2.365	2.330	453	
			9	2.360 - 2.430	2.395	459	
		EO-1 ALI	5P	1.200 - 1.300	1.250	643	
			5	1.550 - 1.750	1.650	751	
			7	2.080 - 2.350	2.215	603	
20m	VNIR	Sentinel 2A	5	0.694 - 0.714	0.704	1887	S2 b5 (0.704)
			6	0.731 - 0.749	0.740	1817	
			7	0.768 - 0.796	0.782	1844	
			8a	0.855 - 0.875	0.865	1770	
	SWIR	Sentinel 2A	11	1.565 - 1.655	1.610	1574	S2 b11 (1.610)
			12	2.100 - 2.280	2.190	1446	
15m	VNIR	Landsat 8	8	0.500 - 0.680	0.598	2951	L8 b8 (0.598)
		ASTER	1	0.520 - 0.600	0.560	2826	
			2	0.630 - 0.690	0.660	2852	
			3	0.780 - 0.860	0.820	2861	
10m	VNIR	EO-1 ALI	pan	0.480 - 0.690	0.585	5795	S2 b2 (0.490)
		Sentinel 2A	2	0.458 - 0.523	0.490	7081	
			3	0.543 - 0.578	0.560	7010	
			4	0.650 - 0.680	0.665	6935	
			8	0.785 - 0.900	0.842	6754	

Table 8: Band ratios for highlighting various mineral features using the four utilized sensors

Highlighted mineral feature	ASTER	Landsat 8	Sentinel 2	EO1 ALI
Ferrous iron	5/3 +1/2	7/5 + 3/4	12/8 + 3/4	9/6 or 9/5 3/4
	(van der Meer et al., 2012; Van der Meer et al., 2014)			
Ferric iron (Fe3+/Fe2+ iron oxides)	2/1	4/3	4/3	4/3
	(Pour et al., 2019; van der Meer et al., 2012; Van der Meer et al., 2014)			
Ferric oxide	4/3	6/5	11/8	8/6 or 8/5
	(Pour et al., 2019; van der Meer et al., 2012; Van der Meer et al., 2014)			
Gossan, (Fe3+/Fe2+ iron oxides) ferrous iron oxides	4/2	6/4	11/4	8/4
	(Pour et al., 2019; van der Meer et al., 2012)			
Laterite	4/5		11/12	
	(Van der Meer et al., 2014)			
Ferrous silicates (Biotite, chloride, amphibole)	5/4		12/11	
	(Van der Meer et al., 2014)			
Ferrous iron oxides	2/4	4/6	4/11	4/8
	(Pour et al., 2019)			
All iron oxides (Fe3+/Fe2+ and Fe-OH iron oxides)	-	4/2	4/2	4/2 or 4/1
	(Pour et al., 2019)			
Hydroxyl bearing alteration (Al-OH and Fe, Mg-OH)	4/5 or 6 or 7	6/7	11/12	8/9
	(Pour et al., 2019)			
Sabins ratio in RGB	4/7, 2/1, 4/3	6/7, 4/2, 6/5	11/12, 4/2, 11/8	8/9, 4/1, 8/6
	(Frutuoso et al., 2021)			
Carbonate/chlorite/epidote Mg-Fe-OH	(7 + 9)/8	ASTER bands 5:7 are only covered by band 7	ASTER bands 5:7 are only covered by band 12	ASTER bands 5:7 are only covered by band 9
	(Ninomiya et al., 2005; Pour et al., 2019; van der Meer et al., 2012)			
Dolomite/ Si-OH minerals	((6 + 8)/7)			
	(Pour et al., 2019; van der Meer et al., 2012)			
Epidote/Chlorite/Amphibole	(6 + 9)/(7 + 8)			
	(van der Meer et al., 2012)			
Amphibole /MgOH	(6 + 9)/8 and 6/8			

	(van der Meer et al., 2012)			
Carbonate	13/14			
	(van der Meer et al., 2012)			
Sericite/Muscovite/Illite/Smectite Al/Fe-OH	(5 + 7)/6			
	(Pour et al., 2019; van der Meer et al., 2012)			
Alunite/Kaolinite/Pyrophyllite	(4 + 6)/5			
	(van der Meer et al., 2012)			

Table 9: Thresholds, and anomalies of the detected hydrothermal alterations (and their intersections), using band ratios of the four utilized datasets.

BR	Mean	Standard Deviation	Threshold	Anomalies (Km^2)	Overestimated area
ASTER 4/7	116.73	62.20	178.93	252.1244	148.40755
ASTER 2/1	117.26	57.04	174.3	234.0096	183.1392
ASTER 4/3	132.89	57.37	190.26	217.644	150.767575
S2 11/12	128.86	58.06	186.92	240.2932	136.57635
S2 4/02	86.44	44.71	131.15	209.1736	158.30321
S2 11/8	137.46	56.01	193.47	211.134	144.257575
L8 6/7	111.77	55.52	167.29	219.0264	115.30955
L8 4/2	176.06	60.80	236.86	350.7412	299.8708
L8 6/5	136.79	60.80	197.59	216.6624	149.785975
ALI 8/9	118.64	51.40	170.04	205.8885	102.17165
ALI 4/1	172.55	43.08	215.63	234.5877	183.717313
ALI 8/6	169.39	53.55	222.94	240.5781	173.701675

Intersections	OH	iron oxides	Ferrous oxides
ASTER	252.1244	234.0096	217.644
Sentinel 2	240.2932	136.57635	211.134
L8	219.0264	115.30955	216.6624
ALI	205.8885	102.17165	240.5781
ASTER + Sentinel 2	146.57486	101.63106	114.72246
ASTER +L8	135.4027	87.13305	113.3808
ASTER +ALI	144.8665	73.12402	118.516675
four	103.71685	50.870387	66.876425

Table 10: The Eigenvector matrix values of bands, band ratio indices, and Relative Band Depths utilized for DPCA using the four datasets to highlight various alteration types.

Hydroxyl-bearing minerals				
Eigenvector (ASTER)	B1	B3	B4	B7
DPCA 1	-0.75661	-0.63646	-0.14441	-0.04012
DPCA 2	-0.6277	0.642843	0.419598	0.129167
DPCA 3	-0.18274	0.425821	-0.86022	-0.21286
DPCA 4	**0.01222**	**-0.01853**	**-0.25122**	**0.967676**
Eigenvector (S2)	B2	B8a	B11	B12
DPCA 1	-0.2338	-0.49105	-0.61177	-0.57441
DPCA 2	-0.69378	-0.51409	0.290978	0.411961
DPCA 3	-0.68009	0.68397	-0.04489	-0.26009
DPCA 4	**-0.03857**	**0.163603**	**-0.73421**	**0.65779**
Eigenvector (L8)	B2	B5	B6	B7
DPCA 1	0.18568	0.510246	0.630871	0.554232
DPCA 2	0.501779	0.677057	-0.30644	-0.44261
DPCA 3	**0.390401**	**-0.12282**	**-0.61093**	**0.677691**
DPCA 4	0.749219	-0.51591	0.367229	-0.19405
Eigenvector (ALI)	B2	B6	B8	B9
DPCA 1	-0.20929	-0.43703	-0.64853	-0.58704
DPCA 2	-0.63163	-0.61918	0.290954	0.364706
DPCA 3	**0.018854**	**0.071684**	**-0.69859**	**0.711673**
DPCA 4	-0.74625	0.648453	-0.08204	-0.12607
Iron oxides				
Eigenvector (ASTER)	B1	B2	B3	B4
DPCA 1	0.567561	0.660388	0.479535	0.108667
DPCA 2	**0.715437**	**-0.138838**	**-0.569369**	**-0.380385**
DPCA 3	0.293986	-0.282978	-0.161860	0.898497
DPCA 4	-0.282127	0.681568	-0.647817	0.190268
Eigenvector (S2)	B2	B4	B8a	B11
DPCA 1	0.265453	0.498315	0.529967	0.632734
DPCA 2	0.493719	0.511591	0.102312	-0.69574
DPCA 3	**0.586513**	**0.04036**	**-0.73503**	**0.337798**
DPCA 4	0.584618	-0.6988	0.410368	-0.03864

Eigenvector (L8)	B2	B4	B5	B6
DPCA 1	0.206659	0.455838	0.554507	0.664850
DPCA 2	0.388539	0.477569	0.323917	-0.718362
DPCA 3	**0.778045**	**0.071257**	**-0.590603**	**0.201883**
DPCA 4	-0.448303	0.747705	-0.488660	0.034262
Eigenvector (ALI)	B2	B4	B6	B8
DPCA 1	0.238313	0.483415	0.482739	0.690275
DPCA 2	0.412695	0.523427	0.267211	-0.69592
DPCA 3	**0.768503**	**-0.04186**	**-0.60948**	**0.190231**
DPCA 4	-0.42696	0.700415	-0.5693	0.055022
Ferric/ferrous iron oxides, Al/Fe-OH , and Mg-Fe-OH bearing minerals				
Eigenvector (ASTER)	B2/B1(ferrous)	B4/B2 (ferric)	((B7 + B9)/B8) Mg-Fe-OH	((B5 + B7)/B6) Al/Fe-OH
DPCA 1	0.000343	0.000055	**-0.70566**	**0.708556**
DPCA 2	-0.00023	0.000046	0.708556	0.705655
DPCA 3	**0.999274**	0.038094	0.000405	-0.000084
DPCA 4	0.038094	**-0.99927**	0.000009	0.000069
Eigenvector (S2)	B4/B2 (iron oxides)	B11/B4 (ferrous)	B11/B8a (ferric)	B11/B12 (OH)
DPCA 1	0.283757	0.8326	0.474493	-0.0334